Microwave Imaging for Breast-Cancer Screening

Rubæk, Tonny; Meincke, Peter

Publication date:
2008

Document Version
Publisher's PDF, also known as Version of record

Microwave Imaging for Breast-Cancer Screening

PhD Thesis

Tonny Rubæk

February 2008

The work presented in this thesis was carried out at Ørsted·DTU in partial fulfillment of the requirements for the PhD degree at the Technical University of Denmark.

Supervisor:

Peter Meincke, Associate Professor, PhD,
Department of Electrical Engineering, Technical University of Denmark

Abstract

Microwave Imaging for Breast-Cancer Screening

A study on the use of microwave imaging for breast-cancer screening has been carried out. The study focuses on the development of an imaging algorithm in which nonlinear inverse scattering is used to create images of the interior of the breast. In addition to this, the antenna part of the imaging system is designed.

To investigate the performance of nonlinear inverse scattering applied for breast-cancer screening, the Dartmouth College microwave imaging system is studied. This system uses a Newton-based imaging algorithm to reconstruct the 2-D distributions of the constitutive parameters permittivity and conductivity of the breasts of the patients. Three different algorithms are developed for calculating the updates in this imaging algorithm and the different performances of the algorithms are illustrated by reconstructing data from a phantom measurement. The three algorithms are all based on the iterative CGLS algorithm but differ in how the amount of regularization is determined. Furthermore, it is shown that the imaging system is capable of detecting cancer in the breast of a patient.

In addition to the update algorithms for the Newton-based imaging algorithm, a contrast source inversion algorithm is developed in which the so-called *log-phase* formulation is applied. In this formulation, the measured data is represented using the logarithm of the amplitude and the unwrapped phase of the signals. This has been shown to improve the performance of the Newton algorithm when compared to the more widely used complex phasor formulation. The contrast source inversion algorithm is tested on patient data and the improvement obtained by using the log-phase formulation is demonstrated.

Finally, an algorithm and antenna system for 3-D imaging is developed based on the observations made during the work with the Dartmouth College 2-D imaging system. This system uses 32 antennas in a cylindrical setup and a Newton-based imaging algorithm to reconstruct the unknown distribution of constitutive parameters of a hemispherical imaging domain with a radius of 7.5 cm. The performance of this system is illustrated using simulated data.

Resumé

Mikrobølgebilleddannelse til brystkræftscreening

Et studium af brugen af mikrobølgebilleddannelse til brug ved brystkræftscreening er blevet gennemført. Dette studium fokuserer på udviklingen af en algoritme, hvori ulineær invers spredning benyttes til at skabe billeder af brystets indre. Udover algoritmen designes også antennedelen af mikrobølgesystemet.

For at undersøge, i hvilken grad mikrobølgebilleddannelse egner sig til brystkræftscreening studeres det billeddannelsessystem, der er i brug ved Dartmouth College. Dette system benytter en Newton-baseret algoritme til at rekonstruere den todimensionelle fordeling af permittivitet og ledningsevne i patienternes bryster. Tre forskellige algoritmer udvikles til at udregne opdateringerne i denne billeddannelsesalgoritme og algoritmernes virkemåde illustreres ved at rekonstruere data fra en fantommåling. De tre algoritmer er alle baseret på den iterative CGLS algoritme men bruger forskellige metoder til at bestemme hvor meget regularisering, der benyttes. Udover fantomdata rekonstrueres også data fra en patientmåling. Dette viser, at Newton-algoritmen er i stand til at finde kræftknuder.

Der præsenteres også en algoritme baseret på *contrast source inversion*. I denne algoritme benyttes *log-fase* formuleringen, som har vist sig at forbedre ydelsen af den Newton-baserede algoritme. I log-fase formuleringen bruges de målte signalers fase samt logaritmen af deres amplitude i stedet for den mere udbredte komplekse formulering, hvor signalernes real- og imaginærdel benyttes. Algoritmen testes på patientdata og forbedringen, som kan opnås ved brug af log-fase formuleringen, demonstreres.

Endeligt er der blevet udviklet en algoritme og et antennesystem til 3-D billeddannelse. Designet af dette system er baseret på de erfaringer, der er opnået ved arbejdet med 2-D systemet fra Dartmouth College og anvender 32 antenner i en cylindrisk opsætning samt en Newton-baseret algoritme. Den ukendte fordeling af de konstitutive elektromagnetiske parametre rekonstrueres i et hemisfærisk billeddannelsesområde med en radius på 7.5 cm. Systemets anvendelighed testes ved brug af simulerede data.

Preface

The work presented in this thesis has been carried out at the Ørsted·DTU department of the Technical University of Denmark (now part of the Department of Electrical Engineering). The PhD study was initiated in January 2005 and was funded primarily by a grant from the Danish Technical Research Council with supplemental funding from Trane's foundation, the Otto Mønsted Foundation, and the Villum Kann Rasmussen Foundation.

I thank my supervisor Peter Meincke for his support during the PhD study and my friends and colleagues at the Ørsted·DTU department. A special thank to Niels V. Larsen for his many useful comments on the material presented in this thesis.

In 2006, I was visiting Thayer School of Engineering at Dartmouth College in Hanover, New Hampshire, USA. I thank the entire microwave imaging group there for making my stay pleasant. In particular, I extend my gratitude to Paul M. Meaney for sharing his experience and for providing the data and the foundations of the software on which much of the work I did after I returned to Denmark is based.

The present edition of the thesis has been revised following the defense. The revisions consisted of correcting misprints and spelling errors which occurred in the original manuscript.

Kgs. Lyngby, May 2008

Tonny Rubæk

Table of Contents

Publications

The work carried out during the course of the PhD study is described in this thesis and in the papers found at the very end of the thesis. At the time of writing, these papers have all either been published or submitted for publication. I am the main author of four journal papers [JP1-JP4] and three conference papers [CP1-CP3]. In addition to this, I am the author of an internal report [IR1] and the co-author of one journal paper [JP5].

The four journal papers, of which I am the main author, are included at the end of this thesis:

[JP1] Tonny Rubæk, Paul M. Meaney, Peter Meincke, and Keith D. Paulsen, "Nonlinear microwave imaging for breast-cancer screening using Gauss-Newton's method and the CGLS inversion algorithm," *IEEE Transactions on Antennas and Propagation*, vol. 55, no. 8, pp. 2320-2331, 2007.

[JP2] Tonny Rubæk, Paul M. Meaney, Peter Meincke, and Keith D. Paulsen, "Analysis of the performance of an update algorithm for Newton-based nonlinear microwave imaging for breast-cancer screening," submitted to *IEEE Transactions on Medical Imaging*, October 2007.

[JP3] Tonny Rubæk, Paul M. Meaney, and Peter Meincke, "Microwave imaging for breast-cancer screening using contrast source inversion and the log-amplitude unwrapped phase formulation," submitted to *AEU - International Journal of Electronics and Communications*, February 2008.

[JP4] Tonny Rubæk, Oleksiy Kim, and Peter Meincke, "Computational validation of a 3-D microwave imaging system for breast-cancer screening," submitted to *IEEE Transactions on Antennas and Propagation*, February 2008.

The three conference papers are also included at the end of the thesis. These have all been published and presented:

[CP1] Tonny Rubæk and Peter Meincke, "Including antenna models in microwave imaging for breast cancer screening," *Proceedings of the European Conference on Antennas and Propagation EuCAP, 2006*, 2006.

[CP2] Tonny Rubæk, Peter Meincke, and Oleksiy S. Kim, "Three-dimensional microwave imaging for breast-cancer detection using the log-phase formulation," *Proceedings of the IEEE Antennas and Propagation International Symposium, 2007*, pp. 2184–2187, 2007.

[CP3] Tonny Rubæk, Peter Meincke, Oleksiy Kim, Paul M. Meaney, and Keith D. Paulsen, "Application of the log-phase formulation for three-dimensional microwave imaging," *Proceedings of the European Conference on Antennas and Propagation EuCAP, 2007*, 2007.

The internal report, which was the basis for the journal paper [JP2], is available upon request:

[IR1] Tonny Rubæk, *Analysis of a Euclidean-Distance Penalty Term-Based Update Algorithm for Newton-Based Nonlinear Microwave Imaging for Breast-Cancer Screening*, Report, IR-793, DTU Electrical Engineering, January 2008.

Finally I am the co-author of a paper published in the journal *Medical Physics*:

[JP5] Paul M. Meaney, Qianqian Fang, Tonny Rubæk, Eugene Demidenko and Keith D. Paulsen, "Log transformation benefits parameter estimation in microwave tomographic imaging," *Medical Physics*, vol. 36, no. 6, pp. 2014-2023, 2007.

Chapter 1

Introduction

Breast cancer is the most common type of cancer in women [1–4] and the most important prerequisite for a quick and effective treatment of the cancer is early detection [5]. To this end, screening programmes using X-ray mammography is the most widespread approach. This is due to the relatively low-cost and quick exams provided by this technique, with the exams being performed by nurses and lasting as little as 10 minutes. Such screening programmes have been shown to drastically reduce the frequency of breast-cancer deaths amongst women participating in the programmes compared to those not participating in screening programmes [6, 7].

X-ray mammography is, however, not perfect. In a study of the X-ray screening programs in New Hampshire [8], a sensitivity (ratio between positive diagnoses and the total number of cancers) of 72% and a specificity (ratio between negative diagnoses and the actual number of women without cancer) of 97% were reported but the positive predictive value (the fraction of positive diagnosed patients who actually had cancer) was only 10.6%. Other studies have reported positive predictive values as low as 3.3% [9] and sensitivities as low as 53% [10] with the poorest performance reported for women under the age of 50. The poor performance of X-ray mammography, when applied to younger women, can most likely be contributed to the fact that the breasts of younger women, in general, are denser, i.e., consist of a higher percentage of mammary glands and other non-adipose tissue types, than the breasts of older women [11, 12]. X-rays are attenuated much more in such tissue than in the adipose tissue, implying that cancerous tumors are likely not to show in X-ray images of the breasts of younger women. This is the main reason why X-ray screening programmes are usually offered only to women over the age of 50 [12].

The shortcommings of X-ray mammography imply that there is room for complementary imaging modalities, such as the well-known magnetic resonance and ultrasound imaging techniques [13] which allow for higher sensitivity and positive predictive values. These are, however, not suitable for large-scale screening programmes as they are too expensive and time

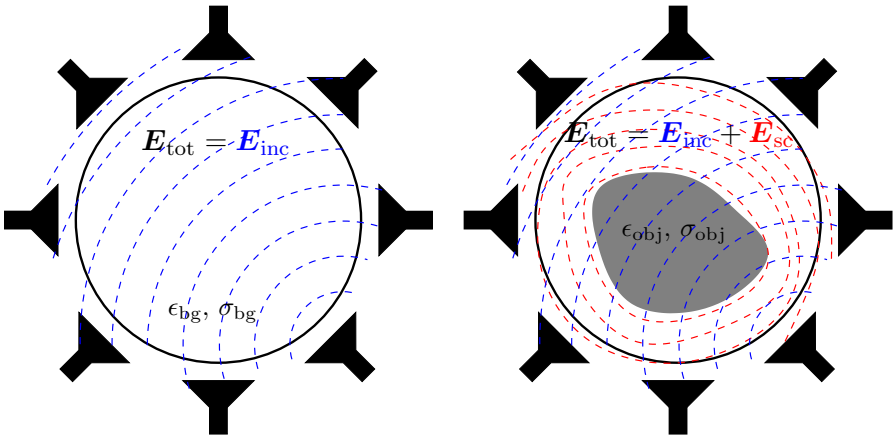

(a) Empty system (b) Object inserted in system

Fig. 1.1: *Schematic of a microwave imaging system. A known incident field is transmitted by one antenna and the response is measured on one or more receiving antennas. When an object with constitutive parameters ϵ_{obj} and σ_{obj} different from those of the background, ϵ_{bg} and σ_{bg}, is present in the imaging domain, a scattered field will arise and the total field measured by the antennas will be the sum of the incident and the scattered field.*

consuming, requiring highly specialized doctors to perform the exams.

1.1 Microwave Imaging

In recent years, an increasing number of research groups have proposed microwave imaging as an imaging modality suitable for breast cancer screening [14–25]. Microwave imaging is based on the fact that an inhomogeneity in the constitutive electromagnetic parameters (permittivity and conductivity) of a material will cause an incident electromagnetic field to scatter. To illustrate the basics of microwave imaging and to introduce the nomenclature used in this thesis, a schematic of a microwave imaging system is shown in Fig. 1.1. The background medium, in which the microwave imaging system is embedded, is characterized by the permittivity ϵ_{bg} and conductivity σ_{bg}[1] and the circular area in the center of the antenna group represents the imaging domain. This domain is irradiated by a transmitting antenna and the total field may be measured by one or more antennas positioned outside the domain. When an object with contrast in the constitutive parameters is positioned inside the imaging domain, a scattered field will arise. The total

[1] Although the permeability μ is also a constitutive electromagnetic parameter, it is common practice to assume that the materials in and around the imaging system are non-magnetic and thus have a permeability equal to that of free space. This is also assumed throughout this thesis.

field, measured by the receiving antennas, is the sum of the incident field and the scattered field

$$\boldsymbol{E}_{\text{tot}} = \boldsymbol{E}_{\text{inc}} + \boldsymbol{E}_{\text{sc}} \tag{1.1}$$

and will thus change when the scattered field is introduced. From this change in the measured field, information about the location and/or constitutive parameters of the scattering object, also known as the scatterer, may be obtained.

1.2 Electromagnetic Properties of Breast Tissue

Since the scattered field only occurs if there is a contrast in the constitutive parameters between the object to be imaged, i.e., the cancerous tumors, and the medium in which it is embedded, i.e., the surrounding tissue, it is of interest to establish if such a contrast exists.

Due to research in radar and communication systems, great advances were made during World War II in research of microwave technology [26]. After the war, this resulted in a surge of research in microwave technology for other purposes, including biomedical applications. In 1949, T. S. England [27] reported the electromagnetic parameters for a range of different human tissues, including breast tissue, at 10 GHz and in 1950 [28] he published a survey for the frequencies 3 GHz and 23.6 GHz. At all three frequencies he found a significant contrast between the cancerous tissue and the surrounding fatty breast tissue, e.g., at 3 GHz the fatty breast tissue was found to have a relative permittivity between 5.2 and 7.2 and a conductivity between 0.26 S/m and 0.29 S/m while the values for the cancerous tissue was found to be between 57 and 62 for the relative permittivity and between 2.5 S/m and 3.0 S/m for the conductivity.

A number of other investigations of the electromagnetic properties of human tissues followed, with comprehensive reviews available in [29–31], and a general trend in these investigations is the high values of permittivity and conductivity of the cancerous tissues when compared to the host tissues, e.g., breast, liver, and lung tissue. This was also the results of the investigation carried out at Duke University and published in 1994 [32] wherein a range of different tissue types were investigated at frequencies ranging from 50 to 900 MHz. In recent years, the increased number of research groups working on microwave imaging for breast cancer detection has resulted in a number of publications on the difference in constitutive parameters between the cancerous tumors of the breast and the surrounding breast tissue. Of these investigations, two are of particular interest: 1) At the University of Wisconsin, Madison a large study has been carried out and the results were published in 2007 [33, 34]; 2) At Dartmouth College, a microwave system has been applied for breast imaging for a number of years and in 2004 [35]

	T. S. England	Dartmouth College	Duke University
Normal tissue	5.2 – 7.2 at 3 GHz 3.6 at 10 GHz 3.0 – 3.3 at 23.6 GHz	6.0 – 36.1 at 600 MHz 7.0 – 16.0 at 1.3 GHz (av.) 8.0 – 29.0 at 1.3 GHz (fib.)	21.0 at 50 MHz 17.0 at 600 MHz 15.0 at 900 MHz
Cancerous tissue	56.9 – 62.3 at 3 GHz 33.8 – 37.4 at 10 GHz 24.0 – 30.7 at 23.6 GHz	– – – – – – – – – – – –	80.0 at 50 MHz 62.4.0 at 600 MHz 62.0 at 900 MHz

Table 1.1: *Summary of the published values of the relative permittivity of normal and cancerous breast tissue reported by T. S. England [27, 28], the research group at Dartmouth College [35, 36], and the research group at Duke University [32]. The data from Dartmouth College [36] is divided into values for the average breast tissue (av.) and fibroglandular tissue (fib.) and does not include cancerous tissue.*

	T. S. England	Dartmouth College	Duke University
Normal tissue	0.26 – 0.29 at 3 GHz 0.50 at 10 GHz 0.92 – 1.92 at 23.6 GHz	0.1 – 1.11 at 600 MHz 0.17 – 0.60 at 1.3 GHz (av.) 0.20 – 0.85 at 1.3 GHz (fib.)	0.11 at 50 MHz 0.14 at 600 MHz 0.18 at 900 MHz
Cancerous tissue	2.53 – 2.96 at 3 GHz 3.55 – 4.46 at 10 GHz 18.6 – 24.8 at 23.6 GHz	– – – – – – – – – – – –	0.60 at 50 MHz 1.00 at 600 MHz 1.12 at 900 MHz

Table 1.2: *Summary of some of the published values of the conductivity (in S/m) of normal and cancerous breast tissue reported by T. S. England [27, 28], the research group at Dartmouth College [35, 36], and the research group at Duke University [32]. The data from Dartmouth College [36] is divided into values for the average breast tissue (av.) and fibroglandular tissue (fib.) and does not include cancerous tissue.*

the preliminary findings for women without cancer were published and additional data were made available in 2007 [36].

A few of the reported values are shown in Tables 1.1 and 1.2 and some of the data from the University of Wisconsin, Madison study are shown in Fig. 1.2. The results, in general, confirm a contrast between the healthy and cancerous breast tissue, albeit the University of Wisconsin, Madison study suggests that some overlap in the constitutive parameters may exist between the most dense healthy tissue (low adipose content) and the cancer tissue. However, information lacks on whether this overlap has been observed in patients or if patients with dense normal tissue also have high-valued cancerous tissue. In the latter case, a contrast between the healthy and cancerous tissue will still exist and microwave imaging may be used to detect the cancer.

In addition to this, the studies reveal three other important characteristics about the breast tissue: First, the constitutive parameters of both the cancerous tissue and the healthy tissue are frequency dependent. Second, the parameters of the normal tissue show considerable variations from patient to patient and between the different types of healthy tissue, e.g., between

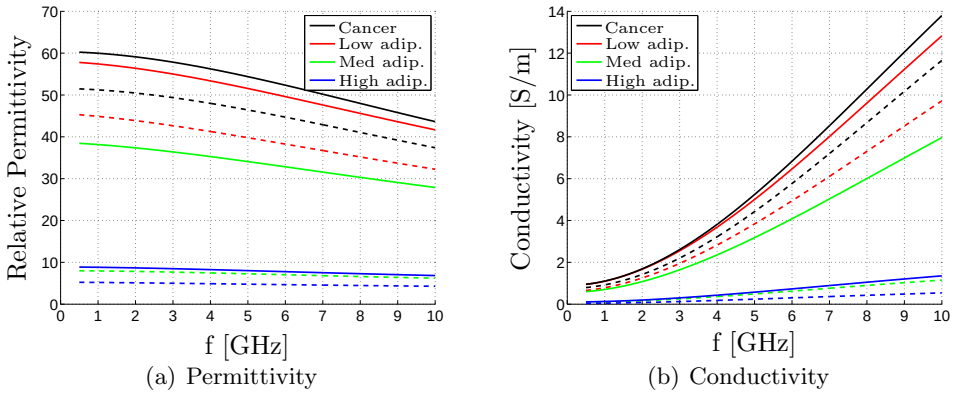

(a) Permittivity (b) Conductivity

Fig. 1.2: *Permittivity and conductivity values from the University of Wisconsin, Madison study [34]. The data represents the values for cancerous tissue (black line) and normal tissue obtained from cancer surgeries with low, medium and high content of adipose tissue (red, green, and blue lines, respectively). For each tissue type, the data for the 25 percentile is given by the dashed line and the data for the 75 percentile by the solid line.*

the fatty and the fibroglandular tissue. In fact, in [37] the breast tissue was classified as the human tissue with largest variations in the constitutive parameters among a number of different tissue types. Third and finally, all except the most fatty breast tissues have considerable losses (as indicated by the increased conductivity), and the losses increase with frequency. This should all be kept in mind when developing microwave imaging systems for breast cancer screening.

1.3 Microwave Imaging Techniques

A number of different microwave imaging setups, modalities, and algorithms exists for extracting information from measurements of the total field. The most simple measurement setup is the monostatic in which the same antenna is used both for transmitting the incident field and for measuring the resulting total field. Additional information about the scatterer may be obtained by moving the antenna to different positions, a technique known as multi-monostatic measurements [38–40]. Ground penetrating radar has been one of the major research topics in microwave imaging [38, 41–45] and for this application, the multi-bistatic setup is widely used [46–49]. In this configuration, two antennas are applied; one transmitting, the other receiving, hence the term bistatic. This pair of antennas may then be moved around the imaging domain to obtain information about the scattering objects from multiple transmit-receive positions. The last type of commonly used measurement setups is the multistatic setup in which several antennas

are used [42, 50–52]. In this setup, the spatial variation of the measurements, obtained by moving the antennas in the multi-monostatic and multi-bistatic setups, is obtained by using each antenna of the measurement system, in turn, as transmitter and measuring the total field at the other antennas of the imaging system.

The imaging modalities may be characterized by the way they utilize the frequency spectrum, e.g., single-frequency [53, 54], multi-frequency [55, 56], or time-domain ultrawideband[2] [15, 24, 57]. The algorithms may be characterized by the way they utilize the measured data, by the assumptions or *a priori* knowledge applied, and by range of contrasts they can accurately reconstruct. A commonly used assumption in microwave imaging algorithms is that the scattering problem is invariant in one direction. In this way, the imaging problem can be reduced to a 2-D scalar problem from the 3-D vectorial problem prescribed by Maxwell's equations, thereby greatly reducing the computational complexity.

1.3.1 Ultrawideband Techniques

The most widespread modality for microwave imaging of the breast is ultrawideband (UWB) techniques in which the incident field is a short pulse. The use of UWB for microwave imaging of the breast was first reported by Hagness *et al.* [58] and Fear *et al.* [59] who applied both multi-monostatic and multistatic imaging systems. Following these preliminary studies, several research groups have published results using UWB radar approaches [14–17, 19, 21, 24, 25]. A common feature in these systems is the use of a coupling liquid for reducing the contrast between the background and the breast, thereby maximizing the amount of energy coupled to the interior of the breast [60–62].

The imaging algorithm most frequently applied for UWB systems is the confocal or delay-and-sum imaging algorithm [14, 19, 59, 63], a technique which has been used in synthetic aperture radar for many years [64, Sec. 6.4]. When this algorithm is used, a short pulse is transmitted and the response in time is measured at the receiving antennas. The interior of the breast is then divided into a number of pixels and the resulting image is created by adding the measured signals delayed by the travel time for the pulse from the transmitting antenna to the individual pixels and back to the receiver. If a scatterer is present at a pixel, the sum of the delayed signals will be at a maximum. This type of algorithm assumes that the scattering effects are due to point scatterers and that the scattered fields from the individual point scatterers do not interact with other scatterers in the imaging domain. Hence, the imaging problem is solved as a linear inverse problem.

[2]The ultrawideband techniques are most often synthesized from a set of single-frequency measurements and could thus also be characterized as multi-frequency techniques.

An accurate estimate of the travel time from the antennas to each pixel in the imaging domain is a necessity for using the confocal imaging algorithm. This implies that the constitutive parameters of the healthy tissue must be known in advance which may pose a problem, given the large variations in tissue properties described above. In addition to this, the confocal imaging algorithm seems to have difficulties in dealing with differences in the background constitutive parameters, i.e., it is required that the coupling liquid is closely matched to the breast tissue of the patient. The most common way to circumvent this problem is by assuming that the breast is primarily fatty with constitutive parameters corresponding to the high-adipose content tissue in Fig. 1.2 and a variation of $\pm 10\%$ or so. The coupling liquid can then be chosen to have parameters equal to the average of the breast tissue. When operating in such environments, where the average background values are known and have only small variations, promising results have been reported for both simulations and phantom measurements [15, 19, 57, 62, 65–69]. However, even in these setups some challenges still exist, especially in terms of removing the reflection from the skin of the breast, known as skin subtraction [70–75]. The reflections from the skin are by far the most dominating contribution to the measured responses and different techniques have been applied for minimizing their influence which otherwise may suppress the response from the tumor.

The delay-and-sum approach has been the subject of a considerable amount of research and has been extended in various ways in order to effectively deal with the difficulties arising when imaging the breast [62, 76–79]. At the time of writing, however, no patient exams have been published and it seems that there are still considerable challenges to be overcome before the algorithm can be applied for imaging actual breasts with unknown and frequency-dependent tissue parameters.

In recent years, finite-difference time-domain (FDTD) based time-reversal has emerged as a technique for UWB microwave imaging of the breast [17, 80–82]. In this technique, a more accurate model is used for back-propagating the electromagnetic field from the antennas to the interior of the imaging domain than in the confocal algorithm, thereby leading to better results. Although the time-reversal algorithms also require an estimate of the background values in the imaging domain they seem to be better able to deal with large regions of unknown constitutive parameters [83] and in particular, the algorithms are able to operate without the skin subtraction [81]. Recent research has shown that multiple targets may be separated, thereby enhancing the ability of the algorithms to detect multiple tumors [84]. Although the FDTD-based time-reversal algorithm is more computationally expensive than the confocal imaging algorithm, the fact that it seems to be better able to handle realistic imaging problems should make it appealing for imaging with UWB imaging systems.

1.3.2 Nonlinear Inverse Scattering

In addition to the UWB imaging systems, nonlinear inverse scattering, also known as nonlinear microwave tomography, has been reported used for microwave imaging of the breast [23, 51, 85]. In nonlinear inverse scattering, the measured field is used as input to an inverse problem with a forward problem based on Maxwell's equations. This forward problem is nonlinear in terms of the unknown constitutive parameters and solving the inverse problem is thus a non-trivial matter. Nonlinear inverse scattering is, however, capable of handling larger regions of unknown constitutive parameters and greater contrasts than the linear UWB algorithms.

Different imaging modalities have been applied for nonlinear inverse scattering for imaging of biological tissue: The most common types are single- or multi-frequency multistatic measurements [51, 56, 86] although multistatic time-domain approaches have also been applied [23]. The method was introduced for imaging of the breast by Meaney *et al.* in 1995 [51] and other significant work was performed by Semenov *et al.* [86, 87] who focused on imaging of the heart. As with the UWB techniques, a coupling liquid is often applied to maximize the power transmitted to the interior of the breast [88].

In most cases, the nonlinear inverse problem is solved using an algorithm based on the iterative Newton scheme or a method derived from this. In these algorithms, the distribution of constitutive parameters in the imaging domain is updated in steps. In each iteration, the scattered field from the current parameter distribution is calculated and compared with the measured field. The update of the distribution may then be found by linearizing the nonlinear inverse problem. A number of different implementations of the Newton algorithm have been reported, such as the Gauss-Newton algorithm [89, 90], the inexact Newton algorithm [55], and the conjugate-gradient algorithm with line search [91]. These techniques require that the scattered field is calculated in each iteration using a forward solver, e.g., based on FDTD [91], the finite-element method (FEM) [92] or the methods of moments (MoM) [90]. Such forward solvers are computationally expensive and this is most likely the reason why the nonlinear imaging algorithms are not as widely applied as the computationally less expensive linear UWB algorithms. Furthermore, most applications of nonlinear inverse scattering has been done using 2-D models [55, 86, 91, 92] or simplified, scalar 3-D models [93] to reduce the computational complexity of the inverse problem with only a few full vectorial 3-D inversion algorithms reported [85, 90].

In addition to the Newton-based algorithms, genetic algorithms have been applied for solving the nonlinear imaging problem [94, 95]. The use of genetic algorithms and similar global optimization algorithms ensures that the solution obtained is the best global solution and not an erroneous local optimum which might be the result of a Newton-based algorithm. The global optimization algorithms, however, require the solutions of a consider-

ably greater number of forward problems than the Newton-based algorithms before convergence is reached. This makes them prohibitively slow for most imaging purposes and explains their limited use.

A third method for solving the nonlinear inverse problem is the iterative contrast source inversion. This approach was introduced in 1997 by van den Berg *et al.* [96] and is capable of solving the nonlinear inverse problem without a forward solver. Instead, two coupled sets of linear equations are solved in each iteration. A number of different implementations of this algorithm exist and have proved successful for microwave imaging of high-contrast objects, including biological tissues [20, 97–102].

1.4 This Thesis

At the Technical University of Denmark (TUD), a research project began in 2005 with the purpose of developing a microwave imaging system suitable for breast-cancer screening. Several persons are or have been involved in this project and all aspects of the design of the imaging system are covered: From the design of the hardware to development of the imaging algorithm. The complete imaging system consists of three major parts: A patient test bed and measurement setup with an array of antennas to transmit the incident field and measure the resulting total field; a microwave system connected to the antennas, capable of feeding the antennas, collect the received signals, and store the data digitally; and finally an imaging algorithm to transform the collected data into images that are easily understood by the end users, i.e., the clinical personnel.

This thesis is intended to give an overview of the work carried out by the author during the PhD study entitled "Microwave Imaging for Breast-Cancer Screening" as part of the development of the TUD imaging system. The PhD study covers the design of the antenna system for the patient test bed and the development of the imaging algorithm. A part of the work has been carried out in cooperation with the microwave imaging group at Dartmouth College, led by Dr. Paul M. Meaney. This cooperation was initiated during a 7 month visit at Dartmouth College in the spring and summer of 2006.

In addition to this overview, 4 journal and 3 conference papers, describing the work carried out during the PhD study, have been published or submitted. These are included at the end of the thesis. At the time of writing, one of the journal papers and all of the conference papers have been published and the remaining three journal papers have been submitted.

This thesis is organized as follows: The work carried out using the Dartmouth College imaging system is presented in Chapter 2. This work is focused on the development and analysis of different update algorithms for the Newton-based imaging algorithm utilized in this system and includes a

description of two new update algorithms developed during the PhD study. Also, a contrast source inversion algorithm developed for imaging of the breast is presented in this chapter. In Chapter 3, the design of the TUD imaging system is presented, including a description of both the antenna system and the imaging algorithm. Also a few results obtained using simulations of the TUD imaging system are presented to illustrate the effects of some of the decisions made when designing the system.

Chapter 2

The Dartmouth College Imaging System

At Dartmouth College, a system for microwave imaging of the breast has been deployed for clinical tests for a number of years. This system uses a multistatic measurement setup and Newton-based nonlinear inverse scattering for creating images. During a stay at Dartmouth College in the spring and summer of 2006, a collaboration between the microwave imaging group at the Technical University of Denmark and the microwave imaging group at Dartmouth College, led by Dr. Paul M. Meaney, was initiated. This collaboration has resulted in a body of research on how to efficiently calculate the updates in the Newton algorithm.

In this chapter, an overview of the research, carried out during the PhD study, using the Dartmouth College imaging system, is presented. The most significant parts of this work are presented in details the journal papers [JP1-JP3, JP5]. In Sections 2.1 and 2.2, the Dartmouth College imaging system and the basics of the Newton-based imaging algorithm are described. In Section 2.3, the different measures of the image-reconstruction quality are introduced. In Section 2.4, the algorithms used for calculating the updates in the Newton algorithm are described. Images of a phantom measurement are presented to illustrate the effects of the different algorithms and in Section 2.5, images from a patient exam is presented to illustrate the use of microwave imaging as a tool for breast-cancer screening. Finally, in Section 2.6, a contrast source inversion algorithm, developed for use with the Dartmouth College microwave imaging system, is presented.

2.1 The Imaging System

The imaging system applied for microwave imaging of the breast at Dartmouth College consists of a 16-antenna setup, capable of operating at frequencies ranging from 500 MHz to 2.3 GHz. Two photos of the imaging system are shown in Fig. 2.1 and schematics are shown in Fig. 2.2. During

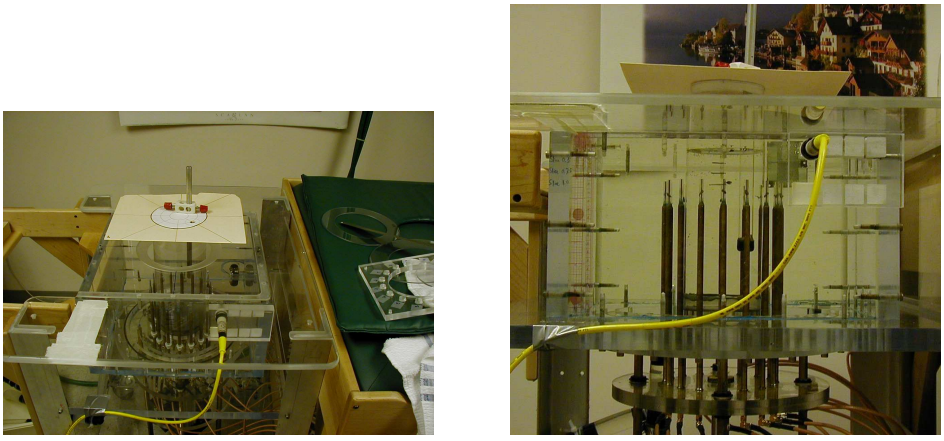

(a) Top view (b) Side view

Fig. 2.1: *The Dartmouth College microwave imaging system. The 16 antennas are positioned in a circular setup which may be moved vertically to different positions to cover the entire breast. During exams, the patient lies prone with her head to the left and feet to the right in the images. The aperture through which the breast is to be suspended is visible in the top of the Plexiglas measurement tank. Photos courtesy of Paul M. Meaney.*

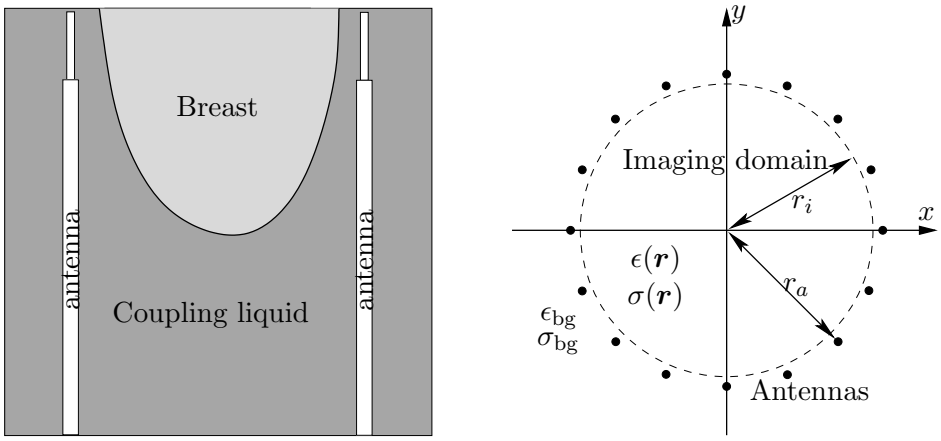

(a) Antennas and breast (b) Imaging domain

Fig. 2.2: *Schematic of the Dartmouth College imaging system. The antennas are moved vertically through seven measurement positions. The antennas are positioned in a circular setup with radius $r_a = 7.56$ cm and the imaging domain has a radius of $r_i = 7.25$ cm.*

exams, the patient is to lie prone on the examination table with her breast suspended through the aperture in the top of the measurement tank, seen in the photos in Fig. 2.1. This tank is filled with a glycerin-water coupling liq-

uid which mimics the constitutive parameters of the breast. The constitutive parameters of the liquid may be changed by changing the glycerin-to-water ratio, thereby allowing for the liquid to be matched to the breast whether this is fatty or dense. Since the liquid is lossy, the reflected signals from the side of the measurement tank are attenuated, implying that the system is not influenced by these reflections or by scattering objects outside the measurement tank.

The $n_{\text{ants}} = 16$ antennas used in the system are of a simple monopole type, consisting of a coaxial cable from which the outermost 3.4 cm of the outer conductor has been stripped [51]. When inserted in the lossy coupling liquid this antenna is quite broadband, with a return loss of no less than 9 dB in the frequency spectrum used in the imaging system.

As indicated by the circular setup, the Dartmouth College imaging system creates images of the breast under the assumption of a 2-D scattering problem. During patient exams, the antennas are moved vertically through 7 different measurement positions to cover the entire breast. At each of the 7 imaging planes, each of the antennas, in turn, acts as transmitter while the response is measured on the remaining 15 antennas, yielding a total of $n_{\text{meas}} = 240$ measurements per imaging plane. The radius of the antenna array is $r_a = 7.56$ cm and the radius of the imaging domain, indicated by the dashed circle in Fig 2.2(b), is $r_i = 7.25$ cm.

For a more thorough description and discussion of the Dartmouth College imaging system, the reader is referred to the extensive body of literature published by Meaney *et al.* [22, 51, 88, 103–106].

2.2 The Newton Algorithm

The imaging algorithm applied for reconstructing the images uses the data measured at a single frequency and the large frequency band covered by the system allows for choosing the best frequency for the reconstruction. The unknown distribution of constitutive parameters in the imaging domain is represented using the squared complex wave number

$$k^2(\boldsymbol{r}) = \omega^2 \mu_0 \epsilon(\boldsymbol{r}) + i\omega\mu_0\sigma(\boldsymbol{r}). \tag{2.1}$$

Herein, the time-notation $\mathrm{e}^{-i\omega t}$ is assumed and ω is the angular frequency. The unknown permittivity and conductivity are given by ϵ and σ, respectively, while the permeability throughout the imaging domain is assumed to be equal to that of free space, μ_0. To reconstruct the distribution of the squared complex wave numbers, the 2-D imaging domain is discretized into L regions in which the wave number is assumed constant, i.e.,

$$k^2(\boldsymbol{r}) = k_l^2 \quad \text{for} \quad \boldsymbol{r} \in \boldsymbol{R_l} \tag{2.2}$$

with $l = 1, 2, 3, \ldots, L$. Using the discretized imaging domain, the distribution of squared complex wave numbers may be found by solving the nonlinear inverse problem

$$\underline{k}^2 = \text{argmin} \left\| \underline{S}_{\text{meas}} - \underline{S}_{\text{calc}}(\underline{k}^2) \right\|_2^2 = \text{argmin} \left\| \underline{S}_{\text{res}}(\underline{k}^2) \right\|_2^2 \quad \text{subj. to regularization.} \tag{2.3}$$

In this expression, the vector $\underline{S}_{\text{meas}}$ holds the measured responses and the vector $\underline{S}_{\text{calc}}(\underline{k}^2)$ holds the corresponding calculated responses for the distribution of squared wave numbers given by $\underline{k}^2$. The vector $\underline{S}_{\text{res}}(\underline{k}^2)$ is the residual vector and since the inverse problem is ill-posed, regularization must be applied when solving it.

The effects of using a 2-D algorithm for reconstructing images of what is actually a 3-D scattering problem has been treated in [107] and in the conference paper [CP3]. It has been found that although the 3-D effects do degrade the performance of the imaging algorithm, the algorithm is still capable of reconstructing accurate images of most scatterers.

The nonlinear inverse problem (2.3) is solved using an iterative Newton scheme in which the following steps are performed at each iteration:

1. Calculate the elements of the vector $\underline{S}_{\text{calc}}(\underline{k}_n^2)$ and the Jacobian of the scattering problem $\underline{\underline{J}}(\underline{k}_n^2)$.

2. Update the residual vector $\underline{S}_{\text{res}}(\underline{k}_n^2)$ and find the update vector $\underline{\Delta k}_n^2$ by solving the linear inverse problem

$$\underline{\Delta k}_n^2 = \text{argmin} \left\| \underline{\underline{J}}(\underline{k}_n^2)\underline{\Delta k}_n^2 - \underline{S}_{\text{res}}(\underline{k}_n^2) \right\|_2^2 \quad \text{subj. to regularization.} \tag{2.4}$$

3. Update the distribution of the squared wave numbers using

$$\underline{k}_{n+1}^2 = \underline{k}_n^2 + \alpha_n \underline{\Delta k}_n^2 \tag{2.5}$$

with α_n being the Newton step [108, Ch. 1].

Step 1, the calculation of the forward solution, is by far the most time consuming step in the algorithm, lasting between 30 and 100 times as long as the other two steps combined. The algorithm is initialized with the elements of $\underline{k}_0^2$ all equal to those of the coupling liquid, i.e., the background of the imaging system. The termination of the algorithm may be determined in different ways as described below but in general the algorithm never uses more than 20 iterations before convergence is reached. As indicated in (2.4), the regularization needed to solve the nonlinear problem (2.3) is applied when calculating the updates in the Newton algorithm.

The PhD study has focused mainly on steps 2 and 3 of the algorithm, that is, on how to best update the constitutive parameters. This work is described in details in Section 2.4.

2.2.1 Forward Solver

The forward solver applied for calculating the elements of $\underline{S}_{\text{calc}}(\underline{k}_n^2)$ uses a 2-D hybrid-element method in which the imaging domain is modeled using a finite-element mesh and the uniform background is modeled using a boundary-element method [92]. The hybrid method is advantageous compared to a pure finite-element method because it eliminates the need for using approximate boundary conditions. In the model, the transmitting antenna is modeled as a point source and the effects of the presence of the non-transmitting antennas in the vicinity of the imaging domain are modeled using electromagnetic sinks at the positions of the antennas as described in [109, 110].

The finite-element representation of the imaging domain uses the dual-mesh scheme presented in [111]. In this way, the imaging domain is represented by 559 nodes when the constitutive parameters are determined, i.e., $L = 559$, while the mesh used for solving the forward scattering problem has a total of 3903 nodes. This ensures that the finite-element mesh used for solving the forward problem has an adequate number of nodes while the number of unknowns in the inverse problem is kept at a level adequate to represent the smallest recoverable objects but no larger, since this would increase the computational burden of calculating the updates.

The adjoint method is applied for calculating the Jacobian matrix of the scattering problem [112]. Using this approach, the calculation of the Jacobian is reduced to a simple matrix product which consumes only a small fraction of the total computational time used by the forward solver.

2.2.2 Log-Phase Formulation

A key feature in the imaging algorithm applied at Dartmouth College is the use of the so-called log-phase formulation which was introduced for microwave imaging by Meaney *et al.* in 2001 [53]. In most imaging algorithms, the measured signals are represented by the difference between the measured complex signals of an empty system and the corresponding signals of a system with a scatterer inserted. In this way, each antenna combination yields two elements, $S_{\Re}^{t,r}$ and $S_{\Im}^{t,r}$, in each of the vectors $\underline{S}_{\text{meas}}$ and $\underline{S}_{\text{calc}}$, given by

$$S_{\Re}^{t,r} = \text{Re}\left\{ S_{\text{obj}}^{t,r} - S_{\text{empty}}^{t,r} \right\} \tag{2.6a}$$

and

$$S_{\Im}^{t,r} = \text{Im}\left\{ S_{\text{obj}}^{t,r} - S_{\text{empty}}^{t,r} \right\} \tag{2.6b}$$

wherein $S_{\text{obj}}^{t,r}$ and $S_{\text{empty}}^{t,r}$ are the signals for antenna t transmitting and antenna r receiving with the scatterer inserted or removed from the imaging domain, respectively. The linear update problem (2.4) is thus an underdetermined $2n_{\text{meas}}$-by-$2L$ (480-by-1118) element problem.

By taking the logarithm of the complex-valued measurement $S^{t,r}$, a complex number is obtained, yielding the logarithm of the amplitude and the phase of the measurement

$$\log S^{t,r} = \log|S^{t,r}| + i\angle S^{t,r}. \tag{2.7}$$

When using the log-phase formulation, this complex number is used as the basis for the elements of the vectors $\underline{S}_{\text{meas}}$ and $\underline{S}_{\text{calc}}$. Each antenna combination is represented by two real-valued elements given by

$$S_{\text{l}}^{t,r} = \log|S_{\text{obj}}^{t,r}| - \log|S_{\text{empty}}^{t,r}| \tag{2.8a}$$

and

$$S_{\angle}^{t,r} = \angle|S_{\text{obj}}^{t,r}| - \angle|S_{\text{empty}}^{t,r}| \tag{2.8b}$$

wherein $\angle$ denotes the unwrapped phase. As described in [53, 113, JP4, CP2, JP5], the improved performance obtained when using the log-phase formulation is due to two things: First, the log-phase formulation weights the measurements with large relative changes more in the reconstructions than measurements with small relative changes. This improves the performance because the signals which change the most relatively when the scatterer is inserted into the imaging domain also hold the most information about the scatterer. The complex formulation, on the other hand, weights the signals based on the absolute changes. In measurement environments with lossy backgrounds, this may pose a problem because large absolute but small relative changes are often observed by receiving antennas neighbouring the transmitting. And since the large relative changes observed by antennas on the opposite side of the measurement system are often quite small in absolute terms, the algorithm is likely to ignore these measurements and the information available in them.

Second, the log-phase formulation allows for the algorithm to solve the imaging problem using multiple Riemann sheets since the unwrapped phase is used. This implies that phase changes of more than $\pm\pi$ may be correctly reconstructed. This is not possible when using the complex formulation wherein all measured signals are mapped to the same Riemann sheet.

In terms of computational demands, there is not much difference between the complex and the log-phase formulations: In both formulations, the linear update problem involves a Jacobian with $2n_{\text{meas}}$-by-$2L$ elements. During the reconstructions, the log-phase formulation requires that the Jacobian is transformed to log-phase formulation, which is easily done using the chain rule. In addition, the log-phase formulation requires that the phases of the measured and calculated signals are unwrapped. The measured signals may be unwrapped using the approach outlined in [53, JP4] which can be implemented efficiently in a simple preprocessor. The phases of the calculated signals are unwrapped in terms of the reconstructed contrast as outlined

in [53, JP4, CP2] and to this end, the Newton step α_n in (2.5) plays an important role. The Newton step may be determined on the basis of the norm of the update vector $\underline{\Delta k}_n^2$ as described in [JP1], on the basis of the linearized phase as described in [JP4], or it may be a fixed scalar as is the case with the imaging algorithm applied at Dartmouth College, described in Section 2.4.

2.3 Measures of Reconstruction Quality

In the journal paper [JP2] and the internal report [IR1], six different measures of the quality of the reconstructed images were presented. Two of these are related to the residual vector while the remaining four are related to the reconstructed distributions of permittivity and conductivity.

The normalized norm of the residual vector is a widely applied measure of the quality of the reconstruction [55, 89, 90], indicating how well the imaging algorithm minimizes (2.3). In this thesis, the normalized norm is given by

$$\eta_n = \frac{\left\| \underline{S}_{\text{res}}(\underline{k}_n^2) \right\|_2}{\left\| \underline{S}_{\text{res}}(\underline{k}_0^2) \right\|_2}. \tag{2.9}$$

The other measure related to the residual vector is the goodness-of-fit value χ^2, indicating how well the distribution of the elements of the residual vector fits a normal distribution with zero mean. As described in [JP5], the distribution of the elements should be normally distributed or it may be shown that the solution is compromised. The best-fit normal distribution with zero mean may be determined using a maximum-likelihood estimator [114, Ch. 8]. To test the fit of the data to this distribution, the range of values covered by the elements of the residual vector is divided into n_{bins} discrete bins and the value of χ^2 is calculated using

$$\chi^2 = \sum_{k=1}^{n_{\text{bins}}} \frac{(O_k - E_k)^2}{E_k} \tag{2.10}$$

wherein O_k and E_k are the observed and expected frequencies, respectively, of the individual bins [114, Ch. 9].

The two quantities above are applied when solving for the updates. The remaining four quantities, related to the norm and the spectrum of the difference between the reconstructed distributions of the constitutive parameters and the true distributions, are described in details in [JP2, Sec. 4] and [IR1, Ch. 4] and will not be dealt with here.

2.4 Update Algorithms

Apart from the accuracy of the forward solver, the algorithm used for calculating the updates is the most important part of the Newton algorithm. The update algorithm influences the performance in two ways: First, it affects how well the imaging algorithm is capable of handling objects of different sizes and contrasts. Second, it influences how many iterations are needed by the Newton algorithm to reconstruct the images. Hence, the update algorithm should be able to quickly and accurately extract information about scatterers from different measurement setups.

As described in [JP1], the update algorithm applied at Dartmouth College uses a Tikhonov-based regularization scheme in which the normal equation of the linear update problem (2.4) is solved, yielding

$$\left(\underline{\underline{J}}_n^T \underline{\underline{J}}_n + \lambda_n \underline{\underline{I}}\right) \underline{\Delta k}_n^2 = \underline{\underline{J}}_n^T \underline{S}_{\text{res}}(\underline{k}_n^2). \tag{2.11}$$

In this expression, $\underline{\underline{J}}_n$ is used instead of $\underline{\underline{J}}(\underline{k}_n^2)$ to improve readability. The regularization parameter λ_n is found using the approach outlined in [115] in which the value of λ_n is determined on the basis of the trace of $\underline{\underline{J}}_n^T \underline{\underline{J}}_n$, and the solution is found using a pivoted LU algorithm [116, Ch. 3]. The value of the Newton step α_n is chosen as a function of the Newton iteration number, starting at 0.1 in the first three iterations and then increased stepwise until it reaches a value of 0.5 after 12 iterations.

2.4.1 Simple Update Algorithm

To make the calculation of the updates more efficient a number of different algorithms have been tested. The iterative conjugate gradient least squares (CGLS) algorithm has been chosen as the underlying basis for the update algorithms due to its performance and computational simplicity. The CGLS algorithm is an iterative method based on the conjugate gradient method [117, Ch. 6]. In each iteration of the algorithm, five simple steps are performed, as outlined in [117, Eq. (6.14)] and [JP1, Sec. IV-A], and the solution to (2.4) obtained after m CGLS iterations, $\left[\underline{\Delta k}_n^2\right]^{(m)}$, is [117, Sec. 6.3]

$$\left[\underline{\Delta k}_n^2\right]^{(m)} = \operatorname{argmin} \left\| \underline{\underline{J}}_n \left[\underline{\Delta k}_n^2\right]^{(m)} - \underline{S}_{\text{res}}(\underline{k}_n^2) \right\|_2^2 \tag{2.12a}$$

subject to

$$\left[\underline{\Delta k}_n^2\right]^{(m)} \in \mathfrak{K}_m \left(\underline{\underline{J}}_n^T \underline{\underline{J}}_n, \underline{\underline{J}}_n^T \underline{S}_{\text{res}}(\underline{k}_n^2) \right). \tag{2.12b}$$

That is, the solution is the least squares solution with the restraint that the solution must lie in the m-dimensional Krylov subspace related to the problem, $\mathfrak{K}_m$. The regularizing effects of the CGLS algorithm can be explained by the fact that the m-dimensional Krylov subspace in most situations is a

good approximation to the subspace spanned by the first m right-hand singular vectors [117, Sec. 6.3.2]. The solution obtained by the CGLS algorithm is thus an approximation of the solution which is obtained if the truncated singular value decomposition is applied with the important difference that it is not necessary to calculate a computationally expensive singular value decomposition.

The regularizing effect of the CGLS algorithm is controlled by the number of iterations it is allowed to run, i.e., the number m of dimensions in the Krylov subspace. As m is increased the regularizing effects of the algorithm is decreased and vice versa. This is expected since increasing the value of m roughly corresponds to increasing the number of right-hand singular vectors in the solution. Hence, the performance of the imaging algorithm is to a large extent governed by the choice of m in the individual Newton iterations. The most simple configuration is to keep m constant throughout the imaging algorithm. This simple configuration was investigated for different values of m in the internal report [IR1]. Herein, it was shown how highly resolved images can be obtained using a fixed number of iterations in the CGLS algorithm if the algorithm is terminated at the right Newton iteration and the value of m is chosen correctly.

To illustrate this, a number of images reconstructed with different values of m are shown in Figs. 2.3 and 2.4. The data set used here is the phantom measurement which was also used in [JP1, JP2] and [IR1]. The phantom consists of three thin-walled cylinders and mimics a fatty breast with a tumor and a fibroglandular inclusion. The "breast" has a radius of 5 cm, relative permittivity 12.6 and conductivity 0.62 S/m. The "tumor" is positioned in the lower left part of the phantom and has a radius of 1.4 cm, relative permittivity 53.4 and conductivity 1.15 S/m. The "fibroglandular" inclusion has a radius of 1.05 cm, a relative permittivity of 32.7, a conductivity of 1.28 S/m, and is positioned in the lower right part of the "breast". The true distribution of the constitutive parameters are shown in Figs. 2.3(a) and (d).

The results obtained after 20 Newton iterations using the Tikhonov regularization scheme (2.11) are shown in Figs. 2.3(b) and (e). When the value of m is kept low, e.g., $m = 2$ both the normalized error η_n and the value of χ^2 decreases over the entire range of Newton iterations. After $n = 20$ Newton iterations, the images shown in Figs. 2.3(c) and (f) are obtained. The resolution in these images is somewhat poorer than that obtained using the Tikhonov algorithm, especially in the permittivity image where the "fibroglandular" inclusion is barely visible. When the value of m is increased to $m = 8$, the value of the normalized error still decreases as the Newton algorithm progresses. The value of χ^2, on the other hand, reaches a minimum after 6 iterations and then increases. The images obtained after 20 Newton iterations are shown in Figs. 2.4(a) and (d) while the images obtained after 6 Newton iterations are shown in Figs. 2.4(b) and (e). It is seen that the

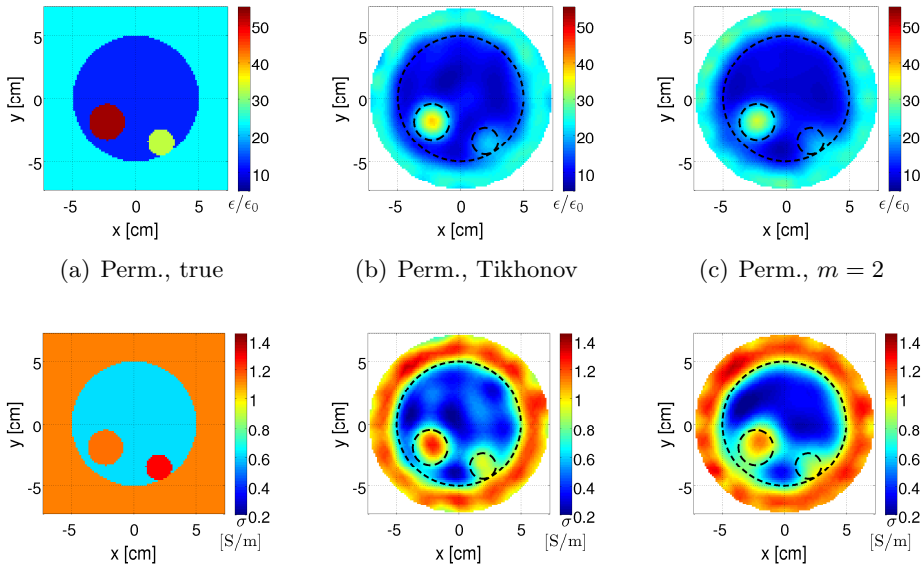

(a) Perm., true (b) Perm., Tikhonov (c) Perm., $m = 2$

(d) Cond., true (e) Cond., Tikhonov (f) Cond., $m = 2$

Fig. 2.3: *Images of the phantom measurement. The true distributions of the constitutive parameters are shown in (a) and (d). The images obtained after 20 iterations with the Tikhonov algorithm are shown in (b) and (e) and the images obtained with the CGLS algorithm with $m = 2$ are shown in (c) and (f). The dashed lines show the positions of the "breast", the "tumor", and the "fibroglandular" inclusion.*

level of the artifacts in the images obtained after 20 Newton iterations is higher than in the images obtained after 6. The normalized errors obtained are $\eta_6 = 0.0345$ and $\eta_{20} = 0.0287$ and thus does not indicate that the images are better after six Newton iterations. This illustrates how the value of χ^2 is a better indicator of when to terminate the algorithm than the normalized error η_n. This has also been reported by other authors [118]. It should be noticed that the reconstructed values obtained at $n = 6$ are somewhat better than those obtained using the Tikhonov and the $m = 2$ CGLS algorithms shown in Fig. 2.3.

The value of m can, however, be too high as illustrated by the images reconstructed using $m = 20$ shown in Fig. 2.4(c) and (f). Here, the algorithm has been terminated after 8 Newton iterations at which point the minimum value of χ^2 is obtained. The images have a significantly higher artifact level than what is seen in both of the $m = 8$ image sets. In particular, the artifact level in the conductivity is very high and the image is more or less useless as it is impossible to distinguish between the actual objects and the artifacts. This illustrates how the choice of m is of great importance when reconstructing the images, even when the value of χ^2 is used to choose the optimum number of Newton iterations.

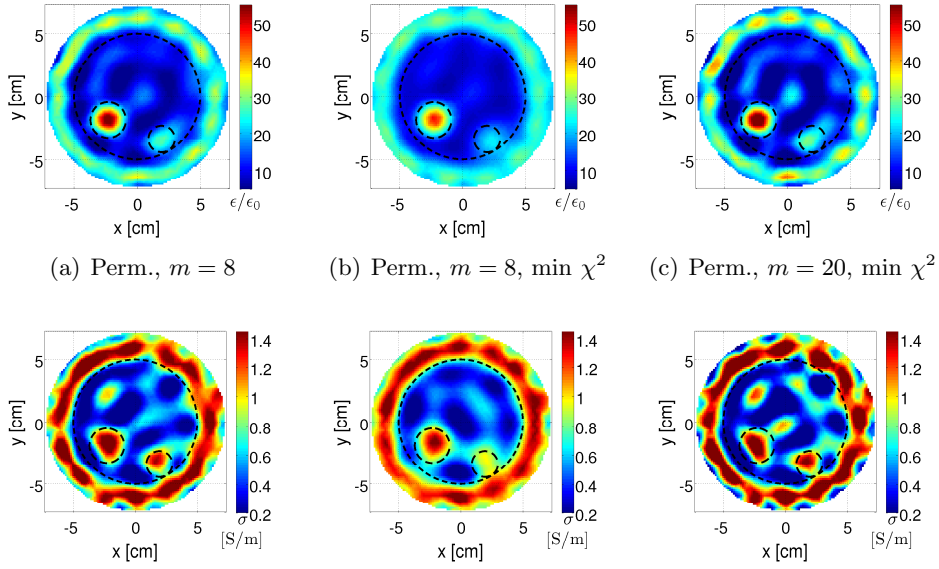

(a) Perm., $m = 8$ (b) Perm., $m = 8$, min χ^2 (c) Perm., $m = 20$, min χ^2

(d) Cond., $m = 8$ (e) Cond., $m = 8$, min χ^2 (f) Cond., $m = 20$, min χ^2

Fig. 2.4: *Images obtained using the CGLS algorithm configured with constant m throughout the reconstruction. The images obtained after 20 Newton iterations with $m = 8$ are shown in (a) and (d), the images obtained after 6 Newton iterations with $m = 8$ are shown in (b) and (e), and the images obtained after 8 Newton iterations with $m = 20$ are shown in (c) and (f). The dashed lines show the positions of the "breast", "tumor", and "fibroglandular" inclusion.*

The level of the artifacts in the conductivity images is seen to be higher than in the permittivity images. This phenomenon has previously been observed, and in [119] a scaling of the elements in the Jacobian matrix and parameter vector $\underline{\Delta k}^2$ was suggested to improve this. In the present study, however, it was found that although such a scaling can decrease the artifact level in the conductivity images, this decrease often comes at the expense of an increase in the level of the artifacts in the permittivity images. It has therefore been decided not to apply the scaling.

2.4.2 Two-Step Algorithm

The number of CGLS iterations needed to obtain the optimum images in the fewest number of Newton iterations is not easy to determine. In the imaging case presented above, the $m = 8$ algorithm is seen to provide high-quality images, but this does not assure that it will do so in other imaging configurations. Since the ill-posedness of the imaging problem changes when the scattering object changes, a value of m which is optimum for one scatterer may cause the imaging algorithm to reach an erroneous result for

another scatterer. Furthermore, it has been found that the amount of regularization needed throughout the different Newton iterations is not constant but generally decreases as the reconstructed distributions converge to the actual distribution. The work presented in the journal paper [JP1] has the objective to obtain an algorithm in which the value of m is chosen in such a way that a highly resolved image is obtained in as few Newton iterations as possible. And this should be achieved without compromising the ability of the algorithm to reconstruct images of even the most ill-posed imaging problems encountered.

The first approach tested was to determine the number of CGLS iterations in each Newton iteration using the L-curve criterion [117, Sec. 7.5]. The L-curve criterion is one of several parameter-choice methods available for estimating the optimum regularization parameter for solving a linear problem, others being the generalized cross validation and the discrepancy principle [117, Ch. 7]. It was, however, found that the optimum amount of regularization for solving the linear update problem is not the optimum amount when solving the nonlinear problem. As shown in [JP1], the optimum update, in particular in the first part of the imaging algorithm, is obtained when an over-regularized solution to the linear update problem (2.4) is used. In the latter part of the imaging algorithm, the amount of regularization should be decreased. Yet, the amount of the regularization found using the standard parameter-choice methods is too low.

These observations led to the development of an algorithm in which the number of CGLS iterations is kept low ($m = 2$) in the first part of the imaging algorithm and is then increased (to $m = 16$) in the latter part, when the solution is closer to convergence. The low value of $m = 2$ in the first part is chosen to make sure that the algorithm can handle even the most difficult imaging problems while the value $m = 16$ has been determined on the basis of a simple trial-and-error procedure.

This algorithm was developed before the importance of the χ^2 value was fully understood. The change from $m = 2$ to $m = 16$, as well as the termination of the algorithm, is therefore determined on basis of the value of η_n and the relative change in η_n between two Newton iterations, as described in [JP1]. The results of applying the algorithm to the fatty breast phantom are shown in Fig. 2.5. The algorithm changes the number of CGLS iterations between Newton iteration 7 and 8 and the intermediate images, obtained after 7 Newton iterations with $m = 2$ are shown in Fig. 2.5(a) and (c). After three Newton iterations with 16 CGLS iterations, the imaging algorithm converges and the images in Fig. 2.5(b) and (d) are obtained. The quality of these images is somewhere in between the images obtained with constant $m = 8$ after 6 Newton iterations and those obtained after 20 Newton iterations using $m = 8$, shown in Fig. 2.4: The resolution is slightly better than in the images obtained after 6 Newton iterations with $m = 8$ but the level of the artifacts is also a little higher, albeit not as high as in the images

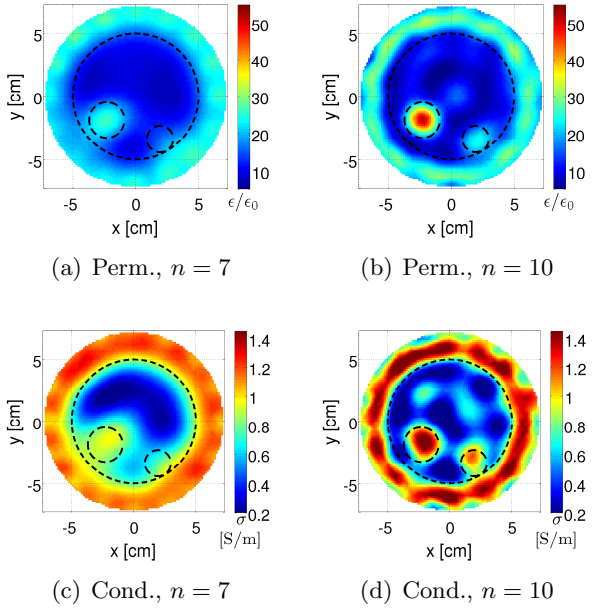

(a) Perm., $n = 7$ (b) Perm., $n = 10$

(c) Cond., $n = 7$ (d) Cond., $n = 10$

Fig. 2.5: *Images obtained using the two-step CGLS algorithm. The algorithm changes from $m = 2$ to $m = 16$ after 7 Newton iterations. The intermediate images are shown in (a) and (c) and the final images obtained after 10 Newton iterations are shown in (b) and (d). The dashed lines indicate the positions of the "breast", the "tumor", and the "fibroglandular" inclusion.*

obtained 20 Newton iterations with $m = 8$.

2.4.3 Euclidean-Distance Penalty Term

Since the increased resolution obtained using the two-step CGLS algorithm also increase the level of the artifacts in the images, an algorithm capable of increasing the resolution without increasing the artifacts has been sought for. To this end, an algorithm based on the introduction of a Euclidean-distance penalty term has been developed and presented in the journal paper [JP2] and the internal report [IR1]. This algorithm is similar to that introduced in [89, 120] with the important addition of an extra layer of regularization.

The algorithm is based on the introduction of a Euclidean-distance penalty term in the latter part of the imaging algorithm. In the first Newton iterations, the algorithm seeks to solve the nonlinear minimization problem

$$\underline{k}^2 = \operatorname{argmin} \left\| \underline{S}_{\text{res}}(\underline{k}^2) \right\|_2^2 \tag{2.13a}$$

by updating the elements of $\underline{k}_n^2$ using the simple linear update problem (2.4),

i.e.,

$$\underline{\Delta k}_n^2 = \operatorname{argmin} \left\| \underline{\underline{J}}_n \underline{\Delta k}_n^2 - \underline{S}_{\text{res}}(\underline{k}_n^2) \right\|_2^2. \tag{2.13b}$$

To this end, the CGLS algorithm using a fixed number of iterations is applied. As with the two-step CGLS algorithm, $m = 2$ is chosen to avoid artifacts from appearing in the image.

After a number N_0 of iterations using this approach, a low-pass intermediate distribution $\underline{k}_{N_0}^2$ is obtained and a Euclidean-distance penalty term is introduced in the nonlinear problem, yielding

$$\underline{k}^2 = \operatorname{argmin} \left\{ \left\| \underline{S}_{\text{res}}(\underline{k}^2) \right\|_2^2 + \lambda_{\text{EDPT}}^2 \left\| \underline{k}_{N_0}^2 - \underline{k}_n^2 \right\|_2^2 \right\}. \tag{2.14a}$$

Here, λ_{EDPT} is a regularization parameter, which determines how much influence the Euclidean-distance penalty term should have. For solving this nonlinear problem, the updates in the Newton algorithm are found by solving the linear problem

$$\underline{\Delta k}_n^2 = \operatorname{argmin} \left\{ \left\| \begin{bmatrix} \underline{\underline{J}}_n \\ \lambda_{\text{EDPT}} \underline{\underline{I}} \end{bmatrix} \underline{\Delta k}_n^2 - \begin{bmatrix} \underline{S}^{\text{res}}(\underline{k}_n^2) \\ \lambda_{\text{EDPT}} \left(\underline{k}_{N_0}^2 - \underline{k}_n^2 \right) \end{bmatrix} \right\|_2^2 \right\} \tag{2.14b}$$

wherein $\underline{\underline{I}}$ is the identity matrix. This linear problem is solved using the CGLS algorithm with the number of CGLS iterations determined by applying the L-curve criterion [117, Sec. 7.5].

During the first Newton iterations, this algorithm obtains a low-pass intermediate image, $\underline{k}_{N_0}^2$. By using this image as the basis for a Euclidean-distance penalty term, extra regularization is obtained and the finer details of the image may be reconstructed without giving rise to artifacts. The extra regularization allows for the algorithm to use the L-curve criterion for determining the optimum amount of regularization in the latter part of the algorithm. The performance of the algorithm is governed by the number of Newton iterations N_0 used to obtain the intermediate image and the value of λ_{EDPT}. The choice of these parameters are described in [JP2] and [IR1].

The reconstructed images of the fatty breast phantom are shown in Fig. 2.6. The intermediate images are obtained after 6 Newton iterations and shown in Fig. 2.6(a) and (c) and the algorithm converges after a total of 10 Newton iterations to the images shown in Fig. 2.6(b) and (d). By comparing the intermediate and the final images, it is clearly seen that the finer details of the images are reconstructed in the latter part of the algorithm. The images obtained here are much like the images obtained using the algorithm with constant $m = 8$ after 6 Newton iterations. The important difference is that to obtain the images using a constant value of m, different values of m must be tested for each imaging situations to find the optimum while the algorithm using the Euclidean-distance penalty term is capable of reconstructing highly resolved images of a wide range of imaging situations without changing the governing parameters.

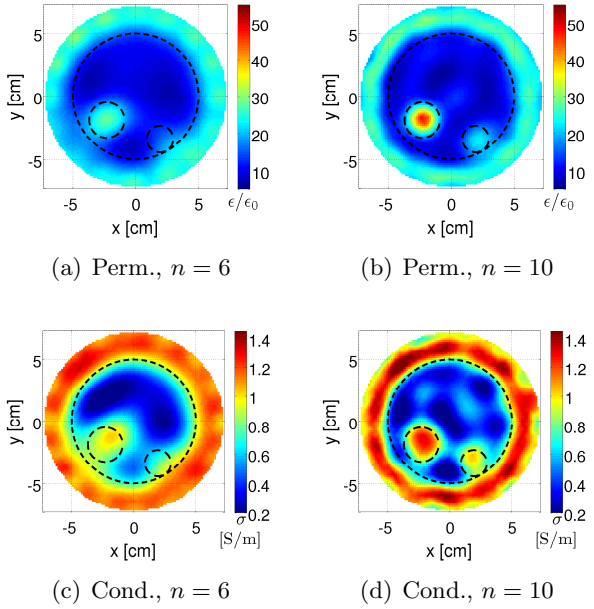

(a) Perm., $n = 6$ (b) Perm., $n = 10$

(c) Cond., $n = 6$ (d) Cond., $n = 10$

Fig. 2.6: *Images reconstructed using the Euclidean-distance penalty term algorithm. The intermediate images obtained after 6 Newton iterations are shown in (a) and (c). The algorithm converges after 10 Newton iterations and the resulting images of the permittivity and conductivity distributions are shown in (b) and (d). The dashed lines indicate the positions of the "breast", the "tumor", and the "fibroglandular" inclusion.*

2.4.4 Other Algorithms

In addition to the algorithms mentioned here, several other algorithms have been tested for calculation of the updates, including the LSQR algorithm [121] and the piecewise-polynomial truncated singular value decomposition (PP-TSVD) algorithm [117, Sec. 5.6],[122].

The LSQR algorithm [121] is based on the use of conjugate gradients, just like the CGLS algorithm. The LSQR algorithm uses the Lanczos bidiagonalization algorithm and by storing the resulting bidiagonal matrix and the left-hand side Lanczos vectors, a hybrid method [117, Sec. 6.6] may be applied for determining the optimum regularization. When using hybrid methods, the large original linear problem is reduced by projecting it onto a subspace, i.e., by using Lanczos bidiagonalization. The smaller problem can then be analyzed to obtain the optimum regularization parameter, e.g., by using the L-curve criterion, and this regularization parameter is then used to regularize the problem. This method was tested for calculating the updates for the imaging algorithm. However, as mentioned above, the best update for the nonlinear problem is not the solution found when applying the optimum amount of regularization as determined using the L-curve cri-

terion, but rather an over-regularized solution. This implies that there is no need for determining the optimum regularization parameter in the classical sense and thus no need for a hybrid method. The more simple CGLS algorithm was therefore chosen as the update algorithm. Later, when the Euclidean-distance penalty term was introduced, the hybrid method was again considered for calculation of the update. Here, however, it was found that the corner of the L-curve is always present within the first few CGLS iterations. This eliminates the need for the hybrid methods, since it is easier to just run the CGLS algorithm a fixed number of iterations, fit the L-curve to the results, and then use the solution from the iteration closest to the corner of the curve.

The PP-TSVD algorithm [117, Sec. 5.6],[122] is capable of reconstructing an image as a set of polynomials with discontinuities between them. This was considered an attracting feature since it would allow for the image to have the value of the background in one pixel and the value of the breast in the neighbouring pixel. This is different from the images created using the CGLS algorithm, which are clearly low-pass filtered, with the change from one value to the another represented by a transition region and not a discontinuity. The PP-TSVD algorithm, however, proved to be very unstable. In reconstructions of simulations, the method could be fine-tuned to give decent results but it proved virtually impossible to obtain images of phantom and patient measurements. Hence, it was decided not to use the PP-TSVD algorithm.

Implementation of a line-search algorithm [123, Ch. 8], [124, Ch. 8] for determining the value of the Newton step α_n has also been considered for improving the performance of the algorithm. However, the line-search algorithms all require additional calls to the forward solver, thereby making them prohibitively expensive in terms of computational demands. This is most likely the reason why only a few reports of using line-search for nonlinear inverse scattering are reported, e.g., [90].

2.5 Patient Images

Data from a phantom measurement was used in Section 2.4 to show the performance of the imaging algorithm with different update algorithms since this allows for comparing the reconstructed images with the known true values. It is, however, also of interest to show that the imaging system is capable of imaging the breast. To this end, images of the right breast of a 36 year old patient with a cancerous tumor are shown in Figs. 2.7 (imaging planes 1 and 3) and 2.8 (imaging planes 5 and 7). The breasts of the patient were classified as scattered-dense and the 4 cm diameter tumor was located near the anterior of the right breast at a 7 clock-face position, viewing the patient en face. The measurements were done at 1.1 GHz and

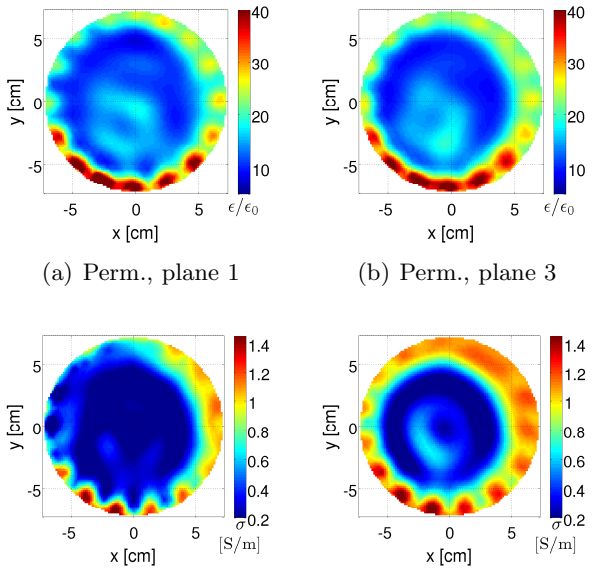

(a) Perm., plane 1 (b) Perm., plane 3

(c) Cond., plane 1 (d) Cond., plane 3

Fig. 2.7: *Images of imaging planes 1 and 3 of the breast of a patient with a tumor. The breast is seen as the circular region of low values in both the permittivity and conductivity images. The influence of the breast being close to the antennas causes the contour of the breast in imaging plane 1 to be smeared in the upper-left part. A weak response from the tumor is seen in plane 3 as a region of raised permittivity and conductivity in the lower part of the breast.*

the Euclidean-distance penalty term algorithm has been used to calculate the updates.

When imaging the breast, the 3-D scattering effects affect the performance of the imaging algorithm in different ways. In imaging plane 1, closest to the chest wall of the patient, the presence of the chest wall close to the antennas influences the performance of the algorithm. Furthermore, the breast here has the largest diameter and may be very close to the antennas, influencing their performance. These effects are seen in the images of imaging plane 1 in Figs. 2.7(a) and (c) where the upper left part of the contour of the breast is not clearly defined.

As the antennas are moved down, the influence of the chest wall is decreased and the cylindrical shape of the breast minimizes the modeling errors stemming from assuming a 2-D scattering problem. The results of this are shown in Figs. 2.7(b) and (d) where the images of imaging plane 3 are presented. Herein, the breast is easily identified as a circular region with low values of both permittivity and conductivity compared to the background. In the lower part of the breast, regions with slightly increased values of permittivity and conductivity are seen. These indicate the presence of the

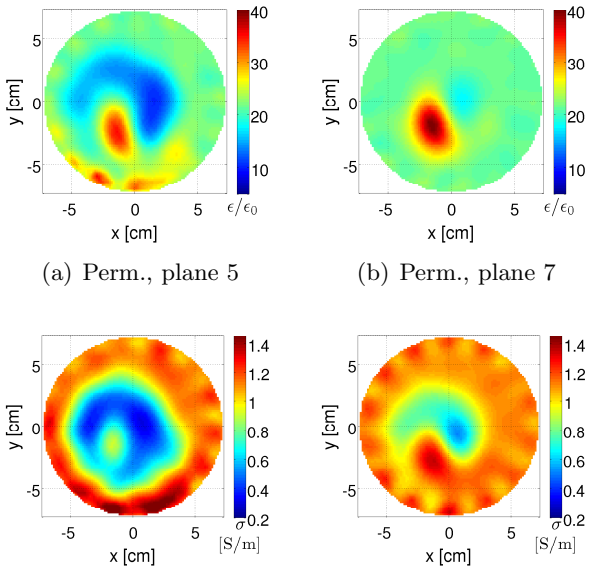

(a) Perm., plane 5 (b) Perm., plane 7

(c) Cond., plane 5 (d) Cond., plane 7

Fig. 2.8: *Images of imaging planes 5 and 7 of the breast of a patient with a tumor. The tumor is clearly visible in imaging plane 5 in both the permittivity and conductivity images. In plane 7, the response from the tumor and/or the nipple is clearly seen as a region of raised permittivity and conductivity while the contour of the breast in the permittivity image is not clearly defined.*

tumor. Moving the antennas further down along the breast to imaging plane 5, the images in Figs. 2.8(a) and (c) are obtained. Here the tumor is clearly visible in the lower left part of the images, and the healthy part of the breast is seen as a region of low permittivity and conductivity.

When the antennas are moved to imaging plane 7, furthest away from the chest wall, the 3-D scattering effects again influence the results. In this region, the breast is more conical than cylindrical in shape and the assumption of a 2-D scattering problem is thus not as accurate as in the planes above. The images of imaging plane 7 are shown in Figs. 2.8(b) and (d) wherein a high-valued region, most likely a combination of the responses from the tumor and the nipple, is seen. In the permittivity image, the healthy breast is barely visible as a low-valued region while the contour of the breast is more readily identified in the conductivity image.

In all of the images, regions of high permittivity and conductivity are present close to the positions of the antennas. This can be explained by the fact that the elements of the Jacobian corresponding to these positions take on higher values than those corresponding to the center of the imaging domain. Modeling errors and noise are thus more likely to result in artifacts close to the antennas.

2.6 Contrast Source Inversion

To avoid the need for solving a forward problem in each iteration, a contrast source inversion (CSI) algorithm [96, 97] has been implemented as described in the journal paper [JP3]. The CSI algorithm is based on the introduction of contrast sources which allows for an iterative solution of the nonlinear inverse scattering problem using two coupled linear inverse problems.

2.6.1 The Coupled Linear Equations

To illustrate the basis of the CSI algorithm, a 2-D scattering problem is considered in which a scalar representation of the electric field is used and the antennas are assumed point sources. Using the time notation $\mathrm{e}^{-i\omega t}$, the scattered field caused by an inhomogeneity may be expressed as

$$E_{\mathrm{scat}}(\boldsymbol{r}) = i\omega\mu_0 \int_D G(\boldsymbol{r}, \boldsymbol{r'}, k) E_{\mathrm{tot}}(\boldsymbol{r'}) O(\boldsymbol{r'}) \,\mathrm{d}^2\boldsymbol{r'} \tag{2.15a}$$

wherein the the integration is to be done over the imaging domain, indicated by D and G is the Green's function. The object function O is given by

$$O(\boldsymbol{r}) = \Delta\sigma - i\omega\Delta\epsilon = (\sigma(\boldsymbol{r}) - \sigma_{\mathrm{bg}}) - i\omega\left(\epsilon(\boldsymbol{r}) - \epsilon_{\mathrm{bg}}\right), \tag{2.15b}$$

and the total field is the sum of the known incident and the scattered field

$$E_{\mathrm{tot}}(\boldsymbol{r}) = E_{\mathrm{inc}}(\boldsymbol{r}) + E_{\mathrm{scat}}(\boldsymbol{r}). \tag{2.15c}$$

The expression in (2.15a) clearly illustrates that the scattering problem is nonlinear since the scattered field is present on both the left-hand side of the equation and in the integral on the right-hand side as part of the total field.

The contrast source ν is now introduced as

$$\nu(\boldsymbol{r}) = E_{\mathrm{tot}}(\boldsymbol{r}) O(\boldsymbol{r}) \tag{2.16}$$

and since the total field in the imaging domain changes when the transmitting antenna changes, each transmitting antenna results in a new distribution of contrast sources. Using the contrast source, two linear equations are introduced. The data equation relates the contrast source to the measured scattered field as

$$E^{(t,r)}_{\mathrm{scat}}(\boldsymbol{r}_{\boldsymbol{r}}) = i\omega\mu_0 \int_D G(\boldsymbol{r}_{\boldsymbol{r}}, \boldsymbol{r'}) \nu^{(t)}(\boldsymbol{r'}) \,\mathrm{d}^2\boldsymbol{r'} \tag{2.17}$$

wherein $E^{(t,r)}_{\mathrm{scat}}$ is the field measured at antenna r when antenna t is transmitting, $\boldsymbol{r}_{\boldsymbol{r}}$ is the position of antenna r, and $\nu^{(t)}$ is the distribution of contrast

sources when antenna t is transmitting. The object equation relates the distributions of the contrast sources to the distribution of the object function O and is given by

$$\nu^{(t)}(\boldsymbol{r}) = E_{\text{tot}}^{(t)}(\boldsymbol{r})O(\boldsymbol{r}) \tag{2.18a}$$

wherein the total field may be expressed using the contrast sources and the incident field, yielding

$$\nu^{(t)}(\boldsymbol{r}) - i\omega\mu_0 O(\boldsymbol{r}) \int_D G(\boldsymbol{r}, \boldsymbol{r'})\nu^{(t)}(\boldsymbol{r'})\,\mathrm{d}\boldsymbol{r'} = E_{\text{inc}}^{(t)}(\boldsymbol{r})O(\boldsymbol{r}). \tag{2.18b}$$

The two linear equations (2.17) and (2.18b) constitute the basis of the CSI algorithm in which the cost functional

$$F_{\text{complex}} = \lambda_{\text{dat}}^2 \sum_{t=1}^{n_{\text{ants}}} \left\| \underline{\underline{G}}_D^{(t)} \underline{\nu}^{(t)} - \underline{E}_{\text{scat}}^{(t)} \right\|_2^2 + \lambda_{\text{obj}}^2 \sum_{t=1}^{n_{\text{ants}}} \left\| \left(\underline{\underline{GO}} + \underline{\underline{I}} \right) \underline{\nu}^{(t)} - \underline{\underline{EO}}^{(t)} \right\|_2^2 \tag{2.19}$$

is minimized. In this expression, the first summation represents the discrete form of the data equations (2.17) and the second summation represents the discrete form of the object equations (2.18b) while λ_{dat} and λ_{obj} determines how the data equations are weighted against the object equations. The discretization procedure and the resulting linear equations are described in details in [JP3].

In each iteration of the CSI algorithm, the distributions of the contrast sources are updated by solving a linear equation combining the data and the object equation. Subsequently, the distribution of the object function O is updated by solving the object equation. In the next iteration, the updated distribution of O will change the linear equation used to update the distribution of ν. In this way, the CSI algorithm will update the distribution of contrast sources and the object function until a convergent distribution of the contrast function is obtained.

To improve the performance of the CSI algorithm, it has been implemented using the log-phase formulation. The details about this implementation can be found in [JP3].

2.6.2 CSI Imaging Results

To compare the performance of the CSI algorithm using the log-phase and complex formulations, images of imaging planes 3 and 5 from the patient exam used in Section 2.5 are shown in Figs. 2.9 and 2.10, respectively.

For imaging plane 3, the images obtained using the log-phase formulation are much like those obtained using the Newton-based imaging algorithm:

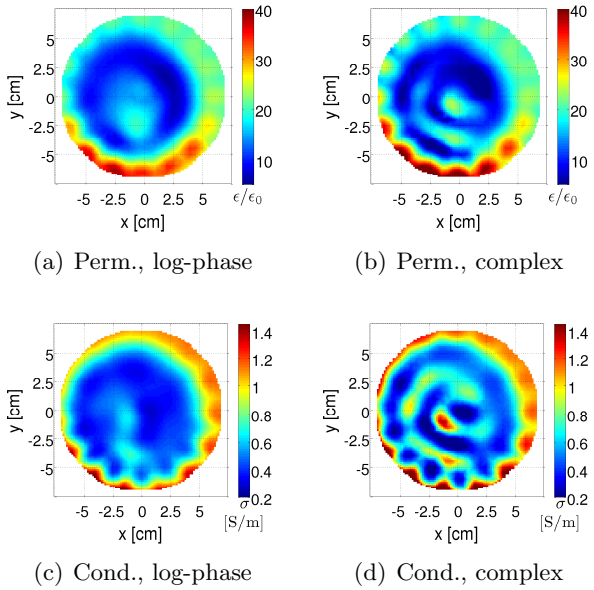

(a) Perm., log-phase (b) Perm., complex

(c) Cond., log-phase (d) Cond., complex

Fig. 2.9: *Images of imaging plane 3 obtained with the CSI algorithm using the log-phase ((a) and (c)) and the complex ((b) and (d)) formulations. The algorithm using the complex formulation is not capable of reconstructing the images correctly because of phase changes outside the range $\pm\pi$. The images obtained using the log-phase formulation are much like those shown in Figs. 2.7(b) and (d).*

The breast is clearly seen as a region of low permittivity and conductivity and a region of slightly raised values are seen at a position, corresponding well with the position of the tumor. In the images obtained using the complex formulation, a region of low permittivity and conductivity, corresponding to the breast, is still visible but artifacts are present inside the breast. In both the permittivity and conductivity images, the artifacts are so dominant that they are likely to be interpreted as tumors. For imaging plane 3, the maximum absolute phase change is 1.27π and these images clearly illustrate how the log-phase formulation improves the performance of the CSI algorithm. Since the complex formulation of the scattering problem maps all the values onto the same Riemann sheet, the phase change of -1.27π is instead mapped to a phase change of 0.73π, leading to an erroneous result.

In imaging plane 5, shown in Fig. 2.10, the maximum absolute phase change is 0.68π, and the log-phase and the complex formulations yield similar images. The tumor is clearly visible in both formulations and in both the permittivity and conductivity images.

Although the CSI algorithm avoids the use of a forward solver it is still quite computationally expensive. In the current implementation, the log-phase formulation of the CSI algorithm converges in approximately 38 minutes while the Newton-based algorithm converges in approximately 6

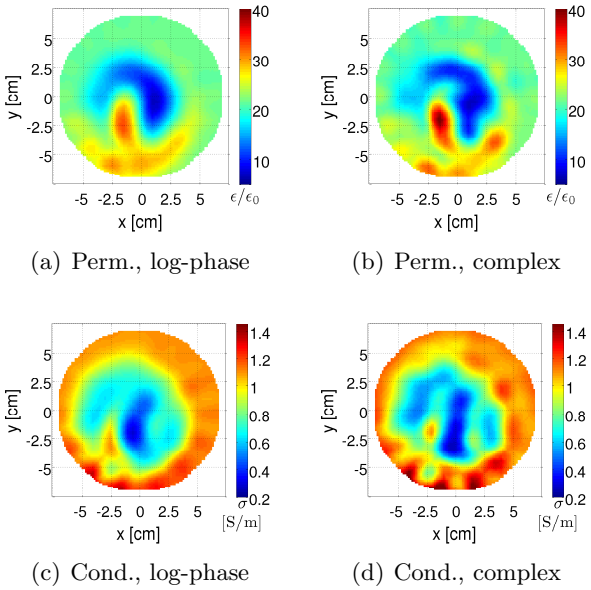

(a) Perm., log-phase (b) Perm., complex

(c) Cond., log-phase (d) Cond., complex

Fig. 2.10: *Images of imaging plane 5 obtained with the CSI algorithm using the log-phase ((a) and (c)) and the complex ((b) and (d)) formulations. Since the phase of the measured signals are all within $\pm\pi$, both formulations obtain good images, similar to those obtained using the Newton-based algorithm in Figs. 2.8(a) and (c).*

minutes. These numbers do not represent a completely fair comparison between the two algorithms since the Newton-based algorithm is implemented in FORTRAN and the CSI algorithm in Matlab which is likely slower than a FORTRAN implementation. Furthermore, the implementation of the CSI algorithm has not been optimized in the same way as the Newton-based which has been in use for several years. However, the observations made during the study does not not suggest that the CSI algorithm should be significantly less computational demanding. This is due to the fact that the CSI algorithm uses a lot more iterations to reach convergence than the Newton-based algorithm, e.g., for plane 3, the Newton-based imaging algorithm reaches convergence in 9 iterations while the CSI algorithm uses 516. Similar high numbers of iterations have been reported for the CSI algorithm in the literature [20, 98, 125–127]. This implies that the relatively low computational demand of each iteration of the CSI algorithm is countered to some extent by the high number of iterations needed to reach convergence.

2.7 Summary

The work carried out on the basis of the 2-D imaging system developed at Dartmouth College was presented. This included an introduction of the

imaging system and a description of the Newton-based imaging algorithm. This 2-D imaging algorithm applies the log-phase formulation to be able to deal with large phase changes in the measured signals.

The performance of the imaging algorithm was seen to be very dependent on the calculation of the updates in the Newton algorithm and different algorithms were presented for calculating these updates, all based on the iterative CGLS algorithm. It was shown how high-quality images can be obtained using a constant number of iterations in the CGLS algorithm if the number of iterations in both the CGLS algorithm and the Newton algorithm are chosen correctly. To this end, the goodness-of-fit parameter χ^2 proved useful.

To avoid having to determine the optimum numbers of CGLS iterations for each imaging problem, two more advanced algorithms were introduced. One is based on using two different number of CGLS iterations in the first and latter part of the imaging algorithm, respectively. This approach provide decent images using relatively few Newton iterations but the artifact level in the images is rather high. This motivated the development of an algorithm in which a Euclidean-distance penalty term is applied to obtain high resolution images with a low artifact level.

In addition to the Newton-based imaging algorithm, a CSI algorithm was presented. When using the log-phase formulation, this algorithm is capable of reconstructing images comparable in quality to those obtained using the Newton-based algorithm. Although the CSI algorithm does not need to solve a forward problem in each iteration, the relatively high number of iterations needed to obtain an image implies that it is uncertain whether the CSI algorithm is significantly faster than the Newton-based algorithm.

Chapter 3

The TUD Imaging System

In this chapter, the imaging system currently being developed at the Technical University of Denmark (TUD) is presented. As mentioned in the Introduction, several people have been involved in the development of the different parts of this system. The present PhD study has focused on developing the imaging algorithm and the antenna system and in this chapter, the imaging system is presented with special emphasis on these two parts.

The design of the TUD imaging system is based on the experiences made while working with the Dartmouth College imaging system. The most significant difference between the two systems is that the TUD imaging system has been designed to reconstruct the 3-D distribution of the constitutive parameters, thereby avoiding the errors stemming from applying a 2-D imaging algorithm to a 3-D scattering problem.

In Section 3.1, the setup of the system is described. A brief description of the imaging algorithm is given in Section 3.2 and finally, in Section 3.3, some images obtained using simulations of the system are presented. The system and imaging algorithm have also been described in the journal paper [JP4] and in the conference paper [CP2].

3.1 System Setup

As mentioned above, the design of the TUD imaging system is based on that of the Dartmouth College system. During the exam, the patient is to lie prone atop a measurement table with her breast suspended through an aperture in the table. Beneath this aperture, a cylindrical measurement tank with a radius of 20 cm is placed and inside this tank, the antenna system is positioned. During the exams, the measurement tank is to be filled with a glycerin-water coupling liquid. Although other liquids have been proposed in the literature, e.g., the saline solution in [128], the glycerin-water mixture has been chosen due to a number of attractive features. The glycerin is non-toxic, low-cost and has an antibacterial effect, implying that the same liquid may be used for several patient exams, thereby lowering the cost of

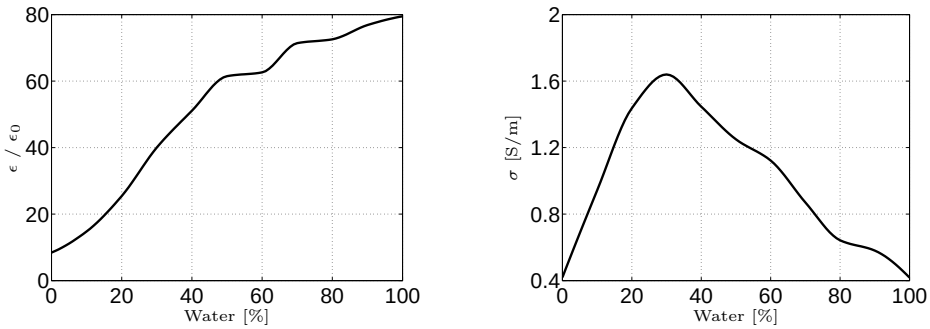

(a) Relative permittivity (b) Conductivity

Fig. 3.1: *Measured relative permittivity and conductivity of the glycerin-water coupling liquid as function of relative water content at 1.3 GHz. Data courtesy of Paul M. Meaney.*

the individual exam. Furthermore, by changing the glycerin-to-water ratio of the coupling liquid, a wide range of conductivity and permittivity values may be obtained, as shown in Fig. 3.1.

The TUD imaging system is designed to operate in the frequency spectrum from 300 MHz to 3.5 GHz. Although only a single frequency is applied for reconstructing the images at present, the wide frequency range allows for choosing the optimum frequency and for later implementation of multi-frequency reconstruction techniques. At the time of writing, the microwave hardware is under construction. However, prototypes of two transmit-receive modules, in combination with two antennas submerged in an 80-20 glycerin-water mixture, have been tested. These tests have shown that the system is capable of correctly reconstructing the amplitude and phase of received signals more than 120 dB below the transmitted signal[1].

3.1.1 Choice of Antenna

The antennas of the TUD system, one of which is depicted in the photo in Fig. 3.2(a), are of the same monopole type as the antennas in the Dartmouth College system. The antenna consists of a 3.6 mm diameter coaxial cable from which the outermost 3.5 cm of the outer conductor has been stripped, exposing the dielectric. This design allows for a return loss of 6 dB or more in most of the frequency spectrum used by the system, as shown in Fig. 3.2(b). The behavior of the antenna changes slightly when the water content of the coupling liquid is changed and at the low end of the frequency spectrum (300 to 500 MHz), return losses of as little as 3 dB are encountered.

[1]The design of the hardware has not been a part of the PhD study presented here but is carried out as part of a separate PhD study.

(a) Antenna

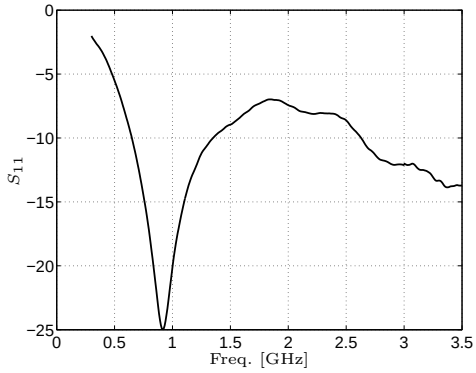

(b) S_{11}

Fig. 3.2: *Photo (a) of one of the antennas used in the TUD imaging system. The antenna consists of a coaxial cable from which the outermost 3.5 cm of the outer conductor has been stripped. The measured reflection coefficient, when the antenna is immersed in an 80-20 glycerin-water liquid, is plotted in (b). The antenna is seen to have a resonance at approximately* 920 *MHz and a return loss of more than* 6 *dB in most of the frequency spectrum used by the system.*

Other broadband antennas have also been suggested for breast-cancer detection. These include horn antennas [129], bow-tie antennas [130–134], resistively loaded dipole antennas [68, 135], and patch antennas [57, 136, 137]. These antenna types have all been considered for the TUD imaging system and although they outperform the simple monopole antenna in many ways, e.g., in terms of return loss and radiation pattern, the monopole has been chosen due to its simplicity and small size. The simplicity implies that the antenna is cheap and easy to manufacture and the small size allows for positioning many antennas close to the imaging domain. Preliminary studies have shown that the antennas may be modeled as Hertzian dipoles, positioned at the end of the outer conductor and oriented parallel to the coaxial cable, in the imaging algorithm.

3.1.2 Antenna Positions

To image the breast in the TUD imaging system, a hemispherical imaging domain with a radius of 7.5 cm, centered at the center of the aperture through which the breast is suspended, has been chosen. The setup is shown in Fig. 3.3, where the imaging domain is given by the green hemisphere.

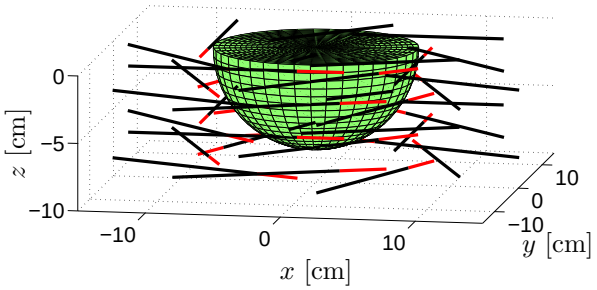

(a) Side view

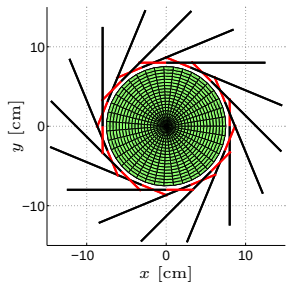

(b) Top view

Fig. 3.3: *Schematic of the TUD imaging system. The green hemispherical imaging domain is surrounded by the cylindrical antenna setup. The monopole antennas are given by the red dielectric and the black coaxial cables.*

To irradiate this domain, 32 antennas positioned in a cylindrical setup with a radius of 8 cm are used. The antennas are oriented horizontally and positioned in 4 rows with 8 antennas in each. In each row, the antennas are positioned with 45° between them and the individual rows are rotated 22.5° with respect to the row above. The top row is positioned at $z = -6$ mm, with $z = 0$ mm being the top of the measurement tank. The remaining three rows are positioned at $z = -30$ mm, $z = -55$ mm, and $z = -80$ mm.

In Fig. 3.3, the exposed dielectric of the antennas are given by the red lines and the coaxial cables are indicated by the black lines. The antennas are held in place by the coaxial cables. By letting the cables be straight all the way to the wall of the measurement tank, the Hertzian-dipole model used in the imaging algorithm has been found to be more accurate than if the cables are bent. As seen in Fig. 3.3, the straight coaxial cables imply that the antennas cannot be positioned in the same plane in each row, since the stripped dielectric and the outer conductor of the neighbouring antennas would then collide. To avoid this, the antennas are positioned with every other antenna in each row 2 mm above the z-positions of the rows given above and the rest 2 mm below.

The choice of using 32 antennas is based on a trade-off between obtaining as many measurements as possible for use in the imaging algorithm and simplifying the measurement hardware. Similarly, the horizontal orientation of the antennas has been chosen as a compromise between obtaining coverage of the top of the imaging domain while keeping the artifact levels of the reconstructed images at a minimum. The results obtained using the setup described here are compared with the results obtained using two others in Section 3.3.

3.2 Imaging Algorithm

The imaging algorithm used in TUD system is very similar to that used at Dartmouth College: The distribution of constitutive parameters is reconstructed using an iterative Newton-based algorithm in which the nonlinear inverse problem (2.3) is solved using the log-phase formulation. In each iteration, a forward solver is applied for calculating the signals for the current parameter distribution and the Jacobian of the problem. This is then used in a linear inverse problem to determine the updates of the wave numbers.

In the current configuration, the imaging domain is divided into 7164 cubic cells with side length 5 mm in which the constitutive parameters are assumed constant. With $32 \cdot 31 = 992$ measurements of the amplitude and phase of the received signals, this results in a linear update problem with a 1984-by-14328 element Jacobian matrix, which is considerably larger than the 480-by-1118 element Jacobian matrix of the 2-D problem. The update algorithms presented in the previous chapter have all been implemented for the 3-D algorithm as well and behave similar to what was observed in 2-D: Good results may be obtained using a CGLS algorithm with constant m if the value of m and the termination of the algorithm are chosen correctly but for better all-round results, the two-step CGLS or the Euclidean-distance penalty term algorithms should be applied.

In general, the size of the imaging problem is the most significant different between the imaging algorithm used in the 2-D Dartmouth College system and the algorithm used in the 3-D TUD system. The increased size and complexity of the problem is especially apparent when reducing the cell size to obtain better resolution: In the 2-D algorithm, a reduction of the distance between the nodes by a factor of 2 will increase the number of nodes, and thus unknowns, by a factor of 4. If the side length of the cubic cells of the TUD system, on the other hand, is reduced by a factor of 2, the number of cells and unknowns increases by a factor of 8. This implies that a lower limit of the cell size is reached very quickly.

3.2.1 Forward Solver

The forward solver used in the imaging algorithm is based on a method of moments code (MoM) developed at TUD. This algorithm is described in Section III-C of the journal paper [JP4] but the development of the algorithm has not been a part of the PhD study presented in this thesis. The special needs of the imaging algorithm has led to certain changes in the implementation algorithm. Most importantly, the algorithm has been changed in such a way that the MoM coefficient matrix may be reused. In this way, the time-consuming task of filling the MoM coefficient matrix needs to be done only once for a given configuration of the antennas and background medium, i.e., coupling liquid, after which the matrix may be reused in later

calls to the forward solver.

Compared to the 2-D forward solver, two things in particular adds to the complexity of the 3-D forward solver. First, the use of 3-D increases the number of different constitutive parameters in the domain, from 559 in the 2-D setup to 7164 in the 3-D as described above. Second, the 2-D scattering problem is scalar while the 3-D problem is vectorial, thereby further adding to the complexity of the problem. At present, the imaging algorithm is implemented on a computer with 2 quad core Intel Xeon E5355 2.66 GHz processors (8 CPUs in total) with 32 GB of RAM. On this machine, the 2-D forward solver takes approximately 16 seconds to calculate the scattered field using a single processor and a little more than 500 MB of RAM. The 3-D forward solver uses approximately 13 minutes when operating in parallel on all 8 CPUs and using a previously created coefficient matrix. Filling the coefficient matrix is also a time consuming task, lasting approximately 3 hours, with the coefficient matrix using just over 8 GB of RAM. The calculation of the updates is done in 0.1 – 0.5 second in the 2-D setup while it lasts 3 – 20 seconds in the 3-D setup, depending on the choice of update algorithm. In both algorithms, convergence is reached after 8–12 iterations, yielding a total time of the 2-D algorithm between 2 and 3.5 minutes while the 3-D algorithm lasts between 1.5 and 2.6 hours. This clearly illustrates how the reconstruction of the images in 3-D is much more demanding in terms of computational power.

3.3 Imaging Results

To illustrate the performance of the imaging system when applied for breast imaging, a simple breast model has been simulated. The model consisted of a hemispherical breast with a radius of 6 cm in which a fibroglandular inclusion with a radius of 2 cm and a tumor with a radius of 1 cm were positioned. The breast was centered in the imaging system, and the tumor had its center at $(x, y, z) = (3\text{ cm}, 0\text{ cm}, -1\text{ cm})$ while the fibroglandular inclusion was centered at $(x, y, z) = (-2\text{ cm}, 0\text{ cm}, -3\text{ cm})$. To avoid the "inverse crime", the breast was modeled using a finer discretization than used in the reconstruction, with the breast divided into 8908 cells.

The simulation was done at the frequency 1.3 GHz since the values of the constitutive parameters for the normal and fibroglandular tissues in [36] are given at this frequency. The breast was modeled as a heterogeneously dense breast with a relative permittivity of 12.5 and a conductivity of 0.35 S/m and the fibroglandular inclusion was assigned a relative permittivity of 21.0 and a conductivity of 0.6 S/m. To model the variations of the tissue, the individual cells in the model were assigned values which were normally distributed with the above-mentioned values as means and a standard deviation of 10% of the means. The tumor was modeled with a relative permittivity of 56

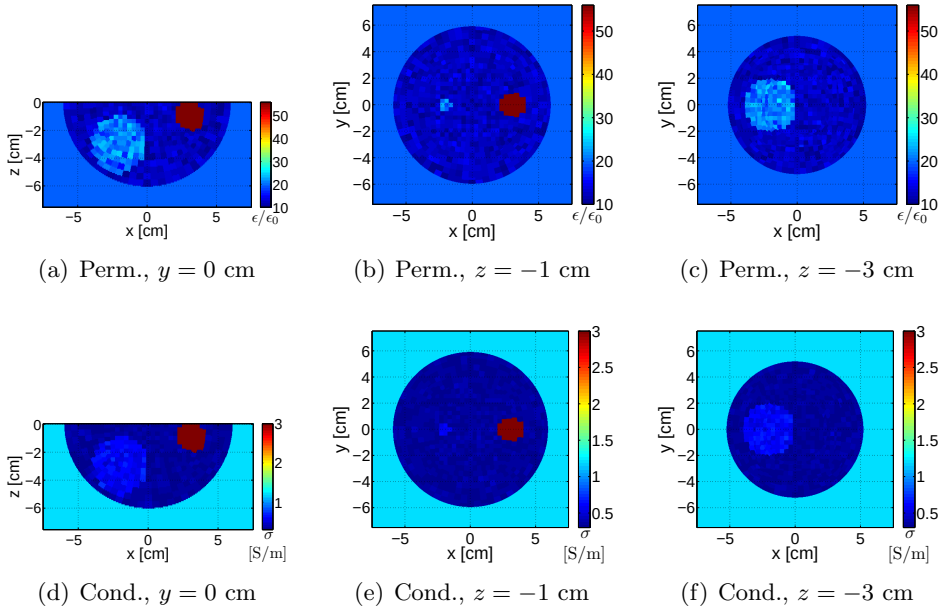

(a) Perm., $y = 0$ cm (b) Perm., $z = -1$ cm (c) Perm., $z = -3$ cm

(d) Cond., $y = 0$ cm (e) Cond., $z = -1$ cm (f) Cond., $z = -3$ cm

Fig. 3.4: *Distributions of the constitutive parameters used in the simulation. The plane $y = 0$ cm is shown in (a) and (d), the plane $z = -1$ cm in (b) and (e), and $z = -3$ cm in (c) and (f).*

and a conductivity of 3 S/m, without variation. Finally, the background was modeled as uniform with relative permittivity 19.6 and conductivity 1.22 S/m, corresponding to an 85-15 glycerin-water coupling liquid.

In the actual measurements, the upper half space ($z > 0$) will be different from the lower since the chest wall and the lid of the measurement tank will be here. It has, however, not been possible to find values for the constitutive parameters for the chest wall and since simulations have shown that the system performs equally well in a setup with two homogeneous half spaces as in a single homogeneous background, the latter has been chosen to illustrate the performance of the system in this thesis. The distributions of the permittivity and conductivity used in the simulations are shown in Fig. 3.4. The antennas were modeled as Hertzian dipoles and the Gaussian noise mimicking the noise floor of the system, 120 dB beneath the transmitted power, has been added to the simulated measurements.

The reconstructed images of the breast are shown in Fig. 3.5. The first thing to notice in these images is that both the breast, the tumor and the fibroglandular inclusion can be clearly identified. The reconstructed values of the tumor are, however, considerably lower than the actual values and looks much like the fibroglandular inclusion in the permittivity images. The higher level of the reconstructed conductivity of the tumor, however, implies that it is possible to distinguish between the tumor and the fibroglandular inclusion.

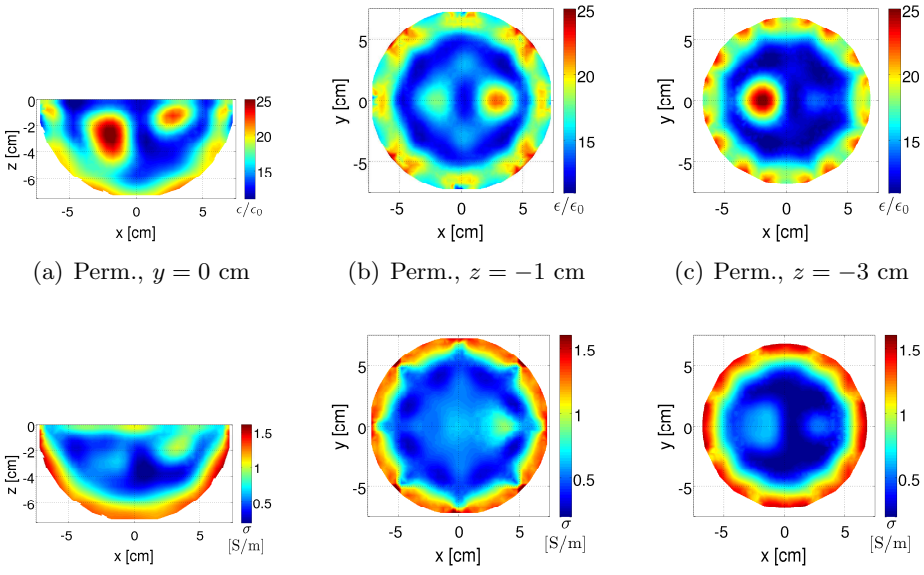

(a) Perm., $y = 0$ cm (b) Perm., $z = -1$ cm (c) Perm., $z = -3$ cm

(d) Cond., $y = 0$ cm (e) Cond., $z = -1$ cm (f) Cond., $z = -3$ cm

Fig. 3.5: *Reconstructed images of the simulation of the breast. The breast, the tumor, and the fibroglandular inclusion are all easily identified although the reconstructed values of the tumor are somewhat lower than the actual values.*

Along the edges of the images, close to the positions of the antennas, artifacts are present. As with the artifacts observed in the 2-D images in the previous chapter, these are the result of the noise in the data which is more likely to manifest itself close to the antennas.

It should be noted that the imaging setup presented here is considered to be a worst-case scenario. In the real imaging setup, the water content of the coupling liquid will be reduced, e.g., to a 90-10 glycerin-water mixture with a relative permittivity close to 14, thereby reducing the contrast between the coupling liquid and the interior of the breast. Furthermore, the position of the tumor in the very top of the breast is a challenge because fewer antennas cover this region than the region in the center of the breast. This effect is further increased by the presence of the large fibroglandular inclusion in the center of the breast, obscuring the tumor. This implies that the total scattered field is dominated by the scattered field resulting from the large contrast between the breast and the coupling liquid and has a considerable contribution from the fibroglandular inclusion whereas only a small contribution comes from the tumor. Finally, the frequency used in this simulation is kept relatively low at 1.3 GHz since the values of the breast tissue were given at this frequency. By increasing the frequency, a better resolution may be obtained although the increased losses at the higher frequencies will have a negative influence on the performance.

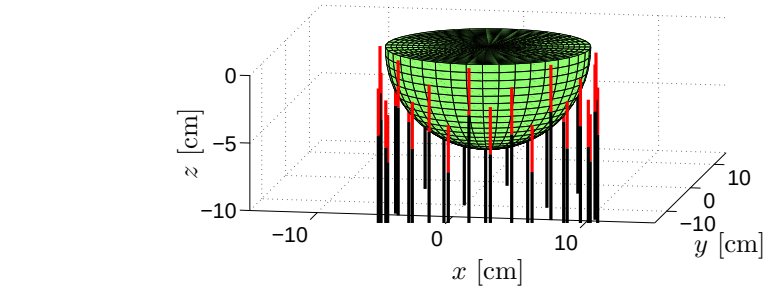

(a) Side view

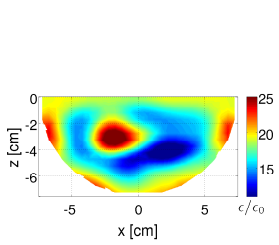

(b) Perm., $y = 0$ cm

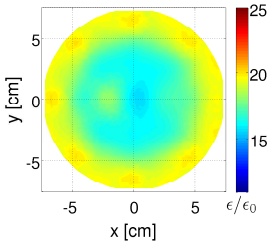

(c) Perm., $z = -1$ cm

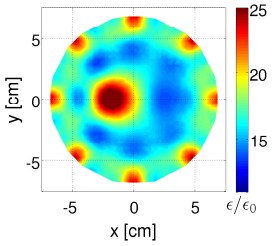

(d) Perm., $z = -3$ cm

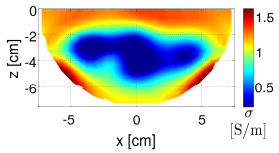

(e) Cond., $y = 0$ cm

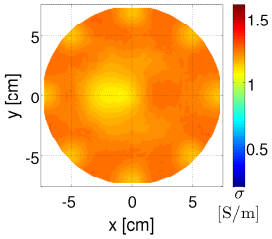

(f) Cond., $z = -1$ cm

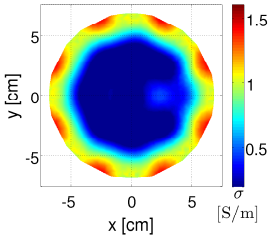

(g) Cond., $z = -3$ cm

Fig. 3.6: *Schematic (a) of the antenna setup using 4 rows of 8 vertically oriented antennas. The reconstructed images of the simulation of the heterogeneously dense breast are shown in (b) – (g). The imaging system is not capable of imaging the top of the imaging domain and hence, the tumor is not visible in the images.*

3.3.1 Other Antenna Configurations

The decision to use the antenna configuration with 4 rows of 8 horizontally oriented antennas was taken after analyzing a number of different configurations. To illustrate the importance of using the right antenna configuration, the images obtained using two other configurations are shown here.

In the first antenna configuration, 4 rows of 8 vertically oriented antennas are used. A schematic of the setup is shown in Fig. 3.6(a). In this setup, the antennas all have the same polarization. This is different from the setup using horizontally oriented antennas in which the antennas have different

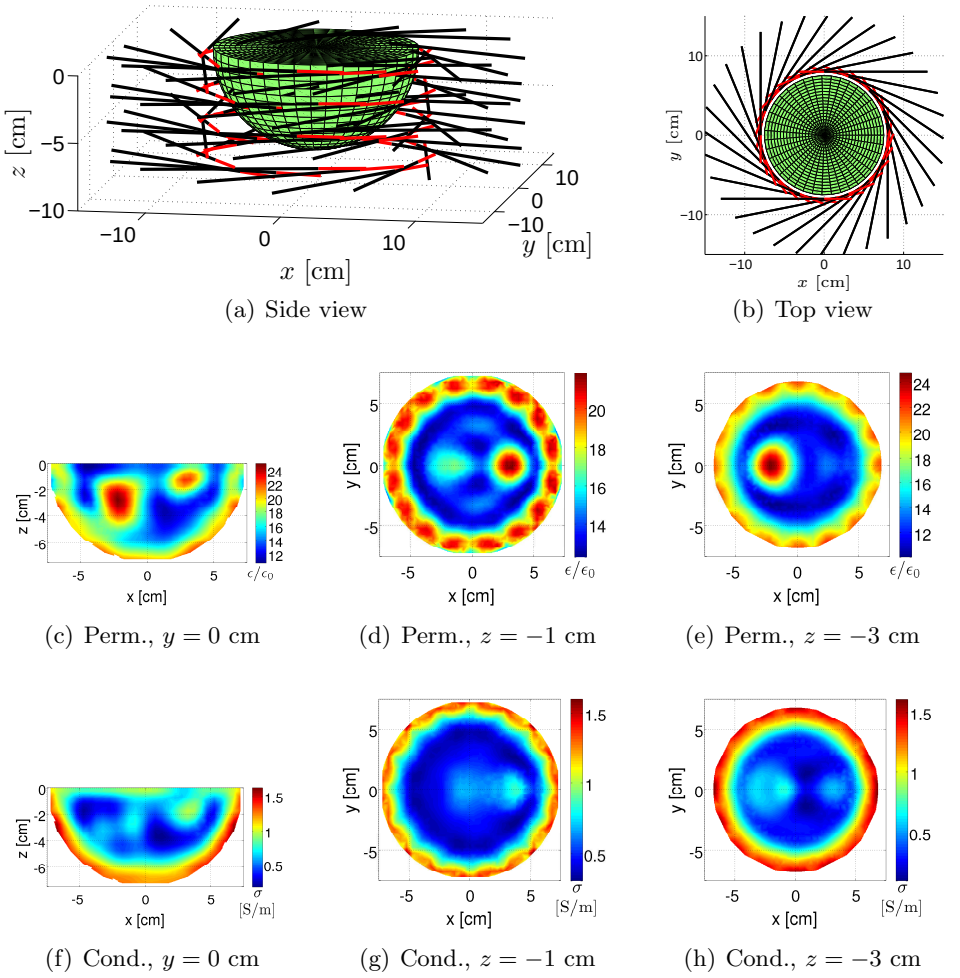

(a) Side view (b) Top view

(c) Perm., $y = 0$ cm (d) Perm., $z = -1$ cm (e) Perm., $z = -3$ cm

(f) Cond., $y = 0$ cm (g) Cond., $z = -1$ cm (h) Cond., $z = -3$ cm

Fig. 3.7: *Schematic (a) and (b) of the antenna setup with 4 rows of 16 antennas. The reconstructed images, shown in (c)–(h), are much like those obtained shown in Fig 3.5 obtained with the 32 antenna setup.*

polarizations depending on their positions in the cylindrical setup. The use of the same polarization on all antennas improves the coupling of energy between the antennas and thus allows for the antennas to detect smaller changes in the scattered field. The vertical orientation, however, impairs the ability of the system to image the top of the imaging domain. This is clearly seen in the reconstructed images of the heterogeneously dense breast, shown in Figs. 3.6(b)–(g). Herein, neither the tumor nor the contour of the breast are reconstructed in the top of the imaging domain. In the lower part of the imaging domain, the contour of the breast is visible and the fibroglandular inclusion is also detected.

To illustrate how the number of antennas influences the performance of

the system, an antenna setup with 4 rows of 16 antennas are simulated. The antennas are oriented horizontally and a schematic of the setup is shown in Figs. 3.7(a) and (b). Due to the design of the microwave hardware, in which power splitters are used to distribute the power to the transmitting antennas, 64 is the next number of antennas which lends itself to practical implementation.

The reconstructed images, shown in Figs. 3.7(c)–(h) are much like those shown in Fig. 3.5, obtained using the 32 antennas setup. The most obvious difference is a slightly more well-defined contour of the breast in the conductivity image of the plane $z = -1$ cm obtained using the 64 antennas. Since the improvements obtained by using 64 antennas are virtually non-existing and the hardware considerably more complicated than that needed for the 32 antennas setup, it has been decided to use the latter.

3.4 Summary

The design of the TUD imaging system was presented and its performance tested on simulated data. The system has been designed to create images of the interior of the breast by application of a Newton-based nonlinear inverse scattering algorithm. Since the system reconstructs the distribution of the constitutive parameters in 3-D it avoids the artifacts in the images which may arise due to modeling errors when using a 2-D algorithm. However, the 3-D imaging algorithm, and in particular the 3-D forward solver, is much more computationally expensive than the 2-D algorithm.

At the time of writing the microwave hardware for the TUD system, designed for operating in the frequency range from 300 MHz to 3.5 GHz, is being constructed. When completed, the system will comprise a cylindrical multistatic measurement setup with 32 horizontally oriented antennas positioned in a measurement tank filled with a glycerin-water coupling liquid. The antennas are of a simple monopole type, similar to that used in the Dartmouth College imaging system, and the patient is to lie prone atop the measurement tank with her breast suspended through an aperture in the lid of the tank.

The performance of the system was illustrated using simulated data at the frequency 1.3 GHz. The system was shown to be able to detect the presence of both a tumor and a fibroglandular inclusion in the breast, even though the contrast between the breast and the surrounding coupling liquid was quite large. Two additional setups of the antenna system were also simulated, illustrating the importance of positioning the antennas correctly to achieve coverage of the entire imaging domain and showing that no significant improvement in the performance of the system is achieved by doubling the number of antennas.

Chapter 4

Conclusion

The use of microwave imaging for breast-cancer screening has been investigated. Study of the literature suggests that a contrast in the electromagnetic constitutive parameters exists at microwave frequencies between the healthy and the cancerous breast tissue. This implies that an incident microwave field will scatter if a tumor is present and microwave imaging may therefore be used for screening for breast cancer.

The microwave imaging system developed for breast-cancer screening at Dartmouth College has been studied. This system uses a 2-D Newton-based algorithm to reconstruct images of the breasts of patients and the nonlinear inverse imaging problem is solved using the so-called log-phase formulation. Three different algorithms for determining the updates in this Newton algorithm have been developed. The simple update algorithm, in which the iterative CGLS algorithm is applied with a constant number of iterations throughout all of the Newton iterations, was shown to provide good results if both the number of CGLS and Newton iterations are chosen correctly. The task of selecting the correct combination is, however, not a trivial task since the combination changes when the object to be imaged changes. Thus, to obtain the optimum images, numerous combinations must be tested for each imaging situation.

For a better all-round performance, a two-step CGLS algorithm has been developed. In this algorithm it is not necessary to choose the governing parameters of the algorithm for each imaging problem. Instead, the same configuration may be used for all imaging problems and the performance was shown to be much like that observed for the optimum configuration of the simple algorithm with a constant number of CGLS iterations.

To further improve the performance of the Newton-based imaging algorithm, an update algorithm using a Euclidean-distance penalty term in the latter part of the Newton algorithm was developed. This algorithm is capable of reconstructing images with resolution equal to or better than that obtained using the two-step CGLS algorithm while reducing the level of the artifacts. This algorithm was then used to reconstruct images from a patient exam, illustrating that microwave imaging may indeed be used for detecting

breast cancer.

In addition to the Newton-based imaging algorithm a contrast source inversion (CSI) algorithm was developed. The algorithm was implemented using the log-phase formulation and when the results obtained using this formulation were compared with those obtained using the more commonly applied complex formulation, a clear improvement was observed. In particular for those imaging problems in which multiple Riemann sheets are needed due to phase changes of more than $\pm\pi$. Although the computationally demanding solution of a forward scattering problem is not needed in the CSI algorithm, the suboptimal implementation of the algorithm resulted in an algorithm which is slower than the Newton-based. Furthermore, the high number of iterations needed by the CSI algorithm to reach convergence suggests that the overall computational burden may not be significantly reduced compared to the Newton-based algorithm.

Based on the experience gained while working with the 2-D Dartmouth College imaging system, the 3-D TUD microwave imaging system was developed. In this system, 32 antennas are positioned in a cylindrical setup and the 3-D nonlinear imaging problem is solved using a Newton-based algorithm. The update algorithms developed for the 2-D system are also used in the 3-D algorithm. The performance of the imaging algorithm was tested by imaging a simulation of a hemispherical breast model. The results suggest that the system is capable of detecting cancer in the breast, even when a large contrast exists between the healthy breast tissue and the surrounding coupling liquid. The effects of using different antenna setups were also investigated, and it was found that the positions and orientations of the antennas in the imaging system are critical for its performance. It was also shown how a doubling of the number of antennas in the system has little effect on the quality of the reconstructed images.

At present, the construction of the hardware for the TUD microwave imaging system is in its final stages. Therefore, the focus of the research currently being carried out is to complete the imaging system hardware and get all the parts of the system to work together. Furthermore, multifrequency imaging algorithms, new antenna designs, and a more efficient implementation of the CSI algorithm are also being investigated.

Using multiple frequencies in the imaging system should improve its performance but since the time needed to solve the forward problem is proportional to the number of frequencies, it must be investigated if the improvement justifies the additional computation time. Furthermore, additional research is needed to obtain an efficient method to include the (unknown) frequency dependency of the different tissue types in a multifrequency algorithm.

The monopole antennas currently used in the imaging system are simple

to manufacture and perform well both in the measurements with the 2-D system and in the simulations of the 3-D system. However, due to the symmetrically radiation pattern of these antennas, a large portion of the energy is radiated away from the imaging domain, thereby reducing the overall performance of the system. An antenna with a more suitable radiation pattern could therefore improve the performance of the system. Such an antenna must, however, be small enough to be position in such a way that the top of the imaging domain is covered.

Finally, work is being carried out to create a more efficient implementation of the CSI algorithm. Not only will this allow for a more fair comparison between the computational demands of the CSI and the Newton-based algorithm, but it is also a necessity if the CSI algorithm is to be used for 3-D imaging in which case the computational burden will be much greater than for 2-D.

List of References

[1] D. M. Parkin, "Global cancer statistics in the year 2000," *Lancet Oncology*, vol. 2, no. 9, pp. 533–543, 2001.

[2] Sundhedsstyrelsen, *Cancerregisteret 2001 (foreløbige tal for 2002-2003)*, ser. Nye tal fra Sundhedsstyrelsen. Copenhagen, Denmark: Sundhedsstyrelsen – Danish National Board of Health, 2005.

[3] ——, *Kræftstatistik baseret på landspatientregisteret 2000–2004*, ser. Nye tal fra Sundhedsstyrelsen. Copenhagen, Denmark: Sundhedsstyrelsen – Danish National Board of Health, 2006.

[4] American Cancer Society, Inc., *Cancer Facts & Figures 2007*. American Cancer Society, 2007.

[5] J. S. Michaelson, M. Silverstein, J. Wyatt, G. Weber, R. Moore, E. Halpern, D. B. Kopans, and K. Hughes, "Predicting the survival of patients with breast carcinoma using tumor size," *Cancer*, vol. 95, no. 4, p. 713, 2002.

[6] L. Tabar, M.-F. Yen, B. Vitak, H.-H. T. Chen, R. A. Smith, and S. W. Duffy, "Mammography service screening and mortality in breast cancer patients: 20-year follow-up before and after introduction of screening," *The Lancet*, vol. 361, no. 9367, pp. 1405–1410, 2003.

[7] A. H. Olsen, S. H. Njor, I. Vejborg, W. Schwartz, P. Dalgaard, M.-B. Jensen, U. B. Tange, M. Blichert-Toft, F. Rank, H. Mouridsen, and E. Lynge, "Breast cancer mortality in Copenhagen after introduction of mammography screening: Cohort study," *BMJ - British Medical Journal - Clinical Research Edition*, vol. 330, no. 7485, p. 220, 2005.

[8] S. P. Poplack, A. N. Tosteson, M. R. Grove, W. A. Wells, and P. A. Carney, "Mammography in 53,803 women from the New Hampshire Mammography Network," *Radiology - Radiological Society of North America*, vol. 217, no. 3, p. 832, 2000.

[9] J. M. Lewin, C. J. D'Orsi, and R. E. Hendrick, "Breast imaging - clinical comparison of full-field digital mammography and screen-film

mammography for detection of breast cancer." *AJR - American Journal of Roentgenology*, vol. 179, no. 3, p. 671, 2002.

[10] A. I. Mushlin, R. W. Kouides, and D. E. Shapiro, "Estimating the accuracy of screening mammography: A meta-analysis," *American Journal of Preventive Medicine*, vol. 14, no. 2, pp. 143–153, 1998.

[11] P. T. Huynh, A. M. Jarolimek, and S. Daye, "The false-negative mammogram," *Radiographics*, vol. 18, no. 5, p. 1137, 1998.

[12] S. J. Nass, C. Henderson, and J. C. Lashof, Eds., *Mammography and Beyond: Developing Techniques for the Early Detection of Breast Cancer*. Washington, DC: National Academy Press, 2000.

[13] M. Sbel and H. Aichinger, "Recent developments in breast imaging," *Physics in Medicine and Biology*, vol. 41, no. 3, pp. 315–368, 1996.

[14] R. Nilavalan, J. Leendertz, I. Craddock, A. Preece, and R. Benjamin, "Numerical analysis of microwave detection of breast tumours using synthetic focussing techniques," *Proceedings of the IEEE Antennas and Propagation Society International Symposium, 2004*, pp. 2440–2443 Vol.3, 2004.

[15] E. Fear, X. Li, S. Hagness, and M. Stuchly, "Confocal microwave imaging for breast cancer detection: Localization of tumors in three dimensions," *IEEE Transactions on Biomedical Engineering*, vol. 49, no. 8, pp. 812–822, 2002.

[16] X. Li and S. Hagness, "A confocal microwave imaging algorithm for breast cancer detection," *IEEE Microwave and Wireless Components Letters*, vol. 11, no. 3, pp. 130–132, 2001.

[17] D. M. Hailu, N. K. Nikolova, and M. H. Bakr, "Sub-wavelength microwave radar imaging for detection of breast cancer tumors," *Proceedings of the ISSSE International Symposium on Signals, Systems and Electronics, 2007*, pp. 107–110, 2007.

[18] Z. Q. Zhang, Q. H. Liu, C. Xiao, E. Ward, G. Ybarra, and W. T. Joines, "Microwave breast imaging: 3-D forward scattering simulation," *IEEE Transactions on Biomedical Engineering*, vol. 50, no. 10, pp. 1180–1189, 2003.

[19] W. C. Khor, H. Wang, M. E. Bialkowski, A. Abbosh, and N. Seman, "An experimental and theoretical investigation into capabilities of a UWB microwave imaging radar system to detect breast cancer," *EUROCON, 2007. The International Conference on Computer as a Tool*, pp. 771–776, 2007.

[20] I. Lager and B. Kooij, "Non-linear imaging algorithm for the detection of female breast cancer in the incipient state," *2005 European Radar Conference*, pp. 217–20, 2006.

[21] W. Liu, H. Jafari, S. Hranilovic, and M. Deen, "Time domain analysis of UWB breast cancer detection," *Proceedings of the 23rd Biennial Symposium on Communications, 2006*, pp. 336–339, 2006.

[22] P. Meaney, M. Fanning, D. Li, S. Poplack, and K. Paulsen, "A clinical prototype for active microwave imaging of the breast," *IEEE Transactions on Microwave Theory and Techniques*, vol. 48, no. 111, pp. 1841–1853, 2000.

[23] P. Hashemzadeh, A. Fhager, L. Baath, and M. Persson, "Experimental results of an optimization approach to two-dimensional time domain electromagnetic inverse problem with application to microwave breast tomography," *Proceedings of the 3rd IASTED International Conference on Biomedical Engineering, 2005*, pp. 192–196, 2005.

[24] P. Kosmas, C. Rappaport, and E. Bishop, "Modeling with the FDTD method for microwave breast cancer detection," *IEEE Transactions on Microwave Theory and Techniques*, vol. 52, no. 8, pp. 1890–1897, 2004.

[25] G. Senaratne, R. Keam, W. Sweatman, and G. Wake, "Microwave scattering at malignant tissue boundaries: A new method for breast screening," *SICE-ICASE, 2006. International Joint Conference*, pp. 193–197, 2006.

[26] S. Silver and H. M. James, Eds., *Microwave Antenna Theory and Design*, ser. IEE Electromagnetic Waves Series. Peter Peregrinus Ltd., 1997.

[27] T. S. England and N. A. Sharples, "Dielectric properties of the human body in the microwave region of the spectrum," *Nature*, vol. 163, pp. 487–488, 1949.

[28] T. S. England, "Dielectric properties of the human body for wavelength in the 1-10 cm range," *Nature*, vol. 1466, pp. 480–481, 1950.

[29] M. Stuchly and S. Stuchly, "Dielectric properties of biological substances – tabulated," *Journal of Microwave Power*, vol. 15, no. 1, pp. 19–26, 1980.

[30] K. Foster and H. Schwan, "Dielectric properties of tissues and biological materials: A critical review," *CRC Critical Reviews in Biomedical Engineering*, vol. 17, no. 1, pp. 25–104, 1989.

[31] L. Sha, E. Ward, and B. Stroy, "A review of dielectric properties of normal and malignant breast tissue," *Proceedings of the IEEE SoutheastCon, 2002*, pp. 457–62, 2002.

[32] W. T. Joines, Y. Zhang, C. Li, and R. L. Jirtle, "The measured electrical properties of normal and malignant human tissues from 50 to 900 MHz," *Medical Physics*, vol. 21, no. 4, pp. 547–50, 1994.

[33] M. Lazebnik, L. McCartney, D. Popovic, C. B. Watkins, M. J. Lindstrom, J. Harter, S. Sewall, A. Magliocco, J. H. Booske, M. Okoniewski, and S. C. Hagness, "A large-scale study of the ultrawideband microwave dielectric properties of normal breast tissue obtained from reduction surgeries," *Physics in Medicine and Biology*, vol. 52, no. 10, 2007.

[34] M. Lazebnik, D. Popovic, L. McCartney, C. B. Watkins, M. J. Lindstrom, J. Harter, S. Sewall, T. Ogilvie, A. Magliocco, T. M. Breslin, W. Temple, D. Mew, J. H. Booske, M. Okoniewski, and S. C. Hagness, "A large-scale study of the ultrawideband microwave dielectric properties of normal, benign and malignant breast tissues obtained from cancer surgeries," *Physics in Medicine and Biology*, vol. 52, no. 20, pp. 6093–6115, 2007.

[35] S. Poplack, K. Paulsen, A. Hartov, P. Meaney, B. Pogue, T. Tosteson, M. Grove, S. Soho, and W. Wells, "Electromagnetic breast imaging: Average tissue property values in women with negative clinical findings," *Radiology*, vol. 231, no. 2, pp. 571–580, 2004.

[36] P. Meaney, M. Fanning, T. Raynolds, C. Fox, Q. Fang, C. Kogel, S. Poplack, and K. Paulsen, "Initial clinical experience with microwave breast imaging in women with normal mammography," *Academic Radiology*, vol. 14, no. 2, pp. 207–218, 2007.

[37] W. Hurt, J. Ziriax, and P. Mason, "Variability in emf permittivity values: Implications for SAR calculations," *IEEE Transactions on Biomedical Engineering*, vol. 47, no. 3, pp. 396–401, 2000.

[38] R. Deming and A. Devaney, "Diffraction tomography for multimonostatic ground penetrating radar imaging," *Inverse Problems*, vol. 13, no. 1, pp. 29–45, 1997.

[39] E. Fear, J. Sill, and M. Stuchly, "Experimental feasibility study of confocal microwave imaging for breast tumor detection," *IEEE Transactions on Microwave Theory and Techniques*, vol. 51, no. 3, pp. 887–892, 2003.

[40] E. Fear and J. Sill, "Preliminary investigations of tissue sensing adaptive radar for breast tumor detection," *Proceedings of the 25th Annual International Conference of the IEEE Engineering in Medicine and Biology Society, 2003*, vol. 4, pp. 3787–3790, 2003.

[41] D. J. Daniels, *Surface Penetrating Radar*, E. Shearman and P. Bradsell, Eds. Stevenage, Herts: The Institution of Electrical Engineers, 1996.

[42] P. Kosmas, Y. Wangd, and C. Rappaport, "Three-dimensional FDTD model for GPR detection of objects buried in realistic dispersive soil," *Proceedings of the SPIE - The International Society for Optical Engineering*, vol. 4742, pp. 330–8, 2002.

[43] R. W. Deming and A. J. Devaney, "Diffraction tomography for multimonostatic ground penetrating radar imaging," *Inverse Problems*, vol. 13, no. 1, pp. 29–45, 1997.

[44] J. van der Kruk, C. P. A. Wapenaar, J. Fokkema, and P. M. van den Berg, "Three-dimensional imaging of multicomponent ground-penetrating radar data," *Geophysics*, vol. 68, no. 4, pp. 1241–1254, 2003.

[45] T. B. Hansen and P. M. Johansen, "Inversion scheme for ground penetrating radar that takes into account the planar air-soil interface," *IEEE Transactions on Geoscience and Remote Sensing*, vol. 38, no. 1, pp. 496–506, January 2000.

[46] C. Rappaport, M. El-Shenawee, and H. Zhan, "Suppressing GPR clutter from randomly rough ground surfaces to enhance nonmetallic mine detection," *Subsurface Sensing Technologies and Applications*, vol. 4, no. 4, pp. 311–326, 2003.

[47] E. Slob, A. Yarovoy, J. Rhebergen, P. Meincke, and X.-Y. Chen, "Efficient fixed-offset GPR scattering analysis," *Proceedings of the Tenth International Conference on Ground Penetrating Radar, 2004*, no. Vol.1, pp. 29–32 Vol.1, 2004.

[48] P. Meincke, "Linear GPR inversion for lossy soil and a planar air-soil interface," *IEEE Transactions on Geoscience and Remote Sensing*, vol. 39, no. 12, pp. 2713–2721, 2001.

[49] S. Tjuatja, A. Fung, and J. Bredow, "Radar imaging of buried objects," *Proceedings of the IEEE International Geoscience and Remote Sensing Symposium, 1998*, vol. 1, pp. 524–526, 1998.

[50] R. Nilavalan, A. Gbedemah, I. Craddock, X. Li, and S. Hagness, "Numerical investigation of breast tumour detection using," *Electronics Letters*, vol. 39, no. 25, pp. 1787–1789, 2003.

[51] P. Meaney, K. Paulsen, A. Hartov, and R. Crane, "An active microwave imaging system for reconstruction of 2-D electrical property distributions," *IEEE Transactions on Biomedical Engineering*, vol. 42, no. 10, pp. 1017–1026, 1995.

[52] I. Craddock, R. Nilavalan, J. Leendertz, A. Preece, and R. Benjamin, "Experimental investigation of real aperture synthetically organised radar for breast cancer detection," *Proceedings of the IEEE Antennas and Propagation Society International Symposium, 2005*, vol. 1B, pp. 179–182 vol. 1B, 2005.

[53] P. Meaney, K. Paulsen, B. Pogue, and M. Miga, "Microwave image reconstruction utilizing log-magnitude and unwrapped phase to improve high-contrast object recovery," *IEEE Transactions on Medical Imaging*, vol. 20, no. 2, pp. 104–116, 2001.

[54] S. Semenov, R. Svenson, A. Bulyshev, A. Souvorov, A. Nazarov, Y. Sizov, A. Pavlovsky, V. Borisov, B. Voinov, G. Simonova, A. Starostin, V. Posukh, G. Tatsis, and V. Baranov, "Three-dimensional microwave tomography: Experimental prototype of the system and vector born reconstruction method," *IEEE Transactions on Biomedical Engineering*, vol. 46, no. 8, pp. 937–946, 1999.

[55] G. Bozza, C. Estatico, A. Massa, M. Pastorino, and A. Randazzo, "Short-range image-based method for the inspection of strong scatterers using microwaves," *IEEE Transactions on Instrumentation and Measurement*, vol. 56, no. 4, pp. 1181–1188, 2007.

[56] Q. Fang, P. Meaney, and K. Paulsen, "Microwave image reconstruction of tissue property dispersion characteristics utilizing multiple-frequency information," *IEEE Transactions on Microwave Theory and Techniques*, vol. 52, no. 82, pp. 1866–1875, 2004.

[57] M. Klemm, I. J. Craddock, J. Leendertz, A. Preece, and R. Benjamin, "Breast cancer detection using symmetrical antenna array," *Proceedings of the European Conference on Antennas and Propagation EuCAP 2007*, 2007.

[58] S. Hagness, A. Taflove, and J. Bridges, "Two-dimensional FDTD analysis of a pulsed microwave confocal system for breast cancer detection: Fixed-focus and antenna-array sensors," *IEEE Transactions on Biomedical Engineering*, vol. 45, no. 12, pp. 1470–1479, 1998.

[59] E. Fear and M. Stuchly, "Microwave system for breast tumor detection," *IEEE Microwave and Guided Wave Letters*, vol. 9, no. 11, pp. 470–472, 1999.

[60] ——, "Confocal microwave imaging for breast tumor detection: Comparison of immersion liquids," *Proceedings of the IEEE Antennas and Propagation Society International Symposium, 2001*, vol. 1, pp. 250–253, 2001.

[61] J. Sill and E. Fear, "Tissue sensing adaptive radar for breast cancer detection: Study of immersion liquids," *Electronics Letters*, vol. 41, no. 3, pp. 113–115, 2005.

[62] S. Davis, X. Li, E. Bond, S. Hagness, and B. van Veen, "Frequency-domain penalized least-squares beamformer design for early detection of breast cancer via microwave imaging," *Proceedings of the IEEE Sensor Array and Multichannel Signal Processing Workshop, 2002*, pp. 120–4, 2002.

[63] S. Hagness, A. Taflove, and J. Bridges, "FDTD modeling of a coherent-addition antenna array for early-stage detection of breast cancer," *Proceedings of the IEEE Antennas and Propagation Society International Symposium, 1998*, vol. 2, pp. 1220–1223, 1998.

[64] C. Elachi, *Introduction to the Physics and Techniques of Remote Sensing*. John Wiley & Sons, 1987.

[65] X. Li, S. Hagness, B. van Veen, and D. van der Weide, "Experimental investigation of microwave imaging via space-time beamforming for breast cancer detection," *Proceedings of the IEEE MTT-S International Microwave Symposium, 2003*, vol. 1, pp. 379–382, 2003.

[66] E. Fear and M. Stuchly, "Confocal microwave imaging for breast tumor detection: A study of resolution and detection ability," *Proceedings of the 23rd Annual International Conference of the IEEE Engineering in Medicine and Biology Society, 2001*, vol. 3, pp. 2355–2358, 2001.

[67] E. Fear, A. Low, J. Sill, and M. A. Stuchly, "Microwave system for breast tumor detection: Experimental concept evaluation," *Proceedings of the IEEE Antennas and Propagation Society International Symposium, 2002*, vol. 1, pp. 819–822, 2002.

[68] J. Sill and B. Fear, "Tissue sensing adaptive radar for breast cancer detection: Preliminary experimental results," *Proceedings of the IEEE MTT-S International Microwave Symposium, 2005*, vol. 2005, pp. 1789–1792, 2005.

[69] B. Zhou, W. Shao, and G. Wang, "The application of multi-look in UWB microwave imaging for early breast cancer detection using hemispherical breast model," *Engineering in Medicine and Biology Society, 2005. IEEE-EMBS 2005. 27th Annual International Conference of the*, pp. 1552–1555, 2005.

[70] E. Fear and M. Stuchly, "Microwave detection of breast cancer," *IEEE Transactions on Microwave Theory and Techniques*, vol. 48, no. 11, pp. 1854–1863, 2000.

[71] ——, "Microwave detection of breast tumors: Comparison of skin subtraction algorithms," *Proceedings of the SPIE - The International Society for Optical Engineering*, vol. 4129, pp. 207–17, 2000.

[72] T. Williams, E. C. Fear, and D. Westwick, "Tissue sensing adaptive radar for breast cancer detection: Investigations of reflections from the skin," *Proceedings of the IEEE Antennas and Propagation Society International Symposium, 2004*, vol. 3, pp. 2436–2439, 2004.

[73] T. C. Williams, E. C. Fear, and D. T. Westwick, "Tissue sensing adaptive radar for breast cancer detection - investigations of an improved skin-sensing method," *IEEE Transactions on Microwave Theory and Techniques*, vol. 54, no. 4, pp. 1308–1313, 2006.

[74] D. W. Winters, J. D. Shea, E. L. Madsen, G. R. Frank, B. D. van Veen, and S. C. Hagness, "Estimating the breast surface using UWB microwave monostatic backscatter measurements," *IEEE Transactions on Biomedical Engineering*, vol. 55, no. 1, pp. 247–256, 2008.

[75] X. Xiao and T. Kikkawa, "Extraction of calibration waveform for confocal microwave imaging for early breast cancer detection," *Proceedings of the IEEE International Symposium on Microwave, Antenna, Propagation and EMC Technologies for Wireless Communications, 2007*, pp. 1287–90, 2007.

[76] E. Bond, X. Li, S. Hagness, and B. van Veen, "Microwave imaging via space-time beamforming for early detection of breast cancer," *IEEE Transactions on Antennas and Propagation*, vol. 51, no. 8, pp. 1690–1705, 2003.

[77] X. Li, E. Bond, B. van Veen, and S. Hagness, "An overview of ultra-wideband microwave imaging via space-time beamforming for early-stage breast-cancer detection," *Antennas and Propagation Magazine, IEEE*, vol. 47, no. 1, pp. 19–34, 2005.

[78] Y. Chen, E. Gunawan, K. S. Low, S.-C. Wang, C. B. Soh, and L. L. Thi, "Time of arrival data fusion method for two-dimensional ultra-

wideband breast cancer detection," *IEEE Transactions on Antennas and Propagation*, vol. 55, no. 10, pp. 2852–2865, 2007.

[79] W. Zhi, F. Chin, and M. Chia, "Near field UWB LCMV imaging for breast cancer detection with entropy based artifacts removal," *Proceedings of the IEEE International Conference on Acoustics, Speech and Signal Processing, 2006*, vol. 2, pp. 577 – 580, 2006.

[80] P. Kosmas and C. Rappaport, "Use of the FDTD method for time reversal: Application to microwave breast cancer detection," *Proceedings of SPIE - The International Society for Optical Engineering*, vol. 5299, pp. 1–9, 2004.

[81] ——, "Time reversal with the FDTD method for microwave breast cancer detection," *IEEE Transactions on Microwave Theory and Techniques*, vol. 53, no. 7, pp. 2317–2323, 2005.

[82] Y. Chen, E. Gunawan, K. S. Low, S.-C. Wang, and C. B. Soh, "Time-reversal imaging for ultra-wideband breast cancer detection: Pulse design criteria considering multiple tumor masses," *Proceedings of the IEEE Antennas and Propagation International Symposium, 2007*, pp. 2164–2167, 2007.

[83] P. Kosmas and C. Rappaport, "A matched-filter FDTD-based time reversal approach for microwave breast cancer detection," *IEEE Transactions on Antennas and Propagation*, vol. 54, no. 4, pp. 1257–1264, 2006.

[84] P. Kosmas, "Application of the DORT technique to FDTD-based time reversal for microwave breast cancer detection," *Microwave Conference, 2007. European*, pp. 306–308, 2007.

[85] Q. H. Liu, C. Yu, J. Stang, M. Yuan, E. Bresslour, R. T. George, G. Ybarra, and W. T. Joines, "Experimental and numerical investigations of a high-resolution 3D microwave imaging system for breast cancer detection," *Proceedings of the IEEE Antennas and Propagation Society International Symposium, 2007*, pp. 2192–2192, 2007.

[86] A. Souvorov, A. Bulyshev, S. Semenov, R. Svenson, A. Nazarov, Y. Sizov, and G. Tatsis, "Microwave tomography: A two-dimensional Newton iterative scheme," *IEEE Transactions on Microwave Theory and Techniques*, vol. 46, no. 11, pp. 1654–1659, 1998.

[87] S. Semenov, V. Baranov, R. Svenson, A. Boulyshev, A. Souvorov, V. Borisov, Y. Sizov, A. Starostin, K. Dezern, and G. Tatsis, "Microwave tomography: Two-dimensional system for biological imaging," *IEEE Transactions on Biomedical Engineering*, vol. 43, no. 9, pp. 869–877, 1996.

[88] P. Meaney, S. Pendergrass, M. Fanning, D. Li, and K. Paulsen, "Importance of using a reduced contrast coupling medium in 2D microwave breast imaging," *Journal of Electromagnetic Waves and Applications*, vol. 17, no. 2, pp. 333–355, 2003.

[89] P. Meaney, E. Demidenko, N. Yagnamurthy, D. Li, M. Fanning, and K. Paulsen, "A two-stage microwave image reconstruction procedure for improved internal feature extraction," *Medical Physics*, vol. 28, no. 11, pp. 2358–2369, 2001.

[90] J. De Zaeytijd, A. Franchois, C. Eyraud, and J.-M. Geffrin, "Full-wave three-dimensional microwave imaging with a regularized Gauss-Newton method – theory and experiment," *IEEE Transactions on Antennas and Propagation*, vol. 55, no. 11, pp. 3279–3292, 2007.

[91] A. Fhager, P. Hashemzadeh, and M. Persson, "Reconstruction quality and spectral content of an electromagnetic time-domain inversion algorithm," *IEEE Transactions on Biomedical Engineering*, vol. 53, no. 8, pp. 1594–1604, 2006.

[92] P. Meaney, K. Paulsen, and T. Ryan, "Two-dimensional hybrid element image reconstruction for tm illumination," *IEEE Transactions on Antennas and Propagation*, vol. 43, no. 3, pp. 239–247, 1995.

[93] A. Bulyshev, A. Souvorov, S. Semenov, R. Svenson, A. Nazarov, Y. Sizov, and G. Tatsis, "Three-dimensional microwave tomography. theory and computer experiments in scalar approximation," *Inverse Problems*, vol. 16, no. 3, pp. 863–875, 2000.

[94] A. Sabouni, D. Flores-Tapia, S. Noghanian, G. Thomas, and S. Pistorius, "Hybrid microwave tomography technique for breast cancer imaging," *Engineering in Medicine and Biology Society, 2006. EMBS06. 28th Annual International Conference of the IEEE*, pp. 4273–4276, 2006.

[95] M. Xu, A. Sabouni, P. Thulasiraman, S. Noghanian, and S. Pistorius, "A parallel algorithmic approach for microwave tomography in breast cancer detection," *Proceedings of the IEEE International Parallel and Distributed Processing Symposium, 2007*, pp. 1–8, 2007.

[96] P. M. van den Berg and R. E. Kleinman, "A contrast source inversion method," *Inverse Problems*, vol. 13, no. 6, pp. 1607–1620, 1997.

[97] P. M. van den Berg, A. L. van Broekhoven, and A. Abubakar, "Extended contrast source inversion," *Inverse Problems*, vol. 15, no. 5, pp. 1325–1344, 1999.

[98] H. Feng, V. Galdi, and D. A. Castanon, "An object-based contrast source inversion method for homogeneous targets," *Subsurface Sensing Technologies and Applications*, vol. 4, no. 4, pp. 355–374, 2003.

[99] A. Abubakar, P. M. van den Berg, and J. J. Mallorqui, "Full non-linear inversion of microwave biomedical data," *Proceedings of SPIE - The International Society for Optical Engineering*, vol. 4684 II, pp. 797–805, 2002.

[100] A. Abubakar, P. M. van den Berg, and T. M. Habashy, "Application of the multiplicative regularized contrast source inversion method on tm- and te-polarized experimental fresnel data," *Inverse Problems*, vol. 21, no. 6, pp. S5–S13, 2005.

[101] A. Abubakar, S. Semenov, V. G. Posukh, and P. M. van den Berg, "Application of the multiplicative regularized contrast source inversion method to real biological data," *Proceedings of the IEEE MTT-S International Microwave Symposium, 2005*, vol. 2005, pp. 1319–1322, 2005.

[102] I. Catapano, L. Crocco, M. D'Urso, A. Morabito, and T. Isernia, "Microwave tomography of breast cancer: A feasibility study," *European Space Agency, (Special Publication) ESA SP*, vol. 626 SP, 2006.

[103] P. Meaney, K. Paulsen, A. Hartov, and R. Crane, "Microwave imaging for tissue assessment: Initial evaluation in multitarget tissue-equivalent phantoms," *IEEE Transactions on Biomedical Engineering*, vol. 43, no. 9, pp. 878–890, 1996.

[104] P. Meaney, K. Paulsen, and J. Chang, "Near-field microwave imaging of biologically-based materials using a monopole transceiver system," *IEEE Transactions on Microwave Theory and Techniques*, vol. 46, no. 1, pp. 31–45, 1998.

[105] P. Meaney, K. Paulsen, J. Chang, and M. Fanning, "Initial microwave imaging experiments in ex-vivo breast tissue," *Proceedings of the First Joint BMES/EMBS Conference, 1999*, vol. 2, p. 1130, 1999.

[106] D. Li, P. Meaney, T. Raynolds, S. Pendergrass, M. Fanning, and K. Paulsen, "A broadband microwave breast imaging system," *Proceedings of the IEEE 29th Annual Bioengineering Conference, 2003*, pp. 83–84, 2003.

[107] P. Meaney, K. Paulsen, S. Geimer, S. Haider, and M. Fanning, "Quantification of 3-D field effects during 2-D microwave imaging," *IEEE Transactions on Biomedical Engineering*, vol. 49, no. 7, pp. 708–720, 2002.

[108] C. T. Kelley, *Solving Nonlinear Equations with Newton's Method*. Philadelphia, PA: SIAM, 2003.

[109] K. Paulsen and P. Meaney, "Nonactive antenna compensation for fixed-array microwave imaging. I. model development," *IEEE Transactions on Medical Imaging*, vol. 18, no. 6, pp. 496–507, 1999.

[110] P. Meaney, K. Paulsen, J. Chang, M. Fanning, and A. Hartov, "Nonactive antenna compensation for fixed-array microwave imaging. II. imaging results," *IEEE Transactions on Medical Imaging*, vol. 18, no. 6, pp. 508–518, 1999.

[111] K. Paulsen, P. Meaney, M. Moskowitz, and J. Sullivan, J.M., "A dual mesh scheme for finite element based reconstruction algorithms," *IEEE Transactions on Medical Imaging*, vol. 14, no. 3, pp. 504–514, 1995.

[112] D. Li, P. M. Meaney, T. Raynolds, S. A. Pendergrass, M. W. Fanning, and K. D. Paulsen, "Parallel-detection microwave spectroscopy system for breast imaging," *Review of Scientific Instruments*, vol. 75, no. 7, pp. 2305–2313, 2004.

[113] P. Meaney, K. Paulsen, M. Fanning, D. Li, and Q. Fang, "Image accuracy improvements in microwave tomographic thermometry: Phantom experience," *International Journal of Hyperthermia*, vol. 19, no. 5, pp. 534–50, 2003.

[114] B. M. Ayyub and R. H. McCuen, *Probability, Statistics, and Reliability for Engineers and Scientists*, 2nd ed. Chapman & Hall / CRC, 2003.

[115] N. Joachimowicz, C. Pichot, and J. Hugonin, "Inverse scattering: An iterative numerical method for electromagnetic imaging," *IEEE Transactions on Antennas and Propagation*, vol. 39, no. 121, pp. 1742–1753, 1991.

[116] G. H. Golub and C. F. v. Loan, *Matrix Computations*, 3rd ed. The John Hopkins University Press, 1996.

[117] P. C. Hansen, *Rank-Deficient and Discrete Ill-Posed Problems: Numerical Aspects of Linear Inversion*, ser. Monographs on Mathematical Modeling and Computation. SIAM, 1998.

[118] J. A. Scales, P. Docherty, and A. Gersztenkorn, "Regularisation of nonlinear inverse problems: Imaging the near-surface weathering layer," *Inverse Problems*, vol. 6, no. 1, pp. 115–131, 1990.

[119] P. M. Meaney, N. K. Yagnamurthy, and K. D. Paulsen, "Pre-scaled two-parameter Gauss-Newton image reconstruction to reduce property

recovery imbalance," *Physics in Medicine and Biology*, vol. 47, no. 7, pp. 1101–1119, 2002.

[120] P. Meaney, N. Yagnamurthy, D. Li, E. Demidenko, and K. Paulsen, "A 2-stage Gauss-Newton reconstruction technique for improved object detection in microwave imaging," *Proceedings of the IEEE Antennas and Propagation Society International Symposium, 2001*, vol. 1, pp. 238–241, 2001.

[121] C. Paige and M. Saunders, "LSQR: An algorithm for sparse linear equations and sparse least squares," *ACM Transactions on Mathematical Software*, vol. 8, no. 1, pp. 43–71, 1982.

[122] P. C. Hansen, M. Jacobsen, J. M. Rasmussen, and H. Sørensen, "The PP-TSVD algorithm for image reconstruction problems," in *Methods and Applications of Inversion*, ser. Lecture Notes in Earth Science, P. C. Hansen, B. H. Jacobsen, and K. Mosegaard, Eds. Berlin: Springer, 2000, vol. 92, pp. 171–186.

[123] J. M. Ortega and W. C. Rheinboldt, *Iterative Solution of Nonlinear Equations in Several Variables*, ser. Classics in Applied Mathematics, R. E. O'Malley, Ed. Philadelphia, PA: SIAM, 2000.

[124] C. T. Kelley, *Iterative Methods for Linear and Nonlinear Equations*, ser. Frontiers in Applied Mathematics. Philadelphia, PA: SIAM, 1995, vol. 16.

[125] A. Abubakar and P. M. van den Berg, "Iterative forward and inverse algorithms based on domain integral equations for three-dimensional electric and magnetic objects," *Journal of Computational Physics*, vol. 195, no. 1, pp. 236–262, 2004.

[126] ——, "The contrast source inversion method for location and shape reconstructions," *Inverse Problems*, vol. 18, no. 2, pp. 495–510, 2002.

[127] A. Abubakar, P. M. van den Berg, and J. J. Mallorqui, "Full non-linear inversion of microwave biomedical data," *Proceedings of SPIE - The International Society for Optical Engineering*, vol. 4684 II, pp. 797–805, 2002.

[128] S. Semenov, R. Svenson, A. Bulyshev, A. Souvorov, A. Nazarov, Y. Sizov, V. Posukh, A. Pavlovsky, P. Repin, A. Starostin, B. Voinov, M. Taran, G. Tatsis, and V. Baranov, "Three-dimensional microwave tomography: Initial experimental imaging of animals," *IEEE Transactions on Biomedical Engineering*, vol. 49, no. 1, pp. 55–63, 2002.

[129] X. Li, S. Hagness, M. Choi, and D. van der Weide, "Numerical and experimental investigation of an ultrawideband ridged pyramidal horn antenna with curved launching plane for pulse radiation," *Antennas and Wireless Propagation Letters*, vol. 2, no. 1, pp. 259–262, 2003.

[130] C. Shannon, M. Okoniewski, and E. Fear, "A dielectric filled ultrawideband antenna for breast cancer detection," *Proceedings of the IEEE Antennas and Propagation Society International Symposium, 2003*, vol. 1, pp. 218–221, 2003.

[131] X. Yun, E. Fear, and R. Johnston, "Broadband cross-polarized bowtie antenna for breast cancer detection," *Proceedings of the IEEE Antennas and Propagation Society International Symposium, 2003*, vol. 3, pp. 1091–1094, 2003.

[132] X. Yun, R. Johnston, and E. Fear, "Radar-based microwave imaging for breast cancer detection: Tumor sensing with cross-polarized reflections," *Proceedings of the IEEE Antennas and Propagation Society International Symposium, 2004*, vol. 3, pp. 2432–2435, 2004.

[133] X. Yun, E. Fear, and R. Johnston, "Compact antenna for radar-based breast cancer detection," *IEEE Transactions on Antennas and Propagation*, vol. 53, no. 8, pp. 2374–2380, 2005.

[134] S. Hagness, A. Taflove, and J. Bridges, "Wideband ultralow reverberation antenna for biological sensing," *Electronics Letters*, vol. 33, no. 19, pp. 1594–1595, 1997.

[135] E. Fear and M. Stuchly, "Microwave breast cancer detection," *Proceedings of the IEEE MTT-S International Microwave Symposium, 2000*, vol. 2, pp. 1037–1040, 2000.

[136] I. Craddock, R. Nilavalan, J. Leendertz, A. Preece, and R. Benjamin, "Experimental investigation of breast cancer detection using a fully-populated array of antennas and real aperture synthetically organised radar," *Proceedings of the 17th International Zurich Symposium on Electromagnetic Compatibility*, pp. 67–70, 2006.

[137] D. Gibbins, A. Yamsiri, I. Craddock, G. Hilton, and D. Paul, "An investigation of a compact UWB antenna by measurement and FDTD simulation," *Proceedings of the European Conference on Antennas and Propagation EuCAP, 2006*, 2006.

Journal Paper 1

Nonlinear Microwave Imaging for Breast-Cancer Screening Using Gauss-Newton's Method and the CGLS Inversion Algorithm

Tonny Rubæk, Paul M. Meaney, Peter Meincke, and Keith D. Paulsen

Status:
Submitted: October 2006
Accepted: May 2007
Published: August 2007
Journal: IEEE Transactions on Antennas and Propagation

Nonlinear Microwave Imaging for Breast-Cancer Screening Using Gauss–Newton's Method and the CGLS Inversion Algorithm

Tonny Rubæk, *Student Member, IEEE*, Paul M. Meaney, *Member, IEEE*, Peter Meincke, *Member, IEEE*, and Keith D. Paulsen, *Member, IEEE*

***Abstract*—Breast-cancer screening using microwave imaging is emerging as a new promising technique as a supplement to X-ray mammography. To create tomographic images from microwave measurements, it is necessary to solve a nonlinear inversion problem, for which an algorithm based on the iterative Gauss–Newton method has been developed at Dartmouth College. This algorithm determines the update values at each iteration by solving the set of normal equations of the problem using the Tikhonov algorithm. In this paper, a new algorithm for determining the iteration update values in the Gauss–Newton algorithm is presented which is based on the conjugate gradient least squares (CGLS) algorithm. The iterative CGLS algorithm is capable of solving the update problem by operating on just the Jacobian and the regularizing effects of the algorithm can easily be controlled by adjusting the number of iterations. The new algorithm is compared to the Gauss–Newton algorithm with Tikhonov regularization and is shown to reconstruct images of similar quality using fewer iterations.**

***Index Terms*—Biomedical electromagnetic imaging, cancer, electromagnetic scattering inverse problems, image reconstruction, imaging, inverse problems, microwave imaging, nonlinear equations.**

I. Introduction

MICROWAVE imaging is emerging as a promising new technique for use in breast-cancer screening [1]–[5]. The use of microwave imaging as a supplement or alternative to the widely used X-ray mammography is considered to be appealing because of the nonionizing nature of the microwaves and because the physical parameters providing contrast in the microwave images are different from those in the X-ray images. This implies that microwave imaging may be useful for detecting tumors that are not visible in X-ray mammography.

The techniques currently applied for microwave imaging of the breast can be divided into two categories. In the first, radar-based approaches are used. This involves transmitting a broadband pulse into the breast and creating images by use of time-reversal algorithms, thereby synthetically focusing the transmitted pulse at different locations within the breast [1], [6], [7].

The other major category is based on tomographic imaging using nonlinear inversion in which a forward model is created using Maxwell's equations [8], [9]. When using the tomographic techniques, the breast is irradiated by one antenna and the response is measured by a number of receiving antennas. By alternating which antenna is transmitting the signal, illumination from all directions can be achieved. These measurements are then inserted into a forward model based on the frequency-domain form of Maxwell's equations which, in turn, can be inverted to obtain the constitutive-parameter distribution of any target inside the imaging domain. The forward model based on Maxwell's equations leads to a nonlinear ill-posed inversion problem and implies that advanced signal processing techniques are necessary to obtain an image from the measurement of the transmit-receive data.

At Dartmouth College, a Gauss–Newton iterative method using a Tikhonov regularization for solving for the updates (GN-T) is applied for solving the nonlinear imaging problem. This method involves solving a forward problem at each iteration and constructing a Jacobian matrix $\underline{\underline{J}}$ from the forward problem to update the values of the constitutive parameters in the imaging domain. The update values are found by solving the normal equation to an under-determined linear problem at each iteration of the GN-T algorithm. This procedure requires the explicit calculation of the matrix $\underline{\underline{J}}^T\underline{\underline{J}}$. Because of the ill-posedness of the underlying problem, regularization is needed for which a Tikhonov algorithm [10, Sec. 5.1] is applied. The speed of the imaging algorithm is governed primarily by two factors, one being the speed of the forward solver, and the other being the ability of the algorithm to update the values of the constitutive parameters as accurately as possible, allowing for fewer calls to be made to the forward solver [11], [12].

The new algorithm for updating the values of the constitutive parameters described in this paper addresses the latter of these factors. The new algorithm uses the conjugate gradient least squares (CGLS) algorithm [10, Sec. 6.3] for calculating the updates at each iteration of the Gauss–Newton algorithm. The CGLS algorithm is an iterative algorithm for solving linear equations and determines the solution of the linear problem by projecting it into a Krylov subspace. The algorithm does not need the explicit calculation of the matrix $\underline{\underline{J}}^T\underline{\underline{J}}$ but is capable of working directly on the Jacobian matrix. Furthermore, the regularizing effects of the CGLS algorithm are governed by the

Manuscript received October 12, 2006; revised January 26, 2007. The work of T. Rubæk and P. Meincke was supported by the Danish Technical Research Council and the work of P. M. Meaney and K. D. Paulsen was supported by the NIH/NCI under Grant P01-CA80139.

T. Rubæk and P. Meincke are with the Technical University of Denmark, DK-2800 Kgs. Lyngby, Denmark (e-mail: tru@oersted.dtu.dk).

P. M. Meaney and K. D. Paulsen are with Thayer School of Engineering, Dartmouth College, Hanover, NH 03755 USA.

Digital Object Identifier 10.1109/TAP.2007.901993

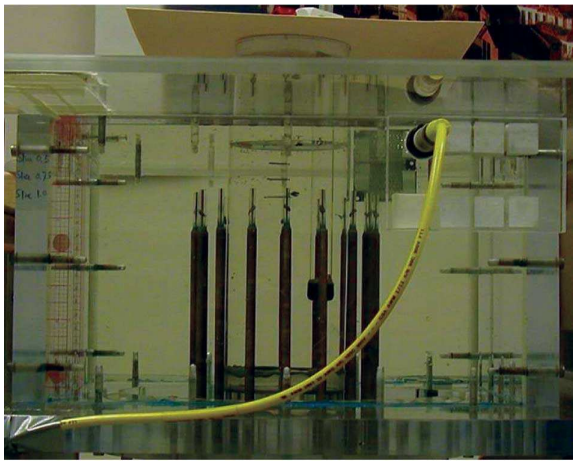

Fig. 1. Photo of imaging system. The monopoles are positioned in a circular setup and during the measurements, the tank is filled with a coupling liquid.

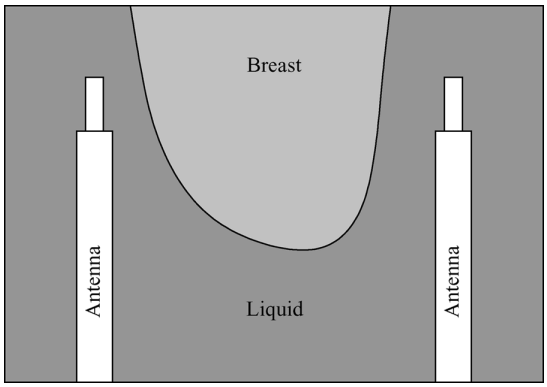

Fig. 2. Measurement setup. The antennas are moved downwards and measurements are taken at 7 planes through the breast, with plane 1 being closest to the chest and plane seven being closest to the nipple.

number of iterations the algorithm is allowed to run, thereby allowing for easier control over the regularizing effects than in the current GN-T algorithm.

This paper contains a brief description of the current imaging system in Section II, and an introduction to solving imaging problems using the Gauss–Newton method in Section III. This section also contains a description of the algorithm currently applied. In Section IV, the new algorithm is introduced based on the CGLS algorithm. Finally, in Section V, the new algorithm is tested and its performance is compared to that of the currently applied algorithm using a simulation, phantom measurements, and patient data.

II. Imaging System

The imaging system at Dartmouth College consists of 16 monopole antennas positioned in a circular array, as shown in Fig. 1, and is designed to operate over the frequency range from 500 to 2300 MHz. The patient lies prone on top of the measurement tank with the breast to be examined suspended through an aperture in the top of the tank as seen in the schematic in Fig. 2. The tank is filled with a coupling liquid, closely mimicking the average constitutive parameters of the breast [13], maximizing the amount of microwave energy coupled into the breast. A more thorough description of the imaging system is found in [14].

During the acquisition of data, the antenna array scans through seven vertical positions at 1 cm increments. At each plane, the antennas sequentially act as transmitters while the response is measured at the remaining 15 antennas. This results in 240 coherent measurements of the scattered field for each plane. Currently, the system operates by creating two-dimensional (2-D) slice images of each of the seven planes and the image reconstruction is based on the assumption that the scattering problem can be reasonably represented as a 2-D problem [11]. The validity of this assumption has been investigated in [15], wherein it was found that although the simplification of the imaging problem to 2-D does introduce some inaccuracies in the reconstructed images, the relatively small radius of the imaging system ensures that the inaccuracies are not critical.

III. Gauss–Newton's Method

When reconstructing the microwave tomographic images, the distribution of the constitutive parameters in the imaging domain is represented by the complex wave number squared

$$k^2(\boldsymbol{r}) = \omega^2 \mu_0 \epsilon(\boldsymbol{r}) + i\omega\mu_0\sigma(\boldsymbol{r}) \tag{1}$$

where the time notation $\mathrm{e}^{-i\omega t}$ is assumed. In this expression, ϵ is the permittivity, σ is the conductivity, μ_0 is the free-space permeability, and ω and i are the angular frequency and complex unit, respectively. The vector $\boldsymbol{r}$ is a position vector in the imaging domain. The distribution of the squared wave numbers is determined by solving the minimization problem

$$\underline{k}^2 = \arg\min \left\{ \left\| \underline{E}^{\mathrm{meas}} - \underline{E}^{\mathrm{calc}}(\underline{k}^2) \right\|_2^2 \right\} \tag{2}$$

where $\underline{E}^{\mathrm{calc}}(\underline{k}^2)$ is a vector of field values calculated using the forward model for a given distribution of constitutive parameters stored in the vector $\underline{k}^2$, and $\underline{E}^{\mathrm{meas}}$ is a vector of the corresponding measurements. The two-norm $\|\cdot\|_2$ of a V-element vector $\underline{x}$ is the square root of the sum of the squares of the elements in the vector given by

$$\|\underline{x}\|_2 = \sqrt{\sum_{j=1}^{V} |x_j|^2} \tag{3}$$

where $|\cdot|$ indicates the complex modulus of the elements.

For this implementation, the image reconstruction is performed in terms of the relative change in phase and amplitude, the so-called log-phase $(\mathrm{l}-\mathrm{p})$ representation [16], as opposed to changes in the absolute complex field values. The measured data is represented using the difference in the logarithm of the amplitude and the unwrapped phase between a measurement

with an empty system and a measurement with a target, i.e., a breast, present. The measurement data is stored in a vector

$$\underline{E}_{\mathrm{l-p}}^{\mathrm{meas}} = \begin{bmatrix} \log\left|\underline{E}_{\mathrm{target}}^{\mathrm{meas}}\right| - \log\left|\underline{E}_{\mathrm{empty}}^{\mathrm{meas}}\right| \\ \mathrm{phase}\underline{E}_{\mathrm{target}}^{\mathrm{meas}} - \mathrm{phase}\underline{E}_{\mathrm{empty}}^{\mathrm{meas}} \end{bmatrix} \tag{4}$$

that is twice the length of the original complex measurement vector, $\underline{E}^{\mathrm{meas}}$. The calculated data is reconfigured in a similar way, yielding the vector

$$\underline{E}_{\mathrm{l-p}}^{\mathrm{calc}}(\underline{k}^2) = \begin{bmatrix} \log\left|\underline{E}^{\mathrm{calc}}(\underline{k}^2)\right| - \log\left|\underline{E}^{\mathrm{calc}}\left(\underline{k}_0^2\right)\right| \\ \mathrm{phase}\underline{E}^{\mathrm{calc}}(\underline{k}^2) - \mathrm{phase}\underline{E}^{\mathrm{calc}}\left(\underline{k}_0^2\right) \end{bmatrix}. \tag{5}$$

In this expression, $\underline{k}_0^2$ denotes the known distribution of constitutive parameters when there is no target present in the system, i.e., the constitutive parameters of the coupling liquid which can easily be measured using a commercially available probe kit. At Dartmouth College, an Agilent Network Analyzer (E5071C) with an Agilent Dielectric Probe Kit (85070E) is used.

The minimization problem to be solved for reconstructing the images can now be rewritten using the new vectors as

$$\underline{k}^2 = \arg\min\left\{\left\|\underline{E}_{\mathrm{l-p}}^{\mathrm{meas}} - \underline{E}_{\mathrm{l-p}}^{\mathrm{calc}}(\underline{k}^2)\right\|_2^2\right\}. \tag{6}$$

The use of the logarithm of the magnitude and unwrapped phase has been shown to emphasize the large relative changes observed at the antennas on the opposite side of the breast, i.e., within the main projection of the target, effectively containing more pertinent information about the scattering problem. At the same time, the signals with higher absolute magnitude measured by the antennas close to the transmitter, in which the object-induced changes are relatively small, are given less weight [16].

The calculation of the forward solution $\underline{E}_{\mathrm{l-p}}^{\mathrm{calc}}$ is based on the 2-D form of Maxwell's equations, yielding a nonlinear optimization problem for which the Gauss–Newton method is applied [17, Ch. 4–6], [18]. Hence, it is assumed that the nonlinear expression for the field as a function of the distribution of squared wave numbers can be approximated locally by a first-order Taylor expansion as

$$\underline{E}_{\mathrm{l-p}}^{\mathrm{calc}}\left(\underline{k}_{n+1}^2\right) = \underline{E}_{\mathrm{l-p}}^{\mathrm{calc}}\left(\underline{k}_n^2\right) + \underline{\underline{J}}\left(\underline{k}_n^2\right)\underline{\Delta k}_n^2 \tag{7}$$

where $\underline{\underline{J}}$ is the Jacobian matrix and

$$\underline{\Delta k}_n^2 = \underline{k}_{n+1}^2 - \underline{k}_n^2 \tag{8}$$

with n being the current iteration number. In this form, the minimization problem can be reformulated as a number of local linear minimization problems given by

$$\underline{k}_{n+1}^2 = \arg\min\left\{\left\|\underline{E}_{\mathrm{l-p}}^{\mathrm{meas}} - \left(\underline{E}_{\mathrm{l-p}}^{\mathrm{calc}}\left(\underline{k}_n^2\right) + \underline{\underline{J}}\left(\underline{k}_n^2\right)\underline{\Delta k}_n^2\right)\right\|_2^2\right\}. \tag{9}$$

The iterative Gauss–Newton method currently applied at Dartmouth College consists of five steps in each iteration.

1) The forward model is used to calculate the electric fields from the distribution of constitutive parameters $\underline{k}_n^2$ and to check for termination of the algorithm.
2) Calculate the Jacobian $\underline{\underline{J}}$ for the current property distribution, $\underline{k}_n^2$.
3) Obtain the Newton direction [18, Sec. 1.6] $\underline{d}_n$ by solving the linear problem

$$\underline{\underline{J}}\left(\underline{k}_n^2\right)\underline{d}_n = \underline{E}_{\mathrm{l-p}}^{\mathrm{meas}} - \underline{E}_{\mathrm{l-p}}^{\mathrm{calc}}\left(\underline{k}_n^2\right) \tag{10}$$

using the normal equation and the Tikhonov regularization algorithm.
4) Determine the Newton step [18, Sec. 1.6] α_n satisfying

$$\alpha_n = \arg\min\left\{\left\|\underline{E}_{\mathrm{l-p}}^{\mathrm{meas}} - \underline{E}_{\mathrm{l-p}}^{\mathrm{calc}}\left(\underline{k}_n^2 + \alpha_n\underline{d}_n\right)\right\|_2^2\right\}. \tag{11}$$

5) Update the values of the constitutive parameters using

$$\underline{\Delta k}_{n+1}^2 = \underline{k}_n^2 + \alpha_n\underline{d}_n. \tag{12}$$

The operations listed above can be divided into two categories. Steps 1 and 2 concern the forward calculations while steps 3 through 5 concern the computation of the new values. The most time consuming part of the iterations of the GN-T algorithm is the forward calculations in steps 1 and 2 which take approximately 1 min per iteration. The computation of the update, on the other hand, takes approximately 1 s. The new CGLS-based algorithm, to be described in Section IV, focuses mainly on improving steps 3 through 5, and aims to reduce the overall time consumption by reducing the number of iterations, and thereby calls to the forward solver, needed for the algorithm to converge. A review of the current implementation of the Gauss–Newton algorithm is presented in the following section.

A. Forward Solver and Jacobian

The forward solver used in the algorithm is a hybrid-element algorithm which uses the finite-element method for representing the electromagnetic scattering problem within the heterogeneous imaging domain and a boundary-element method for representing the homogeneous area outside of the imaging domain [19]. The values of the constitutive parameters are reconstructed on a coarse mesh, in this case with 559 nodes as shown in Fig. 3(a), which are subsequently interpolated onto a finer finite-element mesh, in this case with 3903 nodes as shown in Fig. 3(b), for computation by the forward solver [20].

The influence of the antennas not acting as transmitter or receiver being present in the imaging system is accounted for by representing them as electromagnetic sinks within the surrounding boundary-element zone as described in [21], [22]. The hybrid-element approach is useful as the forward solver here in that it is quite accurate because it does not require approximate boundary conditions. Its efficiency arises from the use of bounded matrix techniques facilitated by the finite-element approach and by the fact that only the target zone requires finite-element discretization [19]. In addition, incorporation of the adjoint technique [14] effectively reduces the calculation of the

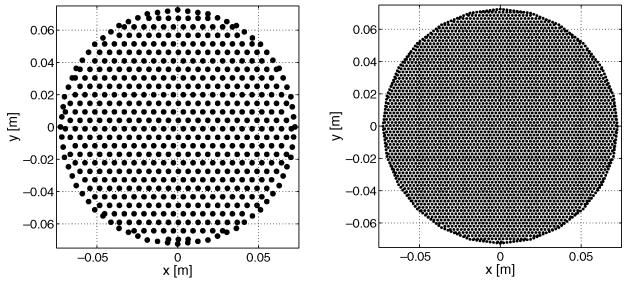

Fig. 3. Nodes of the coarse and fine meshes. The parameters are reconstructed on the coarse mesh and interpolated onto the finer mesh for computation by the forward solver. (a) Coarse mesh; (b) fine mesh.

Jacobian matrix to a set of simple inner product operations, reducing the overall computation time of this task to a fraction of that of the forward solution.

B. Newton Direction

The Newton direction $\underline{d}_n$ is currently found by solving the normal equation of the under-determined matrix equation (10). The normal equation is given in terms of the matrix $\underline{\underline{J}}^T\underline{\underline{J}}$ as

$$\underline{\underline{J}}^T\underline{\underline{J}}\,\underline{d}_n = \underline{\underline{J}}^T\left(\underline{E}_{\text{l-p}}^{\text{meas}} - \underline{E}_{\text{l-p}}^{\text{calc}}\left(\underline{k}_n^2\right)\right) \tag{13}$$

where the argument of the Jacobian matrix has been omitted for improved readability. Since this problem is ill-conditioned, the Tikhonov algorithm [10, Sec. 5.1] is applied, yielding the linear equation

$$(\underline{\underline{J}}^T\underline{\underline{J}} + \lambda\underline{\underline{I}})\underline{d}_n = \underline{\underline{J}}^T\left(\underline{E}_{\text{l-p}}^{\text{meas}} - \underline{E}_{\text{l-p}}^{\text{calc}}\left(\underline{k}_n^2\right)\right) \tag{14}$$

where the regularization parameter λ is found using the method described in [23, Eq. (16)], wherein the trace of the matrix $\underline{\underline{J}}^T\underline{\underline{J}}$ is used as the basis of the calculation.

C. Newton Step

Although advanced algorithms exist for calculation of the Newton step size [17, Ch. 8], the fact that these algorithms all requires multiple calculations of the forward model to determine the optimum value of α_n means that they are not well suited for use in this algorithm where calculation of the forward model is the most time consuming operation. Instead, a simple yet effective method has been implemented in which the Newton step is set to a value determined by the iteration number. Using this method, the value of α_n is set to 0.1 during the first three iterations and then increased gradually in each of the following iterations until it reaches a value of 0.5 after 12 iterations. The small iteration step size has the primary benefit of ensuring relatively slow changes in the phase distribution of the computed fields between iterations thus acting to reduce the possibility of inducing complex nulls in the imaging domain. The avoidance of these nulls is crucial to the stability of this approach [24].

D. Update of Values

The values of the constitutive parameters are updated using the standard formulation

$$\underline{k}_{n+1}^2 = \underline{k}_n^2 + \alpha_n\underline{d}_n. \tag{15}$$

Depending on the noise level and degree of model mismatch, the updated values may contain high-frequency spatial variation. This is minimized by the application of a spatial-filtering algorithm that smooths the values of $\underline{k}_{n+1}^2$ by averaging them with a weighted sum of the values of the neighboring nodes [25, Appendix A].

E. Termination of Algorithm

In general, the algorithm converges within 13 to 15 iterations. In practice, especially while mass processing data from numerous patient exams, the algorithm is allowed to run 20 iterations to ensure convergence is reached.

IV. Gauss–Newton CGLS Algorithm

The new algorithm is focused on steps 3 to 5 in the Gauss–Newton algorithm, that is, determining the update at each iteration. To obtain a more efficient algorithm, the three steps have been merged into a single step based on the use of the CGLS algorithm [10, Sec. 6.3]. The new algorithm is denoted as the Gauss–Newton CGLS (GN-C) algorithm.

A. CGLS Algorithm

The CGLS algorithm is an iterative algorithm of the conjugate gradient type, and is applied for determining the update values at iteration n in the GN-C algorithm $\underline{\Delta k}_n^2$ by solving the linear problem

$$\underline{\Delta k}_n^2 = \arg\min\left\{\left\|\underline{\underline{J}}\left(\underline{\Delta k}_n^2\right)\underline{\Delta k}_n^2 - \left(\underline{E}_{\text{l-p}}^{\text{meas}} - \underline{E}_{\text{l-p}}^{\text{calc}}\left(\underline{\Delta k}_n^2\right)\right)\right\|_2^2\right\} \tag{16}$$

and thus does not work on the normal equation. The solution to this linear equation after m CGLS iterations (m CGLS iterations per each Gauss–Newton iteration n) is given by

$$\left[\underline{\Delta k}_n^2\right]^{(m)} = \arg\min\left\{\left\|\underline{\underline{J}}\left[\underline{\Delta k}_n^2\right]^{(m)} - \left(\underline{E}_{\text{l-p}}^{\text{meas}} - \underline{E}_{\text{l-p}}^{\text{calc}}\right)\right\|_2^2\right\} \tag{17a}$$

subject to

$$\left[\underline{\Delta k}_n^2\right]^{(m)} \in \mathfrak{K}_m\left\{\underline{\underline{J}}^T\underline{\underline{J}}, \left[\underline{\underline{J}}^T\left[\underline{E}_{\text{l-p}}^{\text{meas}} - \underline{E}_{\text{l-p}}^{\text{calc}}\right]\right]\right\} \tag{17b}$$

where $\mathfrak{K}_m$ is the m-dimensional Krylov subspace defined by the Jacobian matrix and the vector of the difference between the measured and calculated fields, and the arguments of the Jacobian and the calculated solution have been omitted for improved readability. The solution after m iterations is thus the least-squares solution to the original problem projected into the m-dimensional Krylov subspace $\mathfrak{K}_m$.

Each iteration of the CGLS algorithm is comprised of five simple steps [10, Eq. (6.14)], allowing for an efficient implementation of the algorithm. The algorithm is initialized with all elements of the update vector set to zero

$$\left[\underline{\Delta k}_n^2\right]^{(0)} = \underline{0}. \tag{18a}$$

In addition to the update vector, the algorithm requires the residual vector $\underline{r}$ which is initialized as

$$\underline{r}^{(0)} = \left(\underline{E}_{\text{l-p}}^{\text{meas}} - \underline{E}_{\text{l-p}}^{\text{calc}}\right) - \underline{\underline{J}}\left[\underline{\Delta k}_n^2\right]^{(0)} = \left(\underline{E}_{\text{l-p}}^{\text{meas}} - \underline{E}_{\text{l-p}}^{\text{calc}}\right) \tag{18b}$$

and an auxiliary vector $\underline{a}$ initialized by

$$\underline{a}^{(0)} = \underline{\underline{J}}^T \underline{r}^{(0)}. \tag{18c}$$

At each iteration $m = 1, 2, \ldots$ of the CGLS algorithm, the value of the update vector $[\underline{\Delta k}_n^2]^{(m)}$ is computed using

$$\left[\underline{\Delta k}_n^2\right]^{(m)} = \left[\underline{\Delta k}_n^2\right]^{(m-1)} + \alpha_m \underline{a}^{(m-1)} \tag{19a}$$

and

$$\alpha_m = \frac{\left\|\underline{\underline{J}}^T \underline{r}^{(m-1)}\right\|_2^2}{\left\|\underline{\underline{J}}\,\underline{a}^{(m-1)}\right\|_2^2}. \tag{19b}$$

Thus, the solution is found as a linear combination of the vectors $\underline{a}^{(m)}$ where the weight of the individual vectors are found as the ratio between the squared two-norms of the matrix products of the Jacobians and the residual and auxiliary vectors, respectively. The residual and auxiliary vectors are updated at each iteration using

$$\underline{r}^{(m)} = \underline{r}^{(m-1)} - \alpha_m \underline{\underline{J}}\,\underline{a}^{(m-1)} \tag{19c}$$

$$\underline{a}^{(m)} = \underline{\underline{J}}^T \underline{r}^{(m)} + \beta_m \underline{a}^{(m-1)} \tag{19d}$$

and

$$\beta_m = \frac{\left\|\underline{\underline{J}}^T \underline{r}^{(m)}\right\|_2^2}{\left\|\underline{\underline{J}}^T \underline{r}^{(m-1)}\right\|_2^2}. \tag{19e}$$

It can be shown that the vectors obtained by the matrix products of the transposed Jacobian and the individual residual vectors $\underline{\underline{J}}^T \underline{r}^{(m)}$, $m = 1, 2, \ldots$ are orthogonal to each other [10, Sec. 6.3]. This implies that the auxiliary vector $\underline{a}^{(m)}$ is updated by adding an orthogonal vector scaled by the ratio between the squared norms of the current and previous residuals β_n to the previously used vector, which corresponds to adding a new dimension to the solution. This illustrates how each iteration of the CGLS algorithm adds a dimension to the Krylov subspace onto which the solution is projected as stated in (17b). It should be noted that in finite precision, the orthogonality of the residual vectors is progressively diminished as the number of iterations with the CGLS algorithm increases due to rounding errors. This implies that there is an effective upper limit on the number of dimensions which can be obtained for the Krylov subspace.

As described in [10, Sec. 6.3.2 and 6.4], the exact details of the regularizing effects of the CGLS algorithm are still not completely understood. It is, however, known that the solutions provided by the CGLS algorithm closely follow the L-curve [10, Sec. 4.6] of the more widely-used Tikhonov algorithm [10, Sec. 5.1], the L-curve being the norm of the solution $[\underline{\Delta k}_n^2]^{(m)}$ as a function of the norm of the residual $\underline{r}^{(m)}$. The first iterations in the CGLS algorithm correspond to a high value of the regularization parameter in the Tikhonov algorithm, whereas the results obtained as the number of iterations increases correspond to decreasing the value of the regularization parameter. In this way, the regularizing effects of the CGLS algorithm is governed by the number of iterations m rather than by an explicit regularization parameter.

B. Determining the Update Values

Usually, when solving a linear problem, the desired solution is that for which the L-curve has the maximum curvature, also known as the corner of the L-curve [10, Sec. 7.5]. However, it has been found in this work that this is not necessarily the case when solving for updates in the nonlinear GN-C algorithm. Instead, the result obtained after only a few iterations of the CGLS algorithm, corresponding to an over-regularized solution, has been found to yield the best results. Further discussion on this topic is found in Section V-A.

A two-step procedure for determining the number of iterations of the CGLS algorithm, similar to that previously suggested in [25], has been developed based on the normalized two-norm η_n given by

$$\eta_n = \frac{\left\|\underline{E}_{\text{l-p}}^{\text{meas}} - \underline{E}_{\text{l-p}}^{\text{calc}}\left(\underline{k}_n^2\right)\right\|_2}{\left\|\underline{E}_{\text{l-p}}^{\text{meas}}\right\|_2}. \tag{20}$$

Early in the reconstruction process, only two iterations of the CGLS algorithm are needed to determine the update values. When the relative change in η_n, defined as

$$\Delta\eta_n = \frac{\eta_{n+1}}{\eta_n} - 1 \tag{21}$$

between two iterations is greater than -10%, the number of iterations in the CGLS algorithm is increased to 16. This is based on the assumption that as the solution gets closer to the actual distribution of the constitutive parameters, the local linearization obtained by the first-order Taylor expansion is a better approximation to the actual problem than when the solution is far from the actual distribution. It should be noted that the value of $\Delta\eta_n$ is negative as long as the value of η_n decreases, i.e., as long as the calculated data approach the measured data.

The termination of the Gauss–Newton algorithm is also based on the normalized two-norm η. The algorithm is terminated when $\Delta\eta_n$ obtains a value greater than -3% or when the value of η_n drops below $\eta_{\text{term}} = 0.03$. These thresholds have been determined by trial and error and are dependent on the noise level in the system. In systems with more noise these values should

be increased while a lower noise level would allow for these thresholds to be decreased.

Since the GN-C algorithm has been designed to terminate at the maximally resolved image by adjusting the number of CGLS iterations in the latter part of the GN-C algorithm, it is important to terminate the algorithm based on the norm η_n. If a fixed number of iterations is used the optimal number of iterations might be exceeded, and a point reached where the algorithm attempts to fit the solution to the unwanted noise-component in the measured data. When the GN-C algorithm reaches the point where it starts to fit the solution to the noise component of the measured data this will usually result in the value of η_n starts to oscillate around some fixed value. This oscillation, in turn, will cause the value of $\Delta\eta_n$ to become positive (larger than -3%) and the algorithm should therefore be terminated.

C. Safeguard

To avoid the GN-C algorithm from getting trapped in a local minimum or an oscillating mode, a safeguard based on the two-norm of the update vector has been implemented. The two-norm of the update values are not allowed to exceed one quarter of the two-norm of the vector holding the k^2 values. To prevent this, the update vector $\underline{\Delta k}_n^2$ is multiplied by a scaling factor α_{CGLS} determined by

$$\alpha_{\mathrm{CGLS}} = \begin{cases} 1 & \text{for } \dfrac{\left\|\underline{k}_n^2\right\|_2}{\left\|\underline{\Delta k}_n^2\right\|_2} > 4 \\ \dfrac{\left\|\underline{k}_n^2\right\|_2}{4\left\|\underline{\Delta k}_n^2\right\|_2} & \text{for } \dfrac{\left\|\underline{k}_n^2\right\|_2}{\left\|\underline{\Delta k}_n^2\right\|_2} < 4 \end{cases} \tag{22}$$

and the value of the vector $\underline{k}^2$ is updated using

$$\underline{k}_{n+1}^2 = \underline{k}_n^2 + \alpha_{\mathrm{CGLS}}\underline{\Delta k}_n^2. \tag{23}$$

The choice of a factor of 4 between the two-norm of the update vector and the two-norm of the vector holding the k^2 values has been chosen from an observation of when the algorithm fails and a considerable margin has been added. In our experience, for most cases the two-norm of the update vector is well below the limit and in the vast majority of cases where it exceeds the limit the algorithm still performs well without the scaling. In some instances, however, the update values can behave quite erratically and the scaling is necessary. When the scaling is applied, there has been no example of the algorithm failing, even though a large number of images of both simulations, phantom measurements, and patient measurements have been reconstructed. If anything, the scaling might be too restrictive, and a more advanced analysis of the update procedure may provide the means for determining it in a more sophisticated manner, thus allowing even faster convergence of the algorithm.

D. Summary of Gauss–Newton CGLS Algorithm

Combining these steps, the GN-C algorithm has the following steps in each iteration.

1) The forward model is used to calculate the electric fields from the distribution of constitutive parameters $\underline{k}_n^2$ and to calculate the value of η_n. The value of η_n is used to check for termination and to check for the number of iterations to be used in the CGLS algorithm;
2) Calculation of the Jacobian $\underline{\underline{J}}$ for the distribution $\underline{k}_n^2$;
3) Use the CGLS algorithm to calculate the update value $[\underline{\Delta k}_n^2]^{(m)}$ with $m = 2$ or $m = 16$ depending on the value of $\Delta\eta_n$ and update the values of the constitutive parameters using

$$\underline{\Delta k}_{n+1}^2 = \underline{k}_n^2 + \alpha_{\mathrm{CGLS}}\left[\underline{\Delta k}_n^2\right]^{(m)}. \tag{24}$$

As with the GN-T algorithm, the most time consuming part of the iterations is the calculation of the forward solution, taking approximately 1 min while the update step takes less than 1 s. No measurable difference has been found in the overall time consumption per Newton iteration for the GN-T and the GN-C algorithms.

V. Test of Algorithm

In this section, the performance of the GN-C algorithm is compared to the performance of the previously used GN-T algorithm using simulation, phantom measurement, and patient data.

A. Simulated Data

A simple 2-D target has been simulated and the images reconstructed using the GN-C algorithm compared with those obtained using the GN-T algorithm. The target was a circular scatterer with a radius of 2 cm and constitutive parameters $\epsilon_{r,\mathrm{t}} = 50$ and $\sigma_{\mathrm{t}} = 1.6\ \mathrm{S/m}$ in a background medium with constitutive parameters $\epsilon_{r,\mathrm{bg}} = 30$ and $\sigma_{\mathrm{bg}} = 1.163\ \mathrm{S/m}$. The target was centered at $(x, y) = (0, 2\ \mathrm{cm})$ and a schematic of the setup is shown in Fig. 4. The 16 point-source antennas were positioned equidistantly about a 15.2 cm diameter circle concentrically surrounding the 14.0 cm diameter imaging zone and the frequency was 1000 MHz. The simulated measurement data had Gaussian noise added with an amplitude mimicking a noise floor of -100 dBm.

The images obtained using the two different algorithms are shown in Fig. 5. The images are seen to be close to identical with the GN-C algorithm reaching a slightly higher maximum value than the GN-T algorithm. Both techniques recover the target quite well in both permittivity and conductivity. The background variation in both conductivity images is quite similar and a direct consequence of the simulated noise which is much higher than that encountered in practice. The value of the normalized two-norm η_n of the two algorithms is shown in Fig. 6 along with $\Delta\eta_n$ for the GN-C algorithms. The GN-C algorithm was terminated after 11 iterations because the value of η_n decreases to a value less than 0.03. The sharp decrease in $\Delta\eta_n$ for the GN-C algorithm at iteration 11 indicates that the algorithm has transitioned from performing two to sixteen iterations in the CGLS algorithm. The value of η_n decreases more quickly in the first few iterations, and subsequently levels out. The value of η_n for the GN-T algorithm reaches a stable level after 13 iterations, and the image does not change significantly during the last seven iterations. The final errors for each are negligibly different which is not surprising given the similarity of the final images.

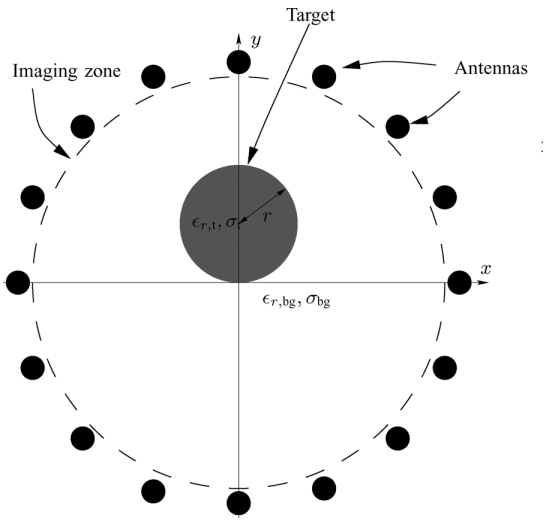

Fig. 4. Schematic of the setup of the simulation. The background has the constitutive parameters $\epsilon_{r,\mathrm{bg}} = 30$ and $\sigma_{\mathrm{bg}} = 1.163\ \mathrm{S/m}$. The circular target is centered at $(x, y) = (0, 2\ \mathrm{cm})$ and has the radius $r = 2\ \mathrm{cm}$. The constitutive parameters of the target are $\epsilon_{r,\mathrm{t}} = 50$ and $\sigma_{\mathrm{t}} = 1.6\ \mathrm{S/m}$.

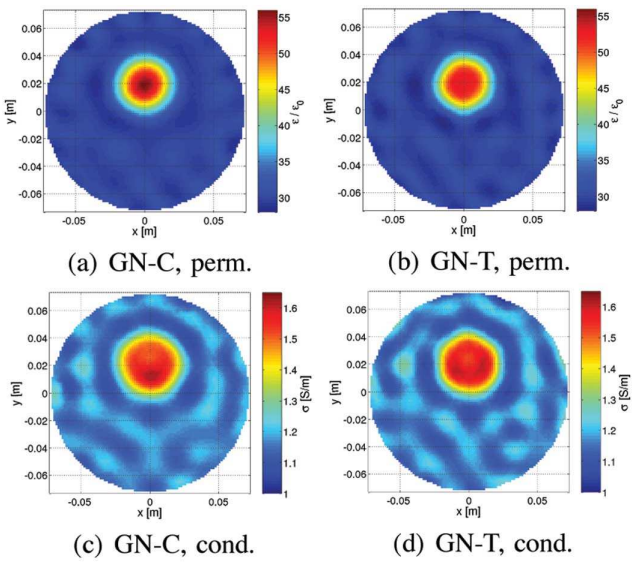

Fig. 5. Comparison of the reconstructed values of the conductivity and permittivity of the simulation case for the GN-C and the GN-T algorithms. The GN-C algorithm reached convergence after 11 iterations while the result of the GN-T algorithm is that of the 20th iteration. (a) GN-C, perm. (b) GN-T, perm. (c) GN-C, cond. (d) GN-T, cond.

To quantitatively compare the reconstructed values with the actual values, transects of the images for the two pairs along the y axis are shown in Fig. 7. The results obtained with the two different algorithms are quite similar. The permittivity reconstructed using the GN-T algorithm seems to be a slightly better fit to the true value with less overshoot of the central target value while no clear difference is seen in the images of the conductivity.

In Fig. 8, the L-curve for the CGLS algorithm for the linear update problem at the first iteration of the GN-C algorithm is plotted against the L-curve that would be obtained using

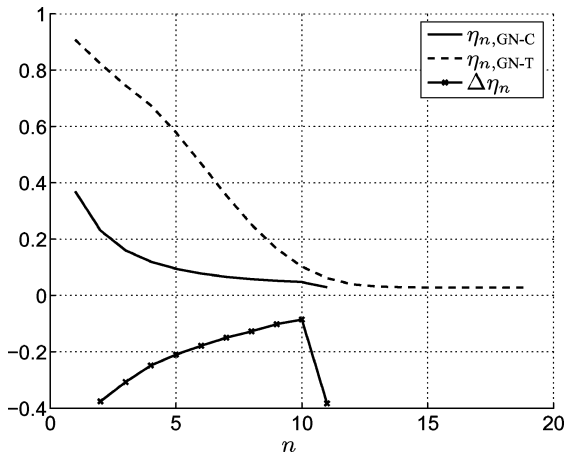

Fig. 6. Normalized two-norm η_n for the two algorithms and $\Delta\eta_n$ for the GN-C algorithm.

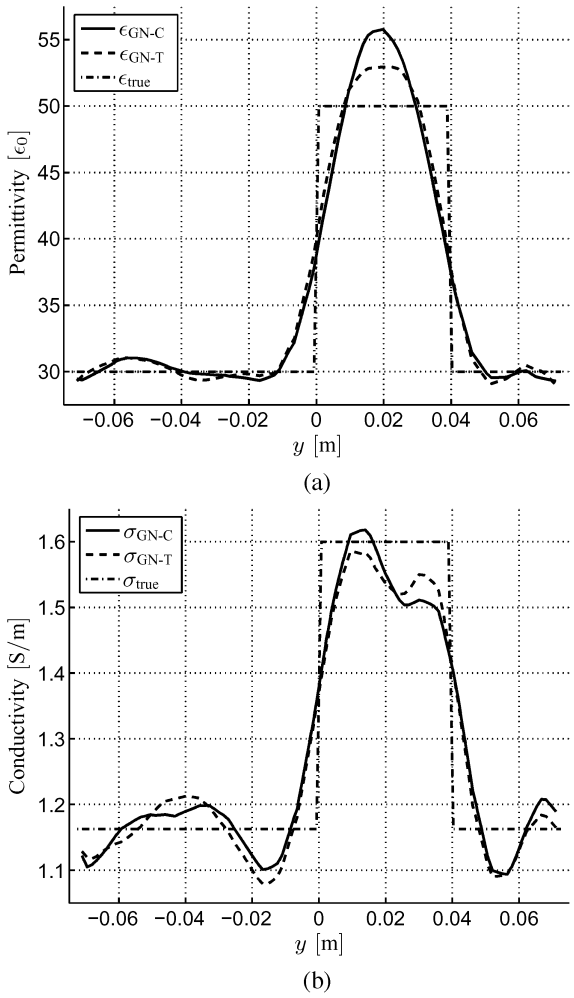

Fig. 7. Comparison of the reconstructed values along the y axis. (a) Permittivity; (b) conductivity.

Tikhonov regularization for the same problem. The solutions obtained using the CGLS algorithm are seen to follow those

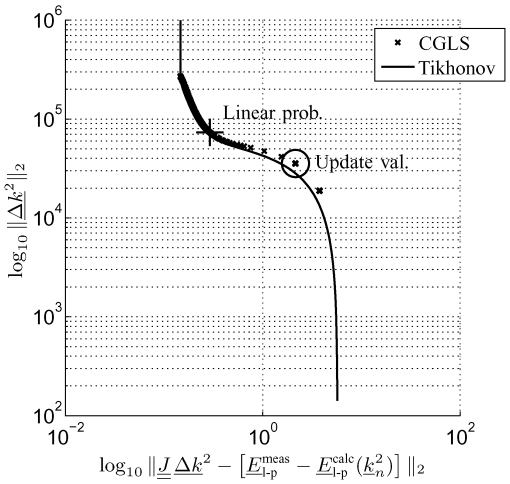

Fig. 8. Comparison of the L-curve obtained using the CGLS algorithm and the L-curve obtained using the Tikhonov regularization algorithm. The solution considered to be optimal for a linear problem is indicated by the + and is obtained after 25 iteration of the CGLS algorithm. The solution used to update the values in the GN-C algorithm is that obtained after two iterations of the CGLS algorithm and is indicated by the circle.

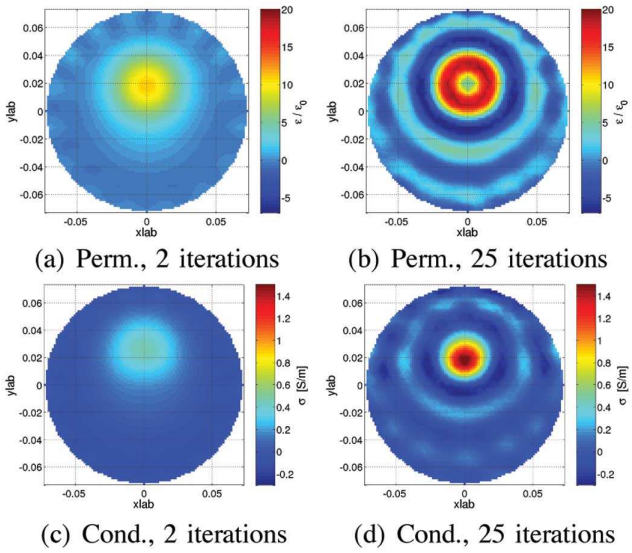

Fig. 9. Comparison of the update vector $[\underline{\Delta k}^2_1]^{(2)}$ found using 2 iterations of the CGLS algorithm and the update vector $[\underline{\Delta k}^2_1]^{(25)}$ found using 25 iterations. (a) Perm., 2 iterations; (b) perm., 25 iterations; (c) cond., 2 iterations; (d) cond., 25 iterations.

obtained with the Tikhonov algorithm closely, with the first iteration yielding the point in the lower right part of the curve. The solution after two iterations, which is used to update the values of the constitutive parameters in the GN-C algorithm is indicated by the circle in the plot. This is quite far from the solution closest to the point where the L-curve has its maximum curvature, the solution which is considered to be optimal when dealing with linear problems [10, Sec. 7.5]. This point is achieved after 25 CGLS iterations and is marked with a "+" in Fig. 8. The update vectors $[\underline{\Delta k}^2_1]^{(2)}$ and $[\underline{\Delta k}^2_1]^{(25)}$ obtained after 2 and 25 CGLS iterations, respectively, are shown in Fig. 9. In this figure, the elements of the vectors have been assigned to the corresponding coordinate positions, yielding

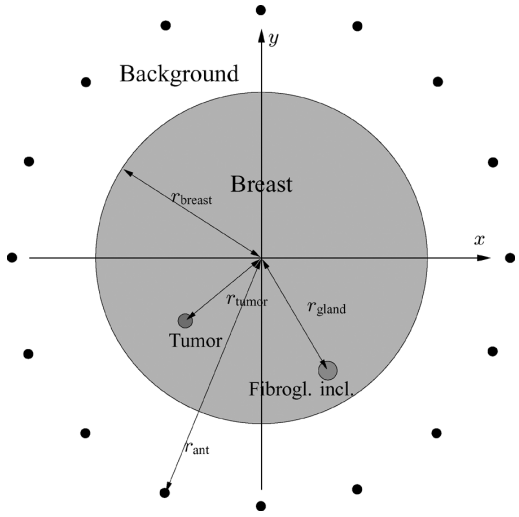

Fig. 10. Breast phantom configuration. The cylindrical breast phantom had a relative permittivity of $\epsilon_{r,\text{breast}} = 12.6$, a conductivity of $\sigma_{\text{breast}} = 0.62\ \text{S/m}$, and a radius of $r_{\text{breast}} = 5\ \text{cm}$. The 28 mm tumor inclusion had its center $r_{\text{tumor}} = 3\ \text{cm}$ from the center of the breast phantom with $\epsilon_{r,\text{tumor}} = 53.4$ and $\sigma_{\text{tumor}} = 1.15\ \text{S/m}$. The 21 mm fibroglandular-tissue inclusion was positioned with its center $r_{\text{gland}} = 4\ \text{cm}$ and $\epsilon_{r,\text{gland}} = 32.7$ and $\sigma_{\text{gland}} = 1.28\ \text{S/m}$. The antennas were positioned in a circular array with a radius of $r_{\text{ant}} = 7.5\ \text{cm}$ and the coupling liquid filling out the background had constitutive parameters $\epsilon_{r,\text{bg}} = 23.3$ and $\sigma_{\text{bg}} = 1.13\ \text{S/m}$. The imaging zone was a 13.5 cm diameter circle.

images showing the spatial distribution of the updates. It is seen that the updates found using two iterations recover the shape of the circular target nicely and has virtually no spatial oscillations in the updates. The updates found using 25 iterations, corresponding to the point on the L-curve with maximum curvature, still detects the target but with many more spatial oscillations present in the update values. The center of the recovered object also has a reduced property artifact. The $m = 25$ solution is therefore not suitable for updating the $\underline{k}^2$ vector.

B. Fatty Breast Phantom

To illustrate the details in the new algorithm and the impact on the image quality when the algorithms are applied to reconstruct tomographic images from measured data, phantom data was acquired at 1100 MHz. A schematic representation of the phantom is shown in Fig. 10. The phantom consisted of a 10 cm diameter thin-walled plastic cylinder filled with a glycerin-water mixture with constitutive parameters $\epsilon_{r,\text{breast}} = 12.6$ and $\sigma_{\text{breast}} = 0.62\ \text{S/m}$ simulating a primarily fatty breast. Inside the breast phantom, two smaller cylinders were positioned with liquids simulating fibroglandular tissue and a tumor. The 28 mm diameter tumor inclusion had constitutive parameters $\epsilon_{r,\text{tumor}} = 53.4$ and $\sigma_{\text{tumor}} = 1.15\ \text{S/m}$ while the 21 mm diameter fibroglandular inclusion was approximated by a liquid with $\epsilon_{r,\text{gland}} = 32.7$ and $\sigma_{\text{gland}} = 1.28\ \text{S/m}$. The center of the tumor was positioned approximately 3 cm from the center of the breast with its center at $(x_{\text{tumor}}, y_{\text{tumor}}) \approx (-2.3\ \text{cm}, -1.9\ \text{cm})$ while the fibroglandular inclusion had its center at $(x_{\text{gland}}, y_{\text{gland}}) \approx (2\ \text{cm}, -3.5\ \text{cm})$, which is approximately 4 cm from the breast center. The coupling liquid had a relative permittivity of $\epsilon_{r,\text{bg}} = 23.4$ and a conductivity of $\sigma_{\text{bg}} = 1.13\ \text{S/m}$.

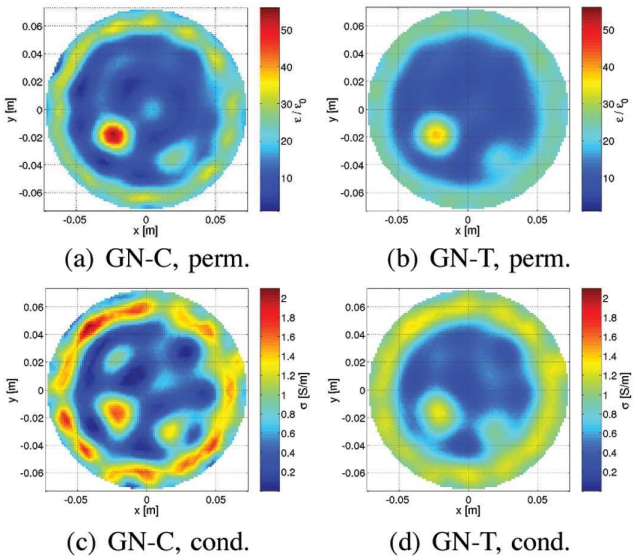

Fig. 11. Comparison of the reconstructed values of the conductivity and permittivity for the GN-C and the GN-T algorithms. The GN-C algorithm reached convergence after 11 iterations while the result of the GN-T is that reached after 20 iterations. (a) GN-C, perm. (b) GN-T, perm. (c) GN-C, cond. (d) GN-T, cond.

The results of the inversion with the GN-C and the GN-T algorithms are shown in Fig. 11. The perimeter of the breast phantom is readily visible in both cases, with a higher degree of artifacts outside the phantom for the GN-C images. Both the size and contrast of the two inclusions are reconstructed better with the GN-C algorithm than with the GN-T algorithm. In contrast, the amplitude of the artifacts within the recovered breast phantom are significantly elevated in the GN-C algorithm compared to that of the GN-T algorithm. The fibroglandular inclusion is localized well in the GN-C images while it appears to blur with the surrounding background in the associated GN-T images. This further illustrates that the increased spatial resolution of the GN-C algorithm comes at the expense of a higher level of the artifacts. By adjusting the number of iterations of the CGLS algorithm in the latter part of the GN-C algorithm, the balance between spatial resolution and artifacts can be adjusted with fewer iterations yielding lower spatial resolution and more iterations yielding higher level of the artifacts.

The normalized two-norm η_n for the GN-C and GN-T algorithms as function of the iteration number are shown in Fig. 12. As was observed for the simulation case, it is readily seen that the value of η_n declines much faster for the GN-C than for the GN-T algorithm.

C. Patient Measurements

Imaging the breast with the 2-D imaging system poses inherent challenges. For the planes closest to the chest wall, the possibility of artifacts arises due to the proximity of higher water content tissue associated with the pectoral muscles and the rib cage. For the planes closest to the nipple, the breast is more conical than cylindrical, posing different challenges for this system. It is therefore of interest to examine the performance of the new algorithm close to the chest wall, at the middle of the breast, and close to the anterior part of the breast.

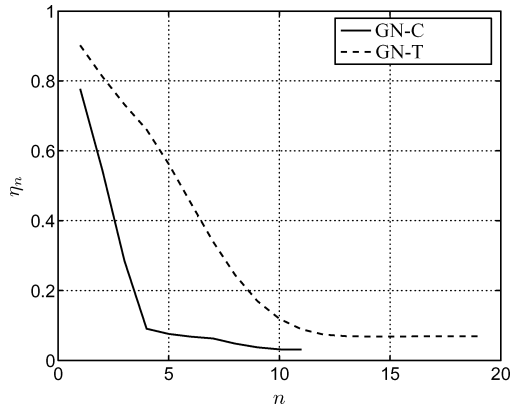

Fig. 12. Comparison of the normalized two-norm η_n for the GN-C and GN-T algorithms.

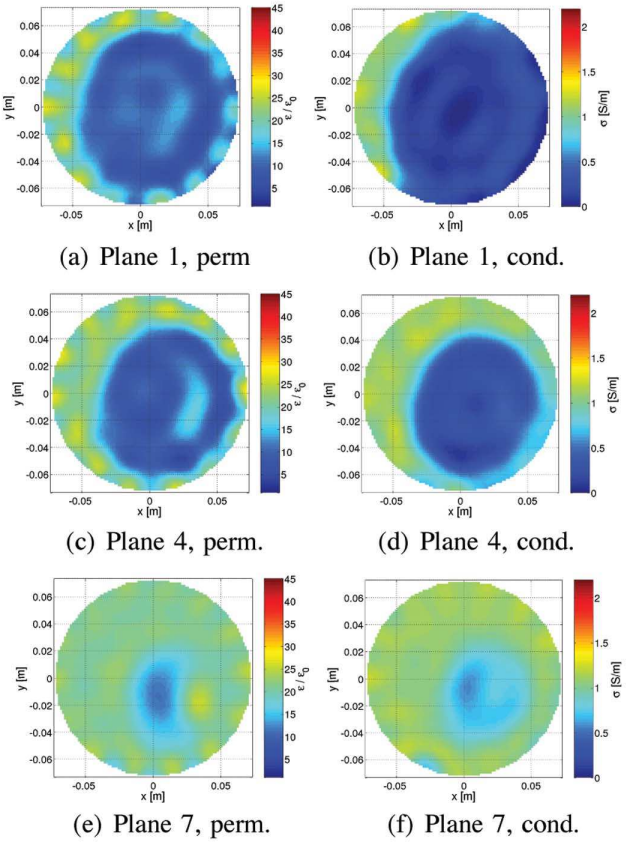

Fig. 13. Results obtained using the GN-T algorithm for the left breast of the test patient at three of the seven planes. All images are created using 20 iterations of the GN-T algorithm. (a) Plane 1, perm. (b) plane 1, cond. (c) plane 4, perm. (d) plane 4, cond. (e) plane 7, perm. (f) plane 7, cond.

Fig. 13 shows the results obtained at 1100 MHz with the GN-T algorithm for planes 1, 4, and 7 (with plane 1 being closest to the chest wall) for the left breast, while the images for the right breast are shown in Fig. 15.

The corresponding images obtained using the GN-C algorithm are shown in Figs. 14 and 16, respectively. The results

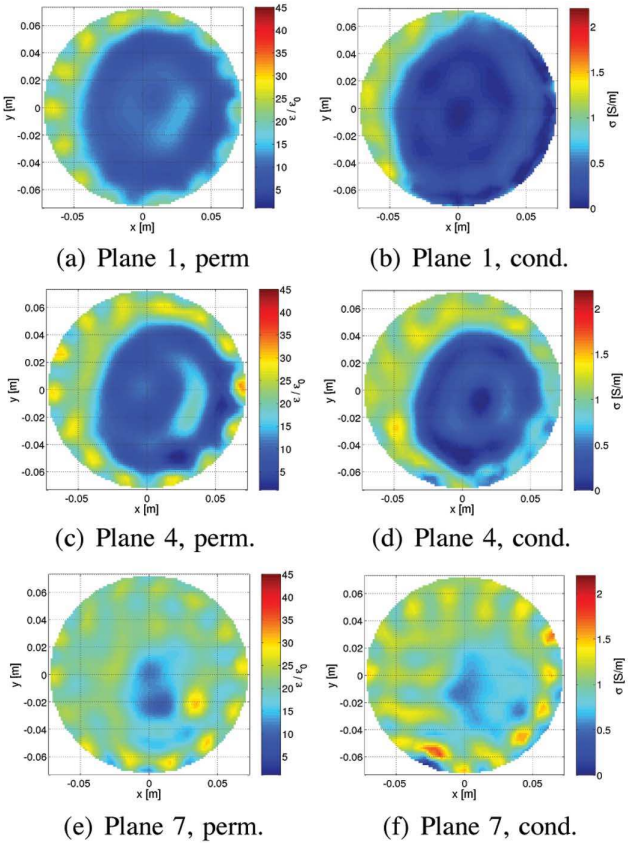

Fig. 14. Results obtained using the GN-C algorithm for the left breast of the test patient at three of the seven planes. The algorithm converge and terminates after 10 iterations of the algorithm for all three planes. (a) Plane 1, perm. (b) plane 1, cond. (c) plane 4, perm. (d) plane 4, cond. (e) plane 7, perm. (f) plane 7, cond.

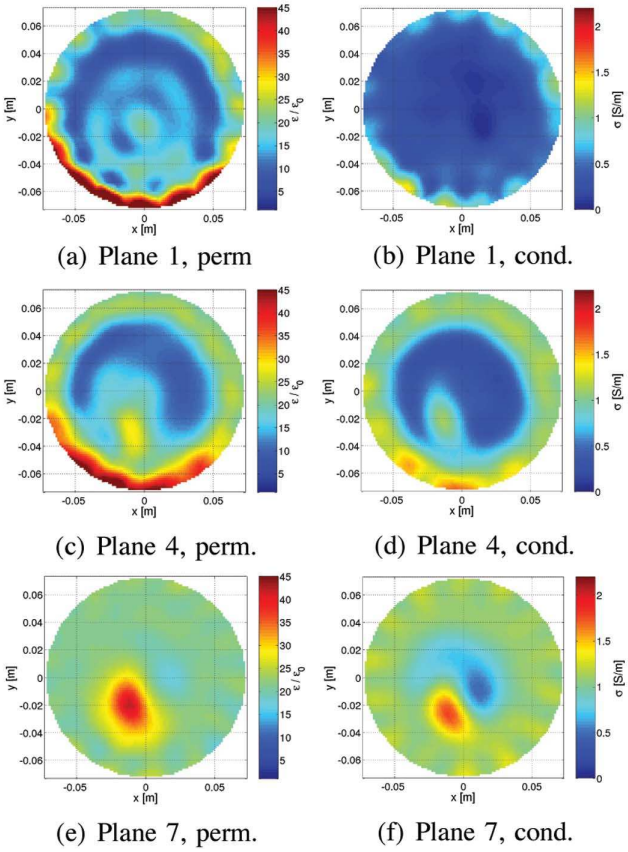

Fig. 15. Results obtained using the GN-T algorithm for the right breast of the test patient at three of the seven planes. All images are created using 20 iterations of the algorithm. (a) Plane 1, perm. (b) plane 1, cond. (c) plane 4, perm. (d) plane 4, cond. (e) plane 7, perm. (f) plane 7, cond.

shown for the GN-T algorithm were reconstructed in 20 iterations while the GN-C algorithm reached convergence after 10 iterations for all three planes of the left breast and after 11 iterations for plane 1, 9 iterations for plane 4, and 11 iterations for plane 7 of the right breast.

The patient in this case was 36 years old, had scattered-density breasts and was imaged with an 80:20 glycerin:water coupling fluid. The tumor was distributed over roughly a 4 cm diameter zone located near the anterior of the right breast at a 7 clock-face orientation, viewing the patient en face. The images for the two methods are quite similar providing a level of confidence for the overall approach. In general, the breast properties are lower than those of the background medium, with the complete perimeter of the breast in plane 1 not entirely visible—most likely due to the breast cross section being either larger than the imaging zone or positioned too close to the antenna array. The conductivity images for plane 1 are quite homogeneous within the breast perimeter. The permittivity images show scattered zones of slightly elevated properties, corresponding to scattered fibroglandular zones. The differences between the GN-C and GN-T algorithm images are minimal for this plane.

The full outline of the breast is more obviously discerned at the fourth imaging plane. Both the permittivity and conductivity images display elevated zones throughout the breast cross section associated with fibroglandular tissue. The elevated zones for the right breast appear to be more concentrated in the lower left quadrant, suggesting some influence from the tumor. This feature seems to be accentuated more by the GN-C algorithm. Likewise, a crescent-shaped feature to the right of the permittivity image of the left breast is also more accentuated in the GN-C images. While this is most likely due to the presence of fibroglandular tissue, it may be an example of the GN-C algorithm overshooting the recovered property values similar to the simulation case above. Of less importance but still noticeable is that the recovered background distribution (i.e., outside the breast perimeter) is more uneven for the GN-C algorithm.

The images for plane 7 also provide useful information about the patient. Obviously the overall breast cross section is smaller than for the previous planes. In addition, similar to that of plane 4, the recovered background distribution is fairly uneven—more so in the GN-C images than in the GN-T counterpart. For the most part, both left breast conductivity images show minimal variation within the breast. The corresponding permittivity images show an elevated zone to the right which may be associated with the higher properties of the nipple and concentrations of fibroglandular tissue. The elevated zone in the GN-C image is more localized with a higher central value than that

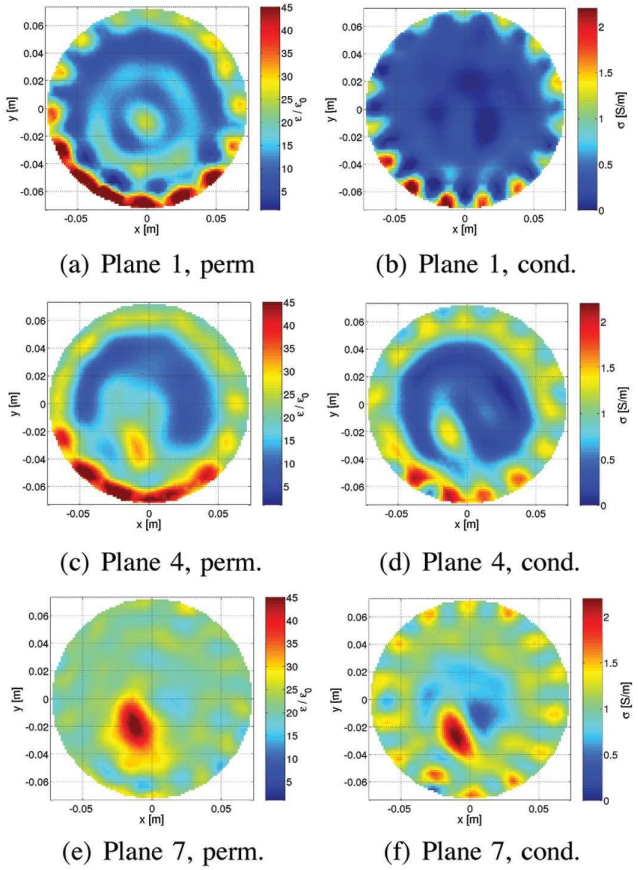

Fig. 16. Results obtained using the GN-C algorithm for the right breast of the test patient at three of the seven planes. The algorithm converges and terminates after 11 iterations for plane 1 and plane 7, and after 9 iterations for plane 4. (a) Plane 1, perm. (b) plane 1, cond. (c) plane 4, perm. (d) plane 4, cond. (e) plane 7, perm. (f) plane 7, cond.

for the GN-T image which appears partially blurred into the surrounding background distribution which is slightly elevated compared with the overall breast properties. The plane 7 images of the right breast all show localized property-enhanced zones in the lower left quadrant associated with the tumor location. The overall breast outline is vaguely visible within the background because of the limited breast/coupling liquid contrast there. The reconstructed tumor zones are more readily distinguished in the GN-C images because the recovered properties are higher.

In addition to the patient data presented in this paper, a number of other reconstructions of patient data have been carried out, and in general the GN-C algorithm is better able to extract internal features at the cost of overall enhanced image artifacts. The increased artifact level is a result of the GN-C algorithm, in the process of extracting all available information from the measurement data, includes an increased amount of the signal noise in the reconstructed image. The enhanced artifacts affects the reconstructed images in two ways. First, the calculated signal changes because of the artifacts. If the reconstruction algorithm is not terminated, this may lead to the algorithm attempting to fit the reconstructed image to a solution in which the noise, and thereby the artifacts, are dominant, yielding unpredictable results and useless images. Second, the enhanced artifacts inside the breast may be interpreted as tumors, thereby causing a false cancer-detection. It is therefore of great importance to terminate the GN-C algorithm as described in Section IV-B.

As mentioned earlier, a significant advantage of the GN-C algorithm is the number of iterations required to reconstruct the images. Given the fact that the time needed to complete one iteration is the same for both algorithms, the use of the GN-C algorithm reduced the overall time consumption by 45% to 55%.

VI. Conclusion

A new algorithm for determining the update values of the constitutive parameters in an iterative Gauss–Newton algorithm for microwave imaging of the breast has been derived. The algorithm is based on the use of the CGLS algorithm for solving the linear problem arising when solving for the image update values. The algorithm has been implemented as a two-stage procedure in which the first iterations of the Gauss–Newton algorithm are used to extract a coarse estimate of the distribution of constitutive parameters in the imaging domain while the latter set are used for extraction of finer details.

When compared to the previously used inversion algorithm, it appears to detect small objects more reliably at the cost of increased image artifacts. The artifacts can potentially be problematic in breast screening by increasing the number of false cancer detections. Further research is currently being pursued with the aim to reduce the level of the artifacts without sacrificing the increased spatial resolution.

Finally, the GN-C has been shown to use fewer iterations to converge, thus reducing the time-consumption by as much as 55%.

References

[1] X. Li, E. Bond, B. Van Veen, and S. Hagness, "An overview of ultra-wideband microwave imaging via space-time beamforming for early-stage breast-cancer detection," *IEEE Antennas Propag. Mag.* , vol. 47, no. 1, pp. 19–34, 2005.

[2] E. C. Fear, P. Meaney, and M. Stuchly, "Microwaves for breast cancer detection?," *IEEE Potentials*, vol. 22, no. 1, pp. 12–18, 2003.

[3] T. Williams, E. C. Fear, and D. Westwick, "Tissue sensing adaptive radar for breast cancer detection: Investigations of reflections from the skin," in *IEEE Antennas and Propagation Society Symp. in conjunction with USNC/URSI National Radio Science Meeting and IEEE Antennas and Propagation Soc. AP-S Int. Symp. Digest* , 2004, vol. 3, pp. 2436–2439.

[4] J. Sill and E. C. Fear, "Tissue sensing adaptive radar for breast cancer detection: Preliminary experimental results," in *IEEE Int. Microwave Symp. MTT-S Digest*, 2005, p. 4.

[5] J. Sill and E. C. Fear, "Tissue sensing adaptive radar for breast cancer detection: Study of immersion liquids," *Electron. Lett.*, vol. 41, no. 3, pp. 113–115, 2005.

[6] J. M. Sill and E. C. Fear, "Tissue sensing adaptive radar for breast cancer detection-experimental investigation of simple tumor models," *IEEE Trans. Microw. Theory Tech.*, vol. 53, no. 11, pp. 3312–3319, 2005.

[7] R. Nilavalan, J. Leendertz, I. Craddock, A. Preece, and R. Benjamin, "Numerical analysis of microwave detection of breast tumours using synthetic focussing techniques," in *Proc. IEEE Antennas and Propagation Society Symp.*, 2004, vol. 3, pp. 2440–2443.

[8] A. Bulyshev, A. Souvorov, S. Semenov, R. Svenson, A. Nazarov, Y. Sizov, and G. Tatsis, "Three-dimensional microwave tomography. Theory and computer experiments in scalar approximation," *Inverse Problems*, vol. 16, no. 3, pp. 863–875, 2000.

[9] S. Semenov, R. Svenson, A. Bulyshev, A. Souvorov, A. Nazarov, Y. Sizov, V. Posukh, A. Pavlovsky, P. Repin, A. Starostin, B. Voinov, M. Taran, G. Tatsis, and V. Baranov, "Three-dimensional microwave tomography: Initial experimental imaging of animals," *IEEE Trans. Biomed. Eng.*, vol. 49, no. 1, pp. 55–63, 2002.

[10] P. C. Hansen, *Rank-Deficient and Discrete Ill-Posed Problems: Numerical Aspects of Linear Inversion*, ser. Monographs on Mathematical Modeling and Computation. Philadelphia, PA: SIAM, 1998.

[11] Q. Fang, P. Meaney, S. Geimer, A. Streltsov, and K. Paulsen, "Microwave image reconstruction from 3-D fields coupled to 2-D parameter estimation," *IEEE Trans. Med. Imaging*, vol. 23, no. 4, pp. 475–484, 2004.

[12] Q. Fang, "Computational methods for microwave medical imaging," Ph.D. dissertation, Thayer School of Engineering, Dartmouth College, Hanover, NH, 2004.

[13] P. Meaney, S. Pendergrass, M. Fanning, D. Li, and K. Paulsen, "Importance of using a reduced contrast coupling medium in 2D microwave breast imaging," *J. Electromagn. Waves Applicat.*, vol. 17, no. 2, pp. 333–355, 2003.

[14] D. Li, P. M. Meaney, T. Raynolds, S. A. Pendergrass, M. W. Fanning, and K. D. Paulsen, "Parallel-detection microwave spectroscopy system for breast imaging," *Rev. Scientific Instruments*, vol. 75, no. 7, pp. 2305–2313, 2004.

[15] P. Meaney, K. Paulsen, S. Geimer, S. Haider, and M. Fanning, "Quantification of 3-D field effects during 2-D microwave imaging," *IEEE Trans. Biomed. Eng.*, vol. 49, no. 7, pp. 708–720, 2002.

[16] P. Meaney, K. Paulsen, B. Pogue, and M. Miga, "Microwave image reconstruction utilizing log-magnitude and unwrapped phase to improve high-contrast object recovery," *IEEE Trans. Med. Imaging*, vol. 20, no. 2, pp. 104–116, 2001.

[17] C. T. Kelley, *Iterative Methods for Linear and Nonlinear Equations*, ser. Frontiers in Applied Mathematics. Philadelphia, PA: SIAM, 1995, vol. 16.

[18] C. T. Kelley, *Solving Nonlinear Equations With Newton's Method*. Philadelphia, PA: SIAM, 2003.

[19] P. Meaney, K. Paulsen, A. Hartov, and R. Crane, "Microwave imaging for tissue assessment: Initial evaluation in multitarget tissue-equivalent phantoms," *IEEE Trans. Biomed. Eng.*, vol. 43, no. 9, pp. 878–890, 1996.

[20] K. Paulsen, P. Meaney, M. Moskowitz, J. Sullivan, and J. M. , "A dual mesh scheme for finite element based reconstruction algorithms," *IEEE Trans. Biomed. Eng.*, vol. 14, no. 3, pp. 504–514, 1995.

[21] K. Paulsen and P. Meaney, "Nonactive antenna compensation for fixed-array microwave imaging—Part I: Model development," *IEEE Trans. Biomed. Eng.*, vol. 18, no. 6, pp. 496–507, 1999.

[22] P. Meaney, K. Paulsen, J. Chang, M. Fanning, and A. Hartov, "Nonactive antenna compensation for fixed array microwave imaging—Part II: Imaging results," *IEEE Trans. Biomed. Eng.*, vol. 18, no. 6, pp. 508–518, 1999.

[23] N. Joachimowicz, C. Pichot, and J. Hugonin, "Inverse scattering: An iterative numerical method for electromagnetic imaging," *IEEE Trans. Antennas Propag.*, vol. 39, no. 121, pp. 1742–1753, 1991.

[24] Q. Fang, P. Meaney, and K. Paulsen, "Multi-dimensional phase unwrapping: Definition and properties," *IEEE Trans. Image Processing*, accepted for publication.

[25] P. Meaney, E. Demidenko, N. Yagnamurthy, D. Li, M. Fanning, and K. Paulsen, "A two-stage microwave image reconstruction procedure for improved internal feature extraction," *Med. Phys.*, vol. 28, no. 11, pp. 2358–2369, 2001.

Tonny Rubæk (S'02) received the M.Sc.E.E. degree from the Technical University of Denmark, Lyngby, in 2004, where he is currently working toward the Ph.D. degree.

His research areas include linear and nonlinear microwave-imaging algorithms and associated hardware.

Paul M. Meaney (M'92) received the A.B. degree in both computer science and electrical engineering from Brown University, Providence, RI, in 1982, the M.S. degree in electrical engineering from the University of Massachusetts, Amherst, in 1985, and the Ph.D. degree in biomedical engineering from Dartmouth College, Hanover, NH, in 1995.

He was an NSF-NATO Postdoctoral Fellow at the Royal Marsden Hospital in Sutton, England, from 1996 to 1997. He was a Research Assistant Professor at Dartmouth College from 1997 to 2003 and a Research Associate Professor since 2003. He has three patents related to microwave imaging and is coauthor on over 120 journal articles and conference proceedings. His interests include developing microwave imaging for biomedical applications—especially breast imaging and hyperthermia monitoring.

Peter Meincke (S'93–M'96) was born in Roskilde, Denmark, on November 25, 1969. He received the M.S.E.E. and Ph.D. degrees from the Technical University of Denmark (DTU), Lyngby, Denmark, in 1993 and 1996, respectively.

In spring and summer of 1995, he was a Visiting Research Scientist at the Electromagnetics Directorate of Rome Laboratory, Hanscom Air Force Base, MA. In 1997, he was with a Danish cellular phone company, working on theoretical aspects of radio-wave propagation. In spring and summer of 1998, he was visiting the Center for Electromagnetics Research at Northeastern University, Boston, MA, while holding a Postdoctoral position from DTU. In 1999, he became a staff member in the Department of Electromagnetic Systems, DTU. He is currently an Associate Professor with Ørsted-DTU, ElectroScience Section, DTU. His current teaching and research interests include electromagnetic theory and scattering, inverse problems, antenna theory, microwave imaging, and wireless communications.

Dr. Meincke won the First Prize Award in the 1996 IEEE Antennas and Propagation Society Student Paper Contest in Baltimore, MD, for his paper on uniform physical theory of diffraction equivalent edge currents. Also, he received the 2000 R. W. P. King Paper Award for his paper entitled, "Time-domain version of the physical theory of diffraction" published in the February 1999 issue of the IEEE TRANSACTIONS ON ANTENNAS AND PROPAGATION.

Keith D. Paulsen (S'85–M'86) received the B.S. degree in biomedical engineering from Duke University, Durham, NC, in 1981 and the M.S. and Ph.D. degrees in biomedical engineering from Dartmouth College, Hanover, NH, in 1984 and 1986, respectively.

From 1986 to 1988, he was an Assistant Professor in the Electromagnetics Group within the Department of Electrical and Computer Engineering, University of Arizona, Tucson. He is currently a Professor at the Thayer School of Engineering, Dartmouth College and the Director of the Radiobiology and Bioengineering Research Program for the Norris Cotton Cancer Center within the Dartmouth-Hitchcock Medical Center, Lebanon, NH. His research interests include computational methods with particular emphasis on biomedical problems in cancer therapy and imaging, and model-guided surgery.

Journal Paper 2

Analysis of the Performance of an Update Algorithm for Newton-Based Nonlinear Microwave Imaging for Breast-Cancer Screening

Tonny Rubæk, Paul M. Meaney, Peter Meincke, and Keith D. Paulsen

Status:
Submitted: October 2007
Accepted: – – – – – –
Published: – – – – – –
Journal: IEEE Transactions on Medical Imaging

Analysis of the Performance of an Update Algorithm for Newton-Based Nonlinear Microwave Imaging for Breast-Cancer Screening

Tonny Rubæk, *Student Member, IEEE,* Paul Meaney, *Member, IEEE,* Peter Meincke, *Member, IEEE,* and Keith D. Paulsen, *Member, IEEE*

***Abstract*— In previously published work, the authors have described how the artifact level of the recovered images in tomographic microwave imaging often increases when the associated reconstruction parameters are adjusted for maximum resolution. In this paper, increased resolution is obtained without increased artifact level by introducing a new algorithm based on a Euclidean-distance penalty term for the calculation of the updates in a Gauss-Newton iterative algorithm for nonlinear microwave imaging of the breast. Furthermore, it is of interest to extract more information from the residual vector than can be done by observing its norm alone. To this end, it is shown that the distribution of the elements in the residual vector, characterized by its goodness of fit or χ^2 value, provides useful information about the reconstruction algorithm. Finally, the reconstructed images are analyzed by observing the spectra of the error of the images. This demonstrates that the reconstructions are biased, implying that the widely applied normalized norm of the error in the reconstructions, on its own, is not a suitable measure of the quality of the reconstructed images.**

***Index Terms*— Biomedical electromagnetic imaging, cancer, electromagnetic scattering inverse problems, image reconstruction, imaging, inverse problems, microwave imaging, nonlinear equations**

I. Introduction

MICROWAVE imaging is emerging as a screening tool for the detection of breast cancer [1], [2]. The use of microwaves for this purpose is based on the contrast in the constitutive electromagnetic parameters between healthy tissue and cancerous tumors in the microwave region, first reported by T. S. England in 1949–1950 [3], [4], and is seen as an appealing supplement to the use of X-ray mammography due to the non-ionizing nature of the microwaves.

There are primarily two different approaches currently being pursued for the detection of cancer in the breasts of women using microwave imaging. One is based on time-domain techniques in which a broadband pulse is transmitted into the breast and the response is measured at either the same antenna or by a number of receiving antennas [1], [5]–[7]. Most of these techniques use radar-based algorithms to locate the targets creating the scattering, i.e., the tumors in the breast [1], [5], [6]. Results have been reported for simulation studies [5], [8] and phantom measurements [9]–[11] although no results for clinical breast exams are available at the time of writing. In addition to the radar-based algorithms, several results have also been reported for nonlinear algorithms based on the inversion of Maxwell's equations in the time domain [7], [12].

The other approach for microwave imaging of the breast is based on frequency-domain tomographic techniques in which images of the distribution of constitutive parameters are reconstructed by solving a nonlinear inversion problem [13], [14]. When this procedure is used, the imaging domain is irradiated by one antenna at a single frequency, while the response is measured on a number of receiving antennas. The measured responses can then be used as input to a Gauss-Newton iterative algorithm based on a frequency-domain formulation of Maxwell's equations. The forward model is nonlinear with respect to the constitutive parameters and the process of inverting it to reconstruct the images is, therefore, a computationally expensive task. The cost due to the increased computational load of the tomographic approach is compensated for by its superior ability to handle scattering problems wherein large regions of the imaging domain have unknown constitutive parameters different from those of the known background. Multifrequency, tomographic approaches have been studied to a limited degree because of the ability to add new information to the inverse scattering process; however, the added challenges include added computational costs and increased problem complexity associated with having to incorporate models of the tissue property dispersion [15], [16]. Frequency-domain techniques have been reported to perform well in a number of biomedical imaging applications, including breast imaging [17]–[19] but also for imaging of complete canine corpses and excised

hearts [14], [20].

For the frequency-domain tomographic imaging system currently being tested at Dartmouth College [21], the nonlinear forward model is inverted using a Gauss-Newton iterative algorithm. In this algorithm, the norm of the residual vector, the difference between the measured data and the computed values for a given distribution of constitutive parameters, is minimized by iteratively updating the distribution. A recently reported update to the algorithm uses the iterative conjugated gradient least squares (CGLS) algorithm in a two-step procedure for determining the property values in each iteration of the Newton algorithm [22]. During the implementation and analysis of this algorithm, a number of issues arose. First, it was observed that the new algorithm could improve the resolution in the reconstructed images; however, this improvement came at the cost of increased artifact levels in the images. Although the augmented resolution might decrease the rate of false negatives in a screening program, the higher artifact level is likely to increase the rate of false positives. An algorithm in which the resolution is improved with only a minimum rise in the artifact level is therefore highly desirable. Second, the norm of the residual vector in the reconstruction problem was found to be insufficient as an indicator for the success of the algorithm to reconstruct the images. This is especially true if the noise level is high, or when the norm of the residual vector becomes small. In these situations, the norm of the residual vector may decrease even while the algorithm attempts to fit the model to the noise component of the data, thereby creating divergent results. An improved measure of the convergence of the reconstruction based on results obtainable during the Gauss-Newton iterative algorithm should therefore be sought to assure that the choice of regularization parameters and number of iterations are optimal. Finally, the analysis of the final images in terms of the errors in the reconstructed constitutive parameters compared to the true values may provide valuable information which may be useful towards improving the imaging algorithms.

In this paper, the three issues mentioned above are addressed. More specifically, an imaging algorithm in which the updates in the iterative algorithm are calculated using a Euclidean distance penalty term (EDPT) is introduced and the performance is analyzed as a function of the parameters governing the performance of the algorithm. The algorithm is closely related to that introduced in [23] but incorporates an additional layer of regularization which increases the robustness of the algorithm. To extract the maximum amount of independent information relating directly to the quality of the results during the reconstruction, the distribution of the residual vector terms, characterized by the goodness of fit metric χ^2 with respect to a normal distribution, as well as the norm of the residual vector are used. To analyze the quality of the reconstructed images, the norms of the errors in the reconstructed permittivity and conductivity images, as well as the spectra of the errors, are introduced.

This paper is organized as follows. In Section II, a brief introduction to the imaging system under consideration is presented. This is followed by a description of the new imaging algorithm in Section III. The measures of the performance used in this paper are introduced in Section IV, and finally, in Section V, the algorithm is applied to reconstruct images in cases of simulation, phantom, and patient measurements and the results are compared with those obtained using the two-step CGLS algorithm introduced in [22].

II. Imaging System

The imaging system being tested at Dartmouth College [21] consists of 16 monopole antennas positioned in a circular setup as shown in Fig. 1. The system is designed for operation in the frequency range from 500 MHz to 2300 MHz, and during the measurements, the patient lies prone on top of a measurement tank with her breast suspended through an aperture in the top of the tank. The tank is filled with a glycerin-water coupling liquid which is used to assure that the energy emitted by the antennas is adequately coupled to the interior of the breast [24]. The 16 antennas are shifted vertically down through seven positions and at each position the antennas, in turn, act as a transmitter while the coherent response $S^{t,r}$, with t and r indicating the transmitting and receiving antenna numbers, is measured by the remaining 15 antennas. This yields a complete set of $n_{\text{meas}} = 240$ measurements of the amplitude and phase of the received signal for each position.

The imaging system operates by creating images of each of the seven measurement planes under the assumption that the 3-D electromagnetic scattering problem in each plane can be accurately represented by a 2-D model. The validity of this assumption has been investigated in [25], [26]. It was found that the 2-D representation of the problem does degrade the image quality somewhat. However, due to the relatively small radius of the imaging system and the highly attenuating nature of the coupling liquid, the effect of the 3-D field propagation not being represented accurately in the 2-D model is minimal.

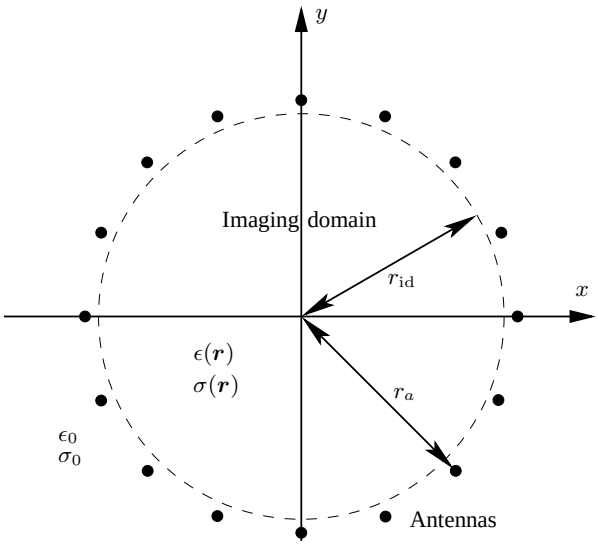

(a) Top view.

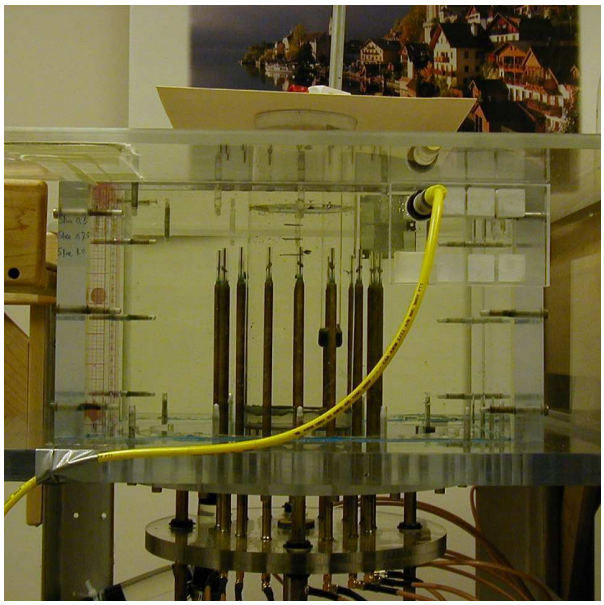

(b) Photo of antenna setup.

Fig. 1. Imaging system: (a) schematic top view and (b) photo of imaging system used for patient exams. The 16 antennas are positioned in a circular setup with radius $r_a = 7.62$ cm. The imaging domain with radius $r_{\mathrm{id}} = 7.25$ cm and unknown constitutive parameters $\epsilon(\boldsymbol{r})$ and $\sigma(\boldsymbol{r})$ is surrounded by the coupling liquid with known constitutive parameters ϵ_0 and σ_0.

III. Imaging Algorithm

As mentioned in the Introduction, the reconstructed images, obtained using a frequency-domain tomographic algorithm, show the spatial distribution of the constitutive electromagnetic parameters, permittivity and conductivity, of the imaging domain. For the reconstruction algorithm presented in this paper, the time notation $\mathrm{e}^{-i\omega t}$ is used (with i and t being the imaginary unit and time) and the constitutive parameters are represented by the spatial distribution of the squared complex wave number of the imaging domain given by

$$k^2(\boldsymbol{r}) = \omega^2\mu_0\epsilon(\boldsymbol{r}) + i\omega\mu_0\sigma(\boldsymbol{r}). \tag{1}$$

Herein, ϵ is the permittivity and σ is the conductivity at the angular frequency ω and position is given by the vector $\boldsymbol{r}$. The entire imaging domain is assumed to be non-magnetic, indicated by the utilizing the free-space permeability, μ_0. The reconstruction algorithm is based on a Gauss-Newton iterative inversion scheme in which the nonlinear, ill-posed minimization problem

$$\begin{aligned}\underline{k}^2 &= \operatorname{argmin}\left\{\left\|\underline{S}_{\mathrm{lp}}^{\mathrm{meas}} - \underline{S}_{\mathrm{lp}}^{\mathrm{calc}}(\underline{k}^2)\right\|_2^2\right\} \\ &= \operatorname{argmin}\left\{\left\|\underline{S}_{\mathrm{lp}}^{\mathrm{res}}(\underline{k}^2)\right\|_2^2\right\} \\ &\qquad \text{subj. to regularization}\end{aligned} \tag{2}$$

is solved. In this expression, $\underline{S}_{\mathrm{lp}}^{\mathrm{meas}}$ is a vector containing the measured data, $\underline{S}_{\mathrm{lp}}^{\mathrm{calc}}$ is a vector containing the corresponding data calculated for a given distribution of constitutive parameters represented by the vector $\underline{k}^2$, and $\underline{S}_{\mathrm{lp}}^{\mathrm{res}}$ is denoted the residual vector. The elements of $\underline{S}_{\mathrm{lp}}^{\mathrm{calc}}$ and the Jacobian of the problem, which is also required in the Gauss-Newton algorithm, are calculated using a dual-mesh, hybrid-element forward model which has been treated extensively elsewhere [27]–[31]. Here it suffices to mention that the finite element imaging domain with a radius of $r_{\mathrm{id}} = 7.25$ cm is represented by a mesh with $n_{\mathrm{nodes}} = 559$ nodes in the reconstruction. The subscript "lp" in (2) indicates that both the measured and the calculated signals are used in their log-magnitude unwrapped phase formulation [13].

In this formulation, the complex signal $S^{t,r}$ for each combination of transmitting and receiving antennas is represented by a pair of elements in each of the vectors $\underline{S}_{\mathrm{lp}}^{\mathrm{meas}}$ and $\underline{S}_{\mathrm{lp}}^{\mathrm{calc}}$ given by the change in the logarithm of the amplitude of the signal

$$S_{\mathrm{l}}^{t,r} = \log(|S_{\mathrm{obj}}^{t,r}|) - \log(|S_{\mathrm{empty}}^{t,r}|) \tag{3a}$$

and the change in the unwrapped phase of the signal

$$S_{\mathrm{p}}^{t,r} = \angle(S_{\mathrm{obj}}^{t,r}) - \angle(S_{\mathrm{empty}}^{t,r}) \tag{3b}$$

between a measurement/calculation with an empty measurement system and a measurement/calculation with the object to be examined (the breast) in the measurement system. This formulation of the problem has been shown to improve the reconstructed images by allowing for the

scattered fields to be represented over several Riemann sheets, and by emphasizing the changes in the small signal levels measured between antennas on opposite sides of the breast, which hold the most information related to the scattering objects inside the breast. This formulation of the reconstruction problem has been thoroughly described in the literature [13], [32], [33].

The algorithm is initialized with $\underline{k}_0^2$, representing the known constitutive parameters of the coupling liquid, and in each iteration of the Newton algorithm, the following three steps are performed, with n being the iteration number starting from 0:

1) The forward model is used to calculate the electric fields from the distribution of constitutive parameters $\underline{k}_n^2$. The corresponding Jacobian matrix $\underline{\underline{J}}_n$ is computed using the adjoint method [26].
2) The calculated signals and Jacobian matrix are transformed to the log-magnitude unwrapped phase formulation.
3) The update of the constitutive parameters $\underline{\Delta k}^2$ is found by solving the the ill-posed problem

$$\underline{\Delta k}_n^2 = \operatorname{argmin}\Big\{ \Big\| \underline{\underline{J}}_n \underline{\Delta k}_n^2 - \underline{S}_{\mathrm{lp}}^{\mathrm{res}}(\underline{k}_n^2) \Big\|_2^2 + \lambda_n^2 \left\| \underline{k}_{N_0}^2 - \underline{k}_{n+1}^2 \right\|_2^2 \Big\} \quad \text{subj. to regularization,} \tag{4}$$

and the constitutive parameters are updated as

$$\underline{k}_{n+1}^2 = \underline{k}_n^2 + \alpha_n \underline{\Delta k}_n^2 \tag{5}$$

wherein α_n is the Newton step [34], [35], [36, Sec. 8.2] and $\underline{k}_{N_0}^2$ is an intermediate image found in Newton iteration N_0.

The new imaging algorithm is characterized by the Euclidean-distance penalty term (EDPT) which is applied for regularizing the ill-posed linear update problem (4). In this equation, the Jacobian matrix is a $(2n_{\text{meas}})$-by-$(2n_{\text{nodes}})$ matrix with real-valued elements corresponding to the derivatives of the logarithm of the amplitudes and the unwrapped phases of the calculated signals with respect to the real and imaginary parts of the squared wave numbers [13]. The new algorithm solves (4) with $\lambda_n = 0$ in the first N_0 Newton iterations (N_0 being a positive integer) and then introduces the EDPT by letting $\lambda_n = \lambda_{\mathrm{EDPT}} \neq 0$ in the latter part of the reconstruction. The details of choosing suitable values of N_0 and λ_{EDPT} are described below. The basic idea behind this two-step procedure is that the algorithm should obtain an intermediate low-pass version $\underline{k}_{N_0}^2$ of the true image and then, by utilizing the additional regularizing effects of the EDPT, extract the high-frequency components of the image in the latter part of the reconstruction. The value of λ_{EDPT} is determined at the Newton iteration where the intermediate image is obtained and kept constant throughout the latter part of the Newton iteration, implying that λ_n takes on only two values; zero for $n \leq N_0$ and λ_{EDPT} for $n > N_0$.

In the two-step CGLS algorithm presented in [22], the updates are found using the CGLS algorithm with two CGLS iterations during the first part of the Newton algorithm and 16 in the latter part. The transition from the low to the higher number of iterations as well as the termination of the algorithm are based on the value of the two-norm of the residual vector.

For both the reconstruction algorithm introduced in [22], as well as the new EDPT algorithm presented here, the computation of the forward solution (step 1) is by far the most time consuming part of the Gauss-Newton algorithm. The speed with which the algorithm can reconstruct an image is therefore largely governed by the number of Newton iterations needed to obtain a satisfactory image.

A. CGLS-Based Update Algorithm with no Penalty Term $(\lambda_n = 0)$

In the first N_0 Newton iterations, $\lambda_n = 0$ and the linear problem (4) for determining the updates reduces to

$$\underline{\Delta k}_n^2 = \operatorname{argmin} \left\{ \left\| \underline{\underline{J}}_n \underline{\Delta k}_n^2 - \underline{S}_{\mathrm{lp}}^{\mathrm{res}}(\underline{k}_n^2) \right\|_2^2 \right\} \tag{6}$$

subject to a suitable regularization. In this paper, the iterative CGLS algorithm [37, Sec. 6.3] is applied to obtain regularization. The CGLS algorithm solves the linear update problem using five simple steps in each of the M_0 CGLS iterations which constitute the basis of the EDPT update algorithm. The regularized solution obtained using the CGLS algorithm, which is described in details in [22], is

$$\left\{ \underline{\Delta k}_n^2 \right\}^{(M_0)} = \operatorname{argmin} \Big\{ \| \underline{\underline{J}}_n \left\{ \underline{\Delta k}_n^2 \right\}^{(M_0)} - \left(\underline{S}_{\mathrm{lp}}^{\mathrm{res}}(\underline{k}_n) \right) \|_2^2 \Big\} \tag{7a}$$

subject to

$$\left\{ \underline{\Delta k}_n^2 \right\}^{(M_0)} \in \mathcal{K}_{M_0} \left(\underline{\underline{J}}_n \underline{\underline{J}}_n^T, \underline{\underline{J}}_n^T \left(\underline{S}_{\mathrm{lp}}^{\mathrm{res}}(\underline{k}_n) \right) \right). \tag{7b}$$

Hence, the solution is the least-squares solution to the linear problem (6) with the constraint that the solution must lie in the M_0-dimensional Krylov subspace $\mathcal{K}_{M_0}$ related to the problem. As the number M_0 of CGLS iterations increases, so does the number of dimensions in the solution. As described in [37, Sec. 6.3], the regularizing effect of the CGLS algorithm is determined by the number of iterations M_0, and, thus, by the number

of dimensions of the Krylov subspace onto which the solution is projected. The regularizing effect is realized because noise and model inaccuracies will be more dominant in the higher dimensions of the Krylov subspace than in the lower.

The performance of the Newton reconstruction algorithm during the first N_0 Newton iterations is governed solely by the number of CGLS iterations M_0 performed to calculate the updates in each Newton iteration. In [22] it was found that standard criterions for determining the regularization parameter, such as the L-curve method [37, Sec. 7.5], is not suited for determining the regularization parameter. This implies that the choice of the parameter M_0 must be based on general considerations and experience from, e.g., phantom measurements. This choice and its influence on the performance of the reconstruction algorithm is dealt with in detail in Section V.

B. Euclidean-Distance Penalty Term Update ($\lambda_n \neq 0$)

After a certain number N_0 of Newton iterations with $\lambda_n = 0$, the intermediate image $\underline{k}^2_{N_0}$ is obtained. By reformulating the minimization problem in (4) for $\lambda_n \neq 0$, the following expression is found for the update values

$$\underline{\Delta k}^2_n = \operatorname{argmin}\left\{ \left\| \begin{bmatrix} \underline{\underline{J}}_n \\ \lambda_n \underline{\underline{I}} \end{bmatrix} \underline{\Delta k}^2_n - \begin{bmatrix} \underline{S}^{\mathrm{res}}(\underline{k}^2_n) \\ \lambda_n \left(\underline{k}^2_{N_0} - \underline{k}^2_n \right) \end{bmatrix} \right\|_2^2 \right\} \quad \text{subj. to regularization.} \tag{8}$$

Herein, $\underline{\underline{I}}$ is the identity matrix and the solution to this linear problem is found using the CGLS algorithm. Compared with the EDPT algorithm introduced in [23], in which the regularization of the linear equation in (8) is solely determined by the value of λ_n, the use of the CGLS algorithm in the new reconstruction algorithm adds an additional layer of regularization. This implies that the choice of λ_n may be performed in a more simple way than that described in [23], since the performance of the reconstruction algorithm is less sensitive to the value of λ_n.

The number of CGLS iterations M_{EDPT} needed to obtain the best solution to (8) is found using the L-curve criterion in each of the Newton iterations where $\lambda_n = \lambda_{\mathrm{EDPT}}$, and the value of M_{EDPT} thereby changes at each iteration. The L-curve criterion is based on the behavior of the norms of the residual and the solution vectors of the problem given by

$$v_{\mathrm{res}} = \begin{bmatrix} \underline{\underline{J}}_n \\ \lambda_n \underline{\underline{I}} \end{bmatrix} \left\{ \underline{\Delta k}^2_n \right\}^{(m)} - \begin{bmatrix} \underline{S}^{\mathrm{res}}(\underline{k}^2_n) \\ \lambda_n \left(\underline{k}^2_{N_0} - \underline{k}^2_n \right) \end{bmatrix} \tag{9a}$$

and

$$v_{\mathrm{sol}} = \left\{ \underline{\Delta k}^2_n \right\}^{(m)}. \tag{9b}$$

As described in [37, Sec. 7.5], an L-shaped curve is obtained if the norm of the solution vector is plotted as a function of the norm of the residual vector for different amounts of regularization (different values of m), and the optimum solution is that for which the regularization yields a result lying at the corner of the L-curve corresponding to $m = M_{\mathrm{EDPT}}$. Hence, the regularized solution belongs to the M_{EDPT}-dimensional Krylov subspace related to the problem. To find the corner of the L-curve, the approach outlined in [37, Sec. 7.5] is applied. This includes smoothing the calculated L-curve and fitting a cubic spline to it. The curvature of the cubic spline can then be found, and the solution closest to the point of maximum curvature may be determined. If the value of λ_n is too small, the augmented linear update problem (8) will be similar to the non-augmented problem (6) and the L-curve criterion will not be applicable for determining the updates.

C. Newton Step

The Newton step α_n in (5) is calculated using the ratio between the norm of the update vector $\underline{\Delta k}^2_n$ and the parameter vector $\underline{k}^2_n$ as

$$\alpha_n = \begin{cases} 1 & \text{if} \quad \frac{\|\underline{\Delta k}^2_n\|_2}{\|\underline{k}^2_n\|_2} \leq \frac{1}{4} \\ \frac{\|\underline{k}^2_n\|_2}{4\|\underline{\Delta k}^2_n\|_2} & \text{if} \quad \frac{\|\underline{\Delta k}^2_n\|_2}{\|\underline{k}^2_n\|_2} > \frac{1}{4} \end{cases}. \tag{10}$$

The scaling of the update vector with the Newton step is thus only applied when the two-norm of the update is greater than one fourth of the two-norm of the current distribution of wave numbers. This scaling serves two purposes. One is to keep the solution from getting stuck in a local minimum. The other is to make sure that the phases of the calculated signals do not change more than $\pm\pi$ which is often the case in the first few iterations. It is necessary to keep the phases from changing too much since the phase-unwrapping of the signals in the reconstruction algorithm is done in terms of the contrast as described in [13].

D. Governing Parameters of the EDPT Algorithm

In short, the performance of the EDPT algorithm presented in this paper is governed by three parameters. The first is the fixed number of CGLS iterations M_0 used in the first part of the algorithm to determine the updates. The second is the number of Newton iterations N_0 used to obtain the intermediate image $\underline{k}^2_{N_0}$ and the third and final is the value of λ_{EDPT} which determines

how much the EDPT should influence the calculation of the update vector in the latter part of the reconstruction algorithm.

The choice of M_0 for the CGLS iterations used in the first part of the algorithm is based on the observation that a high number of iterations is more likely to induce artifacts than a low number, while the algorithm with a low number requires more Newton iterations to obtain a satisfactory intermediate image. It has been found that for the EDPT algorithm, the best choice of M_0 is 2, which is the same number of iterations used in the two-step CGLS algorithm. The choice of N_0 is also determined in much the same way as the number of Newton iterations in the two-step algorithm with two CGLS iterations, i.e., based on the change in the norm of the residual vector. To this end, the normalized two-norm η_n is introduced as

$$\eta_n = \frac{\left\|\underline{S}_{\mathrm{lp}}^{\mathrm{res}}(\underline{k}_n^2)\right\|_2^2}{\left\|\underline{S}_{\mathrm{lp}}^{\mathrm{res}}(\underline{k}_0^2)\right\|_2^2}, \tag{11}$$

and the change in this norm is introduced as $\Delta\eta_n$ given by

$$\Delta\eta_n = \frac{\eta_n - \eta_{n-1}}{\eta_{n-1}}, \tag{12}$$

which is seen to be negative as long as the two-norm of the residual vector decreases.

Whereas the switch between the two CGLS update algorithms in the two-step CGLS algorithm is based solely on observing when the value of $\Delta\eta_n$ reaches a certain threshold, in the new EDPT algorithm this is combined with information available from examining the distribution of the elements in the residual vector. As described in [38], [39], the residuals of the optimal solution of the nonlinear reconstruction problem should have a Gaussian distribution with zero mean under the assumption of Gaussian distributed errors in the measurements. Otherwise, it may be shown that the accuracy of the final solution is compromised [38, Chap. 5]. To quantify how closely the distribution of the residuals resembles a Gaussian distribution, a Gaussian distribution with zero mean is fitted to the data. After the best-fit Gaussian distribution has been found, a histogram with $n_{\mathrm{bins}} = 15$, covering the range of the residuals, is created and the χ_n^2 value is found as [40, Eq. (9.29)]

$$\chi_n^2 = \sum_{i=1}^{n_{\mathrm{bins}}} \frac{(O_i - E_i)^2}{E_i}. \tag{13}$$

In this expression, O_i is the observed number of elements in each of the bins and E_i is the expected number of elements calculated using the best-fit Gaussian distribution. For a perfect fit, $O_i = E_i$ and the value of χ^2 is zero. As the fit between the observed data and the theoretical distribution deteriorates, the value of χ_n^2 increases. The relatively low number of bins is chosen since no bin in the χ^2 test should have an expected frequency less than five [40, Ch. 9]. The calculation of the best-fit Gaussian distribution is a computationally inexpensive operation and can be easily implemented, e.g., using a maximum-likelihood estimator [40, Ch. 8]. The value of N_0 where $\lambda_n = 0$ transitions to $\lambda_n = \lambda_{\mathrm{EDPT}}$ is now chosen as that Newton iteration at which the value of χ_n^2 reaches a minimum after the value of $\Delta\eta_n$ reaches a certain threshold (in this paper a threshold of $\Delta\eta_n = -0.4$ is used). The rationale for this choice will be discussed in more detail in the simulation part of Section V.

The final parameter to be determined is λ_{EDPT}. To this end, it is useful to introduce the normalized sum of the elements of the Jacobian matrix $\underline{\underline{J}}_{N_0}$ as

$$\Sigma_n(\underline{\underline{J}}_{N_0}) = \frac{\sum_{i=1}^{n_{\mathrm{row}}} \sum_{j=1}^{n_{\mathrm{col}}} J_{N_0 i,j}}{n_{\mathrm{col}}}. \tag{14}$$

Herein, n_{col} is the number of columns in the matrix and n_{row} is the number of rows. It has been found empirically that the magnitude of λ_{EDPT} should be of the same order as $\Sigma_n(\underline{\underline{J}}_{N_0})$. Since the L-curve criterion is used for determining the number of CGLS iterations in the latter part of the EDPT algorithm, the exact value of λ_{EDPT} is not critical and it has been found that a value of λ_{EDPT} between $0.1\Sigma_n(\underline{\underline{J}}_{N_0})$ and $\Sigma_n(\underline{\underline{J}}_{N_0})$ all provide satisfactory results, with the lower values providing slightly better resolved images and the higher values a slightly lower artifact level artifacts. A comparison between the images reconstructed using a value which is too low and an adequate value of λ_{EDPT} are shown in the simulation part of Section V.

In addition to the three parameters mentioned above, it is also of interest to determine when the algorithm should be terminated. In the two-step CGLS algorithm, it was found that terminating the algorithm after the right number of Newton iterations is very important to assure that the algorithm does not attempt to invert the noise component of the measured data. In the EDPT algorithm, however, the regularizing effect of the Euclidean distance term in combination with the number of CGLS iterations in the last part of the Newton iterations being determined on the basis of the L-curve criterion implies that terminating the algorithm after the optimal Newton iteration is less important. If the value of the regularizing parameter λ_{EDPT} is sufficiently large, the algorithm will stabilize on a solution after a few Newton iterations, resulting in a constant value of χ_n^2. The total number of Newton iterations N_1 is therefore introduced as the iteration where change in the absolute value of χ_n^2, $\Delta\chi_n^2$,

defined as

$$\Delta\chi_n^2 = \frac{|\chi_n^2 - \chi_{n-1}^2|}{\chi_{n-1}^2}, \tag{15}$$

drops below 0.02. However, because the algorithm unconditionally converges, additional Newton iterations will not degrade the images as is sometimes the case in the two-step CGLS algorithm.

IV. Measures of Image Quality

To analyze the performance, four different quantities are introduced to describe the quality of the reconstructed images. The quantities are related to the difference between the reconstructed image $\underline{k}^2$ and the true distribution of the constitutive parameters $\underline{k}^2_{\text{true}}$. In addition to the measures of the image quality, the number of iterations of the Newton algorithm, and thereby the speed with which the algorithms reach an acceptable result, is also of interest, as is a subjective evaluation of the image quality. The normalized two-norms

$$\kappa_r = \frac{\left\|\Re\left\{\underline{k}^2_{\text{true}} - \underline{k}^2\right\}\right\|_2}{\left\|\Re\left\{\underline{k}^2_{\text{true}}\right\}\right\|_2} \tag{16a}$$

and

$$\kappa_i = \frac{\left\|\Im\left\{\underline{k}^2_{\text{true}} - \underline{k}^2\right\}\right\|_2}{\left\|\Im\left\{\underline{k}^2_{\text{true}}\right\}\right\|_2}, \tag{16b}$$

wherein $\underline{k}^2_{\text{true}}$ is the true distribution of the squared wave numbers and $\underline{k}^2$ is the reconstructed distribution of squared wave numbers, indicate how well the real (subscript "r") and imaginary (subscript "i") parts of the squared wave numbers are reconstructed. In addition to the norms of the difference in constitutive parameters, the spatial frequency spectrum of the difference is also used as a measure of the image quality. This is based on the observation that if the reconstructed constitutive parameters have a constant or near-constant offset, and thus a spatial frequency distribution of the error dominated by low-frequency components, scattering objects (cancerous tumors) can still be detected as will be shown in the phantom measurement part of Section V. If, on the other hand, the error in the reconstructed constitutive parameters is dominated by high-frequency components, it may be an indication either of the reconstruction algorithm not being able to reconstruct the fine details in the true distribution, or that artifacts are present in the images. This may lead to false negative or false positive diagnostics, respectively. The spatial frequency spectra used in this paper are all defined with respect to the deviation of the constitutive parameters from the known background. The spectrum of the relative permittivity is defined as

$$\mathscr{F}_\epsilon(k_x, k_y) = \int_{-\infty}^{\infty}\int_{-\infty}^{\infty} (\epsilon_r(x,y) - \epsilon_{r,\text{bg}}) \cdot \mathrm{e}^{i(k_x x + k_y y)}\,\mathrm{d}x\,\mathrm{d}y \tag{17a}$$

and that of the conductivity by

$$\mathscr{F}_\sigma(k_x, k_y) = \int_{-\infty}^{\infty}\int_{-\infty}^{\infty} (\sigma(x,y) - \sigma_{\text{bg}}) \cdot \mathrm{e}^{i(k_x x + k_y y)}\,\mathrm{d}x\,\mathrm{d}y. \tag{17b}$$

Herein, σ_{bg} and $\epsilon_{r,\text{bg}}$ are the conductivity and relative permittivity of the background medium (the coupling liquid). From these expressions, the amplitude spectra of the errors presented in Section V are defined as

$$\mathscr{E}_\epsilon(k_x, k_y) = \left|\left(\mathscr{F}_{\epsilon_{\text{true}}}(k_x, k_y) - \mathscr{F}_{\epsilon_{\text{recon}}}(k_x, k_y)\right)\right| \tag{18a}$$

and

$$\mathscr{E}_\sigma(k_x, k_y) = \left|\left(\mathscr{F}_{\sigma_{\text{true}}}(k_x, k_y) - \mathscr{F}_{\sigma_{\text{recon}}}(k_x, k_y)\right)\right| \tag{18b}$$

wherein the subscripts "true" and "recon" indicate the spectra of the true and reconstructed distributions, respectively.

To calculate the value of κ_r, κ_r, $\mathscr{E}_\sigma$, and $\mathscr{E}_\sigma$, the true distributions in the images must be known. Therefore, they cannot be applied to reconstructions of patient data in which the distribution is unknown. They can, however, still provide valuable information when applied to reconstructions of simulation and phantom data where the distributions are known.

V. Performance

The update algorithm has been tested on simulated data, data from phantom measurements, and patient data. A number of different simulation and measurement setups have been tested but due to the limited space available in this paper, only one representative example from each of the three categories will be presented. To compare the performance of the new algorithm with the two-step CGLS algorithm introduced in [22], the reconstructions are performed using both algorithms.

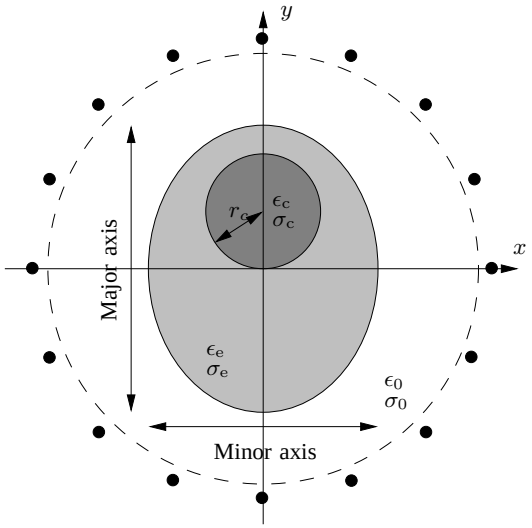

Fig. 2. Setup of simulation. The ellipse is centered at the origin of the coordinate system with a major axis of 10 cm and a minor axis of 8 cm. The circular scatterer is centered at $(x, y) = (0, 2)$ cm with radius $r_c = 2$ cm. The relative permittivity of the background is $\epsilon_{0,r} = 31$ and the conductivity of the conductivity is $\sigma_0 = 1.163$ S/m. The antenna positions are indicated by the black dots and the imaging domain by the dashed circle.

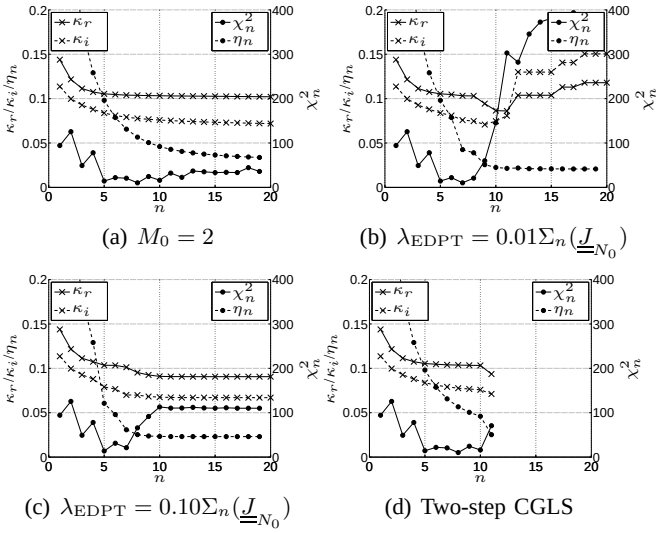

(a) $M_0 = 2$ (b) $\lambda_{\mathrm{EDPT}} = 0.01\Sigma_n(\underline{\underline{J}}_{N_0})$

(c) $\lambda_{\mathrm{EDPT}} = 0.10\Sigma_n(\underline{\underline{J}}_{N_0})$ (d) Two-step CGLS

Fig. 3. Values of κ_r, κ_i, η_n, and χ_n^2 for (a) the CGLS algorithm without EDPT, (b) the EDPT algorithm with $M_0 = 2$, $N_0 = 5$, and $\lambda_{\mathrm{EDPT}} = 0.01\Sigma_n(\underline{\underline{J}}_{N_0})$, (c) the EDPT algorithm with $M_0 = 2$, $N_0 = 5$, and $\lambda_{\mathrm{EDPT}} = 0.10\Sigma_n(\underline{\underline{J}}_{N_0})$, and (d) the two-step CGLS algorithm introduced in [22].

A. Simulated Data

The update algorithm has been tested on a simulated 2-D data set using the setup in Fig. 2 at $f = 1$ GHz with the antennas being modeled as point sources. In this setup, an elliptical scatterer with relative permittivity $\epsilon_{e,r} = 25.0$ and conductivity $\sigma_e = 0.85$ S/m, in which a circular inclusion with relative permittivity $\epsilon_{c,r} = 50.0$ and conductivity $\sigma_c = 1.3$ S/m is inserted, is placed in a background medium with relative permittivity $\epsilon_{0,r} = 31.0$ and conductivity $\sigma_0 = 1.163$ S/m. The elliptical scatterer has a minor axis of 8 cm parallel to the x axis and a major axis of 10 cm parallel to the y axis. The 4 cm diameter circular inclusion is centered at $(x_c, y_c) = (0, 2)$ cm. The radiated power level at the antennas is 0 dBm and Gaussian noise representing a noise floor of -100 dBm has been added to the simulated measured signals. In all simulations, the forward solutions for the synthetic measurement data were computed with the property distribution imposed on a refined finite-element mesh compared to the mesh used for the reconstruction to avoid the possibility of an inverse crime.

In Fig. 3, the values of κ_r, κ_i, η_n, and χ_n^2 are plotted for four different algorithms. In Fig. 3(a), the updates are found using the CGLS algorithm with $M_0 = 2$ and $\lambda_n = 0$ for all of the Newton iterations. In Fig. 3(b), the values of κ_r, κ_i, η_n, and χ_n^2 are plotted for the EDPT algorithm using $M_0 = 2$, a threshold of $\Delta\eta_n > -0.4$, and $\lambda_{\mathrm{EDPT}} = 0.01\Sigma_n(\underline{\underline{J}}_{N_0}) = 4.70 \cdot 10^{-8}$. In Fig. 3(c), the value of λ_{EDPT} is changed to $0.10\Sigma_n(\underline{\underline{J}}_{N_0}) = 4.70 \cdot 10^{-7}$, and finally, in Fig. 3(d), the results of the two-step CGLS algorithm are shown. The reconstructed images are shown in Fig. 4.

The results in Fig. 3(a) illustrates the need for determining the number N_0 of Newton iterations using $\lambda_0 = 0$ based on both the value of χ_n^2 and the value of η_n. In the first Newton iterations, the value of χ_n^2 fluctuates, and if the choice of N_0 were to be based on the minimum of χ_n^2 alone, this would imply a choice of $N_0 = 1$ since it is not possible to know whether or not a lower value of χ_n^2 would result at a later iteration. On the other hand, the value of η_n varies considerably during the first few Newton iterations, indicating that an optimum intermediate image might not have been obtained. A suitable solution is therefore to choose the value of N_0 based on when the value of $\Delta\eta_n$ is low and the value of χ_n^2 reaches a minimum.

In the EDPT algorithms using $\lambda_{\mathrm{EDPT}} = 0.01\Sigma_n(\underline{\underline{J}}_{N_0})$ and $\lambda_{\mathrm{EDPT}} = 0.10\Sigma_n(\underline{\underline{J}}_{N_0})$, for which the results are shown in Figs. 3(b) and 3(c), the threshold value for $\Delta\eta_n$ is reached after four Newton iterations and the first minimum in χ_n^2 after $N_0 = 5$ iterations. The intermediate images of the conductivity of permittivity are shown in Figs. 4(a) and 4(b). In the algorithm using $\lambda_{\mathrm{EDPT}} = 0.01\Sigma_n(\underline{\underline{J}}_{N_0})$, the value of the regularization is clearly too low as indicated by the increase in the value of κ_r and κ_i and the erratic behavior of χ_n^2. The reconstructed images are shown in Figs. 4(c) and 4(d),

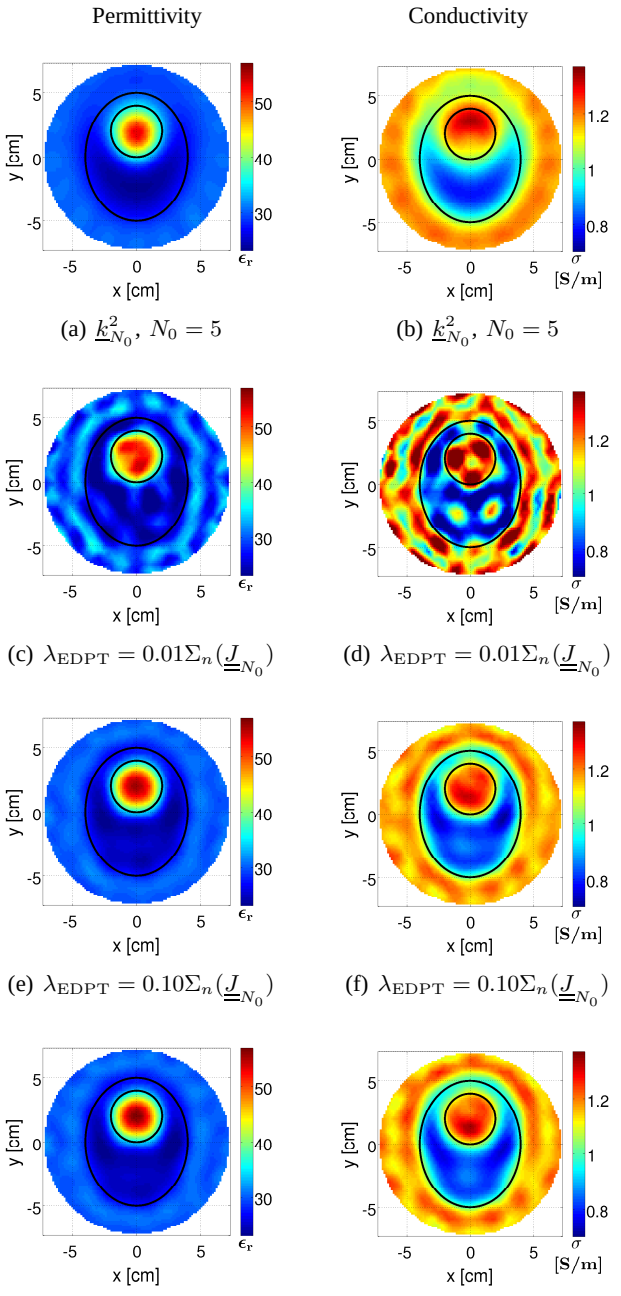

(a) $\underline{k}^2_{N_0}$, $N_0 = 5$ (b) $\underline{k}^2_{N_0}$, $N_0 = 5$

(c) $\lambda_{\mathrm{EDPT}} = 0.01\Sigma_n(\underline{\underline{J}}_{N_0})$ (d) $\lambda_{\mathrm{EDPT}} = 0.01\Sigma_n(\underline{\underline{J}}_{N_0})$

(e) $\lambda_{\mathrm{EDPT}} = 0.10\Sigma_n(\underline{\underline{J}}_{N_0})$ (f) $\lambda_{\mathrm{EDPT}} = 0.10\Sigma_n(\underline{\underline{J}}_{N_0})$

(g) Two-step CGLS (h) Two-step CGLS

Fig. 4. Comparison of the images obtained using the EDPT algorithm and the two-step CGLS algorithm on the simulated data. The actual position of the elliptical and spherical scatterers are shown by the black lines.

and although both the elliptical and the circular scatterers are visible in the images, the artifact level is quite high. It should be noted that the behavior of the value of η_n does not indicate that the algorithm reaches convergence after 18 Newton iterations. On the contrary, the value of η_n stabilizes at approximately 0.03 after only 11 Newton iterations, illustrating that η_n by itself should not be used as an indicator of convergence of the algorithm.

The images obtained using the $\lambda_{\mathrm{EDPT}} = 0.10\Sigma_n(\underline{\underline{J}}_{N_0})$, shown in Figs. 4(e) and 4(f), are significantly improved and virtually free from artifacts with both scatterers clearly visible and reconstructed with values close to the actual values. The values of both η_n and χ^2_n for this reconstruction become constant after $N_1 = 11$ Newton iterations and in the following Newton iterations the images do not change, illustrating that a termination based on the behavior of χ^2_n is suitable. The two-step CGLS algorithm terminates after 11 Newton iterations as indicated by the plot shown in Fig. 3(d). The values of κ_r, κ_i, and η_n are all close to the corresponding values for the $\lambda_{\mathrm{EDPT}} = 0.10\Sigma_n(\underline{\underline{J}}_{N_0})$ EDPT algorithm and the reconstructed images are also very similar to those obtained using the EDPT algorithm.

To further investigate the behavior of the EDPT algorithm, the spectra of the errors in the reconstructed images have been analyzed. In Fig. 5, the spectra $\mathscr{E}_\epsilon$ and $\mathscr{E}_\sigma$ for the images in Fig. 4 are shown. The change from the spectra of the intermediate images to the spectra of the images obtained $\lambda_{\mathrm{EDPT}} = 0.10\Sigma_n(\underline{\underline{J}}_{N_0})$ shows that the algorithm behaves as expected: The components of the errors corresponding to high absolute values of the spatial frequencies k_x and k_y decrease in amplitude, indicating that the algorithm reconstructs the high-frequency spatial components of the images in the latter Newton iterations. The spectra of the error of the two-step CGLS algorithm is very similar to that of the EDPT algorithm, with slightly elevated regions for the high absolute values of k_x and k_y in the $\mathscr{E}_\sigma$ spectra. This is to be expected when considering the similarity of the reconstructed images.

It is interesting to note the area of elevated values around $(k_x, k_y) = (0, 0)$ in the $\mathscr{E}_\epsilon$ spectra. This indicates that the solutions are biased and has been observed in all of the reconstructions performed. Since the simulation has been performed using the same assumptions in the forward model as used in the reconstruction algorithm, the offset cannot be due to modeling errors. The exact reason for this error has not been determined and, since similar investigations for nonlinear imaging have not been found in the literature, it is unknown whether or not the offset is a general characteristic of this type of

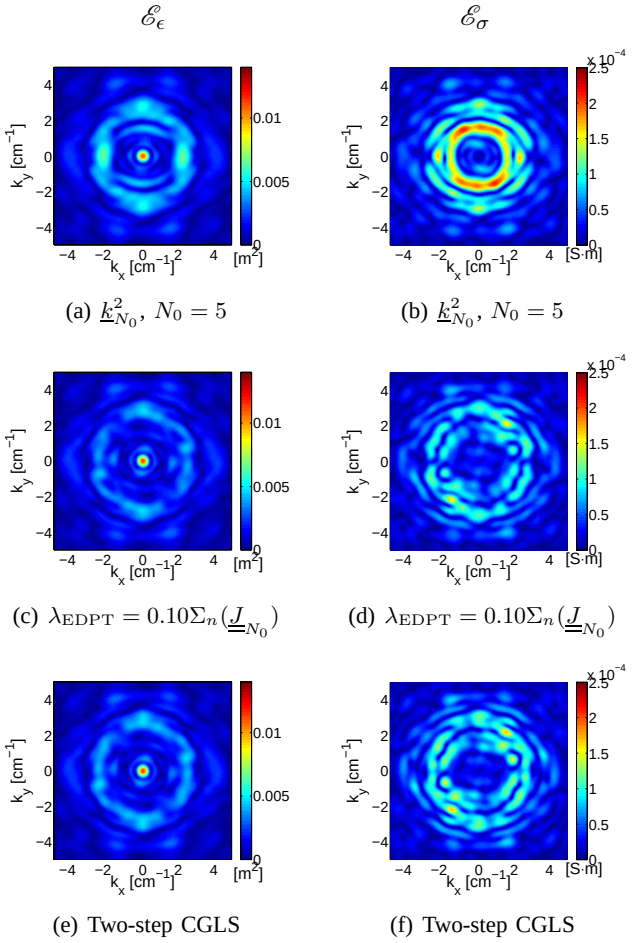

(a) $\underline{k}^2_{N_0}$, $N_0 = 5$ (b) $\underline{k}^2_{N_0}$, $N_0 = 5$

(c) $\lambda_{\mathrm{EDPT}} = 0.10\Sigma_n(\underline{\underline{J}}_{N_0})$ (d) $\lambda_{\mathrm{EDPT}} = 0.10\Sigma_n(\underline{\underline{J}}_{N_0})$

(e) Two-step CGLS (f) Two-step CGLS

Fig. 5. Amplitude spectra of errors in reconstructed images of the simulation. In (a) and (b), the spectra of the intermediate image are shown, (c) and (d) show the spectra of the images reconstructed using the EDPT algorithm. The spectra of the images reconstructed using the two-step CGLS algorithm are shown in (e) and (f).

microwave imaging or a characteristic specific to the algorithm presented here.

B. Phantom Measurement

The forward data created in the simulation has the advantage, with regards to the reconstruction of the images, of being created assuming a two-dimensional setup which is also assumed in the forward model used in the inversion. In addition to this, the modeling of the antennas used for creating the forward data is the same as that used in the reconstruction. This implies that none of the modeling errors present in the real measurements are included in the simulation data. It is therefore of interest to investigate the performance of the update algorithms with real measurement of a known phantom. The setup of the phantom is shown in Fig. 6, and mimics a fatty breast with fibroglandular and tumor inclusions. The measurement setup is constructed using

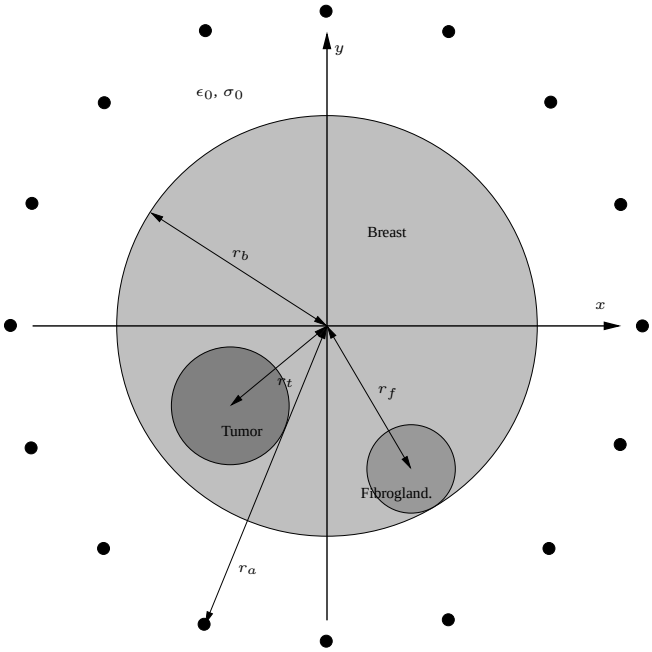

Fig. 6. Setup of the phantom measurement. The "tumor" is positioned $r_t \approx 3$ cm and the "fibroglandular" inclusion $r_f \approx 4$ cm from the center of the "breast" with radius $r_b = 5$ cm. The antennas are positioned in a circular setup with radius $r_a = 7.62$ cm.

three thin-walled plastic cylinders. A large cylinder with a radius of 5 cm, filled with a glycerin–water mixture relative permittivity $\epsilon_{b,r} = 12.6$ and conductivity $\sigma_b = 0.62$ S/m, was used for modeling the fatty breast. The tumor was modeled by a 14 mm-radius cylinder filled with a mixture with relative permittivity $\epsilon_{t,r} = 53.4$ and conductivity $\sigma_t = 1.15$ S/m. Finally, the fibroglandular inclusion was modeled by a cylinder with a radius of 10.5 mm filled with a liquid with relative permittivity $\epsilon_{f,r} = 32.7$ and conductivity $\sigma_f = 1.28$ S/m positioned against the wall of the cylinder representing the breast. The entire setup was immersed in a coupling liquid with relative permittivity $\epsilon_{0,r} = 23.3$ and conductivity $\sigma_0 = 1.13$ S/m. The measurement was conducted at 1100 MHz.

The values of κ_r, κ_i, χ^2_n, and η_n obtained using the EDPT algorithm with $M_0 = 2$, a threshold value for $\Delta\eta$ of -0.4, and $\lambda_{\mathrm{EDPT}} = 0.25\Sigma_n(\underline{\underline{J}}_{N_0}) = 2.01 \cdot 10^{-5}$ are shown in Fig. 7(a) and the values obtained using the two-step CGLS algorithm are shown in Fig. 7(b). The slightly higher value of λ_{EDPT} is an indication of the inversion problem being more ill-posed than in the simulation case, something which is most likely partially caused by the 3-D propagation effects of the fields. The two-step algorithm terminates after 11 Newton iterations while the EDPT algorithm converges after $N_1 = 15$ iterations. The images obtained using the EDPT algorithm are shown in

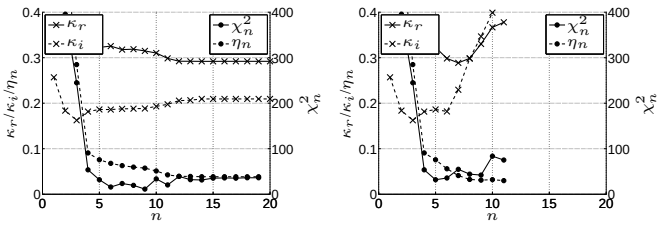

(a) $\lambda_{\mathrm{EDPT}} = 0.25\Sigma_n(\underline{\underline{J}}_{N_0})$ (b) Two-step CGLS

Fig. 7. Results obtained when reconstructing the phantom measurement using (a) the EDPT algorithm with $M_0 = 2$, $N_0 = 9$, and $\lambda_{\mathrm{EDPT}} = 0.25\Sigma_n(\underline{\underline{J}}_{N_0})$ and (b) the two-step CGLS algorithm.

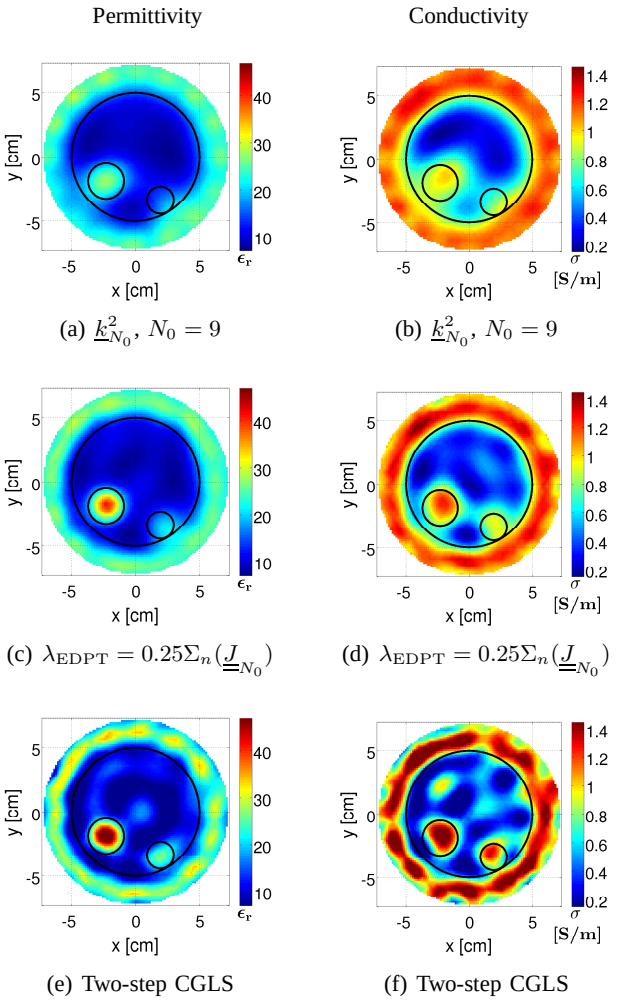

(a) $\underline{k}^2_{N_0}$, $N_0 = 9$ (b) $\underline{k}^2_{N_0}$, $N_0 = 9$

(c) $\lambda_{\mathrm{EDPT}} = 0.25\Sigma_n(\underline{\underline{J}}_{N_0})$ (d) $\lambda_{\mathrm{EDPT}} = 0.25\Sigma_n(\underline{\underline{J}}_{N_0})$

(e) Two-step CGLS (f) Two-step CGLS

Fig. 8. Images of the phantom reconstructed using (b)–(c) the EDPT update algorithm and (d)–(e) the two-step CGLS algorithm. The intermediate images, obtained after $N_0 = 9$ Newton iterations, are shown in (a) and (b). The actual positions of the scattering objects are given by the black lines.

Figs. 8(c) and 8(d) with the intermediate images shown in Figs. 8(a) and 8(b). The permittivity images for all cases are virtually free of artifacts with both the ”tumor” and ”fibroglandular” inclusions clearly visible. In the conductivity image, the level of the artifact is slightly elevated but both inclusions are still clearly visible. For the CGLS images, the level of artifacts in the images is at a level where it is hard to distinguish between artifacts and actual scattering objects. This is especially the case for the conductivity image in which an object seems to appear within the breast phantom approximately at a 10 o’clock position.

For all of the images, artifacts can be seen close to the edge of the imaging domain at positions corresponding to the positions of the antennas. These artifacts are most clearly seen in the conductivity image obtained using the two-step CGLS algorithm, in which the general artifact level is also the highest. The position of these artifacts can be explained by the fact that the elements of the Jacobian matrix corresponding to the areas close to the antennas have a significantly greater amplitude than those further away. Therefore, any modeling errors, such as the ones originating from reconstructing a 3-D scattering problem with a 2-D inversion algorithm, are more likely to give rise to artifacts here than further away from the antennas.

The spectra $\mathscr{E}_\epsilon$ and $\mathscr{E}_\sigma$ are shown in Fig. 9 with the spectra of the intermediate images shown in Figs. 9(a) and (b). Both the $\mathscr{E}_\epsilon$ and $\mathscr{E}_\sigma$ spectra are dominated by components of spatial frequencies close to zero, indicating that all the images are biased. These dominant low-frequency areas are the reason why the individual scattering objects are clearly visible in the images even though the values of κ_r and κ_i are much higher than the corresponding values for the simulation case. This illustrates that the norm of the error in the images, by itself, cannot be used as a reliable measure for the quality of the reconstruction. In both $\mathscr{E}_\epsilon$ spectra obtained using the EDPT algorithm and the $\mathscr{E}_\epsilon$ spectrum obtained using the two-step CGLS algorithm, the two regions of high absolute spatial frequency, visible in the intermediate spectrum, are reduced considerably.

In the $\mathscr{E}_\sigma$ spectra, a slight increase in amplitude and size of the low-frequency component dominating the spectrum of the intermediate image is seen for the EDPT algorithm, whereas the regions of elevated values along the k_y axis, visible in the intermediate image, diminish, explaining the better resolved ”fibroglandular” and ”tumor” inclusions in Fig. 8(d) compared to the intermediate image in Fig. 8(b). The $\mathscr{E}_\epsilon$ and $\mathscr{E}_\sigma$ spectra for the two-step CGLS algorithm have elevated regions at the high absolute values of k_x and k_y, indicating that the improved resolution in these images is at the expense of an increased level of the artifacts. This illustrates that

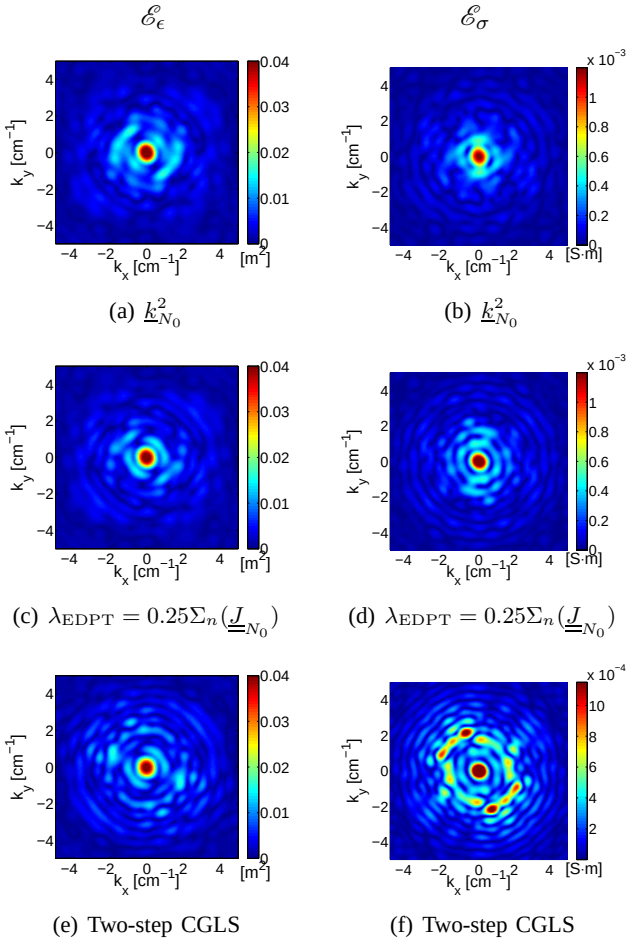

(a) $\underline{k}^2_{N_0}$ (b) $\underline{k}^2_{N_0}$

(c) $\lambda_{\mathrm{EDPT}} = 0.25\Sigma_n(\underline{\underline{J}}_{N_0})$ (d) $\lambda_{\mathrm{EDPT}} = 0.25\Sigma_n(\underline{\underline{J}}_{N_0})$

(e) Two-step CGLS (f) Two-step CGLS

Fig. 9. Spectra of the errors in the reconstructed images of the phantom measurement.

the additional regularizing effects of the EDPT algorithm allows for extracting the same information from the measurement data as in the previous algorithm but with a reduced artifact level. Thus, the aim of creating an algorithm with high resolution and low artifact level has been achieved.

From the images in Fig. 8 and the reconstructed images of the simulation in the previous subsection, it can be concluded that the conductivity images, in general, are more susceptible to the noise in the data, and therefore to artifacts in the final images, than the permittivity images. This should be kept in mind when reconstructing the patient images in the next subsection where the true distributions of the constitutive parameters are not known and a good permittivity image may be accompanied by an artifact-dominated conductivity image. This phenomenon has previously been described in [20], [29] in which the permittivity images are significantly better than the associated conductivity images. In [41], a scaling of the elements of the vector $\underline{k}^2_n$ was proposed to reduce the problem. This method, however, has not shown any significant improvement of the performance of the algorithm presented in this paper and is therefore not included in the algorithm.

In addition to this it should be noted that the value of χ^2_n for the EDPT reconstructions ends at a higher value than the value it has at N_0. This agrees well with the previously mentioned correlation between a poor fit to the normal distribution (and thus a high value of χ^2_n) and a compromised solution: In this case the solutions are compromised by the introduction of the Euclidean penalty term, which means that they are no longer the optimum solution to the problem stated in (2).

C. Patient Measurement

The final test of the algorithm is its ability to reconstruct images of the breast of a patient. In this case, the patient was 36 years old and had scattered density breasts with a single tumor in the right breast with a diameter of approximately 4 cm positioned at what is a 7 o'clock, en face position in the reconstructed images. The measurements were acquired at 1100 MHz using a glycerin–water mixture with $\epsilon_r = 21.5$ and $\sigma = 1.11$ S/m as coupling liquid. In this paper, the images of planes 3, 5, and 7 of the right breast, with plane 1 being closer to the chest wall and plane 7 being close to the nipple, are analyzed. In Fig. 10, the reconstructed images using the EDPT algorithm with a regularization parameter of $\lambda_{\mathrm{EDPT}} = 0.50\Sigma_n\underline{\underline{J}}_{N_0}$ are shown. The increased relative value of the regularization parameter is again an indication that the 3-D propagation effects impact the patient measurement more than the phantom measurements. This is most likely because of the somewhat conical shape of the breast. The algorithm reaches the threshold value for η_n after 2, 3, and 2 iterations for imaging plane 3, 5, and 7, respectively, and the values of N_0 for the three planes are 4, 5, and 10. The algorithm converges at $N_1 = 12$, $N_1 = 12$, and $N_1 = 14$ Newton iterations, respectively. The corresponding images reconstructed using the two-step CGLS algorithm are shown in Fig. 11 and this algorithm terminates after 10, 6, and 10 Newton iterations in the three imaging planes.

The reconstructions of imaging plane 3, shown in Figs. 10(a) and 10(b), show the contour of the breast, inside of which the values of both permittivity and conductivity are lower than in the background. High-level artifacts are present in the lower part of the images, and this suggests that the breast was too close to the antennas positioned here. Similar artifacts to some extent are visible in plane 5, shown in Figs. 10(c) and 10(d)

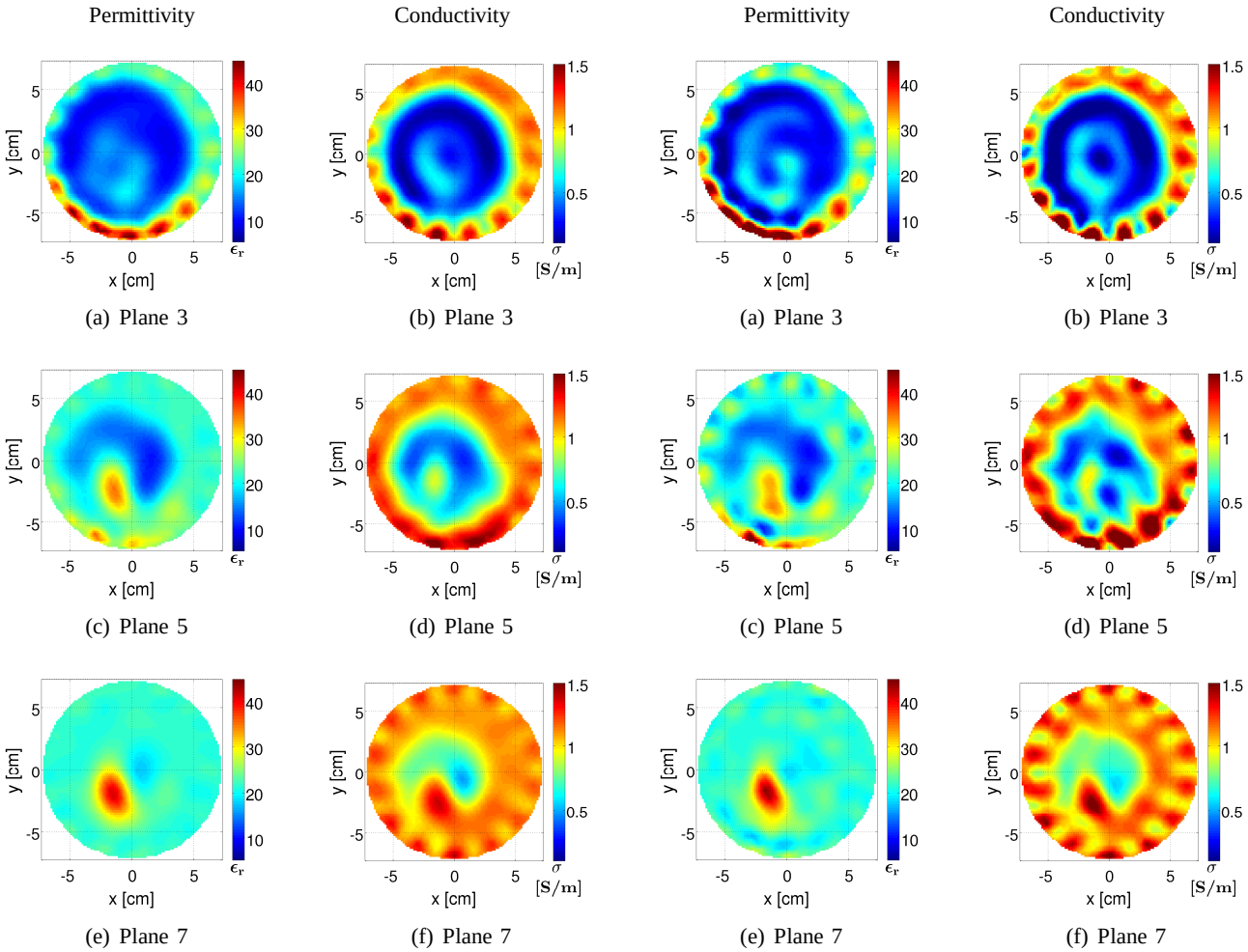

(a) Plane 3 (b) Plane 3
(c) Plane 5 (d) Plane 5
(e) Plane 7 (f) Plane 7

Fig. 10. Images of the three imaging planes 3, 5, and 7 of the breast using the EDPT algorithm.

(a) Plane 3 (b) Plane 3
(c) Plane 5 (d) Plane 5
(e) Plane 7 (f) Plane 7

Fig. 11. Images of the three imaging planes 3, 5, and 7 of the breast. The images have all been reconstructed with the two-step CGLS algorithm.

whereas the images of plane 7, shown in Figs. 10(e) and 10(f), where the breast, due to its conical shape, is further away from the antennas do not show these artifacts. The artifacts are also clearly visible in the CGLS images shown in Fig. 11. In the EDPT images of plane 3, the contour of the breast is still visible with low values inside the breast. In addition, a region with raised conductivity is visible in the lower-left part of the breast. A region with slightly raised permittivity values is seen at the same position, and the position corresponds well with the position of the tumor. Similar regions of high-level permittivity and conductivity are seen in the images reconstructed using the CGLS algorithm shown in Figs. 11(a) and 11(b). However, the overall artifact level is considerably elevated and the high-level regions have even higher values and are smoothed out over a much larger area, including regions not covered by the tumor. In plane 5, both the contour of the breast and the tumor are readily identified on the EDPT images in Figs. 10(c) and 10(d). For the CGLS images, both the breast and the tumor can be identified but the contours of both the breast and the tumor are affected by the presence of the artifacts. Also, the areas with erroneous values of the background liquid close to the positions of the antennas are much more pronounced in these images.

Finally, in the images of plane 7, the tumor is still visible in both sets of images and so is a low-valued region, corresponding to the healthy part of the breast, in the images reconstructed using the EDPT algorithm. In the permittivity image reconstructed using the two-step CGLS algorithm, shown in Fig. 11(e), the low-value region is not visible, although in the corresponding conductivity image, shown in Fig. 11(f), the contour of the breast can be seen. As with the two other previous imaging planes, the overall level of the artifacts is lower in the images reconstructed using the EDPT algorithm than in the two-step CGLS counterparts. These

observations further support the notion that the new algorithm outperforms the previously reported two-step CGLS algorithm when it comes to suppressing artifacts in the images while preserving high resolution.

VI. Conclusion

In this paper, a new algorithm for calculating the updates in a Gauss-Newton based nonlinear microwave imaging algorithm was presented. The algorithm is based on the introduction of a Euclidean-distance penalty term in the latter part of the Newton algorithm and differs from the previously reported algorithms in that it applies two layers of regularization to this part of the algorithm, one being the Euclidean-distance penalty term, the other being the CGLS algorithm. The performance of the new algorithm was compared with that of a previously reported algorithm and was seen to provide highly resolved images with a lower overall level of artifacts. The performance of the algorithms was analyzed using the norm of the residual vector as well as the χ_n^2 for the residual vector as a measure of the distribution of its elements. Further analysis included the norm of the difference between the true and the reconstructed distributions of constitutive parameters and the spectra of these differences.

The analysis of the algorithms showed that by including χ_n^2 as a measure of the reconstruction quality, valuable information, not available by observing the norm alone, can be extracted from the residual vector. The analysis of the norm and the spectra of the errors revealed that the norm of the error vector should not, by itself, be used as a measure of the reconstruction quality since low-frequency components in the error may bias the solution but still provide highly resolved images. Furthermore, it was seen that the algorithm behaves as expected, recovering the components of high spatial frequency of the images in the latter part of the Newton algorithm where the Euclidean penalty term is included.

Further research should be carried out to determine how the low-frequency components of the error can be minimized to obtain images which are both highly resolved and provide the correct values of the constitutive parameters. In addition to this, it is of interest to investigate the possibility of extracting even more information from the residual vector, thereby allowing for a more adaptive choice of the regularization parameters.

VII. Acknowledgments

The Danish Technical Research Council and the Villum Kann Rasmussen Foundation are acknowledged for supporting the work of Tonny Rubæk and Peter Meincke. The work of Tonny Rubæk is also supported by The Otto Mønsted Foundation and Trane's Foundation. The work of Paul M. Meaney and Keith D. Paulsen is supported by NIH/NCI grant no. P01-CA080139.

References

[1] E. Fear, A. Low, J. Sill, and M. A. Stuchly, "Microwave system for breast tumor detection: Experimental concept evaluation," *Proceedings of the IEEE Antennas and Propagation Society International Symposium, 2002*, vol. 1, pp. 819–822, 2002.

[2] P. Meaney, M. Fanning, D. Li, S. Poplack, and K. Paulsen, "A clinical prototype for active microwave imaging of the breast," *IEEE Transactions on Microwave Theory and Techniques*, vol. 48, no. 111, pp. 1841–1853, 2000.

[3] T. England and N. Sharples, "Dielectric properties of the human body in the microwave region of the spectrum," *Nature*, vol. 163, pp. 487–488, 1949.

[4] T. England, "Dielectric properties of the human body for wavelength in the 1-10cm range," *Nature*, vol. 1466, pp. 480–481, 1950.

[5] R. Nilavalan, J. Leendertz, I. Craddock, A. Preece, and R. Benjamin, "Numerical analysis of microwave detection of breast tumours using synthetic focussing techniques," *Proceedings of the IEEE Antennas and Propagation Society International Symposium, 2004*, pp. 2440–2443 Vol.3, 2004.

[6] S. Hagness, A. Taflove, and J. Bridges, "Three-dimensional FDTD analysis of a pulsed microwave confocal system for breast cancer detection: Design of an antenna-array element," *IEEE Transactions on Antennas and Propagation*, vol. 47, no. 5, pp. 783–791, 1999.

[7] P. Hashemzadeh, A. Fhager, and M. Persson, "Experimental investigation of an optimization approach to microwave tomography," *Electromagnetic Biology and Medicine*, vol. 25, no. 1, pp. 1–12, 2006.

[8] E. Fear, X. Li, S. Hagness, and M. Stuchly, "Confocal microwave imaging for breast cancer detection: Localization of tumors in three dimensions," *IEEE Transactions on Biomedical Engineering*, vol. 49, no. 8, pp. 812–822, 2002.

[9] I. Craddock, R. Nilavalan, J. Leendertz, A. Preece, and R. Benjamin, "Experimental investigation of real aperture synthetically organised radar for breast cancer detection," *Proceedings of the IEEE Antennas and Propagation Society International Symposium, 2005*, vol. 1B, pp. 179–182 vol. 1B, 2005.

[10] E. Fear, J. Sill, and M. Stuchly, "Experimental feasibility study of confocal microwave imaging for breast tumor detection," *IEEE Transactions on Microwave Theory and Techniques*, vol. 51, no. 3, pp. 887–892, 2003.

[11] ——, "Experimental feasibility of breast tumor detection and localization," *Proceedings of the IEEE MTT-S International Microwave Symposium, 2003*, vol. 1, pp. 383–386, 2003.

[12] A. Fhager, P. Hashemzadeh, and M. Persson, "Reconstruction quality and spectral content of an electromagnetic time-domain inversion algorithm," *IEEE Transactions on Biomedical Engineering*, vol. 53, no. 8, pp. 1594–1604, 2006.

[13] P. Meaney, K. Paulsen, B. Pogue, and M. Miga, "Microwave image reconstruction utilizing log-magnitude and unwrapped phase to improve high-contrast object recovery," *IEEE Transactions on Medical Imaging*, vol. 20, no. 2, pp. 104–116, 2001.

[14] S. Semenov, R. Svenson, A. Bulyshev, A. Souvorov, A. Nazarov, Y. Sizov, V. Posukh, A. Pavlovsky, P. Repin, A. Starostin, B. Voinov, M. Taran, G. Tatsis, and V. Baranov, "Three-dimensional microwave tomography: Initial experimental imaging of animals," *IEEE Transactions on Biomedical Engineering*, vol. 49, no. 1, pp. 55–63, 2002.

[15] Q. Fang, P. Meaney, and K. Paulsen, "Microwave image reconstruction of tissue property dispersion characteristics utilizing multiple-frequency information," *IEEE Transactions on Microwave Theory and Techniques*, vol. 52, no. 82, pp. 1866–1875, 2004.

[16] H. Jia, T. Takenaka, and T. Tanaka, "Time-domain inverse scattering method for cross-borehole radar imaging," *IEEE Transactions on Geoscience and Remote Sensing*, vol. 40, no. 7, pp. 1640–1647, 2002.

[17] D. Li, P. Meaney, and K. Paulsen, "Conformal microwave imaging for breast cancer detection," *IEEE Transactions on Microwave Theory and Techniques*, vol. 51, no. 41, pp. 1179–1186, 2003.

[18] S. Poplack, K. Paulsen, A. Hartov, P. Meaney, B. Pogue, T. Tosteson, M. Grove, S. Soho, and W. Wells, "Electromagnetic breast imaging: Average tissue property values in women with negative clinical findings," *Radiology*, vol. 231, no. 2, pp. 571–580, 2004.

[19] S. P. Poplack, T. D. Tosteson, W. A. Wells, B. W. Pogue, P. M. Meaney, A. Hartov, C. A. Kogel, S. K. Soho, J. J. Gibson, and K. D. Paulsen, "Electromagnetic breast imaging: Results of a pilot study in women with abnormal mammograms," *Radiology - Radiological Society of North America*, vol. 243, no. 2, pp. 350–359, 2007.

[20] S. Y. Semenov, A. E. Bulyshev, V. G. Posukh, Y. E. Sizov, T. C. Williams, and A. E. Souvorov, "Microwave tomography for detection/imaging of myocardial infarction. i. excised canine hearts," *Annals of Biomedical Engineering*, vol. 31, no. 3, pp. 262–270, 2003.

[21] D. Li, P. Meaney, T. Raynolds, S. Pendergrass, M. Fanning, and K. Paulsen, "A broadband microwave breast imaging system," *Proceedings of the IEEE 29th Annual Bioengineering Conference, 2003*, pp. 83–84, 2003.

[22] T. Rubæk, P. M. Meaney, P. Meincke, and K. D. Paulsen, "Nonlinear microwave imaging for breast-cancer screening using Gauss-Newton's method and the CGLS inversion algorithm," *IEEE Transactions on Antennas and Propagation*, vol. 55, no. 8, pp. 2320–2331, 2007.

[23] P. Meaney, E. Demidenko, N. Yagnamurthy, D. Li, M. Fanning, and K. Paulsen, "A two-stage microwave image reconstruction procedure for improved internal feature extraction," *Medical Physics*, vol. 28, no. 11, pp. 2358–2369, 2001.

[24] P. Meaney, S. Pendergrass, M. Fanning, D. Li, and K. Paulsen, "Importance of using a reduced contrast coupling medium in 2D microwave breast imaging," *Journal of Electromagnetic Waves and Applications*, vol. 17, no. 2, pp. 333–355, 2003.

[25] P. Meaney, K. Paulsen, S. Geimer, S. Haider, and M. Fanning, "Quantification of 3-D field effects during 2-D microwave imaging," *IEEE Transactions on Biomedical Engineering*, vol. 49, no. 7, pp. 708–720, 2002.

[26] Q. Fang, P. Meaney, S. Geimer, A. Streltsov, and K. Paulsen, "Microwave image reconstruction from 3-D fields coupled to 2-D parameter estimation," *IEEE Transactions on Medical Imaging*, vol. 23, no. 4, pp. 475–484, 2004.

[27] P. Meaney, K. Paulsen, A. Hartov, and R. Crane, "Microwave imaging for tissue assessment: Initial evaluation in multitarget tissue-equivalent phantoms," *IEEE Transactions on Biomedical Engineering*, vol. 43, no. 9, pp. 878–890, 1996.

[28] K. Paulsen, P. Meaney, M. Moskowitz, and J. Sullivan, J.M., "A dual mesh scheme for finite element based reconstruction algorithms," *IEEE Transactions on Medical Imaging*, vol. 14, no. 3, pp. 504–514, 1995.

[29] P. Meaney, K. Paulsen, and J. Chang, "Near-field microwave imaging of biologically-based materials using a monopole transceiver system," *IEEE Transactions on Microwave Theory and Techniques*, vol. 46, no. 1, pp. 31–45, 1998.

[30] K. Paulsen and P. Meaney, "Nonactive antenna compensation for fixed-array microwave imaging. I. model development," *IEEE Transactions on Medical Imaging*, vol. 18, no. 6, pp. 496–507, 1999.

[31] P. Meaney, K. Paulsen, J. Chang, M. Fanning, and A. Hartov, "Nonactive antenna compensation for fixed-array microwave imaging. II. imaging results," *IEEE Transactions on Medical Imaging*, vol. 18, no. 6, pp. 508–518, 1999.

[32] P. Meaney, Q. Fang, M. Fanning, S. Pendergrass, T. Raynolds, C. Fox, and K. Paulsen, "Microwave breast imaging with an under-determined reconstruction parameter mesh," *Proceedings of the IEEE International Symposium on Biomedical Imaging: Macro to Nano, 2004*, pp. 1369–1372, 2004.

[33] Q. Fang, P. Meaney, and K. Paulsen, "The multidimensional phase unwrapping integral and applications to microwave tomographical image reconstruction," *IEEE Transactions on Image Processing*, vol. 15, no. 11, pp. 3311–3324, 2006.

[34] C. T. Kelley, *Iterative Methods for Linear and Nonlinear Equations*, ser. Frontiers in Applied Mathematics. Philadelphia, PA: SIAM, 1995, vol. 16.

[35] ——, *Solving Nonlinear Equations with Newton's Method*. Philadelphia, PA: SIAM, 2003.

[36] J. M. Ortega and W. C. Rheinboldt, *Iterative Solution of Nonlinear Equations in Several Variables*, ser. Classics in Applied Mathematics, R. E. O'Malley, Ed. Philadelphia, PA: SIAM, 2000.

[37] P. C. Hansen, *Rank-Deficient and Discrete Ill-Posed Problems: Numerical Aspects of Linear Inversion*, ser. Monographs on Mathematical Modeling and Computation. SIAM, 1998.

[38] J. V. Beck and K. J. Arnold, *Parameter Estimation in Engineering and Science*. John Wiley & Sons, 1977.

[39] P. M. Meaney, Q. Fang, T. Rubaek, E. Demidenko, and K. D. Paulsen, "Log transformation benefits parameter estimation in microwave tomographic imaging," *Medical Physics*, vol. 34, no. 6, pp. 2014–2023, 2007.

[40] B. M. Ayyub and R. H. McCuen, *Probability, Statistics, and Reliability for Engineers and Scientists*, 2nd ed. Chapman & Hall / CRC, 2003.

[41] P. M. Meaney, N. K. Yagnamurthy, and K. D. Paulsen, "Pre-scaled two-parameter Gauss-Newton image reconstruction to reduce property recovery imbalance," *Physics in Medicine and Biology*, vol. 47, no. 7, pp. 1101–1119, 2002.

Journal Paper 3

Microwave Imaging for Breast-Cancer Screening Using Contrast Source Inversion and the Log-Amplitude Unwrapped Phase Formulation

Tonny Rubæk, Peter Meincke, and Paul M. Meaney

Status:
Submitted: February 2008
Accepted: – – – – – –
Published: – – – – – –
Journal: AEU - International Journal of Electronics and Communications

AEÜ Int. J. Electron. Commun.
1 (2008) No. 1, 1–1

Jena

Microwave Imaging for Breast-Cancer Screening using Contrast Source Inversion and the Log-Amplitude Unwrapped Phase Formulation

Tonny Rubæk, Peter Meincke, Paul M. Meaney

Abstract **Nonlinear microwave tomography is emerging as a technique for screening of breast cancer. A system using this technique is currently being applied for clinical tests at Dartmouth College, and in this system a Gauss-Newton algorithm is applied for reconstructing the images. In the Gauss-Newton algorithm, a forward scattering problem is solved in each iteration, thereby requiring the implementation of a forward solver using, e.g., the finite element method. In this paper, a contrast source inversion (CSI) algorithm is presented which does not need a forward solver. The CSI algorithm is implemented using the log-amplitude unwrapped phase (log-phase) formulation which has been shown to improve the performance of the Gauss-Newton algorithm. The CSI algorithm is tested on simulated data and on a patient measurement and the performance of the log-phase formulation is compared with that of the standard complex formulation. It is shown that the log-phase formulation improves the performance of the CSI algorithm by reducing the number of iterations used to reconstruct the simulation and more importantly by reducing the artifacts in the images of the patient measurement.**

1. Introduction

Microwave imaging is emerging as a tool for breast-cancer screening. The use of microwave imaging for this purpose is based on the contrast in permittivity and conductivity between normal and malignant tissue in the microwave region of the frequency spectrum [1,2]. To reconstruct the images of the breasts, two different approaches are currently being pursued; ultrawideband radar techniques [3–7] and nonlinear microwave tomographic techniques [8–10].

At Dartmouth College, clinical tests are currently being performed with a microwave imaging system for breast-cancer screening [1]. In this system, the breast is imaged using a series of measurements with a circular antenna array. The images are created using 2-D nonlinear microwave tomography in the form of an iterative frequency-domain Gauss-Newton based reconstruction algorithm [10, 11]. Newton-based reconstruction algorithms have proven their worth for microwave tomography in a number of different setups [9, 12, 13]. A common feature of these algorithms is that in each iteration of the algorithm, a forward scattering problem must be solved for a distribution of constitutive parameters and the corresponding Jacobian matrix must also be found. This requires the implementation of a forward solver, such as a finite-element method [14] or finite-difference time domain algorithm [9]. Although the computational complexity of these methods is a disadvantage, the fact that the Newton-based algorithms have been shown to be quite robust, even when dealing with large scattering objects, implies that the Newton-based algorithms are very appealing.

An important feature of the Gauss-Newton algorithm used at Dartmouth College is the fact that the measured data is represented using the log-amplitude unwrapped phase formulation [15]. In this formulation the change in the logarithm of the amplitude and the phase of the measured signals due to the scattering object are used as input to the reconstruction algorithm. This is different from the more widely used complex formulation in which the difference in the real and imaginary parts of the measured signals are used. The log-amplitude unwrapped phase, or simply log-phase, formulation of the problem has been shown to improve the performance of the algorithm by weighting the relative changes in the measured signals more than the absolute changes used in the complex formulation, and by allowing for the reconstructions to span multiple Riemann sheets [15, 16]. These features allow for reconstructions of images of even stronger scatterers than what the Newton-based algorithms using the complex formulation are capable of.

In addition to the Gauss-Newton based reconstruction algorithms, the contrast source inversion (CSI) algorithm has been applied for nonlinear microwave tomography. The CSI algorithm was introduced in 1997 [17], and solves the nonlinear inverse scattering problem by iteratively solving two coupled linear equations. In this way, the CSI algorithm avoids the need for solving a forward scattering problem in each iteration. Since its introduction, the CSI algorithm has been modified and applied by a large number of authors, both for microwave imaging in general [18–21], and for breast-cancer screening [22, 23]. Recently, a CSI algorithm using the log-phase formulation has been implemented and tested for reconstructing images from the data collected at the patient exams at Dartmouth College. In addition to this, the iterative conjugate gradient least-squares inversion algorithm is used for solving the linear inversion problems present in each iteration of the CSI algorithm.

This paper is organized as follows: In Section 2, the imaging system used at Dartmouth College is presented and in Section 3 the CSI algorithm is presented in both the complex and log-phase formulations. Finally, in Section 4, the two different formulations are applied for reconstruct-

Received February, 2008.

Tonny Rubæk, Ørsted•DTU, Technical University of Denmark, Building 348, DK-2800 Kgs. Lyngby, Denmark, truoersted.dtu.dk
Peter Meincke, Ørsted•DTU, Technical University of Denmark, Building 348, DK-2800 Kgs. Lyngby, Denmark, pmeoersted.dtu.dk
Paul M. Meaney, 8000 Cummings Hall, Thayer School of Engineering, Dartmouth College, Hanover, NH 03755-8000

AEÜ Int. J. Electron. Commun.
1 (2008) No. 1, 1–1

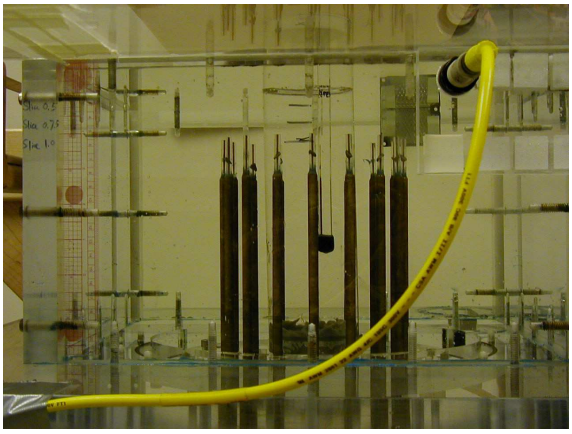

Fig. 1. Photo of the imaging system. The patient lies prone on top of the measurement tank during the exam. The breast is suspended through the aperture in the top of the tank and the antennas are moved vertically with measurements taken at seven different positions.

ing images of a simulated measurement and of an actual patient measurement.

2. Imaging System

A photograph of the imaging system currently being tested at Dartmouth College is shown in Fig. 1. The imaging system consists of $n_{\text{ants}} = 16$ antennas of a simple monopole type [24] positioned in a cylindrical setup with radius 7.64 cm. The antennas are placed inside of a measurement tank on top of which the patient lies prone with her breast suspended through an aperture in the lid of the tank. During exams, the tank is filled with a glycerin-water coupling liquid which mimics the constitutive parameters of the breast tissue. This assures that the microwave power transmitted by the antennas is coupled to the inside of the breast [25].

The coupling liquid is lossy, thus attenuating the current on the outer conductor of the antennas, eliminating the need for a ground plane for the antennas. The coupling liquid also has the positive effect of making the antennas broadband, thereby allowing the system to operate in the frequency range from 500 MHz to 2.3 GHz. Although only a single frequency is used in the reconstructions, the wide frequency range allows for choosing the best frequency at which to do the reconstructions.

At the beginning of an exam, the antennas are positioned as close to the lid of the measurement tank as possible. The antennas are then moved down in 1 cm steps and measurements are obtained in seven different planes. In this way, the entire breast of the patient is imaged. A more thorough description of the imaging system may be found in [26, 27] and discussions about the effects of and problems related to imaging a 3-D scattering problem using a 2-D setup are presented in [28, 29].

3. Imaging Algorithm

To reconstruct the images, a 2-D imaging domain is set up in which the breast is assumed to be fully contained. The imaging domain consists of square cells with side length 5 mm and area $a_{\text{cell}} = 25 \cdot 10^{-6}$ m^2. The radius of the imaging domain is 7.25 cm and in each of the $n_{\text{cells}} = 665$ cells of the domain, the permittivity and conductivity are assumed to be constant.

When dealing with 2-D electromagnetic scattering, a scalar representation may be used and in this paper, the antennas will be considered to be point sources when transmitting while the signals received by the antennas are assumed to be proportional to the field strength at the position of the antennas.

Using the time notation $\mathrm{e}^{-i\omega t}$, the scattered field resulting from an inhomogeneity is given by

$$E_{\text{scat}}(\boldsymbol{r}) = i\omega\mu_0 \int_D G(\boldsymbol{r}, \boldsymbol{r'}, k) E_{\text{tot}}(\boldsymbol{r'}) O(\boldsymbol{r'}) \, \mathrm{d}^2\boldsymbol{r'}. \quad (1)$$

In this expression, E_{scat} is the scattered field, ω is the angular frequency, μ_0 is the free-space permeability, and G is the Green's function for the homogeneous background with complex wave number k. The total field is denoted by E_{tot} and is given by

$$E_{\text{tot}}(\boldsymbol{r}) = E_{\text{scat}}(\boldsymbol{r}) + E_{\text{inc}}(\boldsymbol{r}) \quad (2)$$

where E_{inc} is the known incident field. This equation shows that (1) is nonlinear with respect to the scattered field. The scattering object is represented by its object function O given by

$$O(\boldsymbol{r}) = \Delta\sigma(\boldsymbol{r}) - i\omega\Delta\epsilon(\boldsymbol{r}) = (\sigma(\boldsymbol{r}) - \sigma_{\text{bg}}) - i\omega\left(\epsilon(\boldsymbol{r}) - \epsilon_{\text{bg}}\right) \quad (3)$$

wherein σ_{bg} and ϵ_{bg} are the conductivity and permittivity, respectively, of the background. The contrast source χ is now introduced as

$$\chi(\boldsymbol{r}) = E_{\text{tot}}(\boldsymbol{r'}) O(\boldsymbol{r'}). \quad (4)$$

The contrast source is seen to be dependent on the total field in the imaging domain, implying one distribution of contrast sources for each transmitting antenna.

Using the contrast source, the nonlinear equation (1) may be separated into two linear equations. The *data equation* relates the measured scattered field to the distribution of contrast sources in the imaging domain as

$$E_{\text{scat}}^{(t,r)}(\boldsymbol{r}_{\boldsymbol{r}}) = i\omega\mu_0 \int_D G(\boldsymbol{r}_{\boldsymbol{r}}, \boldsymbol{r'}) \chi^{(t)}(\boldsymbol{r'}) \, \mathrm{d}^2\boldsymbol{r'}. \quad (5)$$

Herein, $E_{\text{scat}}^{(t,r)}$ is the scattered signal measured by antenna r when antenna t is transmitting and $\chi^{(t)}(\boldsymbol{r'})$ is the distribution of contrast sources when antenna t is transmitting.

In addition to the data equation, the *object equation* is introduced as

$$\chi^{(t)}(\boldsymbol{r}) = E_{\text{tot}}^{(t)}(\boldsymbol{r}) O(\boldsymbol{r}) \quad (6a)$$

wherein $E_{\mathrm{tot}}^{(t)}$ is the total field in the imaging domain when antenna t is transmitting. This field may be expressed as the sum of the incident field and the scattered field which, in turn, may be expressed using the contrast sources $\chi^{(t)}$. The resulting expression for the object equation is

$$\chi^{(t)}(\boldsymbol{r}) - i\omega\mu_0 O(\boldsymbol{r}) \int_D G(\boldsymbol{r},\boldsymbol{r'})\chi^{(t)}(\boldsymbol{r'})\,\mathrm{d}\boldsymbol{r'} = E_{\mathrm{inc}}^{(t)}(\boldsymbol{r})O(\boldsymbol{r}). \quad (6b)$$

The data equation (5) and object equation (6) constitute the basis of the iterative contrast source inversion algorithm used for reconstructing the images.

3.1 Complex Formulation

To reconstruct the images using the complex formulation, the cost function F_{complex} is defined as

$$F_{\mathrm{complex}} = \lambda_{\mathrm{dat}}^2 \sum_{t=1}^{n_{\mathrm{ants}}} \left\| \underline{\underline{G}}_D^{(t)} \underline{\chi}^{(t)} - \underline{E}_{\mathrm{scat}}^{(t)} \right\|_2^2 + \lambda_{\mathrm{obj}}^2 \sum_{t=1}^{n_{\mathrm{ants}}} \left\| \left(\underline{\underline{GO}} + \underline{\underline{I}}\right) \underline{\chi}^{(t)} - \underline{EO}^{(t)} \right\|_2^2 \quad (7)$$

and the distributions of contrast sources, represented by the vectors $\underline{\chi}^{(t)}$, and the object function, represented by the vector $\underline{O}$, are determined as the distributions which minimize this function. The cost function is based on a discretization of the data and object equations. The data equation may be cast in its discrete form, yielding

$$\underline{\underline{G}}_{\mathrm{D}}^{(t)} \underline{\chi}^{(t)} = \underline{E}_{\mathrm{scat}}^{(t)} \quad (8)$$

where $\underline{E}_{\mathrm{scat}}^{(t)}$ is an $n_{\mathrm{ants}} - 1$ element vector holding the measured scattered signal, $\underline{\chi}_t$ is an n_{cells} element vector holding the contrast sources for the individual cells of the imaging domain, and $\underline{\underline{G}}_{\mathrm{D}}^{(t)}$ is an $n_{\mathrm{ants}} - 1$ by n_{cells} element matrix. The elements $e_{\mathrm{scat},(m)}^{(t)}$ of the vector $\underline{E}_{\mathrm{scat}}^{(t)}$ are given as the difference between the signal measured when an object is inserted into the system, $E_{\mathrm{obj}}^{(t,r)}$ and the measured signals when the imaging system is empty $E_{\mathrm{empty}}^{(t,r)}$, i.e.,

$$e_{\mathrm{scat},(m)}^{(t)} = E_{\mathrm{obj}}^{(t,m)} - E_{\mathrm{obj}}^{(t,m)} \quad (9)$$

wherein index m represents the different receivers. The elements $g_{\mathrm{D},(m,n)}$ of the matrix $\underline{\underline{G}}_{\mathrm{D}}^{(t)}$ are given by

$$g_{\mathrm{D},(m,n)}^{(t)} = i\omega\mu_0 a_{\mathrm{cell}} G(\boldsymbol{r_m},\boldsymbol{r_n}) \quad (10)$$

and represent the contribution from the contrast sources in each cell (index n) to the scattered field measured at a given antenna (index m).

Similar to this, the object equation may be transformed to a discrete equation, yielding

$$\left(\underline{\underline{GO}} + \underline{\underline{I}}\right) \underline{\chi}^{(t)} = \underline{EO}^{(t)} \quad (11)$$

wherein $\underline{\underline{I}}$ is the identity matrix and $\underline{\underline{GO}}$ is a square n_{cells} by n_{cells} matrix with elements

$$go_{m,n} = -i\omega\mu_0 a_{\mathrm{cell}} O(\boldsymbol{r_m}) G(\boldsymbol{r_m},\boldsymbol{r_n}). \quad (12)$$

The vector $\underline{EO}^{(t)}$ has n_{cells} elements and holds the product of the incident field and the object function in the individual cells, i.e.,

$$eo_m^{(t)} = E_{\mathrm{inc}}^{(t)}(\boldsymbol{r_m}) O(\boldsymbol{r_m}). \quad (13)$$

The weighting factors λ_{dat} and λ_{obj} in (7) determine how the CSI algorithm weights the data equations relative to the object equations. In the original implementation of the CSI algorithm [17] these were chosen as

$$\lambda_{\mathrm{dat}} = \left(\sum_{t=1}^{n_{\mathrm{ants}}} \left\| \underline{E}_{\mathrm{scat}}^{(t)} \right\|_2^2 \right)^{-\frac{1}{2}} \quad (14a)$$

and

$$\lambda_{\mathrm{obj}} = \left(\sum_{t=1}^{n_{\mathrm{ants}}} \left\| \underline{EO}^{(t)} \right\|_2^2 \right)^{-\frac{1}{2}}. \quad (14b)$$

In this way, the contributions to the cost function (7) from both the data equations and the object equations are equal to one if $\chi^{(t)} = 0$. During the development of the algorithm presented in this paper, it has been found that the performance of the algorithm may be improved by adjusting the values of λ_{dat} and λ_{obj}. This is, however, not trivial since the optimum values need to be determined empirically. Furthermore, the optimum values vary when different objects are imaged. Therefore, the values in (14) will be applied in this paper.

In each iteration $l = 2, 3, \ldots L$ of the CSI algorithm, the distribution of contrast sources and the object function, in turn, are updated in order to minimize F_{complex}. The update consists of the following five steps:

1. Determine updates of the n_{ants} distributions of contrast sources by solving

$$\underline{\Delta\chi}^{(t,l)} = \mathrm{argmin} \left\{ \left\| \begin{bmatrix} \lambda_{\mathrm{dat}} \underline{\underline{G}}_{\mathrm{D}}^{(t)} \\ \lambda_{\mathrm{obj}}^{(l)} \left(\underline{\underline{GO}}^{(l)} + \underline{\underline{I}}\right) \end{bmatrix} \underline{\Delta\chi}^{(t,l)} - \begin{bmatrix} \lambda_{\mathrm{dat}} \underline{\delta D}^{(t,l)} \\ \lambda_{\mathrm{obj}}^{(l)} \underline{\delta O}^{(t,l)} \end{bmatrix} \right\|_2^2 \right\} \quad (15)$$

   subject to regularization.

2. Update the distribution of contrast sources using

$$\underline{\chi}^{(t,l)} = \underline{\chi}^{(t,l-1)} + \underline{\Delta\chi}^{(t,l)}. \quad (16)$$

3. Update the total field in the imaging domain for all distributions of contrast sources

$$\underline{E}_{\mathrm{tot}}^{(t,l)} = \underline{E}_{\mathrm{inc}}^{(t)} + \underline{\underline{G}}\,\underline{\chi}^{(t,l)} \quad (17)$$

4. Update the distribution of the object function using

$$O^{(l)}(\boldsymbol{r}) = \operatorname{argmin}\left\{\sum_{t=1}^{n_{\text{ants}}} |\chi^{(t,l)}(\boldsymbol{r}) - E_{\text{tot}}^{(t,l)}(\boldsymbol{r})O^{(l)}(\boldsymbol{r})|\right\} = \frac{\sum_{t=1}^{n_{\text{ants}}} \widetilde{E}_{\text{tot}}^{(t,l)}(\boldsymbol{r})\chi^{(t,l)}(\boldsymbol{r})}{\sum_{t=1}^{n_{\text{ants}}} |E_{\text{tot}}^{(t,l)}(\boldsymbol{r})|^2}. \quad (18)$$

5. Calculate the new values of $\underline{\delta D}$, $\underline{\delta O}$, and F_{complex} and check for termination.

The calculation of the updates of the contrast sources in step 1 is by far the most time consuming aspect of the CSI algorithm. Since the values of the object function O is changed as the CSI algorithm progresses, the elements of the matrix $\underline{\underline{GO}}^{(l)}$ and the vector $\underline{EO}^{(t,l)}$ also change. The elements of these are given by

$$go_{m,n}^{(l)} = -i\omega\mu_0 a_{\text{cell}} G(\boldsymbol{r_m}, \boldsymbol{r_n}) O^{(l-1)}(\boldsymbol{r_m}) \quad (19)$$

and

$$eo_m^{(t,l)} = E_{\text{inc}}^{(t)}(\boldsymbol{r_m}) O^{(l-1)}(\boldsymbol{r_m}). \quad (20)$$

It is noted that the matrices $\underline{\underline{G}}_D^{(t)}$ and the incident fields in the cells of the imaging domain are independent of the iteration number l and therefore may be calculated once and reused.

The vectors $\underline{\delta D}^{(t,l)}$ and $\underline{\delta O}^{(t,l)}$ in (15) are the data and object residual vectors, respectively. These are given by

$$\underline{\delta D}^{(t,l)} = \underline{E}_{\text{scat}}^{(t)} - \underline{\underline{G}}_D^{(t)} \underline{\chi}^{(t,l-1)} \quad (21a)$$

and

$$\underline{\delta O}^{(t,l)} = \underline{EO}^{(t,l-1)} - \left[\underline{\underline{GO}}^{(l-1)} + \underline{\underline{I}}\right] \underline{\chi}^{(t,l-1)}. \quad (21b)$$

The minimization problem in (15) is ill-posed and regularization is needed to obtain a suitable solution. To this end, the conjugate gradient least squares (CGLS) algorithm [30, Sec. 6.3] is applied. The CGLS algorithm is an iterative algorithm and the solution obtained after κ CGLS iterations is the least squares solution to the problem constrained to the κ-dimensional Krylov subspace related to the problem. Because the κ-dimensional Krylov subspace can be considered an approximation to the space spanned by the first κ singular vectors, the solution obtained using the CGLS algorithm is an approximation to the solution obtained using the truncated singular value decomposition, with the important difference that the time consuming singular value decomposition is not needed. During the development of the algorithm is has been found that the best results and the fastest convergence is obtained using only a few CGLS iterations, corresponding to using over-regularization. In the work presented here $\kappa = 5$ will be used.

After the update of the contrast sources has been found, the four remaining steps are relatively simple and computationally inexpensive. The algorithm is terminated when the value of F_{complex} becomes smaller than 0.001 or when l reaches its maximum value $L = 1000$.

In the first iteration of the CSI algorithm, $O^{(0)}$ is unknown and the value of $\underline{\Delta\chi}^{(t,1)}$ can therefore not be determined using (15). Instead, the more simple expression

$$\underline{\Delta\chi}^{(t,1)} = \operatorname{argmin}\left\{\left\|\underline{\underline{G}}_{\text{D}}^{(t)} \underline{\Delta\chi}^{(t,1)} - \underline{E}_{\text{scat}}^{(t)}\right\|_2^2\right\} \quad \text{subj. to regularization} \quad (22)$$

is used. This minimization problem is also solved using 5 iterations with the CGLS algorithm and steps 2–5 in CSI iteration number 1 can be done in the usual manner with the elements of $\underline{\chi}^{(t,0)}$ initialized to zeros.

3.2 Log-Phase Formulation

When the log-phase formulation is applied, the measured data is represented by the difference in the logarithm of the signals measured when the object is inserted into the imaging system and when the imaging system is empty. The resulting expression for the data is

$$E_{\text{lp}}^{(t,r)} = \log(E_{\text{obj}}^{(t,r)}) - \log(E_{\text{empty}}^{(t,r)}) = \log(|E_{\text{obj}}^{(t,r)}|) - \log(|E_{\text{empty}}^{(t,r)}|) + i\left(\angle E_{\text{obj}}^{(t,r)} - \angle E_{\text{empty}}^{(t,r)}\right). \quad (23)$$

In this expression, $\angle$ is the unwrapped phase of the signal. The phase unwrapping is described in details in [15] and the improved performance of the Gauss-Newton algorithm obtained when using the log-phase formulation has been described in a number of publications [15,16,31,32]. Here it suffices to say that the reformulation of the problem in terms of the log-amplitude unwrapped phase increases the weights of the large relative, but small absolute, changes encountered by receivers on the opposite side of the imaging system from the transmitter. This improves the performance of the algorithm since these signals hold the most information on the scattering object. Furthermore, the use of the unwrapped phase implies that the reconstruction can be done on multiple Riemann sheets. This is not possible when using the complex formulation where all measurements are mapped onto the same Riemann sheet.

The cost function for the log-phase F_{lp} formulation is defined as

$$F_{\text{lp}} = \lambda_{\text{dat}}^2 \sum_{t=1}^{n_{\text{ants}}} \left\|\underline{E}_{\text{meas-lp}}^{(t)} - \underline{E}_{\text{calc-lp}}^{(t)}(\underline{\chi}^{(t)})\right\|_2^2 + \lambda_{\text{obj}}^2 \sum_{t=1}^{n_{\text{ants}}} \left\|\left(\underline{\underline{GO}} + \underline{\underline{I}}\right) \underline{\chi}^{(t)} - \underline{EO}^{(t)}\right\|_2^2 \quad (24)$$

where the only difference compared to the cost function in (7) is the use of the vectors $\underline{E}_{\text{meas-lp}}^{(t)}$ and $\underline{E}_{\text{calc-lp}}^{(t)}$ instead of the data equation. The elements $e_{\text{meas-lp},(m)}^{(t)}$ of

the vector $\underline{E}^{(t)}_{\mathrm{meas-lp}}$ are given by the measured data

$$e^{(t)}_{\mathrm{meas-lp},(m)} = \log|E^{(t,m)}_{\mathrm{meas,obj}}| - \log|E^{(t,m)}_{\mathrm{meas,empty}}| + i\left(\angle E^{(t,m)}_{\mathrm{meas,obj}} - \angle E^{(t,m)}_{\mathrm{meas,empty}}\right) \quad (25a)$$

and the elements $e^{(t)}_{\mathrm{meas-lp},(m)}$ of $\underline{E}^{(t)}_{\mathrm{meas,lp}}$ are given by

$$e^{(t)}_{\mathrm{calc-lp},(m)} = \log|E^{(t,m)}_{\mathrm{calc,obj}}(\chi^{(t)})| - \log|E^{(t,m)}_{\mathrm{calc,empty}}| + i\left(\angle E^{(t,m)}_{\mathrm{calc,obj}}(\chi^{(t)}) - \angle E^{(t,m)}_{\mathrm{calc,empty}}\right) \quad (25b)$$

with m being the index of the receiver. The value of $E^{t,m}_{\mathrm{calc,empty}}$ is easily found with the antennas modelled as point sources and the value of $E^{t,m}_{\mathrm{calc,obj}}(\chi^{(t)})$ is found as the sum of the scattered field found using the data equation and $E^{t,m}_{\mathrm{calc,empty}}$.

The CSI algorithm using the log-phase formulation is very similar to that using the complex notation. The following five steps are carried out in each iteration:

1. Determine updates of the n_{ants} distributions of contrast sources by solving

$$\underline{\Delta\chi}^{(t,l)} = \mathrm{argmin}\left\{\left\|\begin{bmatrix}\lambda_{\mathrm{dat}}\underline{\underline{G}}^{(t,l)}_{\mathrm{D-lp}}\\ \lambda^{(l)}_{\mathrm{obj}}\left(\underline{\underline{GO}}^{(l)} + \underline{\underline{I}}\right)\end{bmatrix}\underline{\Delta\chi}^{(t,l)} - \begin{bmatrix}\lambda_{\mathrm{dat,lp}}\underline{\delta D}^{(t,l)}_{\mathrm{lp}}\\ \lambda^{(l)}_{\mathrm{obj}}\underline{\delta O}^{(t,l)}\end{bmatrix}\right\|_2^2\right\} \quad (26)$$

   subject to regularization.
2. Update the distribution of contrast sources using

$$\underline{\chi}^{(t,l)} = \underline{\chi}^{(t,l-1)} + \alpha^{(l)}\underline{\Delta\chi}^{(t,l)} \quad (27a)$$

   with

$$\alpha^{(l)} = \begin{cases} 1 & \text{for } \frac{\|\underline{\Delta\chi}^{(t,l)}\|_2}{\|\underline{\chi}^{(t,l-1)}\|_2} \le 0.1 \\ \frac{0.1\|\underline{\chi}^{(t,l-1)}\|_2}{\|\underline{\Delta\chi}^{(t,l)}\|_2} & \text{for } \frac{\|\underline{\Delta\chi}^{(t,l)}\|_2}{\|\underline{\chi}^{(t,l-1)}\|_2} > 0.1 \end{cases}. \quad (27b)$$

3. Update the total field for all distributions of contrast sources

$$\underline{E}^{(t,l)}_{\mathrm{tot}} = \underline{E}^{(t)}_{\mathrm{inc}} + \underline{\underline{G}}^{(t)}\,\underline{\chi}^{(t,l)} \quad (28a)$$

   in the imaging domain and the field at the receivers

$$\underline{E}^{(t,l)}_{\mathrm{rec}} = \underline{E}^{(t)}_{\mathrm{rec,empty}} + \underline{\underline{G}}^{(t)}_{D}\underline{\chi}^{(t,l)} \quad (28b)$$

   and calculate of $\underline{E}^{(t)}_{\mathrm{calc-lp}}$.
4. Update the distribution of the object function using

$$O^{(l)}(\boldsymbol{r}) = \frac{\sum_{t=1}^{n_{\mathrm{ants}}}\widetilde{E}^{\mathrm{tot}}_t(\boldsymbol{r})\chi_t}{\sum_{t=1}^{n_{\mathrm{ants}}}|E^{\mathrm{tot}}_t(\boldsymbol{r})|^2}. \quad (29)$$

5. Calculate the new values of $\underline{\delta D}_{\mathrm{lp}}$, $\underline{\delta O}$, and F_{lp} and check for termination.

The most significant difference between the complex and the log-phase formulation of the CSI algorithm is the use of the matrix $\underline{\underline{G}}_{\mathrm{D-lp}}$ and the residual vector $\underline{\delta D}^{(t,l)}_{lp}$ in (26). The matrix $\underline{\underline{G}}_{\mathrm{D-lp}}$ holds the derivative of the object equation with respect to the contrast sources and its elements $g^{(t,l)}_{\mathrm{D-lp},(m,n)}$ are given by

$$g^{(t,l)}_{\mathrm{D-lp},(m,n)} = \frac{1}{|\underline{e}^{(t,l-1)}_{\mathrm{rec},(m)}|^2}\widetilde{\underline{e}}^{(t,l-1)}_{\mathrm{rec},(m)}\underline{g}^{(t)}_{\underline{\underline{\mathrm{D}}},(m,n)} \quad (30)$$

where $\underline{g}^{(t)}_{\underline{\underline{\mathrm{D}}},(m,n)}$ is the discretization of the data equation given by (10). The residual vector $\underline{\delta D}^{(t,l)}_{lp}$ is the residual with respect to the log-phase formulation, given by

$$\underline{\delta D}^{(t,l)}_{lp} = \underline{E}^{(t)}_{\mathrm{meas-lp}} - \underline{E}^{(t)}_{\mathrm{calc-lp}}(\underline{\chi}^{(t,l-1)}). \quad (31)$$

As with the complex formulation, the minimization problem in (26) is solved using five iterations of the CGLS algorithm. When the update has been determined, an extra scaling factor $\alpha^{(l)}$ is introduced in (27). This has been done to make sure that the phase of the signal of any transmit-receive pair of antennas does not change more than $\pm\pi$ in each iteration. This will, in turn, make it easier to unwrap the phase in step 3 since it can be assumed that the new phases are not more than $\pm\pi$ different from the phases of the previous iteration.

The remaining steps of the CSI algorithm in the log-phase formulation are similar to those in the complex formulation. The computational demands for the log-phase formulation are slightly larger than for the complex notation in that the matrix $\underline{\underline{G}}^{(t,l)}_{\mathrm{D-lp},(m,n)}$ needs to be updated in every iteration and because of the additional matrix operation in step 3. However, the most time consuming task is still the solution of the minimization problem and the additional computation time used by the algorithm outside of this operation is hardly noticed.

The log-phase algorithm is initialized by solving the minimization problem

$$\underline{\Delta\chi}^{(t,1)} = \mathrm{argmin}\left\{\left\|\underline{\underline{G}}^{(t,1)}_{\mathrm{D-lp}}\underline{\Delta\chi}^{(t,1)} - \underline{E}^{(t)}_{\mathrm{meas-lp}}\right\|_2^2\right\} \quad (32)$$

using 5 CGLS iterations. The field at the receivers are initialized with the values calculated for an empty system and the contrast sources are initialized as zero.

4. Results

Two different reconstructions are presented here to illustrate the performance of the CSI algorithm in its complex and log-phase formulations. The first example is a reconstruction of a simulated measurement at 1.3 GHz and the second is a reconstruction of a patient measurement performed at 1.1 GHz.

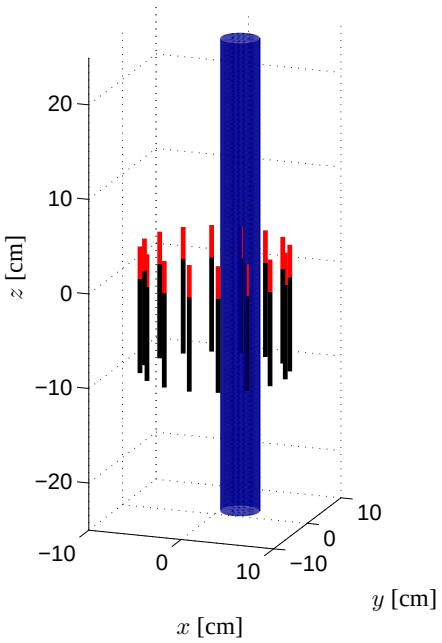

Fig. 2. Simulation setup. The antennas are modeled with a 10 cm long outer conductor and the scatterer is a 50 cm long cylinder. The background is uniform with relative permittivity 36 and conductivity 1 S/m and the cylinder has relative permittivity 72 and conductivity 2 S/m.

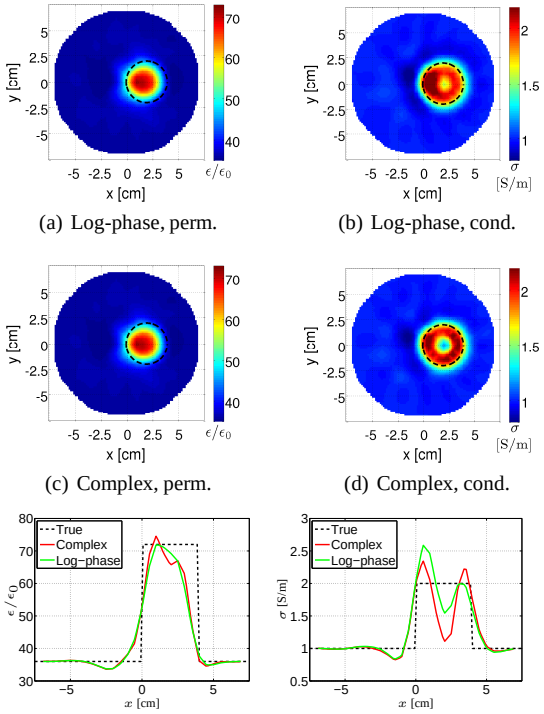

(a) Log-phase, perm. (b) Log-phase, cond.

(c) Complex, perm. (d) Complex, cond.

(e) Cut, perm. (f) Cut, cond.

Fig. 3. Reconstruction of the simulation. The dashed black lines in (a)–(d) represents the actual position of the cylinder. In (e) and (f), the reconstructed profiles along the x-axis are plotted along with the actual values.

4.1 Simulation

The simulation was done at an operating frequency of 1.3 GHz and the antennas were modelled in a uniform background with relative permittivity 36 and conductivity 1 S/m. The simulation was done using a 3-D method of moments code. The antennas are modelled in full with a 3.4 cm long stripped dielectric and a 10 cm long outer conductor, with the imaging plane positioned at $z = 0$. The scatterer was a cylinder with radius 2 cm and length 50 cm oriented parallel to the z-axis with its center at $(x, y, z) = (2\text{ cm}, 0\text{ cm}, 0\text{ cm})$. The relative permittivity and conductivity of the cylinder was 72 and 2 S/m, respectively. A schematic of the setup is shown in Fig. 2. In this figure, the stripped part of the antennas are given by the red lines, the outer conductors are given by the black lines and the scatterer is given by the blue cylinder. Gaussian noise mimicking a noise floor 110 dB beneath the transmitted power has been added to the simulation.

The results of the reconstructions using the complex and log-phase formulations are shown in Fig. 3. In this figure it is seen that both of the algorithms reconstruct the permittivity with great accuracy while the reconstructed conductivity profiles of the scattering cylinder are less accurate. To quantify the quality of the reconstructions, the normalized norm of the errors have been calculated using

$$\eta_{\text{perm}} = \frac{\|\underline{\epsilon}_{\text{true}} - \underline{\epsilon}_{\text{recon}}\|_2}{\|\underline{\epsilon}_{\text{true}}\|_2} \tag{33a}$$

and

$$\eta_{\text{cond}} = \frac{\|\underline{\sigma}_{\text{true}} - \underline{\sigma}_{\text{recon}}\|_2}{\|\underline{\sigma}_{\text{true}}\|_2}. \tag{33b}$$

In these expressions, $\underline{\epsilon}_{\text{true}}$ and $\underline{\sigma}_{\text{true}}$ represents the true distributions of the permittivity and conductivity, respectively, and $\underline{\epsilon}_{\text{recon}}$ and $\underline{\sigma}_{\text{recon}}$ represent the reconstructed. The values for the log-phase formulation are $\eta_{\text{perm}}^{\text{log-phase}} = 0.12$ and $\eta_{\text{cond}}^{\text{log-phase}} = 0.13$ while the values for the complex formulation are $\eta_{\text{perm}}^{\text{complex}} = 0.12$ and $\eta_{\text{cond}}^{\text{complex}} = 0.14$. Thus, the difference between the two solutions are practically non-existing. In terms of computation time, the log-phase formulation reaches convergence after 429 iterations and the complex formulation after 515 iterations. Hence, the complex formulation uses 20% more iterations to reach convergence. In the current *Matlab* implementation of the algorithm, each iteration lasts approximately 7 seconds when run on a 2.2 GHz 64 bit AMD Opteron 848 processor and the complex formulation thus takes an additional 10 minutes to complete.

The relatively poor reconstructions of the conductivity images compared to the permittivity images have previously been seen in image reconstructions obtained using Gauss-Newton based algorithms. In these algorithms it has been found that a scaling of the elements in the parameter vector, corresponding to the update vector $\underline{\Delta\chi}$ in the CSI algorithm, can improve the performance [33]. Research is currently being carried out to investigate whether this is also the case for the CSI algorithm.

4.2 Patient Data

To test the performance of the algorithm when applied to data from patient measurements, a measurement of a patient with a tumor in the right breast has been reconstructed. The patient was 36 years old at the time of measurement and had heterogeneously-dense breasts. The tumor was distributed over a region with a diameter of approximately 4 cm and was located at a 7 clock-face orientation, viewing the patient en face, near the anterior of the breast. The measurement was done using a 80:20 percent glycerin:water coupling liquid at 1.1 GHz.

The images of the imaging planes 2 through 5 obtained using the log-phase formulation are shown in Fig. 4 and the corresponding images obtained using the complex formulation are shown in Fig. 5. In general, the conductivity images show more artifacts than the permittivity images in all planes and for both algorithms.

In plane 2, the antennas are close to the chest wall of the patient and the 2-D modeling of the scattering problem is therefore a suboptimal approximation to the actual 3-D scattering problem. This results in increased artifacts in both the permittivity and conductivity images for both formulations, but the artifacts are more pronounced in the images reconstructed using the complex formulation, and especially in the conductivity image. The poor performance of the complex algorithm in this case may also be a result of the large phase changes in the measured signals. The phase of the measured signals changes as much as 1.4π, and since the complex formulation uses only one Riemann sheet in the reconstruction, this is likely to pose a problem.

As the antennas are moved to imaging plane 3, the tumor becomes visible in the log-phase images as a region of elevated values of permittivity and conductivity inside the breast. As the antennas are moved further down, the tumor is more clearly seen in planes 4 and 5. In plane 5, the conical shape of the breast starts to influence the model accuracy and the contour of the breast is not as well-defined as in the planes above. In all of the images, a region of elevated values close to the antennas at the bottom of the images can be seen. This is likely to be a result of the breast being too close to the antennas at this part of the imaging system, thereby influencing these antennas more than the others.

In all of the images reconstructed using the complex formulation, the artifact level is higher than in the corresponding images obtained using the log-phase formulation. For the imaging planes 2 through 4 this is likely to be a result of the fact that the phase change in the measured signals are greater than $\pm\pi$, i.e., requiring more than a single Riemann sheet for the reconstruction. Even though the level of the artifacts are higher in these images, the tumor may still be detected in plane 4. In plane 5 where the maximum phase change is only 0.8π, the images obtained using the complex formulation are much like those obtained using the log-phase formulation. The most problematic feature of the images reconstructed using the complex formulation is the artifacts in the center of the images in planes 2 and 3. If used for diagnostics, these artifacts will likely result in a false-positive, thereby rendering the images useless for such purposes. Especially because the artifacts seem to have the features of an actual tumor, i.e., high values of both permittivity and conductivity.

The images presented here clearly show the improved performance of the CSI algorithm when the log-phase formulation is applied instead of the complex notation. It

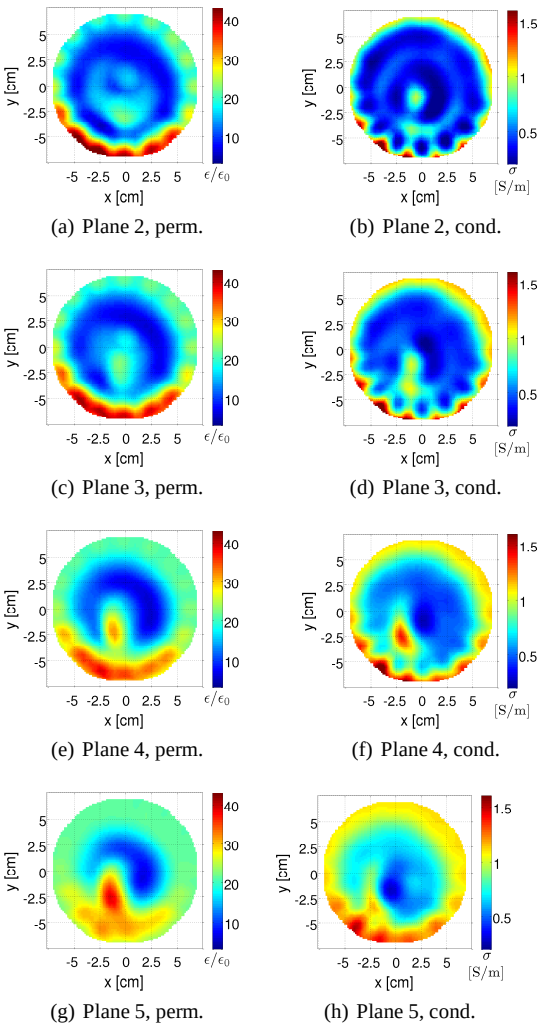

(a) Plane 2, perm. (b) Plane 2, cond.
(c) Plane 3, perm. (d) Plane 3, cond.
(e) Plane 4, perm. (f) Plane 4, cond.
(g) Plane 5, perm. (h) Plane 5, cond.

Fig. 4. Images of four of the seven imaging planes reconstructed using the log-phase formulation. The patient had a tumor near the anterior of the breast at a 7 clock-face position.

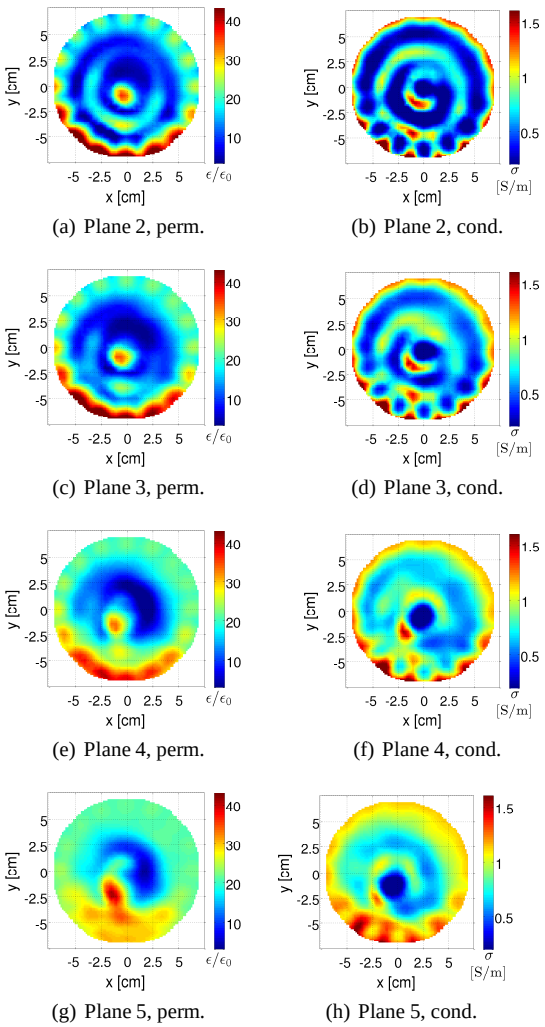

(a) Plane 2, perm. (b) Plane 2, cond.

(c) Plane 3, perm. (d) Plane 3, cond.

(e) Plane 4, perm. (f) Plane 4, cond.

(g) Plane 5, perm. (h) Plane 5, cond.

Fig. 5. Images of four of the seven imaging planes reconstructed using the complex formulation. The patient had a tumor near the anterior of the breast at a 7 clock-face position.

proves especially useful when the changes in the phases of the measured signals changes more than $\pm\pi$ as is the case for imaging planes 2 through 4 where the artifact level in the images is so high that the images are not suited for diagnostics.

5. Conclusion

In this paper, a contrast source inversion (CSI) algorithm has been presented in which the log-amplitude unwrapped phase formulation of the measured signals are applied has been presented. The algorithm uses the iterative conjugate gradient least-squares algorithm to solve the linear minimization problem to determine the updates of the contrast sources in each CSI iteration.

The performance of the log-phase formulation was compared with a CSI algorithm in which the standard complex formulation was applied. For simple problems, the two algorithms performed similarly, although the log-phase formulation reached convergence quicker than the complex formulation. When applied for imaging of patient data, the log-phase formulation clearly outperformed the complex formulation, due to the ability of the log-phase formulation to reconstruct images using data residing in several Riemann sheets.

Ongoing research will determine whether better weighting between the data and object equations for updating the contrast sources can be found and if a scaling of the elements in the update vector can improve the ability to reconstruct the correct conductivity. Finally, a three-dimensional implementation of the algorithm is being tested for use with the imaging system currently being developed at the Technical University of Denmark.

Acknowledgement

The work of Tonny Rubæk and Peter Meincke is supported by The Villum Kann Rasmussen Foundation, The Danish Technical Research Council, Trane's Fond, and The Otto Mønsted Foundation. The work of Paul M. Meaney is sponsored by NHI/NCI grant no. P01-CA080139.

References

[1] Poplack, S. P.; Tosteson, T. D.; Wells, W. A.; Pogue, B. W.; Meaney, P. M.; Hartov, A.; Kogel, C. A.; Soho, S. K.; Gibson, J. J.; Paulsen, K. D.: Electromagnetic breast imaging: Results of a pilot study in women with abnormal mammograms. Radiology - Radiological Society of North America **243** (2007), 350–359.

[2] Lazebnik, M.; McCartney, L.; Popovic, D.; Watkins, C. B.; Lindstrom, M. J.; Harter, J.; Sewall, S.; Magliocco, A.; Booske, J. H.; Okoniewski, M.; Hagness, S. C.: A large-scale study of the ultrawideband microwave dielectric properties of normal breast tissue obtained from reduction surgeries. Physics in Medicine and Biology **52** (2007).

[3] Klemm, M.; Craddock, I. J.; Leendertz, J.; Preece, A.; Benjamin, R.: Breast cancer detection using symmetrical antenna array. Proceedings of the European Conference on Antennas and Propagation EuCAP 2007 (2007), 4 pp.

[4] Sill, J. M.; Fear, E. C.: Tissue sensing adaptive radar for breast cancer detection - experimental investigation of simple tumor models. IEEE Transactions on Microwave Theory and Techniques **53** (2005), 3312–3319.

[5] Li, X.; Bond, E.; Van Veen, B.; Hagness, S.: An overview of ultra-wideband microwave imaging via space-time beamforming for early-stage breast-cancer detection. Antennas and Propagation Magazine, IEEE **47** (2005), 19–34.

[6] Sill, J.; Fear, B.: Tissue sensing adaptive radar for breast cancer detection: Preliminary experimental results. Proceedings of the IEEE MTT-S International Microwave Symposium, 2005 **2005** (2005), 1789–1792.

[7] Kosmas, P.; Rappaport, C.: A matched-filter FDTD-based time reversal approach for microwave breast cancer detection. IEEE Transactions on Antennas and Propagation **54** (2006), 1257–1264.

[8] Zhang, Z. Q.; Liu, Q. H.; Xiao, C.; Ward, E.; Ybarra, G.; Joines, W. T.: Microwave breast imaging: 3-d forward scattering simulation. IEEE Transactions on Biomedical Engineering **50** (2003), 1180–1189.

[9] Fhager, A.; Hashemzadeh, P.; Persson, M.: Reconstruction quality and spectral content of an electromagnetic time-domain inversion algorithm. IEEE Transactions on Biomedical Engineering **53** (2006), 1594–1604.

[10] Meaney, P.; Fang, Q.; Fanning, M.; Pendergrass, S.; Raynolds, T.; Fox, C.; Paulsen, K.: Microwave breast imaging with an under-determined reconstruction parameter mesh. Proceedings of the IEEE International Symposium on Biomedical Imaging: Macro to Nano, 2004 (2004), 1369–1372.

[11] Rubæk, T.; Meaney, P. M.; Meincke, P.; Paulsen, K. D.: Nonlinear microwave imaging for breast-cancer screening using Gauss-Newton's method and the CGLS inversion algorithm. IEEE Transactions on Antennas and Propagation **55** (2007), 2320–2331.

[12] Bozza, G.; Estatico, C.; Massa, A.; Pastorino, M.; Randazzo, A.: Short-range image-based method for the inspection of strong scatterers using microwaves. IEEE Transactions on Instrumentation and Measurement **56** (2007), 1181–1188.

[13] Souvorov, A.; Bulyshev, A.; Semenov, S.; Svenson, R.; Nazarov, A.; Sizov, Y.; Tatsis, G.: Microwave tomography: A two-dimensional Newton iterative scheme. IEEE Transactions on Microwave Theory and Techniques **46** (1998), 1654–1659.

[14] Paulsen, K.; Meaney, P.; Moskowitz, M.; Sullivan, J.M., J.: A dual mesh scheme for finite element based reconstruction algorithms. IEEE Transactions on Medical Imaging **14** (1995), 504–514.

[15] Meaney, P.; Paulsen, K.; Pogue, B.; Miga, M.: Microwave image reconstruction utilizing log-magnitude and unwrapped phase to improve high-contrast object recovery. IEEE Transactions on Medical Imaging **20** (2001), 104–116.

[16] Meaney, P. M.; Fang, Q.; Rubaek, T.; Demidenko, E.; Paulsen, K. D.: Log transformation benefits parameter estimation in microwave tomographic imaging. Medical Physics **34** (2007), 2014–2023.

[17] van den Berg, P. M.; Kleinman, R. E.: A contrast source inversion method. Inverse Problems **13** (1997), 1607–1620.

[18] van den Berg, P. M.; van Broekhoven, A. L.; Abubakar, A.: Extended contrast source inversion. Inverse Problems **15** (1999), 1325–1344.

[19] Abubakar, A.; van den Berg, P. M.; Mallorqui, J. J.: Full nonlinear inversion of microwave biomedical data. Proceedings of SPIE - The International Society for Optical Engineering **4684 II** (2002), 797–805.

[20] Feng, H.; Galdi, V.; Castanon, D. A.: An object-based contrast source inversion method for homogeneous targets. Subsurface Sensing Technologies and Applications **4** (2003), 355–374.

[21] Abubakar, A.; Semenov, S.; Posukh, V. G.; van den Berg, P. M.: Application of the multiplicative regularized contrast source inversion method to real biological data. Proceedings of the IEEE MTT-S International Microwave Symposium, 2005 **2005** (2005), 1319–1322 and 1516922.

[22] Lager, I.; Kooij, B.: Non-linear imaging algorithm for the detection of female breast cancer in the incipient state. 2005 European Radar Conference (2006), 217–20.

[23] Catapano, I.; Crocco, L.; D'Urso, M.; Morabito, A.; Isernia, T.: Microwave tomography of breast cancer: A feasibility study. European Space Agency, (Special Publication) ESA SP **626 SP** (2006).

[24] Meaney, P.; Paulsen, K.; Chang, J.: Near-field microwave imaging of biologically-based materials using a monopole transceiver system. IEEE Transactions on Microwave Theory and Techniques **46** (1998), 31–45.

[25] Meaney, P.; Pendergrass, S.; Fanning, M.; Li, D.; Paulsen, K.: Importance of using a reduced contrast coupling medium in 2D microwave breast imaging. Journal of Electromagnetic Waves and Applications **17** (2003), 333–355.

[26] Meaney, P.; Fanning, M.; Li, D.; Poplack, S.; Paulsen, K.: A clinical prototype for active microwave imaging of the breast. IEEE Transactions on Microwave Theory and Techniques **48** (2000), 1841–1853.

[27] Li, D.; Meaney, P.; Raynolds, T.; Pendergrass, S.; Fanning, M.; Paulsen, K.: A broadband microwave breast imaging system. Proceedings of the IEEE 29th Annual Bioengineering Conference, 2003 (2003), 83–84.

[28] Meaney, P.; Paulsen, K.; Geimer, S.; Haider, S.; Fanning, M.: Quantification of 3-D field effects during 2-D microwave imaging. IEEE Transactions on Biomedical Engineering **49** (2002), 708–720.

[29] Fang, Q.; Meaney, P.; Geimer, S.; Streltsov, A.; Paulsen, K.: Microwave image reconstruction from 3-D fields coupled to 2-D parameter estimation. IEEE Transactions on Medical Imaging **23** (2004), 475–484.

[30] Hansen, P. C.: Rank-deficient and discrete ill-posed problems: Numerical aspects of linear inversion. SIAM, 1998. – (Monographs on Mathematical Modeling and Computation).

[31] Meaney, P.; Paulsen, K.; Fanning, M.; Li, D.; Fang, Q.: Image accuracy improvements in microwave tomographic thermometry: Phantom experience. International Journal of Hyperthermia **19** (2003), 534–50.

[32] Fang, Q.; Meaney, P.; Paulsen, K.: The multidimensional phase unwrapping integral and applications to microwave tomographical image reconstruction. IEEE Transactions on Image Processing **15** (2006), 3311–3324.

[33] Meaney, P. M.; Yagnamurthy, N. K.; Paulsen, K. D.: Prescaled two-parameter Gauss-Newton image reconstruction to reduce property recovery imbalance. Physics in Medicine and Biology **47** (2002), 1101–1119.

Journal Paper 4

Computational Validation of a 3-D Microwave Imaging System for Breast-Cancer Screening

Tonny Rubæk, Oleksiy Kim, and Peter Meincke

Status:
Submitted: February 2008
Accepted: – – – – – –
Published: – – – – – –
Journal: IEEE Transactions on Antennas and Propagation

Computational Validation of a 3-D Microwave Imaging System for Breast-Cancer Screening

Tonny Rubæk, Oleksiy Kim, Peter Meincke

***Abstract*— The microwave imaging system currently being developed at the Technical University of Denmark is described and its performance tested on simulated data. The system uses an iterative Newton-based imaging algorithm for reconstructing the images in conjunction with an efficient method-of-moments solution of the associated forward scattering problem. A cylindrical multistatic antenna setup with 32 horizontally oriented antennas is used for collecting the data.**

It has been found that formulating the imaging algorithm in terms of the logarithm of the amplitude and the unwrapped phase of the measured signals improves its performance when compared to the more commonly used complex phasor formulation. This improvement is illustrated by imaging a simulated hemispherical breast model using both formulations. In addition to this, the importance of using the correct positions and orientations of antennas in the measurement system is shown by imaging the same breast model using a measurement setup in which the antennas are vertically oriented.

***Index Terms*— Cancer, Microwave Imaging, Electromagnetic Scattering Inverse Problems, Biomedical Imaging, Nonlinear Equations**

I. Introduction

BREAST cancer is the most common type of cancer among women [1]–[4], and early detection is one of the most important prerequisites for successful treatment of the cancer [5]. To this end, screening programmes using X-ray mammography is the most widespread approach. X-ray mammography is, however, not perfect, especially when used to screen women under the age of 50 for which sensitivities as low as 53% have been reported [6]. This leaves room for supplementary imaging modalities, such as the well-established magnetic-resonance and ultrasound imaging techniques [7], albeit these are not suitable for screening purposes due to the cost of the individual examination. An emerging imaging modality for breast-cancer screening is microwave imaging which is based on the high contrast in the electromagnetic constitutive parameters between healthy and cancerous breast tissue in the microwave frequency range, reported by several authors [8]–[14]. This contrast causes incident electromagnetic fields in the microwave region of the frequency spectrum to be scattered, allowing for detection of the cancererous tissue. Two different approaches are currently being pursued for microwave imaging of the breast. In one, ultrawideband radar techniques are applied [15]–[23], while in the other, nonlinear inverse scattering techniques, also known as microwave tomography, are used [11], [12], [24], [25].

The inverse scattering techniques seek to determine the distribution of the electromagnetic constitutive parameters, permittivity and conductivity, in the breast. When using this approach, the breast domain is illuminated by one antenna at a time and the response is measured on a number of receiving antennas. These responses may then be used as input to the nonlinear inversion algorithm based on Maxwell's equations. Results for frequency- and time-domain inverse scattering have been reported, both for phantom measurements [25]–[29] and for clinical breast imaging [11], [12], [30] but also for other applications of biomedical imaging [31], [32].

At the Technical University of Denmark (TUD) a microwave imaging system for breast-cancer screening is currently being developed. To reconstruct images of the interior of the breast, frequency-domain nonlinear inverse scattering is applied. The design of the TUD imaging system is inspired by the imaging system currently being used in clinical tests at Dartmouth College. In this system, the breast is imaged using a 2-D measurement setup and reconstructions of the corresponding imaging planes through the breast [11], [28], [30], [33]–[40]. The TUD imaging system, on the other hand, is designed to operate directly on the full 3-D inversion problem, thereby avoiding the inherent errors stemming from applying 2-D algorithms to what is indeed a 3-D problem [41]. The choice of reconstructing the images by solving a full 3-D inverse problem does, however, increase the computational complexity of the problem.

The imaging algorithm is based on a Newton iterative algorithm in which the distribution of the constitutive parameters is updated in each iteration based on a comparison between the measured signals and the signals computed by a forward solver for the current parameter distribution. Since a full 3-D scattering problem must be solved in each iteration of the Newton algorithm, special

attention on the computational efficiency of the forward solver is necessary. To this end, a method of moments code, in which the coefficient matrix is reused in each iteration, has been implemented.

During the development of the imaging algorithm it has been found that the widely used complex formulation of the scattering problem, in which complex phasors are used to represent the measured and calculated scattered field, provides suboptimal results. To remedy this, the log-amplitude unwrapped phase, or simply log-phase, formulation, first introduced for 2-D microwave imaging in [42], has been adapted to the three-dimensional imaging algorithm. Although this formulation is just a coordinate transformation, it significantly improves the performance of the reconstruction algorithm.

In this paper, the design of the TUD imaging system is described and the performace of the system is tested on simulated data. This paper is organized as follows: In Section II, the imaging system is presented and in Section III, the Newton-based imaging algorithm, which may be used with both the complex formulation and the log-phase formulation, is presented. This also includes a presentation of the forward solver as well as the log-phase formulation. Finally, in Section IV, the performance of the system is tested on a simulation of a hemispherical breast model.

II. Imaging System

During examination with the TUD microwave imaging system, the patient is to lie prone atop a measurement tank with her breast suspended through an aperture in the top of the tank. The tank is filled with a glycerin-water coupling liquid to maximize the amount of energy coupled to the interior of the breast. The importance of using such coupling liquid has previously been described by other authors [38], [43]. The system is designed for operation in the frequency domain at a single frequency in the range from 300 MHz to 3.5 GHz and uses $n_{\text{ant}} = 32$ antennas positioned in a cylindrical setup with radius 8 cm. The microwave network of the system is currently under construction but measurements with the prototype indicate that the system will be capable of correctly reconstructing the amplitude and phase of measured signals at levels more than 120 dB below that of the transmitted signal.

The breast is assumed to be fully contained in a hemispherical imaging domain with a radius of 7.5 cm. A schematic of the imaging system is shown in Fig. 1, with the imaging domain indicated by the green hemisphere. Although only a single frequency is used for creating the images, the large frequency range allows for choosing

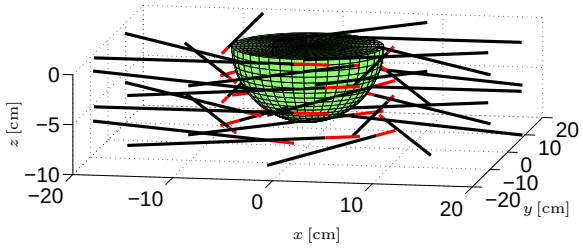

Fig. 1. Schematic of the imaging system. The imaging domain with a radius of 7.5 cm is indicated by the green hemisphere and the antennas are given by the black and red lines. The red part of the lines indicate the stripped dielectric and the black indicates the outer conductor.

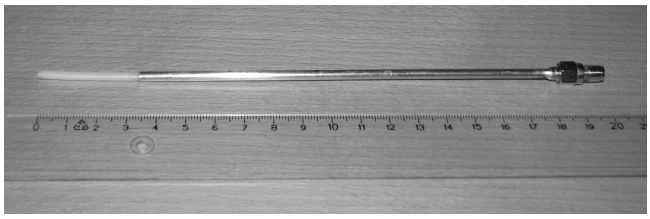

Fig. 2. Photo of one of the antennas of the imaging system. The stripped dielectric has a length of 3.5 cm.

the optimum frequency for imaging and for later implementation of multiple-frequency techniques [44], [45], if needed.

The antennas used in the system, one of which is depicted in the photo in Fig. 2, are of a simple monopole type [30]. The antenna consists of a coaxial cable from which the outer conductor has been stripped from the outermost 3.5 cm of the antenna, exposing the dielectric. This type of antenna has the advantage of being very simple to manufacture and to include in numerical models. Since the glycerin-water coupling liquid is lossy, the current on the outside of the outer conductor is quickly attenuated and thus, there is no need for a ground plane. Furthermore, when operating in the lossy liquid, the antennas are relatively broadband, allowing for operation in the entire frequency band used by the system. In Fig. 1, the stripped dielectric is represented by the red lines while the outer conductor is represented by the black lines. The 32 antennas are positioned in 4 rows with 8 antennas in each row, with $45°$ between the antennas and each row rotated $22.5°$ with respect to the rows above and below. The top row of antennas is positioned at $z = -0.5$ cm and the bottom at $z = -7.5$ cm with $z = 0$ cm being the surface of the liquid. As seen in Fig. 1, the antennas are $\hat{\phi}$-directed, i.e., horizontally oriented. This is necessary to be able to position the antennas close to the surface of the liquid, thereby obtaining coverage in the entire imaging domain, including the top part. The importance of this is illustrated in Section IV-B.

The antenna system is positioned in a cylindrical measurement tank which has a radius of 20 cm with each antenna held in place by the coaxial cable. The lossy liquid assures that reflections from the side and bottom of the tank are attenuated so they do not influence the measurements. Therefore, the antenna system may be considered to be positioned in an infinite halfspace filled with the coupling liquid.

To be able to reference the individual antennas they are enumerated with antennas 1 to 8 being located in the top row, organized counter clockwise and with antenna number 1 positioned at $(x, y) = (8 \text{ cm}, 0 \text{ cm})$. Antennas 9 through 16 are in the second row, organized in the same manner with antenna 9 at $(x, y) = (7.4 \text{ cm}, 3.1 \text{ cm})$. The two bottom rows hold antenna 17 through 24 with antenna 17 directly beneath antenna 1, and 25 through 32 with antenna 25 directly beneath antenna 9.

During a measurement, each antenna in turn transmits while the response is measured on the 31 other antennas. This implies that the total measurement consists of $n_{\text{meas}} = 992$ measurements of the real and imaginary parts of the received signals.

III. Imaging Algorithm

To represent the distribution of constitutive parameters in the imaging domain, the domain is divided into cubic cells. The size of these cells is chosen on the basis of the frequency at which the reconstruction is performed and on the expected size of the objects to be imaged. In this paper, the cubic cells are chosen to have a side length of 5 mm, yielding a total of $n_{\text{cells}} = 7164$ cubic cells in the imaging domain. In each of these cells the constitutive parameters are assumed to be constant and represented by the squared complex wave number of the cell which, when using the time notation $\mathrm{e}^{j\omega t}$, is given by

$$k^2(\boldsymbol{r}) = \omega^2 \mu_0 \epsilon(\boldsymbol{r}) - j\omega\mu_0\sigma(\boldsymbol{r}). \tag{1}$$

In this expression, $\boldsymbol{r}$ is a position vector, ω is the angular frequency, μ_0 is the free-space permeability, ϵ is the permittivity, and σ is the conductivity. Since the constitutive parameters are assumed to be constant within each cell, it holds that

$$k^2(\boldsymbol{r}) = k_l^2 \tag{2a}$$

for

$$\boldsymbol{r} \in \boldsymbol{R_l} \tag{2b}$$

where $\boldsymbol{R_l}$ is the volume covered by cell number $l = 1, 2, 3, \ldots, n_{\text{cells}}$.

The distribution of the squared complex wave numbers is determined by solving the nonlinear minimization problem

$$\begin{aligned} \underline{k}^2 &= \operatorname{argmin}\left\{ \left\| \underline{S}^{\text{meas}} - \underline{S}^{\text{calc}}(\underline{k}^2) \right\|_2^2 \right\} \\ &= \operatorname{argmin}\left\{ \left\| \underline{S}^{\text{res}}(\underline{k}^2) \right\|_2^2 \right\} \end{aligned}$$
subj. to regularization (3)

using an iterative Newton algorithm. In this expression, the $2n_{\text{cells}}$ element vector $\underline{k}^2$ holds the real and imaginary parts of the squared complex wavenumbers, the vector $\underline{S}^{\text{meas}}$ holds the measured signals, while the vector $\underline{S}^{\text{calc}}(\underline{k}^2)$ holds the calculated signals for a given distribution of the squared wave numbers. The vector $\underline{S}^{\text{res}}$ is the residual vector. The nonlinear problem is solved by applying an iterative Newton algorithm, which is initialized with the squared wave numbers in the entire imaging domain set to that of the known coupling liquid, $\underline{k}_0$. In each iteration of the Newton algorithm, the distribution of the squared wave numbers is updated using three steps:

1) Compute $\underline{S}^{\text{calc}}(\underline{k}_n^2)$ and the Jacobian $\underline{\underline{J}}_n$ for the current distribution of squared complex wave numbers.
2) Linearize the problem around the current distribution of constitutive parameters and determine the updates $\underline{\Delta k}_n^2$ by solving the linear minimization problem

$$\underline{\Delta k}_n^2 = \operatorname{argmin}\left\| \underline{\underline{J}}_n \underline{\Delta k}_n^2 - \underline{S}_n^{\text{res}} \right\|_2^2$$
subj. to regularization. (4)

   This problem is ill-posed and underdetermined with a $2n_{\text{meas}}$-by-$2n_{\text{cells}}$ element Jacobian matrix.
3) Update the distribution of the squared wave numbers using

$$\underline{k}_{n+1}^2 = \underline{k}_n^2 + \alpha_n \underline{\Delta k}_n^2 \tag{5}$$

   wherein α_n is the Newton step [46].

Each of the three steps are described in more details below.

A. Log-Phase Formulation

The complex and log-phase formulations differ in how the data is represented in the vectors $\underline{S}^{\text{meas}}$ and $\underline{S}^{\text{calc}}(\underline{k}^2)$. In the complex formulation, each combination of transmitting antenna t and receiving antenna r yields two elements in each vector, resulting in a total of $2n_{\text{meas}}$ elements. In $\underline{S}^{\text{meas}}$, the elements are given by the difference between the measured signals with the object

to be examined inserted in the imaging system and the measured signals when the system is empty, i.e.,

$$S_{\Re}^{t,r} = \mathrm{Re}\left\{S_{\mathrm{obj}}^{t,r} - S_{\mathrm{empty}}^{t,r}\right\} \tag{6a}$$

and

$$S_{\Im}^{t,r} = \mathrm{Im}\left\{S_{\mathrm{obj}}^{t,r} - S_{\mathrm{empty}}^{t,r}\right\}. \tag{6b}$$

In $\underline{S}^{\mathrm{calc}}$, the elements are given in the same way, except here the signals are calculated using the forward solver and not measured. In this way, the Jacobian matrix used when solving the problem in its complex formulation has a size of $2n_{\mathrm{meas}} \times 2n_{\mathrm{cells}}$ and consists of the derivative of the real and imaginary parts of the calculated fields with respect to the real and imaginary parts of the squared complex wave numbers.

In the log-phase formulation, each measurement is also represented by two elements in the vectors $\underline{S}^{\mathrm{meas}}$ and $\underline{S}^{\mathrm{calc}}(\underline{k}^2)$, both based on the logarithm of the complex signals. By taking the logarithm of the measured or calculated signals, a complex number is obtained

$$\log S^{t,r} = \log|S^{t,r}| + j\angle S^{t,r}, \tag{7}$$

wherein $\angle S^{t,r}$ is the unwrapped phase of the signal. The $2n_{\mathrm{meas}}$ elements of the vectors S^{calc} and S^{meas} may now be determined as

$$S_{\mathrm{l}}^{t,r} = \log|S_{\mathrm{obj}}^{t,r}| - \log|S_{\mathrm{empty}}^{t,r}| \tag{8a}$$

and

$$S_{\angle}^{t,r} = \angle|S_{\mathrm{obj}}^{t,r}| - \angle|S_{\mathrm{empty}}^{t,r}|. \tag{8b}$$

The different performances of the reconstruction algorithm when the two formulations are applied can be explained by observing their two major differences. First, the complex formulation deals with absolute changes in the signal level whereas the log-phase formulation deals with relative changes. This implies that, when using the complex formulation, a given change in the signal level is given the same weight in the reconstruction whether the level of the background signal $S_{\mathrm{empty}}^{t,r}$ is large or small. When using the log-phase formulation, on the other hand, a given change in the signal level is given more weight if the background signal level is low (and the change relatively large) than if the background signal is large (and the change relatively small). The signals in which the scattered field has the largest influence, that is, the signals where the relative change is large, also hold more information about the scattering object [47]. Hence, the log-phase formulation improves the performance of the algorithm by weighting the measurements with a high information level more than those with a low information level.

The other major difference between the two formulations is the way in which they handle phase changes. Since the unwrapped phase is used in the log-phase formulation, it is capable of reconstructing images even when the phase in the measured signals changes more than $\pm\pi$, i.e., by using multiple Riemann sheets in the reconstruction. In the complex formulation, on the other hand, the phase information is not retained and all signals will therefore be mapped onto the same Riemann sheet. This implies that if a phase change of more than $\pm\pi$ is encountered, the algorithm will either not reach convergence or reach an erroneous solution since the solution is constrained to a single Riemann sheet.

In terms of computational demands, the two formulations are very similar. The log-phase formulation requires that the Jacobian is expressed in terms of the derivatives of the logarithm of the amplitude and phase with respect to the squared complex wave numbers. This can be done using the chain rule, yielding

$$\frac{\mathrm{d}(\log|S|)}{\mathrm{d}(k^2)} = \frac{1}{|S|^2}\mathrm{Re}\left\{S^*\frac{\mathrm{d}S}{\mathrm{d}(k^2)}\right\} \tag{9a}$$

and

$$\frac{\mathrm{d}(\angle S)}{\mathrm{d}(k^2)} = \frac{1}{|S|^2}\mathrm{Im}\left\{S^*\frac{\mathrm{d}S}{\mathrm{d}(k^2)}\right\} \tag{9b}$$

wherein S^* denotes the complex conjugate of S and $\frac{\mathrm{d}S}{\mathrm{d}(k^2)}$ is found using (23) below.

B. Phase Unwrapping

The phase unwrapping is the most challenging part of using the log-phase formulation. Two different methods are applied when unwrapping the phase: Unwrapping in space and unwrapping in contrast. When the phase is unwrapped in space, it is assumed that the difference in phase of the signals measured by adjacent antennas is no more than $\pm\pi$. An example of the results of spatial unwrapping is seen in Fig. 3. The data in this plot is taken from the simulation of the heterogeneously dense breast described in Section IV-A. The wrapped phase is given by the dashed line while the solid line is the unwrapped phase. Antenna 9 is transmitting and the phase change is shown for the signals received by the other 15 antennas in the two top rows of the imaging system. It is seen that the greatest phase change is observed at the antennas on the opposite side of the breast with respect to the transmitting antenna. The spatial unwrapping approach is used for unwrapping the measured signals and can easily be implemented in a preprocessor.

During the image reconstruction, the distribution of squared complex wave numbers is changed in steps,

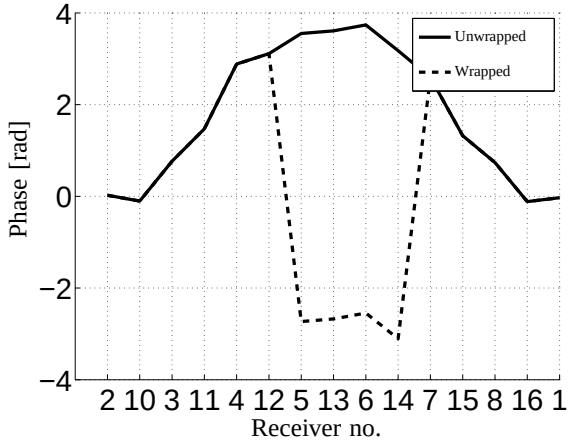

Fig. 3. Phase unwrapping in the spatial domain for antenna 9 transmitting and antennas 1 through 16 receiving. The phase is assumed to change no more than $\pm\pi$ between two adjacent antennas.

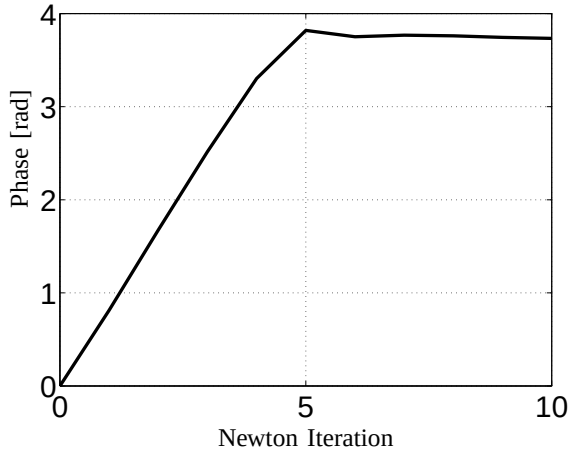

Fig. 4. Phase unwrapping for the breast simulation presented in Section IV-A for antenna 9 transmitting and antenna 6 receiving. The phase changes as the Newton-based reconstruction algorithm progresses and the distribution of the constitutive parameters are updated.

with each iteration of the Newton algorithm changing the distribution of the wave numbers in the imaging domain. This allows for the phase to be unwrapped in contrast in the following manner: Assuming that the phase on any given transmit-receive combination of antennas changes no more than $\pm\pi$ between two successive Newton iteration, the phase of the calculated signals may be unwrapped by comparing the new phase with the phase of the signal in the previous Newton iteration. An example of a phase unwrapping in terms of contrast is shown in Fig. 4, also taken from the simulation of the heterogeneously dense breast in Section IV-A. The phase change of the calculated signal on antenna 6 when antenna 9 is transmitting is shown as function of the Newton iterations and is seen to be unwrapped, reaching a final value of approximately 3.75 radians.

When the phase is unwrapped in terms of the constrast it is important that the phase does not change more than $\pm\pi$ between two Newton iterations, and to this end, the scaling of the calculated update with the Newton step, described below, plays an important role.

C. Forward Solver

To calculate the forward solution $\underline{S}^{\mathrm{calc}}$, Maxwell's equations are formulated as volume integral equations (VIE) and solved using a method of moments (MoM) code. Solving the forward scattering problem using the integral equation technique and MoM consists of two time consuming tasks; filling the MoM matrix and solving the resulting matrix equation.

The electric field volume integral equation for dielectric objects occupying a volume V enclosed by a surface S reads

$$\boldsymbol{E}^i(\boldsymbol{r}) = \frac{\boldsymbol{D}(\boldsymbol{r})}{\epsilon'(\boldsymbol{r})} + j\omega\boldsymbol{A}(\boldsymbol{r}) + \nabla\Phi, \tag{10a}$$

$$\boldsymbol{A}(\boldsymbol{r}) = j\omega\mu_0 \int_V G(\boldsymbol{r},\boldsymbol{r}')K(\boldsymbol{r}')\boldsymbol{D}(\boldsymbol{r}')dV', \tag{10b}$$

$$\Phi(\boldsymbol{r}) = -\frac{1}{\epsilon'_b}\int_V G(\boldsymbol{r},\boldsymbol{r}')\big[\nabla'\cdot K(\boldsymbol{r}')\boldsymbol{D}(\boldsymbol{r}')\big]dV' + \frac{1}{\epsilon'_b}\int_S G(\boldsymbol{r},\boldsymbol{r}')K(\boldsymbol{r}')\big[\boldsymbol{D}(\boldsymbol{r}')\cdot\boldsymbol{dS}'\big], \tag{10c}$$

where $\boldsymbol{E}^i(\boldsymbol{r})$ is the known incident electric field, $\boldsymbol{D}(\boldsymbol{r})$ is the electric flux density, $G(\boldsymbol{r},\boldsymbol{r}')$ is the scalar free space Green's function, ϵ'_b is the complex permittivity of the background medium, and $K(\boldsymbol{r}) = 1 - \epsilon'_b/\epsilon'(\boldsymbol{r})$. The complex permittivity ϵ' may be expressed in terms of the real permittivity ϵ, the conductivity σ, and the angular frequency ω as

$$\epsilon' = \epsilon - j\frac{\sigma}{\omega}. \tag{11}$$

Preliminary studies have shown that the antennas may be modeled as Hertzian dipoles in the imaging algorithm. The incident field $\boldsymbol{E}^i(\boldsymbol{r})$ is thus easily determined.

In each of the cubic cells of the imaging domain, the unknown electric flux density $\boldsymbol{D}(\boldsymbol{r})$ is approximated by the higher-order hierarchical Legendre basis functions $\boldsymbol{f}_n(\boldsymbol{r})$ as shown in [48]. Following the standard Galerkin's procedure and using the fact that the complex permittivity is assumed constant throughout each cell (2),

$$\epsilon'(\boldsymbol{r}) = \epsilon'_l \quad \text{for} \quad \boldsymbol{r} \in \boldsymbol{R_l}, \tag{12}$$

the following matrix equation is obtained for the unknown dielectric flux density

$$\underline{\underline{Z}}\,\underline{D} = \underline{E}^i \tag{13}$$

with $\underline{\underline{Z}}$ being the MoM matrix, $\underline{E}^i$ representing the known incident field, and the unknown flux density being represented by the vector $\underline{D}$. Each of the elements z_{mn} of the matrix $\underline{\underline{Z}}$ is given by

$$\begin{aligned} z_{mn} = &\frac{1}{\epsilon_l'}\Big\langle \boldsymbol{f}_m(\boldsymbol{r}), \boldsymbol{f}_n(\boldsymbol{r})\Big\rangle \\ &-K_l\Bigg\{\omega^2\mu_0\Big\langle \boldsymbol{f}_m(\boldsymbol{r}), \\ &\int\limits_{V_l} G(\boldsymbol{r},\boldsymbol{r}')\boldsymbol{f}_n(\boldsymbol{r}')dV'\Big\rangle \\ &+\frac{1}{\epsilon_b'}\Big\langle \boldsymbol{f}_m(\boldsymbol{r}), \\ &\nabla\Big[\int\limits_{V_l} G(\boldsymbol{r},\boldsymbol{r}')\nabla'\cdot\boldsymbol{f}_n(\boldsymbol{r}')dV' \\ &-\int\limits_{S_l} G(\boldsymbol{r},\boldsymbol{r}')\boldsymbol{f}_n(\boldsymbol{r}')\cdot\boldsymbol{dS}'\Big]\Big\rangle\Bigg\} \\ =&\frac{1}{\epsilon_l'}z_{mn}' + K_l z_{mn}'', \end{aligned} \tag{14}$$

where $<\cdot,\cdot>$ denotes the inner product. The surface integral in (14) is taken just inside the surface of the cell l. It is seen that both z_{mn}' and z_{mn}'' are independent of the constitutive parameters of the cells. The expression (14) is valid only for the higher-order subset of the higher-order hierarchical Legendre basis functions, namely those that are defined within one cell. For the basis functions that span two neighbor cells, e.g. rooftop, so that $\boldsymbol{f}_n(\boldsymbol{r}) = \boldsymbol{f}_n^-(\boldsymbol{r}) + \boldsymbol{f}_n^+(\boldsymbol{r})$, the expression (14) can be modified [49] as

$$\begin{aligned} z_{mn} =&\frac{1}{\epsilon_l'^-}\Big\langle \boldsymbol{f}_m(\boldsymbol{r}), \boldsymbol{f}_n^-(\boldsymbol{r})\Big\rangle \\ &+\frac{1}{\epsilon_l'^+}\Big\langle \boldsymbol{f}_m(\boldsymbol{r}), \boldsymbol{f}_n^+(\boldsymbol{r})\Big\rangle \\ &+K_l^- z_{mn}''^- + K_l^+ z_{mn}''^+ \\ =&\frac{1}{\epsilon_l'^-}z_{mn}'^- + \frac{1}{\epsilon_l'^+}z_{mn}'^+ \\ &+K_l^- z_{mn}''^- + K_l^+ z_{mn}''^+. \end{aligned} \tag{15}$$

As in (14), the quantities $z_{mn}'^{\pm}$ and $z_{mn}''^{\pm}$ do not contain the constitutive parameters of the cell. Thus, the matrices $\underline{\underline{Z}}'^{\pm}$ need only to be computed once for a given combination of antennas and background (coupling liquid) and stored. After this, they can be used in subsequent calls to the forward solver. The first two terms in (15) can be computed on the fly, since no time-consuming Green's function calculations are involved.

To reduce the memory consumption, the adaptive integral method (AIM) can be applied. AIM is based on separation of the MoM matrix elements responsible for near- and far-field interactions as

$$\underline{\underline{Z}} = (\underline{\underline{Z}} - \underline{\underline{Z}}^{\text{far}}) + \underline{\underline{Z}}^{\text{far}} \simeq \underline{\underline{Z}}^{\text{near}} + \underline{\underline{Z}}^{\text{far}}. \tag{16}$$

The matrix $\underline{\underline{Z}}^{\text{near}}$ is sparse due to proximity filtering and thresholding [50]. Its elements are computed explicitly using the decomposition described above. The elements of the matrix $\underline{\underline{Z}}^{\text{far}}$ are calculated implicitly in the matrix-vector product $\underline{\underline{Z}}^{\text{far}}\underline{X}$, where $\underline{X}$ is the solution vector in each iteration of the iterative solution of the MoM matrix equation. To speed up the matrix-vector multiplication the components $f_{n\alpha} \in \{f_{nx}, f_{ny}, f_{nz}, \nabla\cdot\boldsymbol{f}_n\}$ of the basis functions $\boldsymbol{f}_n(\boldsymbol{r})$ are expanded in terms of Dirac delta functions defined at nodes of a regular Cartesian grid enclosing the imaging domain

$$f_{n\alpha}(\boldsymbol{r}) \simeq \sum_{\boldsymbol{u}\in C_n} \Lambda_{n\alpha\boldsymbol{u}}\delta(\boldsymbol{r}-\boldsymbol{u}), \tag{17}$$

where C_n denotes a cube of $(L+1)^3$ nodes. The coefficients $\Lambda_{n\alpha\boldsymbol{u}}$ are chosen so that the expansion reproduces the far field radiated by $f_{n\alpha}$. Then, the elements of the matrix $\underline{\underline{Z}}^{\text{far}}$ can be computed via

$$z_{mn}^{\text{far}} = \sum_{\alpha}\sum_{\boldsymbol{v}\in C_m}\sum_{\boldsymbol{u}\in C_n} \Lambda_{m\alpha\boldsymbol{v}}^L G(\boldsymbol{v}-\boldsymbol{u})\Lambda_{n\alpha\boldsymbol{u}}^R, \tag{18}$$

and the matrix-vector product $\underline{\underline{Z}}^{\text{far}}\underline{X}$ can be efficiently calculated using FFT's as

$$\underline{\underline{Z}}^{\text{far}}\underline{X} = \sum_{\alpha} \underline{\underline{\Lambda}}_{\alpha}^L \mathcal{F}^{-1}\underline{\underline{\tilde{G}}}\mathcal{F}\underline{\underline{\Lambda}}_{\alpha}^R\underline{X}, \tag{19}$$

where $\mathcal{F}$ denotes the FFT operation and $\underline{\underline{\tilde{G}}} = \mathcal{F}\underline{\underline{G}}$.

In the standard implementation of AIM for VIE [51], [52] the coefficient matrices $\underline{\underline{\Lambda}}_{\alpha}^L$ and $\underline{\underline{\Lambda}}_{\alpha}^R$ in (19) are not the transpose of each other due to the presence of the quantity K_l, which is included in the computation of $\underline{\underline{\Lambda}}_{\alpha}^R$ to bring the expression (14) to the symmetric form of (18). To make $\underline{\underline{\Lambda}}_{\alpha}^R$ independent of the material parameters, represented by K_l, the procedure described above is applied once more. In analogy with (15) the expansion (17) is rewritten as

$$\begin{aligned} f_{n\alpha}(\boldsymbol{r}) \simeq &\sum_{\boldsymbol{u}\in C_n^+} \Lambda_{n\alpha\boldsymbol{u}}^+\delta(\boldsymbol{r}-\boldsymbol{u}) \\ &+\sum_{\boldsymbol{u}\in C_n^-} \Lambda_{n\alpha\boldsymbol{u}}^-\delta(\boldsymbol{r}-\boldsymbol{u}), \end{aligned} \tag{20}$$

so that each part of a roof top function is expanded separately. Using this, (18) can be rewritten as

$$\begin{aligned} z_{mn}^{\text{far}} = & K_l^- \sum_{\alpha} \sum_{\boldsymbol{v}\in(C_m^-+C_m^+)} \sum_{\boldsymbol{u}\in C_n^-} \big[\Lambda_{m\alpha\boldsymbol{v}} \\ & \cdot G(\boldsymbol{v}-\boldsymbol{u})\Lambda^-_{n\alpha\boldsymbol{u}}\big] \\ & + K_l^+ \sum_{\alpha} \sum_{\boldsymbol{v}\in(C_m^-+C_m^+)} \sum_{\boldsymbol{u}\in C_n^+} \big[\Lambda_{m\alpha\boldsymbol{v}} \\ & \cdot G(\boldsymbol{v}-\boldsymbol{u})\Lambda^+_{n\alpha\boldsymbol{u}}\big]. \end{aligned} \tag{21}$$

Noting that $\underline{\underline{\Lambda}}_\alpha = \underline{\underline{\Lambda}}_\alpha^- + \underline{\underline{\Lambda}}_\alpha^+$,

$$\begin{aligned} \underline{\underline{Z}}^{\text{far}}\underline{X} = & \sum_\alpha \underline{\underline{\Lambda}}_\alpha \mathcal{F}^{-1}\underline{\underline{\tilde{G}}}\mathcal{F}\big\{\underline{\underline{\Lambda}}_\alpha^{-T}[\underline{\underline{K}}^-]\underline{X} \\ & + \underline{\underline{\Lambda}}_\alpha^{+T}[\underline{\underline{K}}^+]\underline{X}\big\}, \end{aligned} \tag{22}$$

where $\underline{\underline{K}}^\pm$ are diagonal square matrices composed of the corresponding $K_l^\pm$ values. The coefficient matrices $\underline{\underline{\Lambda}}_\alpha^\pm$ are now independent of the material parameters of the scattering object. Hence, they may be calculated once and reused in later calls to the forward solver.

Using the approach described above, the forward solver may be divided into an initialization algorithm, which needs to be called only once for a given coupling liquid, and a solution algorithm which is invoked in all subsequent calls. In the initialization algorithm, the Cartesian grid enclosing the imaging domain is specified and the coefficients $\Lambda_\alpha^\pm$ computed, allowing for computation of the sparse matrices $\underline{\underline{Z}}''^\pm$. These matrices, together with $\Lambda_\alpha^\pm$, are then stored for later use. In the subsequent calls to the solution algorithm, the matrix $\underline{\underline{Z}}^{\text{near}}$ is constructed using the stored matrices $\underline{\underline{Z}}''^\pm$ and the given distribution of consitutive parameters. The MoM matrix equation is then solved using an iterative solver with the product $\underline{\underline{Z}}^{\text{far}}\underline{X}$ calculated from the Fourier transform in (19).

The most time consuming part of the solution is the filling of the matrices in the initialization. In the present parallel implementation on a computer with 2 Intel Xeon 2.66 GHz quad core processors, filling the AIM coefficient matrices takes approximately one hour with the current configuration of the imaging domain but it needs only to be done once. In the subsequent calls to the forward solver, the AIM solution (including the Jacobian) is found in approximately 21 minutes. The solution time in the latter iterations of the Newton-based imaging algorithm is reduced slightly by using the forward solution from the previous inversion iteration as the initial guess of the forward solution. The AIM solver is, however, slower than using a direct (LU) solver on the standard MoM problem. In this case, the forward solution (including the Jacobian) can be found in approximately 13 minutes with the current imaging domain, albeit the filling of the matrix is a much more time consuming task, taking as much as 3 hours. But this operation needs only to be performed once. Thus, the standard procedure is to use the AIM solver when doing investigations requiring changing the antenna positions or the background constitutive parameters while using a direct solver when different objects are imaged with a fixed setup where the matrix can be reused.

When the forward solution has been found, the Jacobian is determined using the adjoint method [53] using the expression

$$\frac{\mathrm{d}S^{t,r}}{\mathrm{d}k_l^2} = \frac{\langle \boldsymbol{E^t}, \boldsymbol{E^r}\rangle_l}{j\omega\mu_0 I_r} \tag{23}$$

where the inner product is to be taken over the cell l and $\boldsymbol{E^t}$ and $\boldsymbol{E^r}$ are the fields in the cell when the antennas t and r, respectively, are transmitting. The quantity I_r is the dipole moment used when calculating the field $\boldsymbol{E^r}$. The inner product is calculated in an inexpensive matrix operation using the flux density $\boldsymbol{D}$ found when solving the forward problem and the constitutive parameters of the individual cells.

D. Calculation of Updates

To determine the updates, the under-determined and ill-posed problem (4) is solved using the two-step algorithm described in [54]. This algorithm is based on the conjugated gradient least squares (CGLS) algorithm which is an iterative algorithm that solves the linear inversion problem in five simple matrix-vector operations in each CGLS iteration [55, Sec. 6.3]. The solution of the linear inversion problem (4) obtained after m CGLS iterations is given by

$$\left[\underline{\Delta k}_n^2\right]^{(m)} = \operatorname{argmin} \left\| \underline{\underline{J}}\,\underline{\Delta k}_n^2 - \underline{S}^{\text{res}}(\underline{k}_n^2)\right\|_2 \tag{24a}$$

subject to

$$\left[\underline{\Delta k}_n^2\right]^{(m)} \in \mathfrak{K}_m\left\{\underline{\underline{J}}^T\underline{\underline{J}}, \underline{\underline{J}}^T\underline{S}^{\text{res}}(\underline{k}_n^2)\right\}. \tag{24b}$$

Hence, the solution obtained is the least squares solution of the linear inversion problem with the restraint that the solution must lie in the m-dimensional Krylov subspace $\mathfrak{K}_m$ defined by the Jacobian matrix and the residual vector. The regularizing effect of the CGLS algorithm is obtained because the m-dimensional Krylov subspace can be seen as an approximation of the subspace spanned by the first m right-hand singular vectors. Thus, the solution obtained using the CGLS algorithm can be regarded an approximation of the solution obtained using the truncated singular value decomposition with the important difference that it is not necessary to perform

a time consuming singular value decomposition of the problem [55]. As the number of iterations with the CGLS algorithm increases, the amount of regularization applied to the problem decreases.

In [54], the algorithm was applied for 2-D microwave imaging but it has been found that the two-step approach is also valid when the algorithm is used for 3-D imaging: In the first few Newton iterations, the number of CGLS iterations used to calculate the updates is kept low. After a number of Newton iterations, the change in the norm of the residual vector between successive Newton iterations will become small. This indicates that the reconstruction algorithm has reconstructed the major features of the image and the number of CGLS iterations used to calculate the updates is now increased to allow the algorithm to reconstruct the finer details of the image.

In the three-dimensional reconstruction algorithm, it has been found that using 2 CGLS iterations in the first part of the reconstruction and 8 in the latter part yields the optimum results. As it was shown in [54], the change between the low and high number of CGLS iterations is most effectively chosen based on the relative change in the normalized norm of the residual vector. The normalized norm η_n is introduced as

$$\eta_n = \frac{\left\|\underline{S}^{\mathrm{res}}(\underline{k}_n^2)\right\|_2}{\left\|\underline{S}^{\mathrm{res}}(\underline{k}_0^2)\right\|_2} \tag{25}$$

wherein $\underline{S}^{\mathrm{res}}(\underline{k}_0^2)$ is the residual vector for the system simulated with no object inserted. The change between successive Newton iterations, $\Delta\eta_n$, may now be introduced as

$$\Delta\eta_n = \frac{\eta_n - \eta_{n-1}}{\eta_{n-1}}. \tag{26}$$

As the reconstruction algorithm progresses, the norm of the residual vector decreases, implying a negative value of $\Delta\eta_n$. When the value of $\Delta\eta_n$ obtains a value greater than -0.1, the number of CGLS iterations used to calculate the updates is changed from 2 to 8.

The values of η_n and $\Delta\eta_n$ are also used to determine when to terminate the algorithm: When η_n drops below 0.02 or if $\Delta\eta_n$ becomes greater than -0.03 after the change from 2 to 8 CGLS iterations has been made, the algorithm is terminated. These threshold values are dependent on the noise level in the system and the accuracy of the forward model: If the noise level is decreased or the accuracy of the forward model improved, these value may be set closer to 0, and vice versa.

E. Newton Step

The scaling of the update $\underline{\Delta k}_n^2$ with the Newton step α_n in (5) serves two purposes. First, it serves to assure that the algorithm does not overshoot the actual solution and starts to diverge. Second, the Newton step is used to assure that the phases of the calculated signals between two successive Newton iterations do not change too much, thereby ruining the possibility of unwrapping the phase in contrast.

It has been found that the best way to determine the size of the Newton step is by assuming a linearized phase change and calculating the maximum phase change caused by the update $\underline{\Delta k}_n^2$. To estimate the maximum phase change caused by the update vector, a new $n_{\mathrm{meas}} \times 2n_{\mathrm{cells}}$ element matrix $\underline{\underline{J}}_n^{\angle}$ is created from the Jacobian by retaining only those rows that relate to the phase of the calculated signals. The assumed maximum phase change is then determined by multiplying $\underline{\underline{J}}_n^{\angle}$ with the update vector and finding the maximum absolute value in the resulting vector

$$\angle_{\max} = \max\left\{\left|\underline{\underline{J}}_n^{\angle}\underline{\Delta k}_n^2\right|\right\}. \tag{27}$$

If $\angle_{\max}$ exceeds a given value, e.g. 1 (radian), the Newton step is applied to assure that the phase change is kept at an acceptable level while a value of $\angle_{\max}$ less than the threshold results in a unity Newton step, i.e.,

$$\alpha_n = \begin{cases} 1 & \text{for} \quad \angle_{\max} \le 1 \\ \frac{1}{\angle_{\max}} & \text{for} \quad \angle_{\max} > 1 \end{cases}. \tag{28}$$

When the complex formulation is used in the imaging algorithm, the change in phase between two successive Newton iterations is no longer important. In this case, the main purpose of scaling the update by the Newton step is to avoid the reconstruction algorithm getting stuck in a local minimum or that an oscillating, diverging solution is obtained. This implies that the Newton step may be determined by simply observing the ratio between the norm of the update vector $\underline{\Delta k}_n^2$ and the norm of the parameter vector $\underline{k}_n^2$. If this ratio exceeds 0.5 the Newton step is used to scale the update, otherwise the Newton step is kept at unity

$$\alpha_n = \begin{cases} 1 & \text{for} \quad \frac{\|\underline{\Delta k}_n^2\|_2}{\|\underline{k}_n^2\|_2} \le 0.5 \\ \frac{\|\underline{k}_n^2\|_2}{2\|\underline{\Delta k}_n^2\|_2} & \text{for} \quad \frac{\|\underline{\Delta k}_n^2\|_2}{\|\underline{\Delta k}_n^2\|_2} > 0.5 \end{cases}. \tag{29}$$

The importance of using the Newton step is reduced by the fact that an over-regularized solution to the linear update problem (4) is found because only 2 iterations are used in the CGLS algorithm. This reduces the chances of the reconstruction algorithm getting stuck in a local minimum, as it was shown in [54].

IV. Imaging Results

Since the microwave circuitry of the system is under construction, the performance of the system will be

tested using simulated data. The difference between using the log-phase and the complex formulation of the scattering problem is demonstrated using a simulation of a hemispherical breast model. In this simulation, the breast was modeled as a heterogeneously dense breast with a tumor of radius 1 cm and a fibroglandular inclusion of radius 2 cm positioned inside. The breast was centered in the imaging system and the tumor and fibroglandular inclusion were centered at $(x, y, z) = (3\text{ cm}, 0\text{ cm}, -1\text{ cm})$ and $(x, y, z) = (-2\text{ cm}, 0\text{ cm}, -3\text{ cm})$, respectively. The simulation was done at 1.3 GHz, using the constitutive parameters for the average breast and fibroglandular tissue given in [11]. The breast was modeled with a mean value of the relative permittivity of 12.5 and a mean conductivity of 0.35 S/m. The corresponding values for the fibroglandular are 21.0 and 0.6 S/m. The constitutive parameters of both the breast tissue and the fibroglandular tissue were assigned using a normal distribution with a standard deviation of 10% of the mean values to represent the natural variations in the tissue. The tumor was modeled with a relative permittivity of 56.0 and a conductivity of 3.0 S/m. The coupling liquid was assigned a relative permittivity of 19.6 and a conductivity of 1.2, corresponding to a 85-15 glycerin-water mixture. The setup of the simulation is shown in Fig. 5 and Gaussian noise mimicking the noise floor of the system 120 dB below the transmitted signal level has been added to the simulated data.

To avoid the ”inverse crime”, the simulations have been performed with a forward model using a different mesh than the one used in the reconstructions. In addition to this, the simulations and reconstructions are all performed using a homogeneous background. The performance of the TUD imaging system has been found to be the same whether a uniform background is used or an interface is inserted at $z = 0$. Since no reliable information about the constitutive parameters of the chest wall has been found in the literature it has been chosen to do the simulations and reconstructions in a homogeneous background with constitutive parameters equal to those of the coupling liquid rather than using a randomly chosen chest wall. In addition to this, it is hard to estimate the impact of the interface in the final system until measurements have been performed. The interface in this case will be a combination of a chest wall behind the breast, air around the breast above the coupling liquid, and the Plexiglas lid of the measurement tank in the regions around the aperture through which the patients breast is protruding.

The antennas are modelled using Hertzian dipoles positioned at the end of the outer conductor, oriented parallel to the inner conductor. Preliminary studies have shown that the Hertzian dipole is a relatively accurate representation of the monopole antenna.

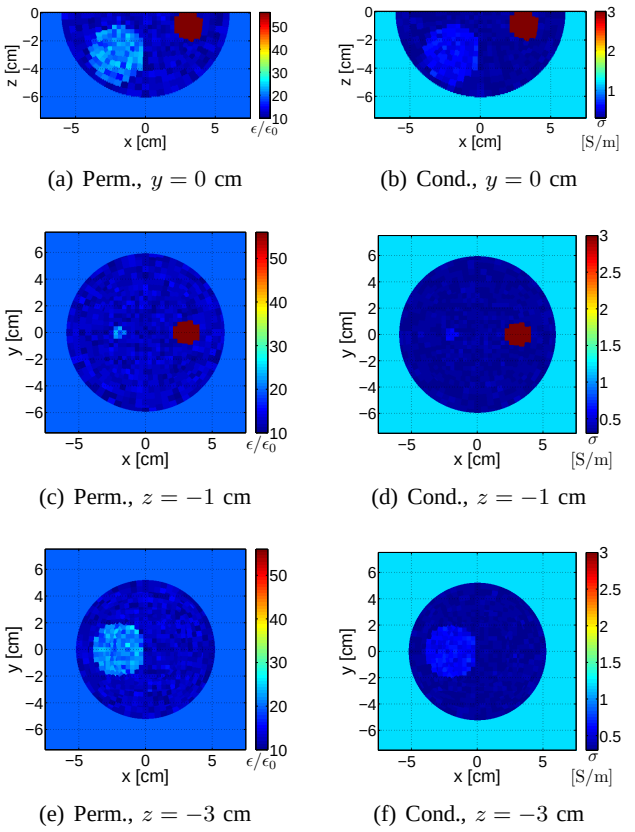

(a) Perm., $y = 0$ cm (b) Cond., $y = 0$ cm

(c) Perm., $z = -1$ cm (d) Cond., $z = -1$ cm

(e) Perm., $z = -3$ cm (f) Cond., $z = -3$ cm

Fig. 5. Distributions of relative permittivity and conductivity used in the simulation of the heterogeneously dense breast. The relative permittivity values of the breast and the fibroglandular inclusion are normally distributed with mean 12.5 and 21, respectively, and a standard deviation of 10% of the means. The conductivities are normally distributed with means 0.35 S/m and 0.6 S/m. The tumor has a relative permittivity of 56 and a conductivity of 3.0 S/m.

A. Log-Phase vs. Complex Formulation

The reconstructed images of the heterogeneously dense breast model obtained using the log-phase formulation are shown in Fig. 6 and the images obtained using the complex formulation are shown in Fig. 7.

When the log-phase formulation is used, the algorithm is seen to reconstruct both the breast, the tumor, and the fibroglandular inclusion. The reconstructed permittivity and conductivity of the tumor are considerably lower than the actual values but the fact that a rise in the conductivity is detected implies that the tumor may be distinguished from the fibroglandular inclusion. The log-phase algorithm changes from 2 to 8 iterations in the

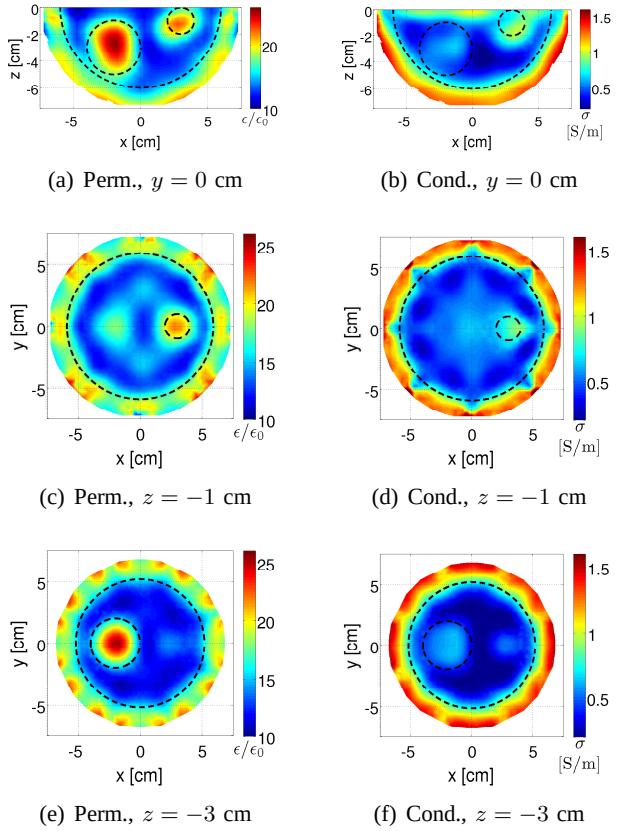

(a) Perm., $y = 0$ cm (b) Cond., $y = 0$ cm

(c) Perm., $z = -1$ cm (d) Cond., $z = -1$ cm

(e) Perm., $z = -3$ cm (f) Cond., $z = -3$ cm

Fig. 6. Images of the simulated heterogeneously dense breast obtained using the log-phase formulation. The dashed lines indicate the contours of the breast, tumor, and fibroglandular inclusion. Both the tumor and the fibroglandular inclusion are visible, although the reconstructed values of the tumor are somewhat lower than the actual values.

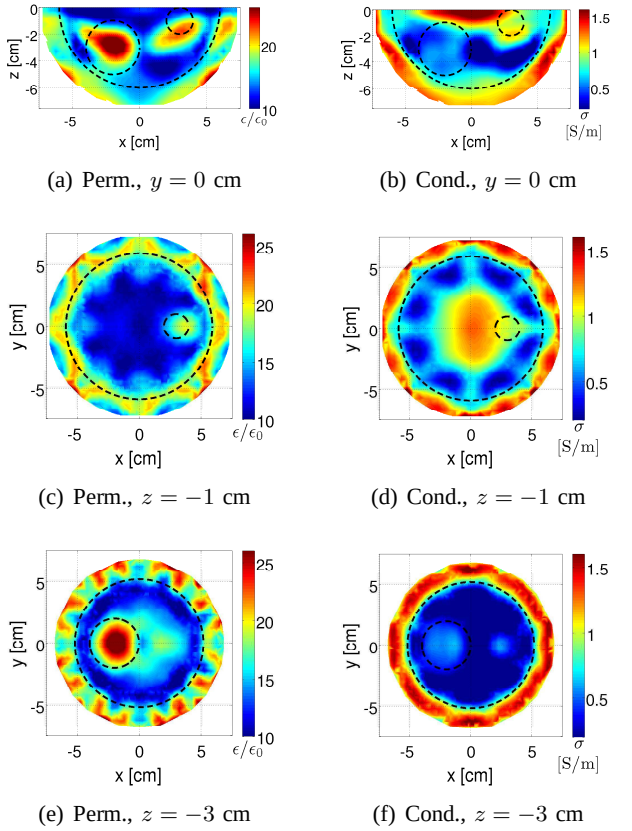

(a) Perm., $y = 0$ cm (b) Cond., $y = 0$ cm

(c) Perm., $z = -1$ cm (d) Cond., $z = -1$ cm

(e) Perm., $z = -3$ cm (f) Cond., $z = -3$ cm

Fig. 7. Images obtained using the complex formulation. The dashed lines indicate the contours of the breast, tumor, and fibroglandular inclusion. Due to the large phase changes of the measured signals, the algorithm fails to accurately recover the position and size of the tumor and fibroglandular inclusion.

CGLS algorithm after 6 Newton iterations and reaches convergence after 10 Newton iterations.

In the images reconstructed using the complex formulation, the tumor and the fibroglandular inclusion are still visible. They are, however, not as well defined as in the log-phase images and, in general, the level of the artifacts is considerably higher. In particular, the reconstruction of the top part of the imaging domain is worse than when using the log-phase formulation. This is in good agreement with the fact that the largest changes in phase are encountered in the measurements with the antennas of the top rows of the system. The use of a single Riemann sheet in the complex formulation will therefore be more evident in this part of the imaging domain.

When using the complex formulation, the algorithm changes from the low to the high number of CGLS iterations in the update algorithm after Newton iteration number 14. The algorithm converges after 19 iterations, and thus uses considerably more time to converge than when the log-phase formulation is applied.

In both sets of images, the most dominant artifacts are positioned close to the antennas. This is due to the fact that the value of the elements of the Jacobian matrix corresponding to these positions are considerably higher than the values corresponding to positions in the center of the imaging domain. Hence, the added noise is more likely to give rise to artifacts close to the antennas.

The simulation setup presented here is chosen to illustrate the performance of the TUD imaging system in what is considered to be a worst-case scenario. First, because of the large difference in constitutive parameters between the coupling liquid and the breast, the scattered field created by this contrast dominates the measurements. In clinical trials a 90:10 glycerin-water coupling liquid with a relative permittivity of approximately 14 and a conductivity of approximately 0.9 S/m will be used to reduce the contrast between the coupling liquid and the expected average value of the breast tissue [11], thereby allowing for more of the microwave energy to

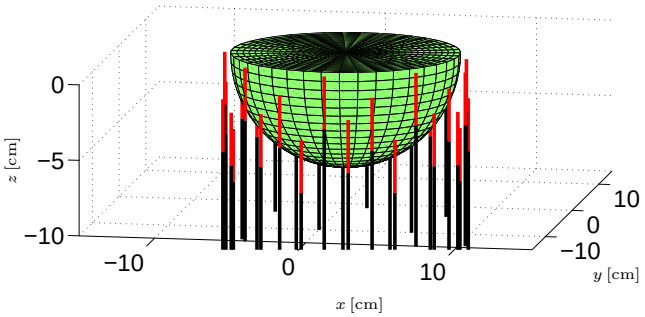

Fig. 8. Schematic of antenna system with vertically oriented antennas. The exposed dielectric of the antennas are represented by the red lines while the outer conductor of the coaxial lines are represented by the black lines.

be coupled to the interior of the breast.

Second, the tumor is positioned close to the top of the imaging domain. This implies that only the measurements involving the top row of antennas have a notable contribution from the tumor while in the vast majority of the measurements, the tumor response is insignificant. The effects of this are further enhanced by the presence of the fibroglandular inclusion in the center of the breast. In most of the measurements, the response from this inclusion is far greater than the tumor response.

Finally, the reconstruction is performed at the rather low frequency 1.3 GHz, because the values in [11] were given at this frequency. By increasing the frequency, a better resolution is obtained and smaller objects may be imaged.

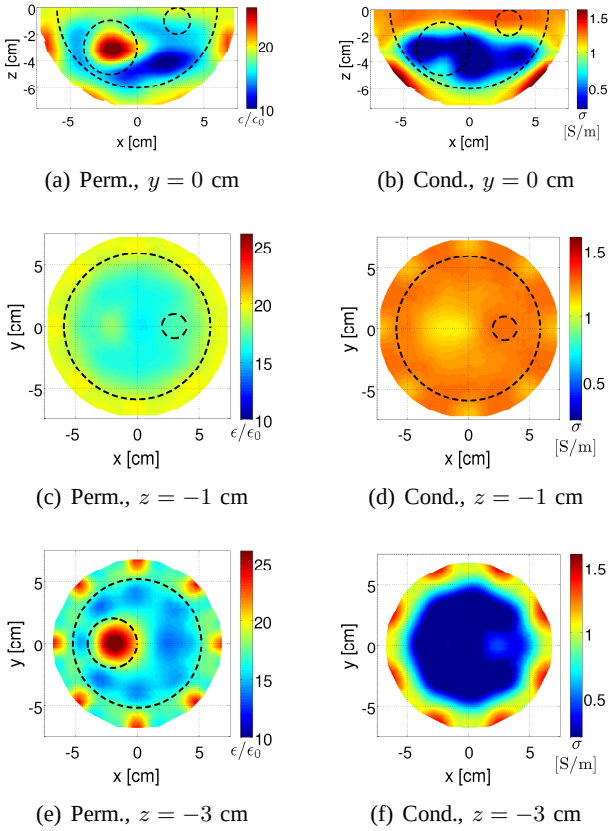

(a) Perm., $y = 0$ cm (b) Cond., $y = 0$ cm

(c) Perm., $z = -1$ cm (d) Cond., $z = -1$ cm

(e) Perm., $z = -3$ cm (f) Cond., $z = -3$ cm

Fig. 9. Images obtained using the vertically oriented antennas and the log-phase formulation. The system is not capable of imaging the top part of the imaging domain, thereby missing the tumor. The dashed lines indicate the positions of the breast, the tumor, and the fibroglandular inclusion.

B. Influence of Antenna Configuration

To illustrate the importance of choosing the right antenna configuration, the performance of an antenna configuration with 4 rows of 8 vertically oriented antennas, shown in Fig. 8, has been tested. The antennas are organized in a cylindrical setup with a radius of 8 cm with the top row of antennas positioned with the tip of the antennas at $z = -1$ mm and the bottom row positioned with the tip of the antennas at $z = -5.5$ cm.

The images obtained when applying this antenna configuration for imaging the heterogeneously dense breast are shown in Fig. 9. The most important thing to notice in these images is how the system is not capable of reconstructing the top part of the imaging domain due to the lack of spatial variation in the z-positions of the antennas covering this region. Both the tumor and the contour of the breast are missing in this part of the images. In the middle and lower parts of the imaging domain, where the coverage is better, the fibroglandular inclusion is detected and the outline of the breast is also reconstructed although some artifacts are present. These images clearly illustrates the importance of organizing the antennas of the imaging system to assure the best possible coverage.

V. Conclusion

The TUD microwave imaging system for breast-cancer screening was presented. The imaging system consists of 32 antennas in a cylindrical setup and is designed to operate at a single frequency in the range from 300 MHz to 3.5 GHz. The large frequency range allows for choosing the optimum frequency at which to do the image reconstruction.

The reconstruction algorithm is based on an iterative Newton scheme in which the measured data is represented using the log-phase formulation. This has been shown to improve the performance of the imaging algorithm with a minimum of additional computation time. The updates in the Newton algorithm are calculated using a CGLS algorithm and the number of CGLS iterations is increased as the algorithm approaches conver-

gence, corresponding to a reduction in the regularization of the solution of the linear update problems. The Newton algorithm requires the calculation of the scattered field in each iteration. To this end, a method of moment (MoM) solver has been implemented in which the time consuming operation of filling the coefficient matrix needs only to be done once after which the matrix may be stored and reused in the following Newton iterations. Furthermore, the MoM code has been augmented using the adaptive integral method which drastically reduces the memory consumption.

To illustrate the performance of the system, a model of a heterogeneously dense breast with a large fibroglandular inclusion and a smaller tumor was used. Images of this simulated data set were reconstructed using both the complex and the log-phase formulation and the images obtained using the log-phase formulation were seen to have less artifacts and more well-defined contours of the individual objects than those images obtained using the complex simulation. Although the tumor in this reconstruction was not reconstructed with the actual values of permittivity and conductivity, the fact that the position and size was determined correct, along with a raised conductivity indicating a tumor, shows that the imaging system is capable of detecting tumors in less-than-ideal imaging conditions.

In addition to a comparison of the log-phase and complex formulations of the imaging problem, the effects of changing the antenna setup were investigated. Here, it was found that it is of great importance to organize the antennas of the imaging system in a suitable way to make sure the entire imaging domain is covered by the antennas.

In this paper, the system has been simulated at the frequency 1.3 GHz since average values for the normal and fibroglandular breast tissue was available for this frequency. The system is, however, capable of working at frequencies up to 3.5 GHz, thereby providing better resolution. At the time of writing, research is being focused on completing the microwave circuitry for the imaging system. When phantom measurements are done, more accurate estimates of the resolution of the system will be available. Furthermore, it will be investigated whether using multiple frequency measurements improves the performance of the system.

VI. Acknowledgments

The work of the authors are supported by the Danish Technical Research Council, Trane's Foundation, the Villum Kann Rasmussen foundation, and the Otto Mønsted Foundation.

The authors thank Dr. Paul M. Meaney of Dartmouth College for many fruitful discussions.

References

[1] American Cancer Society, Inc., *Cancer Facts & Figures 2007*. American Cancer Society, 2007.

[2] Sundhedsstyrelsen, *Cancerregisteret 2001 (foreløbige tal for 2002-2003)*, ser. Nye tal fra Sundhedsstyrelsen. Copenhagen, Denmark: Sundhedsstyrelsen – Danish National Board of Health, 2005.

[3] ——, *Kræftstatistik baseret på landspatientregisteret 2000–2004*, ser. Nye tal fra Sundhedsstyrelsen. Copenhagen, Denmark: Sundhedsstyrelsen – Danish National Board of Health, 2006.

[4] D. M. Parkin, "Global cancer statistics in the year 2000," *Lancet Oncology*, vol. 2, no. 9, pp. 533–543, 2001.

[5] J. S. Michaelson, M. Silverstein, J. Wyatt, G. Weber, R. Moore, E. Halpern, D. B. Kopans, and K. Hughes, "Predicting the survival of patients with breast carcinoma using tumor size," *Cancer*, vol. 95, no. 4, p. 713, 2002.

[6] A. I. Mushlin, R. W. Kouides, and D. E. Shapiro, "Estimating the accuracy of screening mammography: A meta-analysis," *American Journal of Preventive Medicine*, vol. 14, no. 2, pp. 143–153, 1998.

[7] S. J. Nass, C. Henderson, and J. C. Lashof, Eds., *Mammography and Beyond: Developing Techniques for the Early Detection of Breast Cancer*. Washington, DC: National Academy Press, 2000.

[8] T. S. England and N. A. Sharples, "Dielectric properties of the human body in the microwave region of the spectrum," *Nature*, vol. 163, pp. 487–488, 1949.

[9] T. S. England, "Dielectric properties of the human body for wavelength in the 1-10 cm range," *Nature*, vol. 1466, pp. 480–481, 1950.

[10] W. T. Joines, Y. Zhang, C. Li, and R. L. Jirtle, "The measured electrical properties of normal and malignant human tissues from 50 to 900 MHz," *Medical Physics*, vol. 21, no. 4, pp. 547–50, 1994.

[11] P. Meaney, M. Fanning, T. Raynolds, C. Fox, Q. Fang, C. Kogel, S. Poplack, and K. Paulsen, "Initial clinical experience with microwave breast imaging in women with normal mammography," *Academic Radiology*, vol. 14, no. 2, pp. 207–218, 2007.

[12] S. P. Poplack, T. D. Tosteson, W. A. Wells, B. W. Pogue, P. M. Meaney, A. Hartov, C. A. Kogel, S. K. Soho, J. J. Gibson, and K. D. Paulsen, "Electromagnetic breast imaging: Results of a pilot study in women with abnormal mammograms," *Radiology - Radiological Society of North America*, vol. 243, no. 2, pp. 350–359, 2007.

[13] M. Lazebnik, L. McCartney, D. Popovic, C. B. Watkins, M. J. Lindstrom, J. Harter, S. Sewall, A. Magliocco, J. H. Booske, M. Okoniewski, and S. C. Hagness, "A large-scale study of the ultrawideband microwave dielectric properties of normal breast tissue obtained from reduction surgeries," *Physics in Medicine and Biology*, vol. 52, no. 10, 2007.

[14] M. Lazebnik, D. Popovic, L. McCartney, C. B. Watkins, M. J. Lindstrom, J. Harter, S. Sewall, T. Ogilvie, A. Magliocco, T. M. Breslin, W. Temple, D. Mew, J. H. Booske, M. Okoniewski, and S. C. Hagness, "A large-scale study of the ultrawideband microwave dielectric properties of normal, benign and malignant breast tissues obtained from cancer surgeries," *Physics in Medicine and Biology*, vol. 52, no. 20, pp. 6093–6115, 2007.

[15] R. Nilavalan, J. Leendertz, I. Craddock, A. Preece, and R. Benjamin, "Numerical analysis of microwave detection of breast tumours using synthetic focussing techniques," *Proceedings*

of the IEEE Antennas and Propagation Society International Symposium, 2004, pp. 2440–2443 Vol.3, 2004.

[16] X. Li and S. Hagness, "A confocal microwave imaging algorithm for breast cancer detection," *IEEE Microwave and Wireless Components Letters*, vol. 11, no. 3, pp. 130–132, 2001.

[17] E. Fear and M. Stuchly, "Microwave system for breast tumor detection," *IEEE Microwave and Guided Wave Letters*, vol. 9, no. 11, pp. 470–472, 1999.

[18] Y. Xie, B. Guo, L. Xu, J. Li, and P. Stoica, "Multistatic adaptive microwave imaging for early breast cancer detection," *IEEE Transactions on Biomedical Engineering*, vol. 53, no. 8, pp. 1647–1657, 2006.

[19] M. Klemm, I. J. Craddock, J. Leendertz, A. Preece, and R. Benjamin, "Breast cancer detection using symmetrical antenna array," *Proceedings of the European Conference on Antennas and Propagation EuCAP 2007*, 2007.

[20] E. Fear, X. Li, S. Hagness, and M. Stuchly, "Confocal microwave imaging for breast cancer detection: Localization of tumors in three dimensions," *IEEE Transactions on Biomedical Engineering*, vol. 49, no. 8, pp. 812–822, 2002.

[21] E. Fear, J. Sill, and M. Stuchly, "Experimental feasibility study of confocal microwave imaging for breast tumor detection," *IEEE Transactions on Microwave Theory and Techniques*, vol. 51, no. 3, pp. 887–892, 2003.

[22] P. Kosmas and C. Rappaport, "Use of the FDTD method for time reversal: Application to microwave breast cancer detection," *Proceedings of SPIE - The International Society for Optical Engineering*, vol. 5299, pp. 1–9, 2004.

[23] C. Rappaport, "Cardiac tissue ablation with catheter-based microwave heating," *International Journal of Hyperthermia*, vol. 20, no. 7, p. 769, 2004.

[24] Q. H. Liu, C. Yu, J. Stang, M. Yuan, E. Bresslour, R. T. George, G. Ybarra, and W. T. Joines, "Experimental and numerical investigations of a high-resolution 3D microwave imaging system for breast cancer detection," *Proceedings of the IEEE Antennas and Propagation Society International Symposium, 2007*, pp. 2192–2192, 2007.

[25] P. Hashemzadeh, A. Fhager, and M. Persson, "Experimental investigation of an optimization approach to microwave tomography," *Electromagnetic Biology and Medicine*, vol. 25, no. 1, pp. 1–12, 2006.

[26] A. Fhager, P. Hashemzadeh, and M. Persson, "Reconstruction quality and spectral content of an electromagnetic time-domain inversion algorithm," *IEEE Transactions on Biomedical Engineering*, vol. 53, no. 8, pp. 1594–1604, 2006.

[27] P. Meaney, K. Paulsen, J. Chang, M. Fanning, and A. Hartov, "Nonactive antenna compensation for fixed-array microwave imaging. II. imaging results," *IEEE Transactions on Medical Imaging*, vol. 18, no. 6, pp. 508–518, 1999.

[28] P. Meaney, K. Paulsen, A. Hartov, and R. Crane, "Microwave imaging for tissue assessment: Initial evaluation in multitarget tissue-equivalent phantoms," *IEEE Transactions on Biomedical Engineering*, vol. 43, no. 9, pp. 878–890, 1996.

[29] S. Semenov, R. Svenson, A. Bulyshev, A. Souvorov, A. Nazarov, Y. Sizov, A. Pavlovsky, V. Borisov, B. Voinov, G. Simonova, A. Starostin, V. Posukh, G. Tatsis, and V. Baranov, "Three-dimensional microwave tomography: Experimental prototype of the system and vector born reconstruction method," *IEEE Transactions on Biomedical Engineering*, vol. 46, no. 8, pp. 937–946, 1999.

[30] P. Meaney, M. Fanning, D. Li, S. Poplack, and K. Paulsen, "A clinical prototype for active microwave imaging of the breast," *IEEE Transactions on Microwave Theory and Techniques*, vol. 48, no. 111, pp. 1841–1853, 2000.

[31] S. Semenov, R. Svenson, A. Bulyshev, A. Souvorov, A. Nazarov, Y. Sizov, V. Posukh, A. Pavlovsky, P. Repin, A. Starostin, B. Voinov, M. Taran, G. Tatsis, and V. Baranov, "Three-dimensional microwave tomography: Initial experimental imaging of animals," *IEEE Transactions on Biomedical Engineering*, vol. 49, no. 1, pp. 55–63, 2002.

[32] S. Y. Semenov, A. E. Bulyshev, V. G. Posukh, Y. E. Sizov, T. C. Williams, and A. E. Souvorov, "Microwave tomography for detection/imaging of myocardial infarction. i. excised canine hearts," *Annals of Biomedical Engineering*, vol. 31, no. 3, pp. 262–270, 2003.

[33] P. Meaney, K. Paulsen, A. Hartov, and R. Crane, "An active microwave imaging system for reconstruction of 2-D electrical property distributions," *IEEE Transactions on Biomedical Engineering*, vol. 42, no. 10, pp. 1017–1026, 1995.

[34] P. Meaney, K. Paulsen, and J. Chang, "Near-field microwave imaging of biologically-based materials using a monopole transceiver system," *IEEE Transactions on Microwave Theory and Techniques*, vol. 46, no. 1, pp. 31–45, 1998.

[35] P. Meaney, K. Paulsen, J. Chang, and M. Fanning, "Initial microwave imaging experiments in ex-vivo breast tissue," *Proceedings of the First Joint BMES/EMBS Conference, 1999*, vol. 2, p. 1130, 1999.

[36] D. Li, P. Meaney, and K. Paulsen, "Conformal imaging with a non-contacting microwave antenna array," *Proceedings of the IEEE MTT-S International Microwave Symposium, 2001*, vol. 1, pp. 563–566, 2001.

[37] D. Li, P. Meaney, T. Raynolds, S. Pendergrass, M. Fanning, and K. Paulsen, "A broadband microwave breast imaging system," *Proceedings of the IEEE 29th Annual Bioengineering Conference, 2003*, pp. 83–84, 2003.

[38] P. Meaney, S. Pendergrass, M. Fanning, D. Li, and K. Paulsen, "Importance of using a reduced contrast coupling medium in 2D microwave breast imaging," *Journal of Electromagnetic Waves and Applications*, vol. 17, no. 2, pp. 333–355, 2003.

[39] Q. Fang, P. Meaney, S. Geimer, A. Streltsov, and K. Paulsen, "Microwave image reconstruction from 3-D fields coupled to 2-D parameter estimation," *IEEE Transactions on Medical Imaging*, vol. 23, no. 4, pp. 475–484, 2004.

[40] P. Meaney, Q. Fang, M. Fanning, S. Pendergrass, T. Raynolds, C. Fox, and K. Paulsen, "Microwave breast imaging with an under-determined reconstruction parameter mesh," *Proceedings of the IEEE International Symposium on Biomedical Imaging: Macro to Nano, 2004*, pp. 1369–1372, 2004.

[41] P. Meaney, K. Paulsen, S. Geimer, S. Haider, and M. Fanning, "Quantification of 3-D field effects during 2-D microwave imaging," *IEEE Transactions on Biomedical Engineering*, vol. 49, no. 7, pp. 708–720, 2002.

[42] P. Meaney, K. Paulsen, B. Pogue, and M. Miga, "Microwave image reconstruction utilizing log-magnitude and unwrapped phase to improve high-contrast object recovery," *IEEE Transactions on Medical Imaging*, vol. 20, no. 2, pp. 104–116, 2001.

[43] J. Sill and E. Fear, "Tissue sensing adaptive radar for breast cancer detection: Study of immersion liquids," *Electronics Letters*, vol. 41, no. 3, pp. 113–115, 2005.

[44] Q. Fang, P. Meaney, and K. Paulsen, "Microwave image reconstruction of tissue property dispersion characteristics utilizing multiple-frequency information," *IEEE Transactions on Microwave Theory and Techniques*, vol. 52, no. 82, pp. 1866–1875, 2004.

[45] G. Bozza, C. Estatico, A. Massa, M. Pastorino, and A. Randazzo, "Short-range image-based method for the inspection of strong scatterers using microwaves," *IEEE Transactions on Instrumentation and Measurement*, vol. 56, no. 4, pp. 1181–1188, 2007.

[46] C. T. Kelley, *Solving Nonlinear Equations with Newton's Method*. Philadelphia, PA: SIAM, 2003.

[47] P. M. Meaney, T. Zhou, S. A. Geimer, and K. D. Paulsen, "Implications of reduced measurement data sets on overall microwave tomographic image quality," *Proceedings of the European Conference on Antennas and Propagation EuCAP, 2007*, 2007.

[48] O. S. Kim, P. Meincke, O. Breinbjerg, and E. Jørgensen, "Method of moments solution of volume integral equations using higher-order hierarchical Legendre basis functions," *Radio Science*, vol. 39, RS5003, doi:10.1029/2004RS003041, 2004.

[49] O. S. Kim and P. Meincke, "3-dimensional iterative forward model for microwave imaging," in *Proc. 4th International Workshop on Biological Effects of Electromagnetic Fields*, vol. 1, Hersonissou, Greece, October 2006, pp. 306–310.

[50] E. Bleszynski, M. Bleszynski, and T. Jaroszewicz, "AIM: Adaptive integral method for solving large-scale electromagnetic scattering and radiation problems," *Radio Science*, vol. 31, no. 5, pp. 1225–1251, Sept.-Oct. 1996.

[51] Z. Q. Zhang and Q. H. Liu, "A volume adaptive integral method (VAIM) for 3-D inhomogeneous objects," *IEEE Antennas Wireless Propagat. Lett.*, vol. 1, pp. 102–105, 2002.

[52] W.-B. Ewe, L.-W. Li, and M.-S. Leong, "Fast solution of mixed dielectric/conducting scattering problem using volume-surface Adaptive Integral Method," *IEEE Trans. on Antennas and Propagation*, vol. 52, no. 11, pp. 3071–3077, November 2004.

[53] D. Li, P. M. Meaney, T. Raynolds, S. A. Pendergrass, M. W. Fanning, and K. D. Paulsen, "Parallel-detection microwave spectroscopy system for breast imaging," *Review of Scientific Instruments*, vol. 75, no. 7, pp. 2305–2313, 2004.

[54] T. Rubæk, P. M. Meaney, P. Meincke, and K. D. Paulsen, "Nonlinear microwave imaging for breast-cancer screening using Gauss-Newton's method and the CGLS inversion algorithm," *IEEE Transactions on Antennas and Propagation*, vol. 55, no. 8, pp. 2320–2331, 2007.

[55] P. C. Hansen, *Rank-Deficient and Discrete Ill-Posed Problems: Numerical Aspects of Linear Inversion*, ser. Monographs on Mathematical Modeling and Computation. SIAM, 1998.

Conference Paper 1

Including Antenna Models in Microwave Imaging for Breast Cancer Screening

Tonny Rubæk and Peter Meincke

Status:
Conference: European Conference on Antennas and Propagation 2006, Nice, France
Published: 2006

INCLUDING ANTENNA MODELS IN MICROWAVE IMAGING FOR BREAST CANCER SCREENING

Tonny Rubæk and Peter Meincke

Technical University of Denmark, Ørsteds Plads, Building 348, DK-2800 Kgs. Lyngby, Denmark, Email: [tru/pme]@oersted.dtu.dk

ABSTRACT

Microwave imaging is emerging as a tool for screening for breast cancer, but the lack of methods for including the characteristics of the antennas of the imaging systems in the imaging algorithms limits their performance. In this paper, a method for incorporating the full antenna characteristics, in terms of the transmission-matrix representation, in a frequency-domain imaging algorithm is presented. The algorithm is tested on a simulation of the Physical-Anomaly Tomography (PAT) scanner imaging system developed at the Technical University of Denmark and is shown to have superior performance when compared to a simple algorithm in which the antennas are assumed to be ideal dipoles.

1. INTRODUCTION

During the last decade, the use of microwave imaging as a screening tool for detection of breast cancer has gained the attention of an increasing number of research groups [1–5]. The use of microwave imaging is seen as an appealing alternative or supplement to the widely used X-ray mammography for two main reasons. First, the microwaves are non-ionizing, and therefore less hazardous to the health of the women being screened. Second, the physical parameters creating contrast in the microwave region are different from those creating the contrast in X-ray images. This implies that tumors that are not visible in the X-ray images mmight be detectable when using microwave imaging, thus possibly allowing for the screening of the breasts of premenopausal women.

One of the difficulties encounteredwhen creating imaging algorihtms for microwave-imaging systems is the incorporation of the antenna characteristics in the algorithms. In the time-reversal based imaging algorithms [2], the antennas are most often characterized by their impulse response and otherwise assumed to have a somewhat uniform radiation pattern [6, 7]. In the frequency-domain based techniques, some attempts have been made to include the antenna characteristics in the imaging algorithms, especially in the realm of ground penetrating radar [8]. When used for breast cancer screening, the antennas are widely assumed to be point sources [4, 9].

In this paper, a method for including the complete antenna model is presented, thereby allowing for the imaging algorithm to adopt the antennas most suitable for the setup of the imaging system. The method is based on a transmission-matrix representation of the antennas in the microwave imaging system using the spherical-wave formulation. The spherical-wave formulation has been chosen due to the geometry of the imaging system under consideration in this paper. The concept is tested on a linear inverse scattering problem but is believed to be efficient when applied to Newton-based iterative nonlinear inversion schemes, similar to those described in [9, 10], as well.

This paper is organized as follows: In Section 2, the imaging system currently being developed at the Technical University of Denmark is introduced while the spherical wave expansion is incorporated into a linear-inversion algorithm based on the first-order Born approximation in Section 3. The algorithm is tested on simulated data in Section 4 and the results are compared to those obtained using a simple inversion algorithm in which the antennas are assumed to be ideal dipoles.

The time-dependency $\mathrm{e}^{-i\omega t}$ is assumed and suppressed in the frequency domain formulations throughout this paper.

2. IMAGING SYSTEM

The imaging system considered in this paper is the first-generation Physical-Anomaly Tomography (PAT) scanner developed at the Technical University of Denmark. The system is depicted in Figure 1, and consists of 32 air-supported patch antennas, designed for operating in the frequency domain at 5 GHz, positioned on the inside of a metallic hemisphere. The

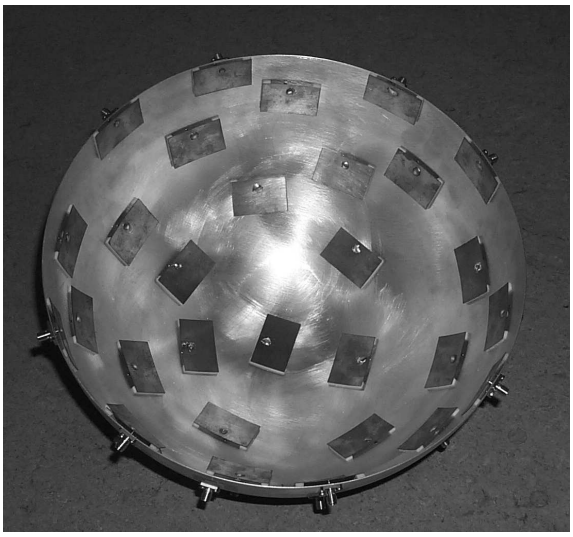

Figure 1. Picture of the PAT scanner. The system is designed to work at the frequency 5 GHz and consists of a aluminum hemisphere inside of which is positioned conformal patch antennas made of copper plating.

positions of the antennas have been determined by the use of a genetic algorithm to provide the best possible spacial coverage on the hemisphere.

The metallic hemisphere has a radius of 15 cm and the square patch antennas have been shaped to be conformal with the hemispherical ground plane. Each of the air-supported antennas are identical with the dimensions 26.9 mm by 40 mm and a schematic of an antenna is seen in Figure 2. The distance between the patches and the hemisphere is $h = 2$ mm and the feed is positioned $l_f = 7$ mm from the edge of the patch.

The antennas are predominantly linearly polarized although the axial ratio of the polarization ellipse is not well-defined inside the imaging domain due to the presence of the metallic hemisphere.

Each antenna is connected to a network analyzer through a coaxial cable and a switching network. It is assumed that the only propagating wave modes in the coaxial cables are a TEM wave propagating towards the antenna and a TEM wave propagating away from the antenna. The wave propagating toward the antenna is characterized by the complex voltage v^+ and the wave propagating away from the antenna is characterized by the complex voltage v^-.

During measurements, the object to be imaged is positioned inside the metallic hemisphere and the antennas in turn acts as the transmitter. The S parameters, that is, the ratio between v^+ on the transmitting antenna and v^- on the transmitting and the 31

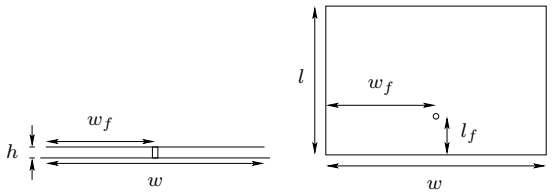

Figure 2. Schematic of patch antenna used in the PAT scanner. Each antenna has a width of $w = 40$ mm, a length of $l = 26.9$ mm, and is positioned at a height of $h = 2$ mm above the metallic hemisphere. The feed is positioned at $w_f = 20$ mm and $l_f = 7$ mm.

receiving antennas, are then measured, providing 32 sets of 32 S parameters, one set for each antenna.

3. IMAGING ALGORITHM

To test the effect of including the antenna characteristics in the imaging algorithm, a simple linear imaging problem is investigated. By assuming that there is only a single small and low contrast object present in the imaging system, the first-order Born approximation can be used as the basis for the imaging algorithm. Under the first-order Born approximation, the scattered field $\boldsymbol{E_s}$ is assumed to be a linear function of the incident field $\boldsymbol{E_{inc}}$ given by the integral equation [11, (8.9.14)]

$$\boldsymbol{E_s}(\boldsymbol{r},\omega) = i\omega\mu \int_V \bar{\bar{\boldsymbol{G}}}(\boldsymbol{r},\boldsymbol{r'},\omega) \cdot \boldsymbol{E_{inc}}(\boldsymbol{r'},\omega) o(\boldsymbol{r'},\omega)\,\mathrm{d}^3\boldsymbol{r'}. \quad (1)$$

In this expression, $\bar{\bar{\boldsymbol{G}}}$ is the dyadic Green's function for observation point $\boldsymbol{r}$ and source point $\boldsymbol{r'}$ [11, (7.1.27)] and o is the object function given by the contrast in permittivity and conductivity of the scattering object as

$$o(\boldsymbol{r'},\omega) = \Delta\sigma(\boldsymbol{r'}) - i\omega\Delta\epsilon(\boldsymbol{r'}) = [\sigma(\boldsymbol{r'}) - \sigma_0] - i\omega\,[\epsilon(\boldsymbol{r'}) - \epsilon_0] \quad (2)$$

where ϵ_0 and σ_0 are the constitutive parameters of the background medium. It is well-known that the scattered field can be expressed in terms of the equivalent scattering current $\boldsymbol{J_{scat}}$ given by

$$\boldsymbol{J_{scat}}(\boldsymbol{r},\omega) = \boldsymbol{E_{inc}}(\boldsymbol{r},\omega) o(\boldsymbol{r},\omega). \quad (3)$$

3.1. Transmission-Matrix Representation

The antennas are characterized using a transmission-matrix representation based on the spherical-wave

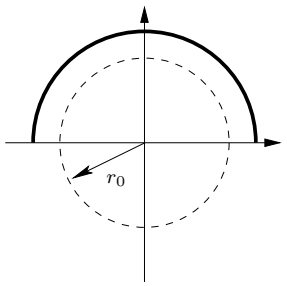

Figure 3. Schematic of the imaging domain with radius r_0 in the PAT scanner. The field inside the domain can be fully described using the $\boldsymbol{F}^{(\mathbf{1})}$ functions.

expansion. The spherical-wave expansion has been chosen due to the geometry of the PAT scanner. The spherical-wave expansion is given in terms of the power-normalized generating functions introduced in [12]. Inside the imaging domain of the PAT scanner, shown in Figure 3 with a radius of $r_0 = 12$ cm, the field can be expressed using the generating function $\boldsymbol{F}^{(\mathbf{1})}$, representing a standing wave, as

$$\boldsymbol{E}(r,\theta,\phi,\omega) = \frac{k}{\sqrt{\frac{\epsilon}{\mu}}} \cdot \sum_{s=1}^{2}\sum_{n=1}^{N}\sum_{m=-n}^{n} a_{s,m,n}\boldsymbol{F}^{(\mathbf{1})}_{\boldsymbol{s,m,n}}(r,\theta,\phi) \quad (4)$$

where $a_{s,m,n}$ is the spherical-wave expansion coefficients. The summation in n has been truncated at N. The value of N can be found using [12, (2.31)] as

$$N = \mathrm{int}(kr_0) + 10 = \mathrm{int}(104.73\ \mathrm{m}^{-1} \cdot 0.12\ \mathrm{m}) + 10 = 22. \quad (5)$$

Here it has been assumed that the radius of the imaging domain may be set to 12 cm, allowing for half a wave length of free space along the metallic hemisphere.

The transmission matrix $\underline{t}$ can now be introduced for characterizing the antennas in the PAT scanner. The transmission matrix is a column matrix satisfying the relation

$$\begin{bmatrix}\Gamma \\ \underline{t}\end{bmatrix} v^+ = \begin{bmatrix}v^- \\ \underline{a}\end{bmatrix}. \quad (6)$$

In this expression, Γ is the complex reflection coefficient measured at the terminal of the antenna, $\underline{a}$ is a column matrix holding the spherical-wave coefficients, and v^+ and v^- is the voltages of the wave incident on and reflected back into the terminals of the antenna as described in Section 2. The transmission matrix for each of the antennas in the PAT scanner can be found by using the orthogonality of the spherical-wave functions as described in [12, Sec. A.1.4].

3.2. Receiving Characteristics from Transmission Matrix

To obtain a relation between the equivalent scattering current and the change in the measured S parameters, the theorem of reciprocity [13, Eq.(1.67)] has been applied. The approach taken is similar to that used in [12, Sec. 2.3.2], and the resulting expression for the voltage v^-, characterizing the wave propagating away from any one of the antennas operating in receiver mode is given by

$$v^- = \frac{-Z_{\mathrm{coax}}k}{2\sqrt{\frac{\epsilon}{\mu}}} \int_V \boldsymbol{J}_{\mathrm{scat}}(\boldsymbol{r'}) \cdot \sum_{s=1}^{2}\sum_{n=1}^{N}\sum_{m=-n}^{n} \Big[t_{s,m,n}\boldsymbol{F}^{(\mathbf{1})}_{\boldsymbol{s,m,n}}(\boldsymbol{r'}) \Big] \, \mathrm{d}^3\boldsymbol{r'} \quad (7)$$

with Z_{coax} being the characteristic impedance of the coaxial cable. By using the expression for the equivalent scattering current given in (3), the following expression is found for the change in the measured S parameters as a function of the object function

$$S_{r,t} = \frac{v_r}{v_t} = \frac{-Z_{\mathrm{coax}}k^2}{2\frac{\epsilon}{\mu}} \int_V o(\boldsymbol{r'}) \cdot \sum_{s_t=1}^{2}\sum_{n_t=1}^{N}\sum_{m_t=-n_t}^{n_t} \Big[t^{(t)}_{s_t,m_t,n_t}\boldsymbol{F}^{(\mathbf{1})}_{\boldsymbol{s_t,m_t,n_t}}(\boldsymbol{r'}) \Big] \cdot \sum_{s_r=1}^{2}\sum_{n_r=1}^{N}\sum_{m_r=-n_r}^{n} \Big[t^{(r)}_{s_r,m_r,n_r}\boldsymbol{F}^{(\mathbf{1})}_{\boldsymbol{s_r,m_r,n_r}}(\boldsymbol{r'}) \Big] \, \mathrm{d}^3\boldsymbol{r'}, \quad (8)$$

where the transmission coefficients of the transmitting and receiving antennas are given by $t^{(t)}$ and $t^{(r)}$, respectively. The forward model of the imaging problem can now be constructed by the 32^2 integral equations obtained when using all possible combinations of transmitting and receiving antennas. Due to the reciprocity of the problem, one half of the equations are identical to the other half and may be omitted. It has, however, been found that the impact of noise decreases if all of the equations are utilized in the forward model.

3.3. Matrix Equation

The imaging algorithm can now be constructed by casting the integral equations for the scattering parameters into a discrete matrix equation. The transformation from integral equation to matrix equation is accomplished by dividing the imaging domain inside the PAT scanner into N_v voxels, each characterized by the position of their center $\boldsymbol{r_n}$ and their volume v_n. The voxels are assumed to be so small that both the object function o and the spherical vector

functions $\boldsymbol{F^{(1)}}$ may be considered constant within the individual voxels.

The discretization leads to the following matrix equation

$$\underline{\underline{P}}\,\underline{o} = \underline{s}. \tag{9}$$

In this expression, the matrix

$$\underline{\underline{P}} = \begin{bmatrix} P(1,1,\boldsymbol{r_1}) & \dots & P(1,1,\boldsymbol{r_{N_v}}) \\ P(1,2,\boldsymbol{r_1}) & \dots & P(1,2,\boldsymbol{r_{N_v}}) \\ \dots & \dots & \dots \\ P(32,32,\boldsymbol{r_1}) & \dots & P(32,32,\boldsymbol{r_{N_v}}) \end{bmatrix} \tag{10}$$

holds the discrete form of the forward model from the transmitting antenna to the receiving antenna. When using the PAT scanner, the matrix has 1024 rows, which is the number of S parameters available. The complex function P is given by

$$P(r,t,\boldsymbol{r_n}) = \frac{-Z_{\text{coax}}k^2}{2\frac{\epsilon}{\mu}} v_n \sum_{s_t=1}^{2}\sum_{s_r=1}^{2}\sum_{n_t=1}^{N}\sum_{n_r=1}^{N}\sum_{m_t=-n_t}^{n_t}\sum_{m_r=-n_r}^{n_r} \left[t^t_{s_t,m_t,n_t} \cdot t^r_{s_r,m_r,n_r} \boldsymbol{F^{(1)}_{s_t,m_t,n_t}}(\boldsymbol{r_n}) \cdot \boldsymbol{F^{(1)}_{s_r,m_r,n_r}}(\boldsymbol{r_n})\right] \tag{11}$$

wherein it has been applied that the spherical-vector functions are considered constant in each of the small voxels. When filling the matrix $\underline{\underline{P}}$ the most time consuming operation by far is the calculation of the spherical-wave functions. These, however, need only to be calculated once for each voxel and can then be reused for all of the antenna combinations.

The column matrix $\underline{o}$ in (9) holds the unknown object function for each of the N_v voxels in the imaging domain. When operating in a free-space setup, the imaging domain is typically divided into box-shaped voxels with side lengths of $\frac{\lambda}{10}$. At 5 GHz this implies a side length of 6 mm and using a hemispherical imaging domain with a radius of 12 cm the total number of voxels is $N_v = 14943$. This will also be the number of columns in the matrix $\underline{\underline{P}}$.

The column-matrix on the right-hand side of (9)

$$\underline{s} = \begin{bmatrix} S^{obj}_{1,1} - S^{cal}_{1,1} \\ S^{obj}_{1,2} - S^{cal}_{1,2} \\ \vdots \\ S^{obj}_{32,32} - S^{cal}_{32,32} \end{bmatrix} \tag{12}$$

holds the difference in the S parameters measured with the object inside the PAT scanner and the S parameters measured when no object is present. The subtraction of the calibration measurement is necessary because the matrix $\underline{\underline{P}}$ does not include information on the background field in the PAT scanner.

The matrix equation can be solved using the truncated singular value decomposition method [14, Sec. 3.2] or similar methods such as the iterative conjugated gradient line search algorithm [14, 6.3].

3.4. Dipoles in Free Space

For comparison a simple algorithm using the assumption that the antennas in the PAT scanner are adequately represented using dipoles has been derived. The antennas are assumed to be dipoles positioned in free space and the voltage measured on the terminals of the antennas is assumed to be equal to the component of the scattered field parallel to the dipole.

Using (1), the voltage across the terminals of the $\hat{\boldsymbol{p}}_{\boldsymbol{r}}$-directed receiving antenna is given as

$$v_r = i\omega\mu \int_V \hat{\boldsymbol{p}}_{\boldsymbol{r}} \big(\bar{\bar{\boldsymbol{G}}}(\boldsymbol{r_r},\boldsymbol{r'},\omega) \cdot \boldsymbol{E_{inc}}(\boldsymbol{r'},\omega) o(\boldsymbol{r'},\omega)\big)\,\mathrm{d}^3\boldsymbol{r'}. \tag{13}$$

The incident field $\boldsymbol{E_{inc}}$ at the point $\boldsymbol{r'}$ is found using the Green's function and the dipole moment of the $\hat{\boldsymbol{p}}_{\boldsymbol{t}}$ directed transmitting antenna [15, (10)] as

$$\boldsymbol{E_{inc}}(\boldsymbol{r'},\omega) = i\omega\mu I(\omega)\bar{\bar{\boldsymbol{G}}}(\boldsymbol{r'},\boldsymbol{r_t},\omega)\cdot\hat{\boldsymbol{p}}_{\boldsymbol{t}} = i\omega\mu\frac{v_t}{Z_{\text{in}}}\hat{\boldsymbol{p}}_{\boldsymbol{t}}\cdot\bar{\bar{\boldsymbol{G}}}(\boldsymbol{r'},\boldsymbol{r_t},\omega) \tag{14}$$

with Z_{in} being the impedance at the terminals of the antennas.

By use of this expression, the expression for the S parameters can be found as

$$S_{r,t} = \frac{v_r}{v_t} = \frac{-\omega^2\mu^2}{Z_{\text{in}}}\int_V \left[\hat{\boldsymbol{p}}_{\boldsymbol{r}}\cdot\bar{\bar{\boldsymbol{G}}}(\boldsymbol{r_r},\boldsymbol{r'},\omega)\right] \cdot \left[\hat{\boldsymbol{p}}_{\boldsymbol{r}}\cdot\bar{\bar{\boldsymbol{G}}}(\boldsymbol{r_r},\boldsymbol{r'},\omega)\right] o(\boldsymbol{r'},\omega)\,\mathrm{d}^3\boldsymbol{r'}. \tag{15}$$

This expression can be cast into a matrix equation in much the same way as the expression for the algorithm including the antenna characteristics. The resulting expression is

$$\underline{\underline{P}}_{fs}\,\underline{o} = \underline{s} \tag{16}$$

where the elements of the matrix $\underline{\underline{P}}_{fs}$ are given by

$$P_{fs}(r,t,\boldsymbol{r_n}) = \frac{-\omega^2\mu^2 v_n}{Z_{\text{in}}}\left[\hat{\boldsymbol{p}}_{\boldsymbol{r}}\cdot\bar{\bar{\boldsymbol{G}}}(\boldsymbol{r_r},\boldsymbol{r_n},\omega)\right] \cdot \left[\hat{\boldsymbol{p}}_{\boldsymbol{r}}\cdot\bar{\bar{\boldsymbol{G}}}(\boldsymbol{r_r},\boldsymbol{r_n},\omega)\right]. \tag{17}$$

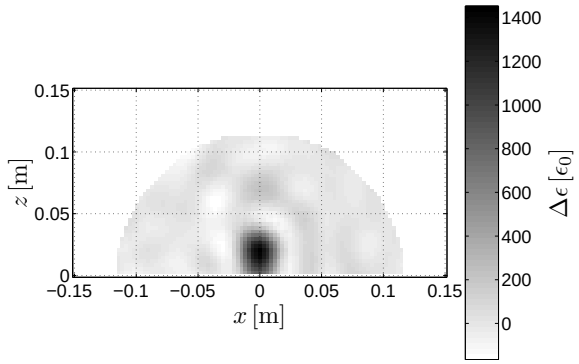

(a) Ideal dipoles in free space

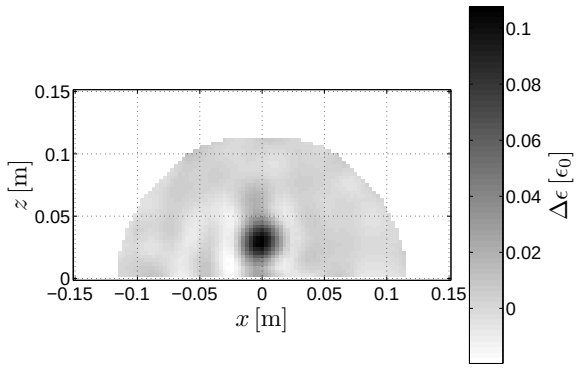

(b) Antenna models included

Figure 4. Results obtained using (a) the algorithm assuming ideal dipoles and (b) the algorithm including the antenna models for constant $y = 0$. The spherical scatterer is centered at $(x, y, z) = (0, 0, 3\ cm)$, has a radius of 1.5 cm, and a contrast of $\Delta\epsilon = 0.1\epsilon_0$.

4. TEST OF ALGORITHM

The algorithm has been tested using simulated data. In the simulation, the PAT scanner is operating in a free-space setup with the only other object present being the scattering object inside the system. The complete setup is simulated using a method of moments code [16].

In the simulation, a single spherical object is positioned inside the PAT scanner. The radius of the object is 1.5 cm and the center of the object is positioned at $(x_c, y_c, z_c) = (0, 0, 3\ \text{cm})$. The scatterer has a relative permittivity of $\epsilon_r = 1.1$, implying $\Delta\epsilon = 0.1\epsilon_0$.

The results of the inversion using the algorithm including the antenna characteristics and the algorithm assuming dipoles positioned in free space are seen in Figure 4. Both algorithms seem to detect the position of the scatterer. The algorithm including the antenna models, however, is also capable of recreating the actual contrast whereas the algorithm using

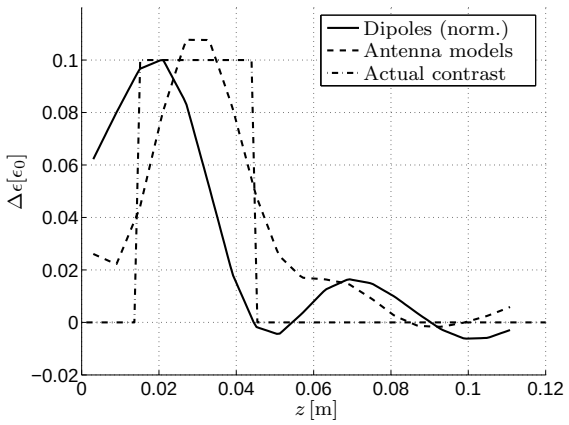

Figure 5. Comparison of contrast obtained using the two different algorithms along the line from $(x, y, z) = (0, 0, 0)$ to $(x, y, z) = (0, 0, 15\ cm)$. The result of the inversion with the algorithm using the dipole assumption has been normalized to allow for a comparison of its ability to detect the location of the scatterer.

the simple dipole models yields a contrast which is far from the actual contrast of the scatterer. Also, the position of the scatterer is slightly offset in the negative $\hat{\boldsymbol{z}}$ direction in the image created by the algorithm based on the dipole assumption whereas the inclusion of the full antenna models allows for a very accurate estimate of the position and extend of the scatterer.

In Figure 5, the contrast obtained using the two different algorithms along the line $(x, y) = (0, 0)$ are plotted against the actual contrast. The contrast obtained with the ideal-dipole algorithm has been normalized, allowing for a better comparison. In this plot it is clearly seen that the algorithm including the antenna models detects the position of the scatterer very accurate with the maximum contrast being at the center of the scatterer, and returns an accurate estimate of the contrast of the scatterer. The offset in the negative $\hat{\boldsymbol{z}}$ direction of the simple dipole-based model is also clearly seen.

Similar results have been observed as the scatterer is moved around inside the PAT scanner; the inclusion of the full antenna models in the algorithm yields results that are clearly better than when the dipole model is used, both in terms of location of the object and in terms of the level of the contrast.

5. CONCLUSION

The concept of including the antenna characteristics in frequency-domain microwave imaging has been shown to improve the image quality when applied

to a linear imaging algorithm. The algorithm was tested on a simulated model of the first-generation PAT scanner developed at the Technical University of Denmark, and compared to an algorithm in which the antennas were assumed to be ideal dipoles, the performance of the new algorithm was superior in terms of determining both location and contrast of the scattering object. The antenna characteristics were defined in terms of the spherical-wave expansion to fit the geometry of the measurement system.

The incorporation of the antenna-characteristics in an iterative Newton-based non-linear is the subject of ongoing research and is believed to be achievable with relative ease. Furthermore, the scattering-matrix representation of the antennas in the imaging system can easily be reformulated in terms of cylindrical or plane waves if the algorithm is to be applied for an imaging system with a different geometrical setup of the antennas.

ACKNOWLEDGMENTS

The Danish Technical Research Council is acknowledged for supporting the work of Tonny Rubæk and Peter Meincke. Mario Fernandez is acknowledged for creating the genetic algorithm for determining the position of the antennas.

REFERENCES

1. E. Fear, P. Meaney, and M. Stuchly, "Microwaves for breast cancer detection?" *IEEE Potentials*, vol. 22, no. 1, pp. 12–18, 2003.

2. X. Li, E. Bond, B. Van Veen, and S. Hagness, "An overview of ultra-wideband microwave imaging via space-time beamforming for early-stage breast-cancer detection," *Antennas and Propagation Magazine, IEEE*, vol. 47, no. 1, pp. 19–34, 2005.

3. R. Nilavalan, J. Leendertz, I. Craddock, A. Preece, and R. Benjamin, "Numerical analysis of microwave detection of breast tumours using synthetic focussing techniques," *Antennas and Propagation Society Symposium, 2004. IEEE*, pp. 2440–2443 Vol.3, 2004.

4. P. Meaney, K. Paulsen, A. Hartov, and R. Crane, "An active microwave imaging system for reconstruction of 2-d electrical property distributions," *Biomedical Engineering, IEEE Transactions on*, vol. 42, no. 10, pp. 1017–1026, 1995.

5. P. Hashemzadeh, A. Fhager, and M. Persson, "Experimental investigation of an optimization approach to microwave tomography," *Electromagnetic Biology and Medicine*, vol. 25, no. 1, pp. 1–12, 2006.

6. E. Fear, A. Low, J. Sill, and M. A. Stuchly, "Microwave system for breast tumor detection: Experimental concept evaluation," *IEEE Antennas and Propagation Society, AP-S International Symposium (Digest)*, vol. 1, pp. 819–822, 2002.

7. C. Shannon, E. Fear, and M. Okoniewski, "Dielectric-filled slotline bowtie antenna for breast cancer detection," *Electronics Letters*, vol. 41, no. 7, pp. 11–12, 2005.

8. P. Meincke and T. Hansen, "Plane-wave characterization of antennas close to a planar interface," *Geoscience and Remote Sensing, IEEE Transactions on*, vol. 42, no. 6, pp. 1222–1232, 2004.

9. P. Meaney, K. Paulsen, and J. Chang, "Near-field microwave imaging of biologically-based materials using a monopole transceiver system," *Microwave Theory and Techniques, IEEE Transactions on*, vol. 46, no. 1, pp. 31–45, 1998.

10. D. Li, P. Meaney, and K. Paulsen, "Conformal imaging with a non-contacting microwave antenna array," *Microwave Symposium Digest, 2001 IEEE MTT-S International*, vol. 1, pp. 563–566 vol.1, 2001.

11. W. C. Chew, *Waves and Fields in Inhomogeneous Media*, ser. IEEE Press Series on Electromagnetic Waves, D. G. Dudley, Ed. New York: IEEE Press, 1995.

12. J. Hald, J. E. Hansen, F. Jensen, and F. H. Larsen, *Spherical Near-Field Antenna Measurements*, ser. IEE Electromagnetic Waves Series, J. E. Hansen, Ed. Peter Peregrinus Ltd., 1988, vol. 26.

13. R. E. Collin and F. J. Zucker, *Antenna Theory, part I.* New York: McGraw-Hill, 1969.

14. P. C. Hansen, *Rank-Deficient and Discrete Ill-Posed Problems: Numerical Aspects of Linear Inversion*, ser. Monographs on Mathematical Modeling and Computation. SIAM, 1998.

15. P. Meincke, "Linear gpr inversion for lossy soil and a planar air-soil interface," *Geoscience and Remote Sensing, IEEE Transactions on*, vol. 39, no. 12, pp. 2713–2721, 2001.

16. E. Jørgensen, J. L. Volakis, P. Meincke, and O. Breinbjerg, "Higher order hierarchical legendre basis functions for electromagnetic modeling," *IEEE Transactions on Antennas and Propagation*, vol. 52, no. 11, pp. 2985–2995, nov 2004.

Conference Paper 2

Three-Dimensional Microwave Imaging for Breast-Cancer Detection using the Log-Phase Formulation

Tonny Rubæk, Peter Meincke, and Oleksiy S. Kim

Status:
Conference: IEEE Antennas and Propagation International Symposium 2007, Honolulu, Hawaii, USA
Published: 2007

Three-Dimensional Microwave Imaging for Breast-Cancer Detection using the Log-Phase Formulation

Tonny Rubæk, Peter Meincke, and Oleksiy S. Kim
Oersted•DTU, Technical University of Denmark,
[tru/pme/osk]@oersted.dtu.dk

The log-phase formulation is applied for the reconstruction of images from a simulation of a three-dimensional imaging system. By using this formulation, a clear improvement in the quality of the reconstructed images is achieved compared to the case in which the usual complex phasor notation is employed.

Introduction

Microwave imaging is emerging as a tool for biomedical imaging [1–5]. In particular, microwave imaging is a promising tool for screening for breast cancer due to the high contrast between malignant tumors and the healthy breast tissue [1–3, 5].

One of the most challenging aspects of microwave imaging is to reconstruct images of large, high-contrast objects since such objects cause the associated inverse scattering problem to become non-linear. Such image-reconstruction problems are often encountered when imaging the breast where, in addition to any tumors, large inclusions of fibroglandular tissue, with constitutive parameters very different from those found in the rest of the breast, may be present. An algorithm for imaging of the breast must therefore be capable of coping with such multiple large, high-contrast inclusions and still be able to detect the smaller tumors. At Dartmouth College, an iterative Gauss-Newton based imaging algorithm, in which the reconstruction problem is solved in 2-D, is currently being tested on data collected from breast-cancer patients [6]. For this algorithm it has been found that to cope with the complexity of the imaging problem it is useful to reformulate the inverse scattering problem from using the usual complex phasor notation of the measured signals to involve the logarithm of the magnitude of the signals and their unwrapped phase. This is referred to as the log-phase formulation [1, Sec. II].

At the Technical University of Denmark, the Physical Anomaly Tomography (PAT) Scanner is currently being developed. This imaging system operates in a three-dimensional setup and to reconstruct the images, an algorithm based on the iterative Gauss-Newton scheme is applied. In this paper, the improvement in the image quality obtained using the log-phase formulation of the measured scattering data as opposed to the complex phasor formulation in a three-dimensional microwave-imaging setup is shown for the first time. The two different formulations are tested on simulated data and it is shown that even for objects with relatively low contrasts, the log-phase formulation clearly improves the capability of the algorithm to reconstruct the images.

Imaging System and Algorithm

The PAT Scanner consists of 32 antennas arranged in a hemispherical setup. During patient exams, the patient is to lie prone on an exam bed above the imaging system with her breast suspended through an aperture in the lid of the imaging system as seen in Figure 1. The breast and antennas are immersed in a coupling liquid to maximize the energy coupled from the antennas to the inside of the breast. The scattering (S) parameters of every possible combination of transmitting and receiving antenna are then measured, yielding a total of 992 measurements.

In the imaging algorithm currently applied at the Technical University of Denmark, the constitutive parameters of the imaging domain is represented by the squared complex wave numbers

$$k^2(\boldsymbol{r}) = \mu_0\omega^2\epsilon(\boldsymbol{r}) + i\mu_0\omega\sigma(\boldsymbol{r}). \tag{1}$$

The reconstruction of the images is then performed by discretizing the imaging domain into N_v voxels and solving the non-linear optimization problem

$$\underline{k}^2 = \operatorname{argmin}\left\{\|\underline{S}^{\text{meas}} - \underline{S}^{\text{calc}}(\underline{k}^2)\|_2\right\} \tag{2}$$

using an iterative Gauss-Newton algorithm. In (2), the 1984-element vectors $\underline{S}^{\text{meas}}$ and $\underline{S}^{\text{calc}}$ contains the measured and calculated data, respectively, in either the complex phasor formulation or in the log-phase formulation. The vector $\underline{k}^2$ holds the squared complex wave numbers. When the complex phasor formulation is used, the elements in the vectors holding the measured and calculated data are given by $\Re\{S_{rt,\text{object}}\} - \Re\{S_{rt,\text{empty}}\}$ and $\Im\{S_{rt,\text{object}}\} - \Im\{S_{rt,\text{empty}}\}$, that is, the real and imaginary parts of the difference in the measured or calculated S parameters between a measurement/calculation with an object in the system and a measurement/calculation with no object in the system. When using the log-phase formulation, the elements of the vectors are given by $\log|S_{rt,\text{object}}| - \log|S_{rt,\text{empty}}|$ and $\angle S_{rt,\text{object}} - \angle S_{rt,\text{empty}}$. For high-contrast targets, the change in phase may lie outside $\pm\pi$, and the phase is unwrapped using a method similar to that outlined in [1].

In each iteration of the Gauss-Newton algorithm, the forward data $\underline{S}^{\text{calc}}$ is calculated using a volume integral equation [7] and from the results, the corresponding Jacobian is determined using perturbation theory. The Jacobian $\underline{\underline{J}}_n$ is then used for solving for the update of the constitutive parameters $\underline{\Delta k}_n$ using

$$\underline{\underline{J}}_n\,\underline{\Delta k}_n^2 = \underline{S}^{\text{meas}} - \underline{S}^{\text{calc}}(\underline{\Delta k}_n^2). \tag{3}$$

This equation is ill-posed and regularization must therefore be applied to determine the update vector. The updated values of the constitutive parameters are then found as

$$\underline{k}_{n+1}^2 = \underline{k}_n^2 + \underline{\Delta k}_n^2. \tag{4}$$

Depending on the formulation of the problem, the Jacobian must be given in either its complex form or its log-phase formulation. The latter is easily found from the complex form by application of the chain rule.

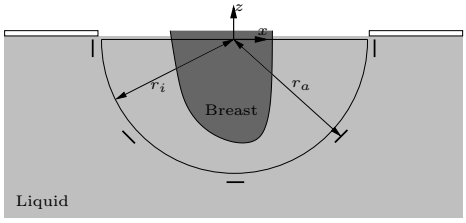

Figure 1: Schematic of the PAT Scanner. The 32 antennas are positioned in a hemispherical setup with radius $r_a = 8$ cm and the imaging domain has a radius of $r_i = 7.5$ cm. The breast is suspended through an aperture in the lid of the measurement tank.

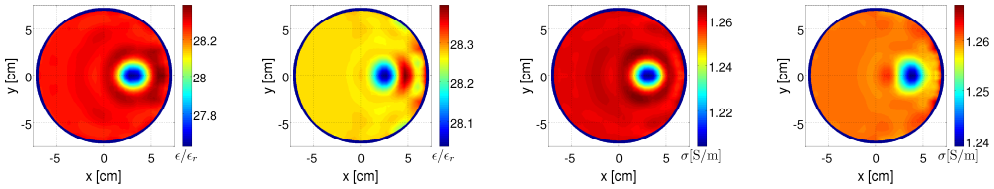

(a) Lp, perm. (b) Ph, perm. (c) Lp, cond. (d) Ph, cond.

Figure 2: Reconstructed permittivity and conductivity images of the scatterer (x-y plane for constant $z = -2$ cm). The images obtained using the log-phase formulation are shown in (a) and (c) and are seen to reconstruct the actual constitutive parameters and position of the scatterer better than the images obtained using the complex phasor notation shown in (b) and (d). Note the different color scales.

Results

The effect of using the log-phase formulation is illustrated by the reconstruction of a simulated data set using the frequency 1100 MHz. The coupling liquid has a relative permittivity of $\epsilon_{r,\mathrm{cl}} = 28.27$ and conductivity $\sigma_{\mathrm{cl}} = 1.26$ S/m. A local coordinate system with origin at the center of the aperture in the lid of the imaging system is introduced and a single, spherical scatterer with a radius of 1 cm is positioned with its center at $(x_{c_1}, y_{c_1}, z_{c_1}) = (3, 0, -2)$ cm. The scatterer has a relative permittivity of $\epsilon_{r,\mathrm{s}_1} = 27$ and a conductivity of $\sigma_{\mathrm{s}_1} = 1.15$ S/m and is thus a low-contrast scatterer. The results of the reconstructions are seen in Figure 2 where the color scales have been chosen individually for the two reconstructions to better show the effect of the log-phase algorithm. It is seen that both algorithms detect the position of the scatterer and reconstruct the approximate size of the scatterer. The log-phase formulation, however, is closer to reconstructing the actual constitutive parameters and position of the scatterer. Furthermore, when using the complex phasor notation, the relative level of the artifacts in the images is greater than when using the log-phase formulation.

The results shown here are typical for small scatterers in the lossy coupling liquid where the log-phase formulation benefits from emphasizing the small absolute but large relative changes in the scattering parameters measured between antennas on opposite sides of the imaging system, containing the most information on the scatterer. For larger objects, the log-phase formulation benefits not only from emphasizing the large relative changes but also from the additional information available

in the unwrapped phase. The algorithm using the complex phasor notation, on the other hand, fails completely when large, high-contrast objects are present in the imaging system. For imaging problems in a lossless environment, the two algorithms have similar performances as long as the change in phase is within $\pm\pi$. For changes in phase outside this interval, the log-phase formulation still performs better due to the additional information available in the unwrapped phase.

Conclusion

The log-phase formulation has been applied to a three-dimensional microwave imaging problem. When compared to the images obtained using the usual complex phasor notation, the log-phase formulation shows a significant improvement in the quality of the reconstructed images.

Acknowledgments

The Danish Technical Research Council is acknowledged for supporting the work of T. Rubæk, P. Meincke, and O. S. Kim. The authors also thank the researchers with The Microwave Imaging Group at Dartmouth College, and Dr. P. M. Meaney in particular, for their cooperation and inputs.

References

[1] P. Meaney, *et al.*, "Microwave image reconstruction utilizing log-magnitude and unwrapped phase to improve high-contrast object recovery," *Medical Imaging, IEEE Transactions on*, vol. 20, no. 2, pp. 104–116, 2001.

[2] T. C. Williams, E. C. Fear, and D. T. Westwick, "Tissue sensing adaptive radar for breast cancer detection - investigations of an improved skin-sensing method," *IEEE Transactions on Microwave Theory and Techniques*, vol. 54, no. 4, pp. 1308–1313, 2006.

[3] X. Li, *et al.*, "An overview of ultra-wideband microwave imaging via space-time beamforming for early-stage breast-cancer detection," *Antennas and Propagation Magazine, IEEE*, vol. 47, no. 1, pp. 19–34, 2005.

[4] S. Semenov, *et al.*, "Three-dimensional microwave tomography: initial experimental imaging of animals," *Biomedical Engineering, IEEE Transactions on*, vol. 49, no. 1, pp. 55–63, 2002.

[5] R. Nilavalan, *et al.*, "Numerical analysis of microwave detection of breast tumours using synthetic focussing techniques," *Antennas and Propagation Society Symposium, 2004. IEEE*, pp. 2440–2443 Vol.3, 2004.

[6] S. Poplack, *et al.*, "Electromagnetic breast imaging: average tissue property values in women with negative clinical findings," *Radiology*, vol. 231, no. 2, pp. 571–580, 2004.

[7] O. Kim, *et al.*, "Method of moments solution of volume integral equations using higher-order hierarchical legendre basis functions," *Radio Science*, vol. 39, RS5003, sep 2004.

Conference Paper 3

Application of the Log-Phase Formulation for Three-Dimensional Microwave Imaging

Tonny Rubæk, Peter Meincke, Oleksiy Kim, Paul M. Meaney, and Keith D. Paulsen

Status:
Conference: European Conference on Antennas and Propagation 2007, Edinburgh, Scotland
Published: 2007

APPLICATION OF THE LOG-PHASE FORMULATION FOR THREE-DIMENSIONAL MICROWAVE IMAGING

T. Rubæk*, P. Meincke*, O.S. Kim*, P.M. Meaney†, K.D. Paulsen†

*Technical University of Denmark, Denmark, [tru/pme/osk]@oersted.dtu.dk

†Thayer School of Engineering, Dartmouth College, USA, [paul.m.meaney/keith.d.paulsen]@dartmouth.edu

Keywords: Microwave imaging, electromagnetic inverse scattering, inverse problems, cancer.

Abstract

The performance of a three-dimensional reconstruction algorithm for microwave breast cancer detection is compared with that of a two-dimensional reconstruction algorithm. Both algorithms are based on inverse scattering and the configuration of the imaging system is the same in both cases. In the imaging system, data is collected at seven different planes and it is found that by combining the data from these seven planes, and performing the reconstruction for the entire three-dimensional imaging domain, better results are obtained than when the two-dimensional algorithm is applied for reconstructing each of the planes separately.

1 Introduction

It is a well-established fact that malignant breast tumors have different constitutive parameters in the microwave frequency spectrum than those of normal breast tissue [1-3]. This contrast implies that microwave imaging is suitable for detecting breast cancer [4].

One type of microwave imaging is based on non-linear inverse scattering. With this method one seeks to determine the distribution of constitutive parameters, that is, permittivity and conductivity, in the imaging domain by solving a non-linear inverse problem. The forward model used in the reconstruction is based on the frequency-domain formulation of Maxwell's equations, and the input used is the measured response on a number of receiving antennas when a single antenna is transmitting. Since the measurements and reconstructions are done at a single frequency, the problem of accurately modelling dispersion effects, encountered in wideband techniques, is avoided. Although the application of an exact forward model based on Maxwell's equations increases the complexity of the problem, the result is an algorithm capable of reconstructing quantitative images, even when large regions of the imaging domain have unknown constitutive parameters that are different from those of the known background.

At Dartmouth College, a microwave imaging system in which the images are reconstructed using a two-dimensional (2-D) non-linear inverse-scattering based reconstruction algorithm is currently being tested [3,5]. In this system, the data is collected by moving an array of 16 antennas along the breast to be examined, collecting data in seven so-called imaging planes.

The use of a 2-D algorithm to reconstruct what is inherently a three-dimensional (3-D) problem introduces inaccuracies in the reconstructed images. The 2-D configuration has, however, some appealing features in that it is more simple than the 3-D configuration, both in terms of the imaging system hardware and in terms of the computational requirements. A reconfiguration of the hardware of the imaging system to optimize it for 3-D inversion is a cumbersome and expensive process, whereas a replacement of the inverse-scattering based reconstruction algorithm is a more simple task. Combining this with the fact that still faster and less expensive computers are available, which are able to handle the additional computational demands of the 3-D algorithm, implies that it is of interest to investigate how much the reconstructed images can be improved by applying a 3-D reconstruction algorithm to the data collected by the 2-D imaging system.

In this paper, the impact of applying a 3-D reconstruction algorithm to data collected using the 2-D imaging system is investigated. Although the imaging system is not designed for 3-D imaging as such, with the data being collected only from measurements with antennas in the same plane, the relatively high total number of transmit-receive combinations means that a 3-D reconstruction is possible.

The paper is organized as follows. In Section 2, a brief introduction to the imaging system is given and the reconstruction algorithms are presented in Section 3. In Section 4, the results obtained using the 2-D and 3-D algorithms are compared.

2 Imaging system

The imaging system consists of a circular array with 16 antennas which are moved along the breast to be examined. During the exam, the patient lies prone on top of the imaging system with her breast suspended through an aperture in the top of the measurement tank. The tank is filled with a coupling liquid to maximize the amount of energy coupled to the interior of the breast. A schematic of the circular array is shown in Fig. 1. The imaging domain, in which the breast is assumed to be confined, has a radius of 7.25 cm and in the case of the 3-D algorithm, the imaging domain is extended into the three-dimensional shape of a cylinder with a length of 10 cm.

During patient exams, the antenna array is moved to seven positions, 1 cm apart in the z direction with the upper plane, referred to as plane 1, being located at $z=-2$ cm. Each of the 16 antennas, in turn, is used to transmit while the response is measured with the remaining 15 antennas, yielding a total of 240 transmit-receive combinations for each plane.

3 Reconstruction algorithms

Both 2-D and 3-D reconstruction algorithms are applied in this paper to reconstruct images of the simulated measurements. The major difference between these two reconstruction algorithms is the assumptions made on the scattering problem. In the 2-D reconstruction algorithm it is assumed that the scattering problem can be represented as a 2-D problem in each of the seven imaging planes. Hence, for each measurement, seven individual reconstructions are applied to investigate the entire 3-D imaging domain. For the 3-D reconstruction algorithm, the full vectorial scattering problem is considered and only a single reconstruction is applied to determine the distribution of constitutive parameters in the entire imaging domain. Both reconstruction algorithms are based on the same Newton algorithm, to be described in the following section.

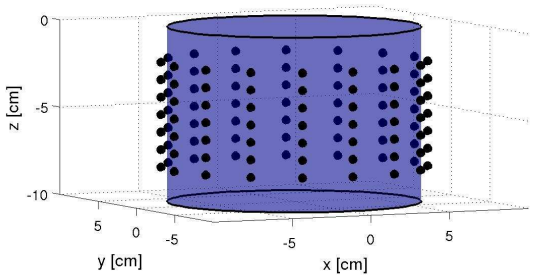

Fig. 1: Schematic of imaging system. The antenna positions are represented by the black dots and the imaging domain by the blue cylinder.

3.1 Newton algorithm

When inverse scattering is used for microwave imaging, the reconstructed images show the distribution of the constitutive parameters, permittivity and conductivity, in the imaging domain.

In both reconstruction algorithms, the images are reconstructed by solving the ill-posed non-linear optimization problem

$$k^2 = \operatorname{argmin}\left\{\left\|S^{\text{l-p}}_{\text{meas}} - S^{\text{l-p}}_{\text{calc}}(k^2)\right\|_2^2\right\} = \operatorname{argmin}\left\{\left\|\underline{S}^{\text{l-p}}_{\text{res}}(\underline{k}^2)\right\|_2^2\right\}. \quad (1)$$

In this expression, $\underline{S}^{l-p}_{meas}$ is a vector holding the measured data and $\underline{S}^{l-p}_{calc}$ is a vector holding the data calculated for a given distribution of squared complex wave numbers given by the vector $\underline{k}^2$. The superscript "l-p" in this expression indicates that the signals are used in their log-amplitude unwrapped phase (log-phase) formulation. When using this formulation, the signals are represented by the change in the unwrapped phase and the logarithm of the amplitude, as opposed to the more commonly used difference in real and imaginary parts resulting from the use of the complex phasor notation of the signals. This formulation has shown to be able to deal with phase changes in the measured signals of more than 180° and to emphasize the large relative changes in signals measured on antennas on opposite sides of the

scattering object rather than the large absolute changes measured on antennas close to the transmitter, thereby leading to better results [6,7]. The signal for each of the combinations of transmitter and receiving antenna is thus represented by two elements in the vectors $\underline{S}^{l-p}$

$$S^l = \log|S_{obj}| - \log|S_{empty}| \quad (2a)$$

$$S^p = \measuredangle S_{obj} - \measuredangle S_{empty} \quad (2b)$$

wherein the subscripts "obj" and "empty" indicate whether the imaging system is empty or an object is present when the measurement is done.

The Newton algorithm consists of three steps in each iteration:

1. The forward problem is solved and the Jacobian matrix of the problem is found.
2. The update in Newton iteration n is found by solving

   $$\Delta \underline{k}_n^2 = \text{argmin}\left\{\left\| \underline{\underline{J}}_n \Delta \underline{k}_n^2 - \underline{S}_{res}^{l-p}(\underline{k}_n^2)\right\|_2^2\right\} \quad (3)$$

   subject to a suitable regularization. Herein, $\underline{\underline{J}}_n$ denotes the Jacobian matrix. An over-regularizing Conjugate Gradient Least Squares (CGLS) algorithm is applied to solve (3).
3. The distributions of the squared wave numbers are updated as

   $$\underline{k}_{n+1}^2 = \underline{k}_n^2 + \alpha_n \Delta \underline{k}_n^2 \quad (4)$$

   where α_n denotes the Newton step.

Both the 2-D and 3-D reconstruction algorithms converge after 10-15 iterations. In both cases the initial distribution of the squared wave numbers is chosen to be a uniform distribution of the background constitutive parameters.

3.2 2-D algorithm

In the 2-D algorithm, the antennas are assumed to be point sources and the forward solver is based on the hybrid-element algorithm in which the scattering problem is solved using a circular mesh with a radius of 7.25 cm, discretized using 559 nodes [8]. The total time used for solving the forward problem and calculating the Jacobian matrix is just under one minute per iteration.

3.3 3-D algorithm

In the 3-D algorithm, the forward solution is calculated using a method-of-moments code in which the related volume integral equation is solved using the adaptive integral method [9]. The imaging domain is a cylinder extending from z=0 cm to z=-10 cm with the same radius (7.25 cm) as the imaging domain used in the 2-D algorithm, discretized in 13300 cubic cells with a side length of 5 mm. The total time per Newton iteration in this algorithm is approximately 90 minutes.

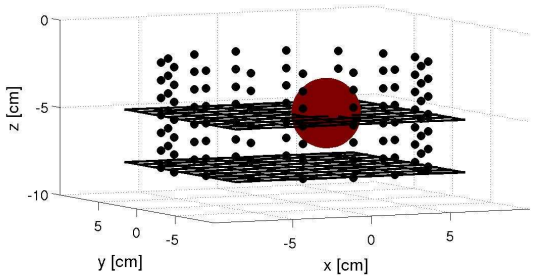

Fig. 2: Schematic of the sphere inserted in the imaging domain. The two imaging planes 4 and 7 are shown in the figure.

4. Results

To illustrate the performance of the imaging system when the 2-D and 3-D algorithms are applied for the image reconstruction, a spherical scatterer with radius 2 cm is positioned in the imaging system. In the simulation, the sphere has the permittivity $\epsilon_{r,\text{sp}}=50$ and conductivity $\sigma_{\text{sp}}=1.11$ S/m and its centre is positioned at $(x,y,z)=(2,0,-5)$ cm in a background medium with relative permittivity $\epsilon_{r,\text{bg}}=21.45$ and conductivity $\sigma_{\text{bg}}=1.11$ S/m. The frequency is 1.1 GHz and the transmitting antenna is accepting a power of 0 dBm. Gaussian noise mimicking a system noise floor of -100 dBm has been added to the data. This configuration is shown in Fig. 2, in which imaging planes 4 and 7 are also visible.

The results of applying the 2-D reconstruction algorithm to imaging plane 4, which is located at $z=-5$ cm through the center of the sphere, are shown in Figs. 3 and 4. In these images the sphere is clearly visible at the correct position. The reconstructed value of the permittivity is a little too low and the size of the scatterer is also a little too small. The reconstructed conductivity shows a slightly reduced conductivity (approximately 15% below the background value) at the position of the scatterer compared to the

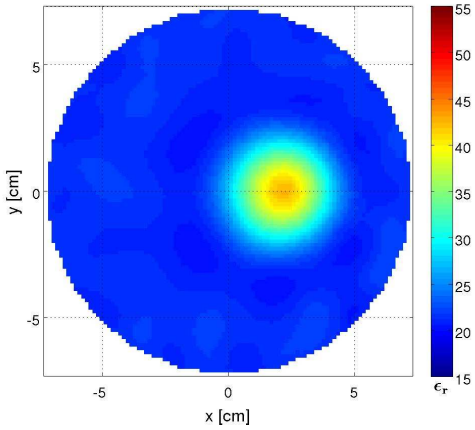

Fig. 3: Permittivity reconstructed using the 2-D algorithm for plane 4 (through the centre of the sphere).

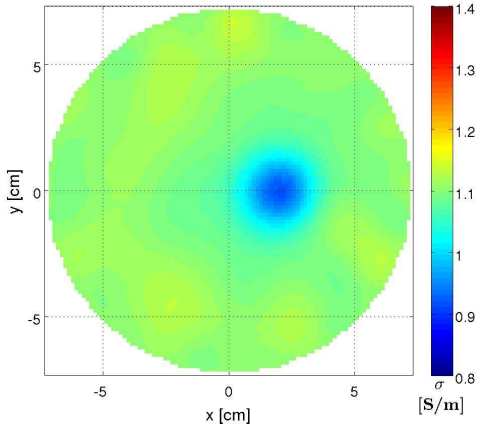

Fig. 4: Conductivity reconstructed using the 2-D algorithm for plane 4 (through the centre of the sphere).

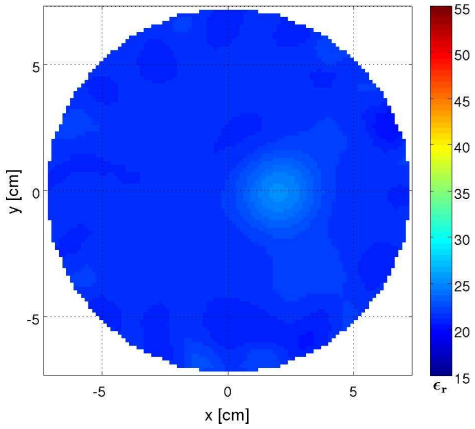

Fig. 5: Permittivity reconstructed using the 2-D algorithm for plane 7 ($z=-8$ cm).

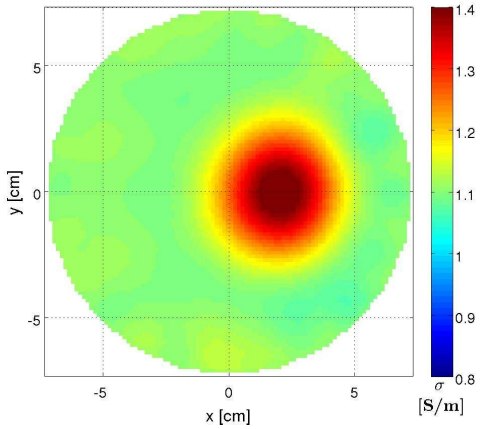

Fig. 6: Conductivity reconstructed using the 2-D algorithm for plane 7 ($z=-8$ cm).

background. This should of course not be present since the scatterer has the same conductivity as the background. However, the overall results are acceptable and fulfils the requirements for a successful reconstruction. In Figs. 5 and 6 the permittivity and conductivity images for imaging plane 7 at $z=-8$ cm are shown. This plane is positioned 1 cm below the sphere and should therefore not show any contrast. In the permittivity image, a region of slightly elevated permittivity is seen at the position of the scatterer, but the overall image is very well reconstructed. The conductivity image, on the other hand, shows a large region of elevated conductivity at the position of the scatterer, although the scatterer is not present in this imaging plane. The presence of this high-valued zone clearly illustrates that the assumption of a 2-D scattering problem can cause problems and considerable inaccuracies in the reconstructed images.

In Figs. 7 and 8, the permittivity and conductivity reconstructed using the 3-D algorithm in plane 4 ($z=-5$ cm) are shown. The position and size of the spherical scatterer are clearly visible. The reconstructed permittivity of the scatterer is somewhat closer to the actual value than what was found using the 2-D algorithm. The conductivity is slightly elevated at the position of the scatterer with the reconstructed values approximately 10% above that of the background. The overall quality of the reconstruction is slightly better than that of the 2-D reconstruction due to the fact that the size and value of the permittivity are reconstructed more accurately. In Figs. 9 and 10, the reconstructed permittivity and conductivity in plane 7 ($z=-8$ cm) are shown. In the permittivity image a region of slightly elevated values is seen. The conductivity image shows only a low-valued random variation caused by the

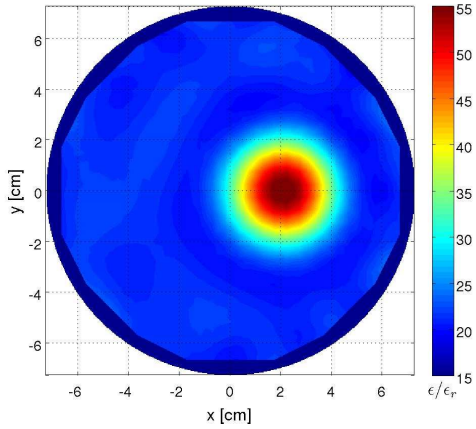

Fig. 7: Permittivity reconstructed using the 3-D algorithm for plane 4 (through the centre of the sphere).

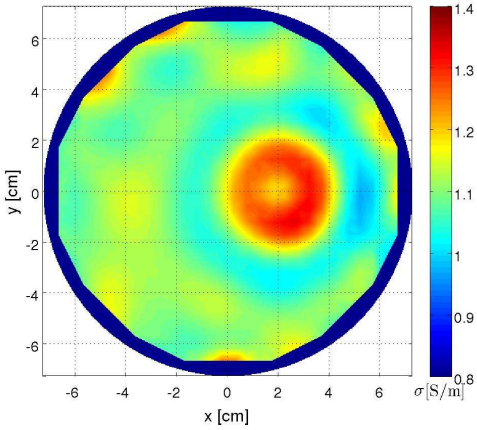

Fig. 8: Conductivity reconstructed using the 3-D algorithm for plane 4 (through the centre of the sphere).

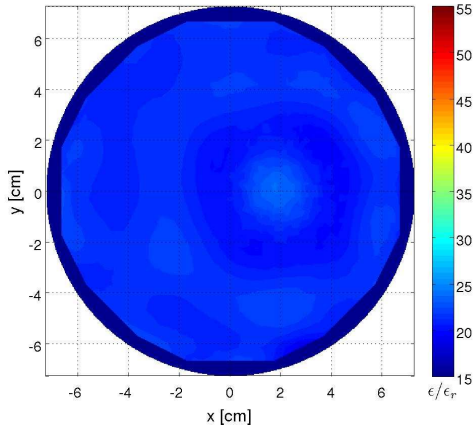

Fig. 9: Permittivity reconstructed using the 3-D algorithm for plane 7 ($z=-8$ cm).

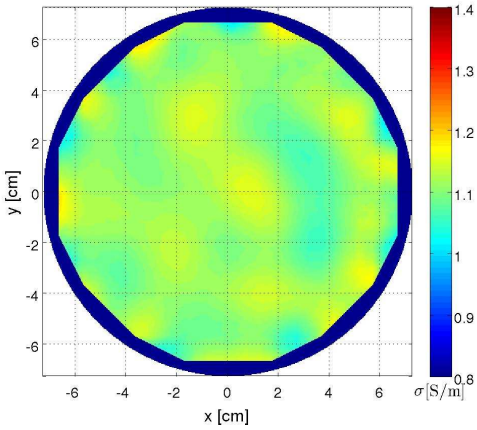

Fig. 10: Conductivity reconstructed using the 3-D algorithm for plane 7 ($z=-8$ cm).

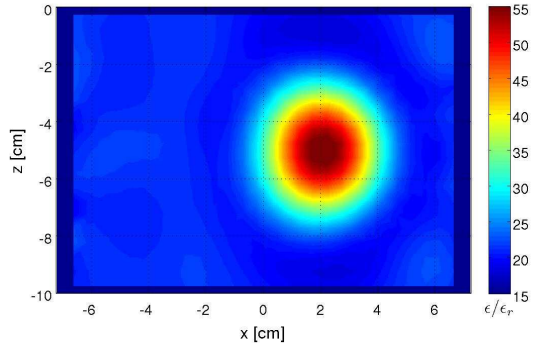

Fig. 11: Reconstructed permittivity in the plane $y=0$ cm.

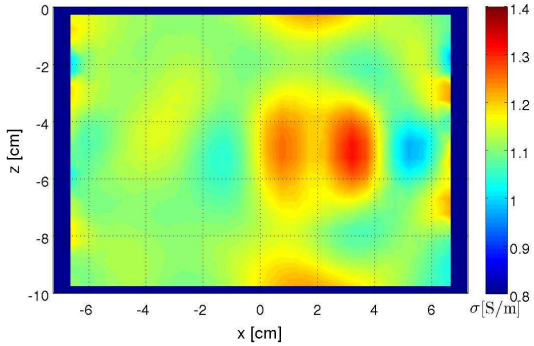

Fig. 12: Reconstructed conductivity in the plane $y=0$ cm.

added Gaussian noise. This is a significant improvement compared to the images reconstructed using the 2-D algorithm in that the possibility for falsely assuming that a scattering object is present at this position. Finally, in Figs. 11 and 12 the reconstructed permittivity and conductivity in the xz plane $y=0$ cm are shown obtained using the 3-D algorithm. In the permittivity image the spherical scatterer is clearly visible. The quality of the reconstruction is much like that found in plane 4, with both the position and permittivity of the scatterer correctly reconstructed. The conductivity image shows some artifacts at the position of the scatterer, but the overall reconstruction quality is very good.

5. Conclusion

By applying a 3-D reconstruction algorithm for non-linear inverse scattering on data collected by a system designed for 2-D inverse scattering it is possible to achieve a significant improvement in the ability of the imaging system to correctly locate scattering objects. This is of great importance and use since a change of the imaging algorithm is much easier than changing the measurement hardware of the imaging system.

References

[1] T. S. England, N. A. Sharples. "Dielectric properties of the human body in the microwave region of the spectrum", *Nature*, **163**, pp. 487-488, (1949).

[2] M. Lazebnik, L. McCartney, D. Popovic, C. B. Watkins, M. J. Lindstrom, J. Harter, S. Sewall, A. Magliocco, J. H. Booske, M. Okoniewski, S. C. Hagness. “A large-scale study of the ultrawideband microwave dielectric properties of normal breast tissue obtained from reduction surgeries”, *Physics in Medicine and Biology*, **52**, pp. 2637-2656, (2007).

[3] S. P. Poplack, T. D. Tosteson, W. A. Wells, B. W. Pogue, P. M. Meaney, A. Hartov, C. A. Kogel, S. K. Soho, J. J. Gibson, K. D. Paulsen. "Electromagnetic breast imaging: results of a pilot study in women with abnormal mammograms", *Radiology - Radiological Society of North America*, **243**, pp. 350-359, (2007).

[4] E. C. Fear, P. M. Meaney, M. A. Stuchly. "Microwaves for breast cancer detection?", *IEEE Potentials*, **22**, pp. 12-18, (2003).

[5] D. Li, P. M. Meaney, T. Raynolds, S. A. Pendergrass, M. W. Fanning, K. D. Paulsen. “A broadband microwave breast imaging system”, *Proceedings of Bioengineering Conference*, pp. 83-84, (2003).

[6] P. M. Meaney, K. D. Paulsen, B. W. Pogue, M. I. Miga. “Microwave image reconstruction utilizing log-magnitude and unwrapped phase to improve high-contrast object recovery”, *IEEE Trans. on Medical Imaging*, **20**, pp. 104-116, (2001).

[7] P. M. Meaney, Q. Fang, T. Rubæk, E. Demidenko, K. D. Paulsen. "Log transformation benefits parameter estimation in microwave tomographic imaging", *Medical Physics*, **34**, pp. 2014-2023, (2007).

[8] K. D. Paulsen, P. M. Meaney, M. J. Moskowitz, J. M. Sullivan. "A dual mesh scheme for finite element based reconstruction algorithms", *IEEE Trans. on Medical Imaging*, **14**, 504-514, (1995).

[9] O. S. Kim, P. Meincke. ”Adaptive integral method for higher-order hierarchical method of moments”, *Proc. of the European Conference on Antennas and Propagation EuCAP 2006*, (2006).